

# **Integrated Design, Optimization, and Experimental Realization of a Steam-Driven Micro Recirculation Fan for Solid Oxide Fuel Cell Systems**

**Thèse N° 9337**

Présentée le 28 février 2019

à la Faculté des sciences et techniques de l'ingénieur  
Laboratoire de conception mécanique appliquée  
Programme doctoral en énergie

pour l'obtention du grade de Docteur ès Sciences

par

**Patrick Hubert WAGNER**

Acceptée sur proposition du jury

Prof. F. Maréchal, président du jury  
Prof. J. A. Schiffmann, Dr J. Van Herle, directeurs de thèse  
Prof. A. F. Massardo, rapporteur  
Prof. J. Brouwer, rapporteur  
Dr P. Ott, rapporteur

2019



To my uncle Balthasar "Baldi" Lange...



# Acknowledgements

I would like to express my sincere gratitude to:

- Everyone that was directly or indirectly involved in the **RECOGEN** project, but especially:
- Professor Jürg Schiffmann, for having accepted me as a student in his young and dynamic group, providing such an interdisciplinary topic to me. He gave me the opportunity to build something from scratch and to implement many of my own ideas, while sharing with me his profound knowledge on gas film bearings, and helping me with the rotor, bearing, and mechanical design.
- Dr. Jan Van herle, for the excellent experience he facilitated at the SOFC XIV conference in Glasgow and the Modval 13 conference in Lausanne, his guidance and help throughout my thesis, and for leading the RECOGEN project.
- Dr. Zacharie Wullemin, for his dedication to making the fuel cell technology viable, his comments, suggestions, and his indispensable help during the in-situ testing of the fan-turbine unit.
- Dr. Stefan Diethelm, for co-organizing the RECOGEN project and his advice on estimating the carbon deposition risk in the reformer.
- David Constantin, for his help with mechanical parts, building up the test rigs, assisting with the experimentation, and for all of his efforts, dedication, and sleepless nights.
- SOLIDpower and its recent and former employees (Dr. Antonello Nesci, Dr. Arata Nakajo, Cédric Beetschen, Christian Scherrer, Fabrice Scherer, Florian Waeber, Dr. Mardit Matian, Dr. Siu Fai, Sylvain Dajoz, and Yannik Antonetti), for helping with the SOFC system simulation and realizing the possibility of in-situ testing the fan-turbine unit coupled with an SOFC.
- Olivier Bucheli, for providing insights into SOLIDpower and its products.
- The entire team of the IPESE laboratory, but especially Professor François Maréchal, for providing the OSMOSE package, advice, and feedback on the system simulation and optimization.
- Professor em. Daniel Favrat, for recommending me to Professor Jürg Schiffmann and for decades dedicated to research in the energy field.
- Dr. Julie Lenoble and Chantal Donaaghey, for their administrative organization of my doctoral studies, as well as the RECOGEN project.
- Cécile Taverney, for her kindness and all the organization within the EDEY doctoral program.
- The Canton de Vaud, for providing the project's funding and the evaluation board (Christoph Hadorn, Dominique Reynmond, Ivan Gomez, Jean-Michel Stauffer, and Lea Tchoumi).

## Acknowledgements

---

- The entire **Group of Energy Materials (GEM)**, but especially:
  - Vaibhav Singh, for his contributions to the SOFC system simulation and optimization, his advice on OSMOSE and Belsim Vali, and for the kind collaboration.
  - Dr. Priscilla Caliandro, for her advice and help with the SOFC system simulation and optimization.
  - Isha Shukla, for her contributions to the SOFC system simulation and optimization.
  - Nicola Accardo for the scanning electron microscope analysis of the turbine stator deposits.
- 
- All recent and former employees of the **Laboratory for Applied Mechanical Design (LAMD)**, for their kind help and contributions to this thesis, but especially:
  - Christoph Darioli, for sharing his profound knowledge on experimentation and mechanical design.
  - Dr. Violette Mounier, for introducing me to the “art of rotor balancing”.
  - Markus Diehl, for the many discussions about turbomachines, the student projects that we supervised together, and his feedback and suggestions on the fan blade tip clearance study.
  - Dr. Adeel Javed, for sharing his profound knowledge of turbomachinery with me, his advice on turbomachinery design, and for helping me with the numerical simulations.
  - Dr. Ceyhun Sahin, for her advice and help with setting up the experiments and her idea to measure the rotational speed via the blade passing frequency.
  - Dr. Lili Gu, for the internship that we supervised together, as well as for her help in better understanding the spiral-grooved thrust bearing and the involved leakage phenomena.
  - Kossi Agbeviade, for helping me with the electronics and the differential capacitance manometers.
  - Dr. Ansgar Weickgenant, for helping me troubleshoot my experimental setup.
  - Cyril Picard, for his help with any IT problem and his efforts to advance the laboratory’s IT infrastructure.
  - Elliott Guenat, for sharing with me his profound knowledge on gas film bearings.
  - Dr. Karim Shalash, for all the discussions we had and for sharing his profound knowledge on foil gas film bearings.
  - Thierry Mesot, for his kind help, as well as the climbing and skiing excursions.
  - Eric Olmedo, for proofreading the chapter conclusions, as well as being an excellent colleague, flatmate, and friend.
  - All the students with whom I worked (Arno Aeschbacher, Bastien Rauzier, Conti Romain, Cyril Picard, Dirix Pietro, Emmanuelle Burdet, Etienne Droz, Jordan Holweger, Julien Schneider, Konstantinos Drakopoulos, Luca Massera, Marcos Armenteras Font, Pierre Nibourel, Rémi Beall, Timothée Frei, and Tom Voiblet), for their collaboration, motivation, and contributions to this thesis.

- Every person that assisted me with **technical challenges**, but especially:
  - The industrial manufacturing partner, for the excellent cooperation.
  - The two teams in the mechanical workshops of ATPR and ATME , but especially to Marc Jeanneret, for the help and discussions on mechanical design.
  - Joël Currit, for his fast, uncomplicated, and professional help with any mechanical parts.
  - Professor Herbert Shea, for providing me access to his microscopy facilities.
  - Dr. Peter Van der Wal, for his detailed introduction to the light microscope.
  - Karl Ilg, for his profound explanation and detailed help with the quarter circle nozzle volume flow rate measurement device.
  - Andreas Losenegger, for helping troubleshoot the Coriolis mass flow rate measurement device.
- 
- The **jury members** (Dr. Peter Ott, Professor Artistide Massardo, and Professor Jack Brouwer) for their helpful feedback and suggestions.
- 
- The Electrochemical Society, Inc for providing the permission of reproducing and altering Figure 2.2, its original version was published in [1].
  - John Wiley & Sons Limited for providing the permission of publishing and altering Figure 2.5, its original version was published in [2].
  - David Constantin for providing the permission of publishing and altering Figure 6.1 b) and c), its original version was unpublished.
- 
- All of my **friends**, but especially:
  - Dr. Luis Mendoza and Dr. Marianna Figuera, for all the pleasant moments we spent together.
  - Dr. David Forrest, for his hospitality in Glasgow (long live Scotland!).
  - David Alloun, Daniel Pinto, and Hedi Romani, for their friendship.
  - Fabian Gerlinghaus and Markus Lehmann, for accepting and supervising an EPFL student, their hospitality in San Francisco, showing me their start-ups, and the great time we had together in Black Rock City.
  - Alexander Zehler, Otto Brandstetter, and Timo Kalks for their long friendship.
- 
- All of my **family** for their efforts and support, but especially:
  - My uncle Hubert Wagner.
  - My grandmother Karin Wagner and my grandfather Georg Wagner.
  - My grandmother Kunigunda Dippold and my grandfather Helmuth Dippold.
  - My aunt Monika Lange, for her visits to Neuchâtel, her understanding, and her never-ending support.
  - My father Lorenz Wagner, my mother Manuela Wagner, and my sister Melissa Wagner, for all the energy, confidence, and always being there.





# Abstract

This thesis presents the results of the design and experimental investigation of a patented 10 kW<sub>el</sub> SOFC system with a thermally-driven anode off-gas recirculation (AOR) fan, the so-called fan-turbine unit (FTU). The system has the advantage of higher global fuel utilization, and thus higher efficiencies and/or lower local fuel utilization, increasing the fuel cell stack lifetime. Electrical net DC efficiencies, based on the lower heating value (LHV) of 65 % for a global fuel utilization of 92 % are demonstrated with a system simulation and optimization. This correlates to an electrical gross DC efficiency based on the LHV of 69 %. Additionally, the waste heat of the SOFC stack can be used for local cogeneration in heating or cooling applications leading to a net utilization ratio (cogeneration of heat and electricity) of 90 %. Other advantages of this system design include the absence of a water supply, a simplified water treatment system, and the reduction of the evaporator and pump component size, which reduces the system's initial and maintenance costs.

A first FTU proof-of-concept was designed, manufactured, and extensively experimentally tested. The radial inducer-less fan with a tip diameter of 19.2 mm features backward-curved prismatic blades with a constant height. Prior to coupling the recirculation fan with the SOFC, the fan was experimentally characterized with air at 200 °C. At the nominal operational point of 168 000 rpm, the measured inlet mass flow rate was 4.9 kg h<sup>-1</sup> with a total-to-total pressure rise of 55 mbar, an isentropic total-to-total efficiency of 55 %, and a power of 18 W. Although the consumed fan power is very low, this FTU can increase the net efficiency of a 10 kW<sub>el</sub> SOFC system by five percentage points.

The fan and shaft are propelled by a radial-inflow, partial-admission (21 %), low-reaction (13 %) steam turbine with prismatic blades. This turbine has a diameter of 15 mm and consists of 59 rotor blades with a radial chord of 1 mm and a blade height of 0.6 mm. At the design point, it has a total-to-total pressure ratio of 1.9, an inlet mass flow rate of 2.1 kg h<sup>-1</sup>, and an isentropic total-to-static efficiency of 38 %, yielding a power of 36 W. To the best of the author's knowledge, it is one of the smallest steam turbines in the world.

The shaft features one single-sided spiral-grooved thrust and two herringbone-grooved journal

## Abstract

---

gas film bearings. Nominally, these bearings operate with water vapor at temperatures up to 220 °C. The bearings were tested with ambient air, hot air, and water vapor to rotational speeds up to 220 000 rpm, suggesting very stable operation (rotor orbit less than 0.002 mm). Within this work, the recirculation unit operated for more than 300 hours.

In a final step, the FTU was coupled in-situ to a 6 kW<sub>el</sub> SOFC system, reaching electrical gross DC efficiencies, based on the LHV, of 66 % in part load (4.5 kW<sub>el</sub>) and 62 % in full load (6.4 kW<sub>el</sub>) for a global fuel utilization of 85 %. To the best of the author's knowledge, this was the first time that a steam-driven AOR fan was demonstrated in-situ with an SOFC system.

Keywords: steam-driven recirculation fan, gas film bearing, solid oxide fuel cell, anode off-gas, radial turbomachinery, optimization, integrated design, experimental testing

# Résumé

Cette thèse présente les résultats de la conception et des essais expérimentaux d'un système breveté de pile à combustible à oxyde solide (SOFC) de  $10 \text{ kW}_{el}$  équipé d'un recirculateur du gaz d'échappement de l'anode, nommé fan-turbine unit (FTU). Le système a l'avantage d'une utilisation globale du combustible élevée entraînant une augmentation de l'efficacité du système et/ou une utilisation locale du combustible diminuée augmentant la durée de vie de la pile SOFC. Une simulation et optimisation du système SOFC prédit une efficacité électrique (DC) net basée sur le pouvoir calorifique inférieur de 65 % pour une utilisation globale du combustible de 92 %. Cela correspond à une efficacité électrique (DC) brut basée sur le pouvoir calorifique inférieur de 69 %. De plus, la chaleur résiduelle de la pile SOFC est utile pour une cogénération (chaleur et électricité) qui résulte en taux d'énergie utile net de 90 %. Des avantages supplémentaires sont l'absence d'une prise de l'eau, un système traitement de l'eau simplifié et réduction de la de l'évaporateur et de la pompe, ce qui permet de réduire les coûts d'investissement et d'exploitation.

Une première preuve de concept du FTU a été conçue, fabriquée et expérimentée. Le ventilateur radial sans inducteur avec un diamètre de 19.2 mm a des aubes prismatiques et incurvées vers l'arrière avec une hauteur constante. Avant d'être couplé la SOFC, le ventilateur a été caractérisé expérimentalement avec de l'air à  $200 \text{ }^\circ\text{C}$ . Au point nominal avec une vitesse de rotation de 168000 rpm, le débit massique à l'entrée était de  $4.9 \text{ kg h}^{-1}$ , l'augmentation de la pression totale à totale est de 55 mbar, efficacité isentropique totale à totale de 55 % et la puissance de 18 W. Quand bien même la puissance du recirculateur est faible, le FTU peut augmenter l'efficacité de la pile SOFC de cinq points de pourcentage.

Le ventilateur et l'arbre sont propulsés par une turbine radiale à vapeur. Le vapeur entre radialement et l'injection est partielle, sur 21 % de la circonférence. Le degré de réaction est de 13 %. Cette turbine a un diamètre de 15 mm et se compose de 59 aubes de rotor avec une corde radiale de 1 mm et une hauteur de l'aube de 0.6 mm. Au point nominal, la turbine a un rapport de pression total à total de 1.9, un débit massique à l'entrée de  $2.1 \text{ kg h}^{-1}$  et une efficacité isentropique totale à statique de 38 % ce que donne une puissance de 36 W. Selon les connaissances de l'auteur, c'est l'une des plus petites turbines à vapeur du monde.

## Résumé

---

L'arbre a deux paliers à gaz avec des rainures en forme spirale et en chevron. Au point nominal, ces paliers fonctionnent avec de la vapeur d'eau à des températures jusqu'au 220 °C. Les paliers ont été testés avec de l'air ambiant, de l'air chaud et de la vapeur d'eau à des vitesses de rotation jusqu'à 220 000 rpm, ce qui suggère un fonctionnement très stable (orbite du rotor inférieure à 0.002 mm). Dans le cadre de ce travail, l'unité de recirculation a opéré plus de 300 heures.

Lors de la dernière étape, le FTU a été couplé in-situ à un système SOFC de 6 kW<sub>el</sub>. Le système a une efficacité électrique (DC) brut basée sur le pouvoir calorifique inférieur de 66 % pour une charge partielle (4.5 kW<sub>el</sub>) et 62 % pour une charge pleine (6.4 kW<sub>el</sub>). L'utilisation globale du combustible est 85 %. Selon les connaissances de l'auteur, c'est la première fois qu'un système SOFC équipé d'un recirculateur du gaz d'échappement de l'anode a été testé in-situ.

Mots clefs : ventilateur entraîné avec la vapeur, paliers à gaz, pile à combustible à oxyde solide, gaz d'échappement de l'anode, turbomachines radiales, optimisation, design intégré, essais expérimentaux

# Zusammenfassung

Diese Arbeit präsentiert das Design und die experimentelle Untersuchung eines patentierten  $10\text{ kW}_{\text{el}}$  Festoxidbrennstoffzellen (SOFC) Systems mit einem thermisch angetriebenen Anodenabgasrezirkulationsventilator, die sogenannte fan-turbine unit (FTU). Das System hat den Vorteil eines höheren globalen Brennstoffausnutzungsgrades was zu einem höheren Wirkungsgrad und/oder eines niedrigeren lokalen Brennstoffausnutzungsgrades was zu einer erhöhten Lebensdauer des SOFC-Stacks führt. Ein elektrischer DC Nettowirkungsgrad basierend auf dem unteren Heizwert von 65 % für einen globalen Brennstoffausnutzungsgrades von 92 % wird mit Hilfe einer Systemsimulation und -optimierung aufgezeigt. Dies entspricht einem elektrischen DC Bruttowirkungsgrad basierend auf dem unteren Heizwert von 69 %. Zusätzlich kann die Stack-Abwärme für lokale Kraft-Wärme-Kopplung genutzt werden wodurch ein Nettosystemnutzungsgrad von 90 % erreicht werden kann. Ein weiterer Vorteil des Systems ist die Nichtnotwendigkeit eines Wasseranschlusses, eine vereinfachte Prozesswasseraufbereitung und die Verkleinerung des Verdampfers und der Pumpe was eine Reduzierung der Investment- und Betriebskosten zur Folge hat.

Eine erster Demonstrator der FTU wurde entworfen, hergestellt und ausgiebig getestet. Der radiale Fan ohne Vorlaufrad mit einem Durchmesser von 19.2 mm hat rückwärtsgekrümmte prismatische Schaufeln mit konstanter Höhe. Vor dem Betrieb des Rezirkulationsventilators mit der SOFC wurde dieser mit Luft bei  $200\text{ °C}$  experimentell charakterisiert. Am nominalen Betriebspunkt bei  $168000\text{ U/min}$  war der Eintrittsmassenstrom  $4.9\text{ kg h}^{-1}$ , die Totaldruckerhöhung 55 mbar, der isentrope Gesamtwirkungsgrad 55 % und die Leistung 18 W. Obgleich die benötigte Ventilatorleistung sehr gering ist, kann die FTU den elektrischen Nettowirkungsgrades des  $10\text{ kW}_{\text{el}}$  SOFC-Systeme um fünf Prozentpunkte erhöhen.

Der Ventilator und die Welle werden von einer Dampfturbine mit prismatischen Schaufeln angetrieben. Diese Aktionsturbine mit einem Reaktionsgrad von 13 % wird radial durchströmt und ist teilbeaufschlagt (21 %). Die Turbine hat einem Durchmesser von 15 mm, 59 Rotor-schaufeln mit einer radialen Schaufeltiefe von 1 mm und einer Schaufelhöhe von 0.6 mm. Am Auslegungspunkt hat die Turbine ein Totaldruckverhältnis von 1.9, einen Eintrittsmassenstrom von  $2.1\text{ kg h}^{-1}$  und einen isentrope Gesamtwirkungsgrad von 38 % was einer Leistung von 36 W entspricht. Nach dem Kenntnisstand des Autors handelt es sich hierbei um eine der

## Zusammenfassung

---

kleinsten Dampfturbinen der Welt.

Die Welle weist pfeilförmige und spiralförmige Nuten auf, welche Teil der Gaslager sind. Während des Nominalbetriebes ist das Lagerfluid Wasserdampf bei 220 °C. Diese Gaslager wurden mit Umgebungsluft, heißer Luft und heißem Wasserdampf bis zu einer Drehzahl von 220000 U/min getestet. Der Rotororbit ist kleiner als 0.002 mm, weshalb die Lager sehr stabil betrieben werden können. Insgesamt wurde die Rezirkulationseinheit mehr als 300 Stunden betrieben.

Letztendlich wurde die FTU in-situ mit einem 6 kW<sub>el</sub> SOFC-System gekoppelt. Es wurde ein elektrischer DC Bruttowirkungsgrad basierend auf dem unteren Heizwert von 66 % in Teillast (4.5 kW<sub>el</sub>) und 62 % in Vollast (6.4 kW<sub>el</sub>) für einen globalen Brennstoffausnutzungsgrades von 85 % erreicht. Nach dem Kenntnisstand des Autors war es das erste Mal, dass ein dampf angetriebener Anodenabgasrezirkulationsventilator in-situ mit einer SOFC getestet wurde.

Stichwörter: dampfbetriebener Rezirkulationsventilator, Gaslager, Festoxidbrennstoffzelle, Anodenabgas, radiale Turbomaschinen, Optimierung, integrierter Entwurf, experimentelle Untersuchungen

# Contents

<b>Acknowledgements</b>	<b>i</b>
<b>Abstract (English/Français/Deutsch)</b>	<b>v</b>
<b>List of Figures</b>	<b>xv</b>
<b>List of Tables</b>	<b>xxiii</b>
<b>List of Acronyms</b>	<b>xxv</b>
<b>List of Symbols</b>	<b>xxix</b>
<b>1 Introduction</b>	<b>1</b>
1.1 Motivation . . . . .	1
1.2 History of energy modeling, turbomachinery, and SOFC research at EPFL . . .	2
1.3 Objectives and organization . . . . .	3
1.4 Aspects of novelty . . . . .	5
<b>2 State of the Art</b>	<b>7</b>
2.1 Solid oxide fuel cell system . . . . .	7
2.1.1 Basic principles . . . . .	7
2.1.2 Cell composition . . . . .	8
2.1.3 Fuel reforming . . . . .	8
2.1.4 Stack and its efficiency . . . . .	11
2.1.5 Stationary systems . . . . .	13
2.1.6 System efficiency . . . . .	16
2.1.7 Off-gas recirculation . . . . .	17
2.1.8 Carbon deposition . . . . .	20
2.1.9 Research systems . . . . .	21
2.2 Pressure rise units for off-gas recirculation . . . . .	24
2.2.1 Specifications of the pressure rise unit . . . . .	26
2.2.2 Commercial and research recirculation fans . . . . .	27
2.2.3 Comparison of different pressure rise unit technologies . . . . .	28
2.3 Fan . . . . .	31
2.3.1 Nomenclature . . . . .	31

## Contents

---

2.3.2	Velocity triangles and mean-line analysis . . . . .	33
2.3.3	Efficiency and power . . . . .	36
2.3.4	Similarity concepts and scaling laws . . . . .	39
2.3.5	Design procedure and concepts . . . . .	44
2.4	Turbine . . . . .	49
2.5	Intellectual property . . . . .	51
<b>3</b>	<b>SOFC System Design</b>	<b>53</b>
3.1	SOFC system with thermally-driven anode off-gas recirculation fan . . . . .	53
3.2	Methodology . . . . .	54
3.3	Modeling . . . . .	57
3.3.1	Energy flow model . . . . .	57
3.3.2	Small-scale turbomachinery model . . . . .	60
3.3.3	Heat and power integration . . . . .	64
3.3.4	Performance objectives and multi-objective optimization . . . . .	64
3.4	Results and analysis . . . . .	65
3.5	Heat exchanger network design (baseline SOFC system) . . . . .	72
3.6	Sensitivity of steam leakage (baseline SOFC system) . . . . .	73
3.7	Chapter conclusion . . . . .	74
<b>4</b>	<b>Fan-Turbine Unit Design</b>	<b>77</b>
4.1	Small-scale turbomachinery . . . . .	77
4.2	Design procedure of the anode off-gas recirculation unit . . . . .	77
4.3	Fan-turbine unit concept and bearing design . . . . .	78
4.3.1	Concept of the fan-turbine unit . . . . .	78
4.3.2	Gas film bearing and shaft design . . . . .	80
4.4	Radial fan . . . . .	82
4.4.1	Fan specifications . . . . .	82
4.4.2	Fan design summary . . . . .	82
4.4.3	One-dimensional simulation . . . . .	85
4.4.4	Three-dimensional single passage simulation . . . . .	90
4.4.5	Three-dimensional full passage simulation . . . . .	107
4.5	Radial-inflow turbine . . . . .	109
4.5.1	Turbine specifications . . . . .	109
4.5.2	Turbine design summary . . . . .	111
4.5.3	Zero and one-dimensional simulation . . . . .	119
4.5.4	Three-dimensional single passage simulation . . . . .	122
4.5.5	Three-dimensional full passage simulation . . . . .	129
4.6	Thrust force model . . . . .	133
4.7	Chapter conclusion . . . . .	137



<b>5 Fan-Turbine Unit Experiments</b>	<b>141</b>
5.1 Fan-turbine unit propelled by nozzles with pressurized ambient air . . . . .	141
5.2 Turbine propelled by pressurized ambient air . . . . .	145
5.3 Fan and turbine operated with ambient air . . . . .	149
5.4 Calculation of turbomachinery parameters . . . . .	152
5.4.1 Evaluation of the leakage from the turbine to the fan . . . . .	155
5.4.2 Influence of the leakage and heat on the turbomachine power and efficiency	156
5.5 Fan and turbine operated with hot air at 200 °C . . . . .	158
5.6 Fan operated with hot air at 200 °C and turbine operated with water vapor at 220 °C . . . . .	166
5.7 Chapter conclusion . . . . .	171
<b>6 Integration of the Fan-Turbine Unit with the SOFC System</b>	<b>175</b>
6.1 Measurement setup . . . . .	175
6.2 Test at ambient conditions . . . . .	177
6.3 Test with operational SOFC . . . . .	179
6.4 Chapter conclusion . . . . .	184
<b>7 Summary and Conclusions</b>	<b>185</b>
7.1 Summary . . . . .	185
7.2 Future work . . . . .	186
<b>A Commercial, Precommercial, and Postcommercial SOFC Systems</b>	<b>189</b>
<b>B Mesh Sensitivity Analysis for the Fan Impeller</b>	<b>193</b>
<b>C Measurement Uncertainty and Calibration of Equipment</b>	<b>195</b>
<b>D Balancing of the Fan-Turbine Unit</b>	<b>203</b>
<b>E Turbine Stator Blockage</b>	<b>207</b>
<b>Bibliography</b>	<b>218</b>
<b>List of Academic Activities</b>	<b>219</b>
<b>List of Publications</b>	<b>221</b>
<b>Curriculum Vitae</b>	<b>223</b>



# List of Figures

2.1	Stationary SOFC systems with steam reformer, schematic SOFC cell, burner, condenser, evaporator, and anode off-gas recirculation propelled by a) a steam-driven ejector, b) a fuel-driven ejector, c) an electrically-driven fan, d) a patented thermally-driven fan, as well as e) direct steam supply for the steam reforming.	9
2.2	Carbon deposition limit lines in the C-H-O ternary diagram for different constant temperatures and ambient pressure shown with solid lines. The steam reforming of methane is marked with a dotted-dashed red line. Dotted green and dashed blue lines show constant O/C and H/C ratios, respectively (adapted from [1]).	21
2.3	Meridional view of a schematic inducer-less radial fan with splitter blades, diffuser, and volute, as well as the nomenclature of the different sections and important components.	33
2.4	Top view of a schematic fan with backward-curved blades and splitter blades, as well as the velocity triangles at the leading and trailing edge.	36
2.5	Specific speed ( $n_s$ ) and specific diameter ( $d_s$ ) diagram showing the total-to-static isentropic radial turbomachine efficiency ( $\eta_{i_s,tst}$ ). Four anode off-gas recirculation fans with respective efficiencies are shown on the performance map (adapted from [2]).	40
2.6	Design procedure for a turbomachine.	45
2.7	Meridional view of a schematic partial-admission radial-inflow turbine, as well as the nomenclature of the different sections and important components.	50
3.1	Process flow diagram of the steady co-flow SOFC systems with 10 kW <sub>el</sub> .	55
3.2	Methodology of the SOFC system optimization.	56
3.3	Comparison of experimental and simulated results for a short SOFC stack (six cells), cell area 80 cm <sup>2</sup> , and 75 % fuel utilization.	59
3.4	Fan efficiencies for the SOFC system with electrically-driven AOR fan, calculated with the zero-dimensional model (similarity concepts) and one-dimensional model (mean-line analysis) for different specific speed values. Optimized specific speed values are indicated with red stars.	62
3.5	The composite curves of the SOFC systems with the best electrical net efficiency for the electrically-driven AOR (full line [88]) and the thermally-driven AOR (dashed line).	64

## List of Figures

---

3.6	Pareto front of the optimized SOFC systems with electrically-driven AOR fan (non-filled markers) and thermally-driven AOR fan (filled markers). . . . .	65
3.7	Evolution of the fuel cell parameters along the Pareto front (constant current density of $0.4 \text{ A cm}^{-2}$ ). . . . .	66
3.8	Evolution of anode off-gas recirculation ratio, as well as local and global fuel utilization along the Pareto front. . . . .	67
3.9	Evolution of system temperatures (left y-axis) and cathode excess air ratio (EAR) along the Pareto front (right y-axis). . . . .	68
3.10	Evolution of three design variables along the Pareto front. . . . .	69
3.11	Evolution of isentropic fan, mechanical, turbine, and total efficiencies along the Pareto front. . . . .	69
3.12	Evolution of rotor speeds, as well as fan, shaft, and turbine diameters along the Pareto front. . . . .	70
3.13	Evolution of the fan power and the mechanical losses of the journal and thrust bearing. . . . .	71
3.14	Sensitivity analysis of the baseline system for different total steam leakage rates from the turbine to the anode off-gas recirculation. . . . .	74
4.1	Concept of the fan-turbine unit with all parts (right side), some static pressure measurement positions (left side), temperature measurement positions (red dots), and rotational speed measurement with an optical sensor (green dot). . .	79
4.2	Side view of the radial anode off-gas recirculation fan with mounted spinner (left), the diamond-like carbon (DLC) coated shaft with an 8 mm diameter featuring two herringbone-grooved journal bearings, and the radial-inflow turbine (right). The Swiss five centime coin diameter is 17.15 mm. . . . .	80
4.3	Whirl map for the anode off-gas recirculation fan journal bearings with a diameter of 8 mm operated with water vapor at $220^\circ\text{C}$ corresponding to the design point. . . . .	81
4.4	Top view of the radial anode off-gas recirculation fan without mounted spinner featuring holes for balancing (left) and the logarithmic fan volute (right) featuring four pressure taps with a diameter of 0.4 mm at the fan trailing edge, respectively volute inlet. . . . .	84
4.5	Schematic of the one-dimensional fan calculation procedure based on mean-line design. . . . .	86
4.6	Original Balje correlations, adapted model, and comparison to measurements and CFD simulations. . . . .	89
4.7	Domain regions: inlet, rotating fan impeller, and diffuser from left to right. The fluid-to-fluid interfaces between the stationary and rotating domain are marked green. . . . .	91
4.8	Generated mesh for the fan hub, blades, and diffuser for all four blade passages. . . . .	92
4.9	$y^+$ values for the anode off-gas simulation with a zero blade tip clearance. . . . .	93

4.10	Comparison of the blade and channel heights for (1) the single passage CFD simulation, (2) the experimentally investigated fan, and (3) the full passage CFD simulation. . . . .	95
4.11	The three different laser-manufactured shims available for the fan volute: 0.1 mm (left), 0.05 mm (middle), and 0.02 mm (right) with a slotted hole for shim and volute alignment. . . . .	97
4.12	Experimental static pressure measurement (black square) at the shroud (radius of 9.28 mm) and computational blade loading (red points) of a fan blade (the relative tip clearance is 0.071 and the tip is located at $1 - 0.071 = 0.929$ span) at different spans: 0.92 span (upper graph), 0.5 span (middle graph), and zero span (lower graph). The blue line corresponds to the blade angle at different spans: 1.0 span (circles), 0.5 span (dots), and zero span (squares). The line with hexagrams corresponds to the blade angles at the fan leading edge (LE). The green line shows the mass-flow-averaged relative velocity angle ( $\beta$ ). . . . .	99
4.13	Absolute velocity ( $c$ ) of hot air at 200 °C within the blade tip clearance at different spans (absolute blade tip clearance is 0.14 mm). At 100 % blade tip clearance span, i.e., at the shroud surface, the velocity is zero because of the counter-rotating no-slip wall, whereas the velocity is equal to $u = \omega r$ at the blade tip (i.e., at zero blade tip clearance span), because of the rotating no-slip wall. . . . .	100
4.14	Comparison of the static pressure and the relative velocity components (black arrows) that are tangential to the constant span surface at 0.5 span around the main and splitter blade leading edge for the a) single passage and b) full passage CFD simulation for air at 200 °C and a rotational speed of 168 krpm. . . . .	101
4.15	Static pressure at the shroud wall (diameter of 18.55 mm) for air at 200 °C with a tip clearance of 0.14 mm obtained from computational fluid dynamics (CFD) (red line), experimental measurements at a volute angle of $\phi = 0$ (blue dotted line), 120° (green dotted line), and 240° (magenta dotted line) with a low-frequency pressure sensor (averaged value), and the mean value of the numerical pressure profile (red dotted line). . . . .	103
4.16	Comparison of the entropy in the meridional view for the different cases with a 0 (left), 0.04 mm (second from left), 0.09 mm (second from right), and 0.14 mm (right) tip clearance in the case with air at 200 °C (constant blade height of 1.82 mm). . . . .	104
4.17	Change of the fan isentropic total-to-total efficiency with respect to the “ideal” isentropic efficiency of a zero tip clearance fan for different relative blade tip clearances for the anode off-gas case (red dots) and the air case (blue dots), as well as a comparison to the tip clearance loss correlation from Pfleiderer with an experience coefficient ( $a_1$ ) of 2.3 (black dotted line). . . . .	106
4.18	Fluid domain of the measurement (blue, red, orange, and green), for the CFD (red and orange), and position of the pressure taps at the fan trailing edge (0°, 120°, 240°, and blade passing frequency measurement with the Kistler 601CA). . . . .	107

## List of Figures

---

4.19 Comparison of the velocity ( $c$ ) within the volute for different angles ( $\phi$ ) of $0^\circ$ , $90^\circ$ , $180^\circ$ , and $270^\circ$ . . . . .	108
4.20 Absolute velocity at the turbine inducer inlet (4), stator leading edge (5), and stator trailing edge (6), as well as velocity triangles with absolute velocity (green), relative velocity (blue), and circumferential velocity (red) for the turbine rotor leading edge (7) and trailing edge (8) in the case with air at $200^\circ\text{C}$ and a rotational speed of 168 krpm obtained from a single passage CFD simulation (mass-flow-averaged over entire channel width). . . . .	114
4.21 The manufactured partial-admission turbine volute, the removable turbine stator (slightly misaligned in this photo), and the half circle static shroud pressure measurement tap at the rotor-stator interface ( $p_{st,7}$ ). . . . .	115
4.22 The turbine rotor angle and thickness distribution for a blade turning of $102^\circ$ using the NACA TN 3802 primary series and the modified NACA TN 3802. . . .	116
4.23 Optical microscopy with Hirox KH-8700 (left) of the turbine stator and rotor (digitally mirrored) and overview of turbine stator and rotor (upside-down) with turbine inducer (right). . . . .	117
4.24 Domain regions (right): inducer, stator, rotating turbine impeller, and exducer domain from the top to the bottom, and generated mesh (left) at the hub for each domain from the bottom view. The fluid-to-fluid interfaces are marked green. . . . .	123
4.25 Full passage simulation of the partial-admission turbine with the velocity (absolute in non-rotating domain and relative in rotating rotor domain) at a span of 0.5 and at the exducer outlet (turbine section 9). . . . .	129
4.26 Line-averaged hub static pressure profile for the full impeller turbine (red dots) and comparison to the approximated hub static pressure profile for the thrust force calculation with an analytical model (solid blue line), as well as to the measured value at the rotor-stator interface multiplied by 13/61 (up-pointing green triangle). . . . .	131
4.27 Full passage steady CFD simulation of turbine at 150 krpm with ambient air: Power of each turbine blade (1-61) where the first blade corresponds to the first blade in the admission, i.e., the filling, and the 13th blade to the last blade in the admission, i.e., emptying (green squares). The 14th and 61st turbine blade (red dots) in the non-admission area have a positive power, whereas the blades 15 to 60 (down-pointing blue triangle) have a negative power and correspond to the pumping loss (0.18 W). The magenta hexagram corresponds to the result of the single passage simulation and the red dashed-dotted line to the experiment. . .	132
4.28 Axial force of the FTU for the turbine (left) and the fan side (right) close to the nominal point at a rotational speed of 168 krpm. All pressures were measurements except for the axial thrust bearing pressure in brackets (calculated). . . .	134

5.1	The FTU mounted at 45° with four (two front and two back) installed LionPrecision C3S sensors for the radial displacement measurement, one Philtec D20 for thrust bearing axial clearance measurement, a C3S (lower right corner), one pressure tap for the housing pressure, and two TCs measuring the journal bearing temperature. Two pressurized air nozzles at the fan propelled the shaft. . . . .	143
5.2	Comparison of thrust bearing axial clearances at different housing pressures. Top: measurement of static axial clearance (rotor not rotating) between 0 and 0.96 bar(g) (left) and zoomed in view of this graph at the region of the initial fan lift-off, i.e., 0.0162 bar. Middle: dynamic axial clearance measurement with zero housing pressure up to 66 krpm in the time domain (left) and the frequency domain (right). Bottom: dynamic axial clearance measurement with 0.1 bar housing pressure up to 73 krpm in the time domain (left) and the frequency domain (right). . . . .	144
5.3	Dynamic thrust bearing axial clearance measurement setup on the fan side (vertically mounted). Pressurized ambient air propels the turbine and thus the shaft (not shown). . . . .	146
5.4	Left: measured thrust bearing axial clearance for ambient air without turbine volute (blue squares) and with turbine volute (red circles), as well as calculated axial clearance (green hexagrams) with turbine volute and hot air, assuming constant thrust force. Right: calculated thrust forces with the measured axial clearance without turbine volute (blue down-pointing triangles) and with turbine volute (red triangles), as well as the thrust force without the effect of the fan impeller wheel (dashed line with black circles) and the calculated thrust force with measured pressures (magenta squares). . . . .	148
5.5	Mechanical losses calculated using the experimental shaft run-out without mounted fan or turbine volute (green), with both fan and turbine volute mounted (blue), and the result of the analytical model (red lines). . . . .	150
5.6	Fan total-to-total pressure rise as a function of the fan inlet volume flow rate and the rotational speed in the case with ambient air. . . . .	151
5.7	Overview of enthalpy streams, power, and heat input and output to the fan fluid domain (green dotted line). . . . .	153
5.8	Comparison of the experimental and analytical (CD=1) leakage mass flow rate from turbine to fan for non-throttled operation. . . . .	155
5.9	Comparison of different efficiency and power definitions for the fan at hot conditions (200 °C). . . . .	157
5.10	Overview of the fan test rig for hot air at 200 °C (without glass fiber insulation). . . . .	159
5.11	Digital image of the fan test rig with the measurement positions (left) and real implementation (right), partly covered with glass fiber insulation. . . . .	161
5.12	The fan characteristic obtained from experiments (Exp.) with the respective measurement uncertainties and from numerical simulations (CFD). The black dot refers to the nominal point (NP) that has the same Mach number and flow coefficient as the design point with the anode off-gas. . . . .	163

## List of Figures

---

5.13	The measured and simulated turbine characteristic with hot air at a total inlet temperature of $220 \pm 2^\circ\text{C}$ and an ambient pressure of $0.96\text{ bar} \pm 0.004\text{ bar}$ . . . . .	165
5.14	The test rig for FTU measurements with hot air at $200^\circ\text{C}$ for the fan and water vapor at $220^\circ\text{C}$ for the turbine. . . . .	167
5.15	The measured and simulated turbine characteristic with water vapor at a total inlet temperature of $220 \pm 2^\circ\text{C}$ and ambient pressure of $0.96\text{ bar} \pm 0.003\text{ bar}$ for the operation with a non-throttled fan. The green square indicates the design point with a total inlet temperature of $220^\circ\text{C}$ , a total inlet pressure of $2.2\text{ bar}$ and a static pressure at section 9 of $1.0\text{ bar}$ . . . . .	170
6.1	a) Schematic of the FTU test rig coupled with the SOFC, as well as b) a digital image with mounted oven, c) the two Venturi nozzles for the recirculation rate measurement, and d) a photo with unmounted oven for the FTU test rig section.	176
6.2	Measured rotational speed, fan pressure rise, volume flow rates of both Venturi nozzles, recirculation rate, and temperatures for the test with $80\text{ l s min}^{-1}$ nitrogen at ambient conditions (stack not operational). . . . .	178
6.3	Measured cell potentials and total stack current for four experiments (1-4, as listed in Table 6.2). . . . .	179
C.1	Left: calibration of Thermocouples (TCs) with two platinum PT 100 reference probes from $15^\circ\text{C}$ to $175^\circ\text{C}$ (FTU operating temperature from $0$ - $220^\circ\text{C}$ ). Right: comparison of the measurement uncertainty of the Scanivalve DSA 3218 ( $0.05\%$ of $250\text{ PSI}$ is $3.1\text{ mbar}$ ) and the MKS 226A ( $0.3\%$ on the read). . . . .	196
C.2	Measurement uncertainty of the mass flow rate at the fan outlet measured with the quarter circle nozzle (blue error bar) and comparison to the measurement uncertainty of the fan inlet mass flow rate measured with the bellmouth (red error bar) at different speeds between $30\text{ krpm}$ (dark blue dot) up to $168\text{ krpm}$ (dark red dot). The fan outlet mass flow rate measurement is up to $21\%$ higher than the fan inlet mass flow rate for the measurements with air at $200^\circ\text{C}$ . . . . .	197
C.3	Calibration of the bellmouth (right) that measures the fan inlet side test section volume flow rate and mass flow rate with the quarter circle nozzle measurement device (left) that measures the fan outlet side test section volume flow rate and mass flow rate. . . . .	198
C.4	Rotational speed at $168.5\text{ krpm}$ measured with the LionPrecision C3S probe (red), the Philtec D20 probe (blue), and the Kistler 601 CA (green). The left side shows the signal in the frequency domain (FFT with $50\,000$ samples) and the right side shows $200$ samples in the time domain ( $50\text{ kHz}$ sampling rate). The C3S measures the rotor orbit in one direction ( $2608 \cdot 0.06 = 168.48\text{ krpm}$ ), the Philtec D20 measures two grooves on the shaft ( $\frac{5615}{2} \cdot 0.06 = 168.45\text{ krpm}$ ), and the pressure sensor measures the blade passing frequency of the eight blades ( $\frac{22458}{8} \cdot 0.06 = 168.435\text{ krpm}$ ). . . . .	200



D.1 The radial inflow turbine with a diameter of 15 mm (left), the screw that fixes the turbine on the shaft with holes for balancing (middle) after several balancing procedures (second from the left) and before balancing (second from the right). A “dummy turbine” for removing the entire shaft during the balancing procedure is shown on the right. . . . . 203

D.2 The measured rotor orbits on the fan and turbine side with the respective phases (positive in the direction of rotation) for different iterations (it.) of the balancing procedure and the initial state (It.0). . . . . 205

E.1 Turbine volute and stator (left), as well as turbine seal and rotor (right) with deposits: ceramics, salt, and glass fibers. . . . . 208

E.2 Deposits in the turbine rotor and zoom of the turbine stator leading edge. Only three stator rows (marked with 1, 2, and 3) out of 13 were partially open. . . . . 208



# List of Tables

2.1	Comparison of different pressure rise units for anode off-gas recirculation. A full circle indicates best performance, whereas a blank circle indicates poor performance. . . . .	29
2.2	Comparison of the main parameters for three radial anode off-gas recirculation fans (electrically-driven) and the patented thermally-driven fan-turbine unit (FTU) developed within this thesis. . . . .	42
3.1	Decision variables and the ranges for the multi-objective optimization. . . . .	57
3.2	SOFC stack parameters. . . . .	58
3.3	Constraints on minimum approach temperature in the heat exchangers. . . . .	60
3.4	Design parameters for the fan shaft and bearings. . . . .	63
3.5	Heat exchanger network (HEX) for the baseline SOFC system with thermally-driven anode off-gas recirculation fan, the minimum approach temperature ( $\Delta T$ ), the inlet (in) and outlet (out) temperatures for the hot ( <b>h</b> ) and cold (c) sources, the exchanged heat ( $\dot{Q}$ ), and HEX effectiveness ( $c_{HEX}$ ) for the respective HEXs. . . . .	72
3.6	Operational characteristics of the SOFC system with electrically and thermally-driven AOR fan, as well as the baseline design (three serial 220 cm <sup>2</sup> cells) at the best electrical net efficiency (LHV DC) point, assuming a blade tip clearance of 80 $\mu\text{m}$ for turbine and fan. . . . .	76
4.1	Geometrical parameters of the radial anode off-gas recirculation fan (fan sections 1 to 8 as defined in Figure 2.3). . . . .	83
4.2	Relative blade tip clearance and mesh data for the four different cases. . . . .	92
4.3	Operational conditions for the experiment and numerical simulation with air. The machine inlet total pressure is 0.96 bar and the total temperature is 200 °C, which is the reference case (marked in <b>bold</b> ) for the numerical simulation with the anode off-gas (constant Mach number and constant flow coefficient $\Phi$ ). The thrust bearing axial clearance, which corresponds to the fan impeller blackface clearance, in the case without mounted fan volute is measured at ambient conditions, whereas the other values are predictions (pred.) assuming constant thrust force. . . . .	94

## List of Tables

---

4.4	Comparison of experiment (Exp), full passage (FP) with volute, and single passage (SP) with virtual diffuser CFD simulations for hot air with a total inlet temperature of $200 \pm 0.5$ °C, a total inlet pressure of $0.96 \pm 0.0005$ bar, a rotational speed of $168 \pm 0.5$ krpm, and a mass flow rate of $5.29 \pm 0.05$ kg h <sup>-1</sup> with a TE diameter of 19.2 mm (constant $h_4$ of 1.82 mm and $\beta_{4,blade} = 17^\circ$ ). . . . .	102
4.5	Comparison of single passage (SP) with virtual diffuser CFD simulations for the anode off-gas with a total inlet temperature of 200 °C, a total inlet pressure of 0.96 bar, a rotational speed of 175.5 krpm, and a mass flow rate of 4.71 kg h <sup>-1</sup> with a TE diameter of 19.2 mm (constant $h_4$ of 1.82 mm and $\beta_{4,blade} = 17^\circ$ ). . .	105
4.6	Radial-inflow turbine parameters at the design point (CFD values in the first row) and experimentally measured parameters at off-design conditions. . . . .	110
4.7	Geometrical parameters of the radial-inflow turbine (turbine sections 1 to 12 as defined in Figure 2.7). . . . .	118
4.8	Comparison of the single passage turbine CFD and the experiment (exp.) in the case with air at a total inlet temperature of $220.3 \pm 0.5$ °C, a total inlet pressure of $2.73 \pm 0.003$ bar, an ambient pressure of $0.97 \pm 0.0005$ bar, and a rotational speed of $168.2 \pm 0.5$ krpm. . . . .	124
4.9	Comparison of the single passage turbine CFD and the experiment (exp.) in the case with water vapor at a total inlet temperature of $220.1 \pm 0.5$ °C, a total inlet pressure of $1.83 \pm 0.003$ bar, an ambient pressure of $0.96 \pm 0.0005$ bar, and a rotational speed of $147.0 \pm 0.5$ krpm. . . . .	127
5.1	Fan and turbine inlet and outlet temperature and pressure measurements. . . . .	160
6.1	Coupling process of the FTU (steam-driven) with a 6 kW <sub>el</sub> SOFC stack (240x80 cm <sup>2</sup> cells). The cathode air mass flow rate was maintained at 5.1 kg h <sup>-1</sup> . The global fuel utilization was constant (0.7). The turbine and fan inlet total temperatures were maintained at $215$ °C $\pm$ 5 °C and at $195$ °C $\pm$ 5 °C, respectively. The injected steam to the reformer was gradually replaced by anode off-gas recirculation. . .	181
6.2	6 kW <sub>el</sub> SOFC stack (240x80 cm <sup>2</sup> cells) with anode off-gas recirculation (FTU ,steam-driven). The cathode air mass flow rate was maintained at 5.1 kg h <sup>-1</sup> . The turbine and fan inlet total temperatures were maintained at $215$ °C $\pm$ 5 °C and at $195$ °C $\pm$ 5 °C, respectively. . . . .	183
A.1	Commercial, precommercial, and postcommercial SOFC systems, power, and efficiency as defined in eqs. 2.21 and 2.23. . . . .	191
B.1	Mesh sensitivity analysis with relative change (RC) between two consecutive values. . . . .	193
C.1	Measurement uncertainties of utilized equipment. . . . .	201

# List of Acronyms

AC	alternating current
AOR	anode off-gas recirculation
BoP	balance of plant
CFCL	Ceramic Fuel Cells Limited
CFD	computational fluid dynamics
CGO	cerium gadolinium oxide
COR	cathode off-gas recirculation
CPOX	catalytic partial oxidation
DAQ	data acquisition
DC	direct current
DLC	diamond-like carbon
DoE	Department of Energy
EAR	excess air ratio
EPFL	École Polytechnique Fédérale de Lausanne
FEM	finite element method
FFT	fast Fourier transformation
FTU	fan-turbine unit
FU	fuel utilization
GEM	Group of Energy Materials
H/C	hydrogen-to-carbon ratio
HEX	heat exchanger
HHV	higher heating value
HV	heating value
IPESE	Industrial Process and Energy Systems Engineering

## List of Acronyms

---

LAMD	Laboratory for Applied Mechanical Design
LE	leading edge
LENI	Laboratoire d'Énergétique Industrielle
LHV	lower heating value
LSCF	lanthanum strontium cobaltite ferrite
MCFC	molten carbonate fuel cell
MITI	Mohawk Innovative Technology, Inc.
MOO	multi-objective optimizer
NACA	National Advisory Committee for Aeronautics
NASA	National Aeronautics and Space Administration
NIST	National Institute of Standards and Technology
O/C	oxygen-to-carbon ratio
OSMOSE	“optimisation multiobjectif de systemes energetiques integres”
PEM	proton exchange membrane
PRU	pressure rise unit
PS	pressure side
PTFE	polytetrafluoroethylene
RANS	Reynolds-averaged Navier-Stokes equations
RECOGEN	“unité de cogération à pile à combustible SOFC avec recirculation”
RR	recirculation ratio
S/C	steam-to-carbon ratio
SCM	streamline curvature method
SECA	Solid State Energy Conversion Alliance
SOFC	solid oxide fuel cell
SR	steam reforming
SS	suction side
TC	thermocouple
TE	trailing edge
US	United States
USA	United States of America

VTT	Technical Research Centre of Finland
YSZ	yttria-stabilized zirconia





# Nomenclature

## Greek Symbols

$\alpha$	Absolute velocity angle [rad]
$\beta$	Relative velocity angle [rad]
$\Gamma$	Logarithmic decrement
$\gamma$	Molar fraction
$\Delta$	Deviation [rad]
$\Delta G$	Gibbs free reaction energy [J mol <sup>-1</sup> ]
$\Delta H$	Reaction enthalpy [J mol <sup>-1</sup> ]
$\Delta S$	Reaction entropy [J mol <sup>-1</sup> K <sup>-1</sup> ]
$\delta$	Measurement uncertainty
$\delta_h$	Degree of reaction based on enthalpies
$\delta_p$	Degree of reaction based on pressures
$\epsilon$	Exergetic efficiency
$\epsilon_a$	Degree of admission (turbine)
$\epsilon_e$	Blade trailing edge (TE) mean diameter to blade leading edge (LE) mean diameter
$\zeta$	Utilization ratio
$\zeta$	Loss coefficient
$\eta$	Efficiency
$\theta$	Wrap angle [rad]
$\kappa$	Heat capacity ratio
$\lambda$	Inducer inlet hub radius to shroud radius

## List of Symbols

---

$\lambda$	Air-fuel equivalence ratio
$\lambda_c$	Thermal conductivity [ $\text{WK}^{-1} \text{m}^{-1}$ ]
$\mu$	dynamic viscosity [ $\text{kgm}^{-1} \text{s}$ ]
$\mu$	Coefficient of friction
$\mu_0$	Coefficient of static friction
$\xi$	Mass fraction
$\xi_{ext}$	External-to-total reforming fraction
$\xi_{red}$	Reducing species fraction
$\xi_{sr}$	Steam recirculation fraction
$\Pi$	Pressure ratio
$\rho$	Density [ $\text{kgm}^{-3}$ ]
$\Phi$	Flow coefficient (based on the mass flow rate)
$\Phi$	Flow coefficient (based on the meridional velocity)
$\phi$	Angle within the volute [rad]
$\psi$	Work coefficient
$\omega$	Angular velocity [ $\text{rads}^{-1}$ ]

## Roman Symbols

$A$	Area [m]
$a$	Empirical coefficient based on experience
$b$	(Channel) width [m]
$c$	Absolute velocity [ $\text{ms}^{-1}$ ]
$CD$	Discharge coefficient
$D$	(Outer) diameter [m]
$d$	(Inner) diameter [m]
$d_s$	Specific diameter
$EX$	Exergy [ $\text{J mol}^{-1}$ ]
$F$	Force [N]

<b><i>F</i></b>	Faraday constant [ $\text{C mol}^{-1}$ ]
<i>f<sub>u</sub></i>	Fuel utilization
<i>g</i>	Gravitational acceleration [ $\text{m s}^{-2}$ ]
<i>h</i>	Specific enthalpy [ $\text{J kg}^{-1}$ ]
<b><i>h</i></b>	(Blade) height [m]
<i>H/C</i>	Hydrogen-to-carbon ratio
<i>HV</i>	Heating value [ $\text{J mol}^{-1}$ ]
<i>I</i>	Current [A]
<i>i</i>	Incidence [rad]
<i>j</i>	Natural number
<i>k<sub>p</sub></i>	Correction factor for compressibility effects
<i>l</i>	Length [m]
<i>La</i>	Laval number
<i>LHV</i>	Lower Heating Value [ $\text{J mol}^{-1}$ ]
<i>M</i>	Moment [N m]
<i>m</i>	Meridional coordinate
<b><i>m</i></b>	Mass [kg]
<i>ṁ</i>	Mass flow rate [ $\text{kg s}^{-1}$ ]
<i>Ma</i>	Mach number
<i>ṅ</i>	Molar flow rate [ $\text{mol s}^{-1}$ ]
<i>n<sub>s</sub></i>	Specific speed
<i>n<sub>rot</sub></i>	Rotational speed [krpm]
<i>O/C</i>	Oxygen-to-carbon ratio
<i>P</i>	Power [W]
<i>p</i>	Pressure [Pa]
<i>Q̇</i>	Heat transfer rate [W]
<i>R</i>	Universal gas constant [ $\text{J mol}^{-1} \text{K}^{-1}$ ]

## List of Symbols

---

<b><i>R</i></b>	Radius [m]
<i>r</i>	Radius [m]
$R_s$	Specific gas constant [ $\text{J kg}^{-1} \text{K}^{-1}$ ]
$Re_b$	Reynolds number based on the channel width
$Re_D$	Reynolds number based on the diameter
<i>RMS</i>	Root mean squared surface roughness
<i>RR</i>	Recirculation ratio
<b><i>RR</i></b>	Recycle ratio
<i>s</i>	Specific entropy [ $\text{J kg}^{-1} \text{K}^{-1}$ ]
<b><i>s</i></b>	(Blade tip) clearance [m]
<i>S/C</i>	Steam-to-carbon ratio
<i>T</i>	Temperature [K]
<i>t</i>	(Blade) thickness [m]
<i>U</i>	Potential [V]
<i>u</i>	Circumferential velocity [ $\text{m s}^{-1}$ ]
$\dot{V}$	Volumetric flow rate [ $\text{m}^3 \text{s}^{-1}$ ]
<i>w</i>	Relative velocity [ $\text{m s}^{-1}$ ]
<i>z</i>	Number of blades
$z_e$	Number of exchanged electron
ndm	Rotational speed multiplied by shaft diameter [rpm mm]

### Superscripts

0 Variable is at standard state (25 °C and 1 bar)

### Subscripts

aux	auxiliary
ax	axial
b	bellmouth
C	condenser

c	cold
cal	calibration
cond	conduction
crit	critical
el	electrical
exp	experiment
F	fan
h	hub
<b>h</b>	hot
ho	housing
HV	heating value
hyd	hydraulic
is	isentropic
lm	logarithmic mean
m	meridional
<b>m</b>	mean
mech	mechanical
n	nominal
opt	optimal
q	quarter circle nozzle
R	reformer
rad	radial
rec	recirculation
rev	reversible
s	shroud
sh	shaft
st	static

## List of Symbols

---

T	turbine
t	total
tb	thrust bearing
th	thermal
theo	theoretical
therm	thermodynamic
tst	total-to-static
tt	total-to-total
turb	turbine
u	circumferential
V	voltage
v	volumetric

# 1 Introduction

This chapter outlines the main motivation, provides an overview of the previous related research, and describes the scope and structure of this thesis. It concludes with the proposed aspects of novelty.

## 1.1 Motivation

On the 4<sup>th</sup> of November 2016, the Paris Agreement entered into force. Up until November 2018, 184 United Nations parties have ratified it. This is a “response to the threat of climate change, in the context of sustainable development” [3]. The goal is “holding the increase in the global average temperature to well below 2 °C above pre-industrial levels” [3]. Generally, this world-wide effort is known as the energy transition.

In 2004, Pacala et al. [4] published a theory entitled “Stabilization wedges: Solving the Climate Problem for the Next 50 Years with Current Technologies”. The conclusion was that there was not a single technology that could solve the climate problem to realize the energy transition. Rather, a portfolio of different technologies was proposed. Option five read as follows: “Gas baseload power for coal baseload power” [4].

solid oxide fuel cell (SOFC) technology could significantly contribute to option five, since it efficiently generates electricity and heat from natural gas. Off-the-shelf technology attains up to 65 % of electrical net efficiency based on the lower heating value (LHV) of methane. This is superior to the most advanced combined cycle (gas turbine and steam turbine) power plants. In addition, these high SOFC efficiencies are also possible at a small-scale in the range of 1-10 kW<sub>el</sub>.

Thus, the SOFC technology is perfectly suited for the so-called distributed energy conversion (also referred to as the decentralized energy conversion). In 2006, Alanne et al. [5] concluded that “a distributed energy system is a good option with respect to sustainable development”. In comparison to conventional power plants, this decentralized approach has the benefit of close-to-consumer power conversion, where transmission losses are limited, and the consumer can directly use the recovered waste heat for heating or cooling.

Furthermore, SOFC systems can contribute to a sustainable development as follows: (1) operate on renewable biogas, (2) be dynamically dispatched to complement intermittent wind and solar power, and (3) operate on renewable hydrogen that is generated from excess wind and solar power in utility grid networks with very high renewable power use [6].

### 1.2 History of energy modeling, turbomachinery, and SOFC research at EPFL

The academic partners for this thesis are the Industrial Process and Energy Systems Engineering (IPESE) laboratory led by Prof. Maréchal, the Laboratory for Applied Mechanical Design (LAMD) led by Prof. Schiffmann, and the Group of Energy Materials (GEM) led by Dr. Van herle. The following paragraph outlines a brief history of the research performed at these three institutions.

Molyneaux [7] and Leyland [8] developed a MATLAB-based self-tuning multi-objective optimizer (MOO) using an evolutionary algorithm. In 2003, Palazzi [9] and Bolliger [10] initiated the development of the MATLAB-based “optimisation multiobjectif de systemes énergétiques intégrés” (OSMOSE) platform, i.e., a multi-objective optimization for integrated energy systems. This platform combines commercial flow sheeting software, energy integration techniques, performance evaluation, and the previously described MOO algorithm. Since then, many students and researchers (including Andrea Fabiano, Martin Gassner, Hubert Thieriot, Léda Gerber, and Samira Fazlollahi) from the former Laboratoire d’Énergétique Industrielle (LENI) and the IPESE laboratory, contributed to the development of the OSMOSE script. Using these tools, Facchinetti [11] investigated the potential of a patented hybrid system composed of a gas turbine and an SOFC. The theoretical net efficiencies of up to 82 % and 68 % were obtained for a small-scale version with 6 kW<sub>el</sub>.

In cooperation with the industrial partner Fischer AG, Schiffmann [12] designed and tested a 20 mm radial turbocompressor for application in a domestic heat pump. Because of the high rotational speeds of up to 210 krpm, it was supported on gas film bearings. An integrated approach considered the compressor, the bearings, the shaft, and the electrical motor in order to optimize the system with the previously mentioned MOO. Carré [13] continued Schiffmann’s work from 2009 to 2015. In cooperation with the Fischer AG, a twin-stage heat pump supported on gas film bearings with a maximum speed of 190 krpm was tested. Fischer AG designed and provided the two turbocompressor wheels; hence, Carré did not publish any exact geometric details. Between 2006 and 2012, Demierre [14] used Schiffmann’s compressor design and added a radial turbine with a diameter of 18 mm. The unit was used in a thermally-driven heat pump system. Demierre optimized the system layout and heat exchanger network using OSMOSE and MOO. More recently, Mounier [15] theoretically determined further potentials and challenges of this unit.

At the École Polytechnique Fédérale de Lausanne (EPFL), research in the field of SOFCs has been conducted since the early 1990s [16], and since 2013 a self-financed group has been dedicated to this topic. A spin-off from LENI, SOLIDpower (formerly HTceramix) in



Yverdon-les-Bains, already commercialized the SOFC technology and is a vital partner for the development of new technologies and experimental testing. GEM and SOLIDpower focus on planar anode-supported SOFCs with metallic interconnects. Larrain [17] developed models for a counter-flow SOFC with R-design cells (1<sup>st</sup>-generation) and validated the same with experiments. Autissier [18] developed and tested the 2<sup>nd</sup>-generation cell design, termed the S-design. A 1 kW<sub>el</sub> cogeneration system was optimized using OSMOSE. It includes an SOFC, a burner, as well as fuel and air processing. Wullemin [19] focused on the performance, reliability, and degradation of SOFCs using numerical and experimental methods. Wullemin also developed and tested the 3<sup>rd</sup>-generation cell design, the F-design.

### 1.3 Objectives and organization

This thesis is part of the “unité de cogération à pile à combustible SOFC avec recirculation” (RECOGEN) project, which the Canton de Vaud in Switzerland has financed between 2013 and 2018 within the program “100 million pour les énergies renouvelables et l’efficacité énergétique”.

The project partners consist of institutes from EPFL and industry. The industrial partner is SOLIDpower Sa in Yverdon-les-Bains, Canton de Vaud. The institutes from EPFL are the LAMD, GEM, and IPESE laboratory.

**The four main goals** of the RECOGEN project are:

1. Integrated design, simulation, and optimization of a 10 kW<sub>el</sub> SOFC, including the balance of plant (BoP) and a fan-turbine unit (FTU), with respect to electrical net efficiency and utilization ratio (partners involved: LAMD, GEM, IPESE laboratory, and SOLIDpower).
2. Design, manufacturing, and testing of a 10 kW<sub>el</sub> SOFC stack with an electrical efficiency higher than 60 % based on the LHV of methane and steam reforming (GEM and SOLIDpower).
3. Design, manufacturing, and testing of an oil-free FTU for a 10 kW<sub>el</sub> SOFC (LAMD).
4. Testing of the following coupled system: a 10 kW<sub>el</sub> SOFC and an FTU (LAMD, GEM, and SOLIDpower).

In this thesis, the author partly conducted the system optimization (goal 1) and the FTU design and testing (goal 3) for a 10 kW<sub>el</sub> system. Since it was not possible to develop a new 10 kW<sub>el</sub> SOFC system within the time frame of the project, the partners designed and tested a 6 kW<sub>el</sub> system (goal 2). This 6 kW<sub>el</sub> SOFC system was coupled to the FTU designed for the 10 kW<sub>el</sub> system (goal 4) leading to a slightly sub-optimal configuration. Nevertheless, it was possible to operate the designed FTU on non-nominal points. An overview of the thesis chapters is given as follows:

## Chapter 1. Introduction

---

**Chapter 2** introduces the state of the art in the areas of SOFCs, anode off-gas recirculators (fuel or steam-driven ejectors and electrical-driven fans), and small-scale radial turbines.

**Chapter 3** describes the simulation and optimization of the entire SOFC system with the commercial process flowsheeting software Belsim Vali and OSMOSE. The SOFC system comprises the SOFC stack, a reformer, a heat exchanger, a burner, fans, a pump, and the FTU. The steady simulation uses zero-dimensional component models at the nominal SOFC operating point with an electrical output of  $10 \text{ kW}_{\text{el}}$ . The optimization has the two objectives: maximizing the electrical net efficiency, as well as the utilization ratio (cogeneration of heat and power). This allows for a Pareto front to be identified with different optimal system designs and respective parameter sets.

**Chapter 4** presents the entire FTU assembly concept of fan, fan volute, shaft, turbine, turbine volute, turbine seal, journal and thrust bearings, housing, etc.

It describes the three-dimensional design of the fan, turbine, and shaft. The turbomachinery design tools consist of one-dimensional mean-line models, as well as three-dimensional computational fluid dynamics (CFD) and finite element method (FEM) simulations with the Ansys commercial software package. The mean-line analysis defines the basic blade parameters at the fan blade edges. A CFD simulation defines the three-dimensional fan blade, hub, and shroud shape. In a final step, an FEM simulation verifies the fan structural integrity. The turbine design follows a similar methodology.

The FTU has self-acting journal and thrust gas film bearings. Since these types of bearings tend to be unstable, a careful design over the entire FTU operational range is required. In-house models allow for the prediction of the rotor whirl speed and stability maps. For the FTU stability, it is also important to operate well below the first critical bending frequency. Ansys is therefore used to evaluate the respective eigenmodes and -frequencies.

**Chapter 5** lists the conducted experiments chronologically. In order to overcome certain limitations in the measurement campaigns, the author performed several experiments. After successfully balancing the FTU, pressurized air at ambient temperature propels the turbine while the fan volute is not mounted. Thus, the axial clearance of the thrust bearing can be measured. The utilized displacement probes for the rotor orbit measurement cannot operate at elevated temperatures; hence, the fan and turbine were operated at ambient conditions in the first step. In the next step, the FTU was placed inside an oven and operated with air at  $200 \text{ }^\circ\text{C}$ . As the rotational speed control for the steam-driven turbine is very delicate, in a preliminary step, it was driven with hot air at  $220 \text{ }^\circ\text{C}$ . In a final step, hot vapor at  $220 \text{ }^\circ\text{C}$  propelled the turbine. These procedures allow for the determination of fan and turbine characteristics, as well as for the validation of the FTU operation strategy.

**Chapter 6** describes the coupling of the SOFC with the FTU. It also provides an overview of the system flow sheet and the conducted measurements.

### 1.4 Aspects of novelty

The presented thesis contains several aspects of novelty, which are summarized below:

1. Integrated system simulation, design, and optimization of a patented SOFC system that uses a novel steam-driven anode off-gas recirculation unit.
2. The numerical results suggest an electrical net DC efficiency based on the LHV of 65 % for a domestic 10 kW<sub>el</sub> SOFC system (current world record for combined power plants is 63.1 % gross efficiency [20]).
3. Smallest steam-driven anode off-gas recirculation unit (the size of a 330 ml beverage can) for a 10 kW<sub>el</sub> SOFC system was designed, successfully tested, and characterized.
4. One of the smallest partial-admission steam turbines in the world with a tip diameter of 15 mm was designed and successfully tested.
5. Herringbone-grooved journal (shaft diameter of 8 mm) and spiral-grooved thrust gas film bearings operated at temperatures up to 220 °C, both with air and water vapor up to rotational speeds of 220 krpm.
6. In-situ coupling of a steam-driven anode off-gas recirculation fan with a 6.4 kW<sub>el</sub> SOFC stack, reaching 66 % electrical gross DC efficiency in part load (4.5 kW<sub>el</sub>) and 62 % in full load.



## 2 State of the Art

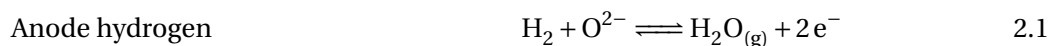
This chapter introduces the main principles of solid oxide fuel cell (SOFC) systems and pressure rise units (PRUs) for off-gas recycling. It offers an overview of off-the-shelf products and important research projects.

### 2.1 Solid oxide fuel cell system

For distributed cogeneration of electricity and heat using state-of-the-art fuel cells, SOFCs and molten carbonate fuel cell (MCFC) are both promising technologies with high efficiencies [21]. For a small-scale application, an SOFC is preferred, due to simpler balance of plant (BoP) equipment. Figure 2.1 shows several state-of-the-art SOFC systems, including the details described within this section, such as the basic principles, the composition and efficiency of a fuel cell stack, the fuel reforming, the entire BoP equipment, and challenges regarding carbon deposition. This section concludes by discussing research SOFC systems with anode off-gas recirculation (AOR).

#### 2.1.1 Basic principles

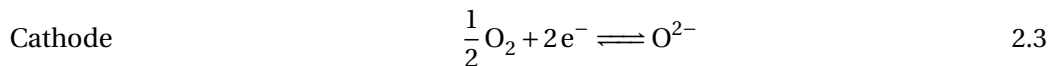
Figure 2.1 shows several stationary SOFC systems with a schematic SOFC cell. This cell has three main components: a dense oxide ion ( $O^{2-}$ ) conducting electrolyte and two electron ( $e^-$ ) conducting porous ceramic layers (the anode and cathode). The electrolyte separates the oxidant ( $O_2$  in air) and the fuel, which is either hydrogen ( $H_2$ ) or carbon monoxide (CO). On the anode at the three-phase boundary, the oxide ion reacts with hydrogen and/or carbon monoxide to form water ( $H_2O$ ), and carbon dioxide ( $CO_2$ ), respectively.



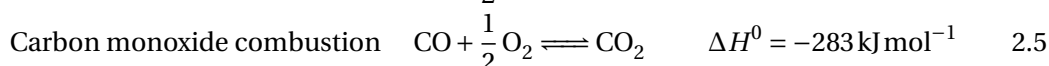
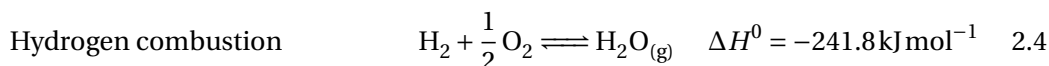
## Chapter 2. State of the Art

---

Each reaction liberates two electrons, which are transferred from the anode through the external circuit to the cathode. On the cathode, the oxygen reacts at the three-phase boundary with electrons originating from the external circuit to form oxide ions.



These ions migrate through the electrolyte to the anode at high temperatures (500 °C to 1000 °C). The combined chemical reactions of the anode and cathode are exothermic.



### 2.1.2 Cell composition

Current SOFC cells are either tubular or flat. Due to its round geometry, the sealing in tubular cells is less critical. Additionally, the tension due to thermal gradients is lower, which allows for less complicated SOFC cycling. Startup times as low as 30 minutes can be achieved, which is favorable for mobile applications [22]. Alternatively, the planar design has a higher power density and is easier to manufacture. Thus, it is favored by most companies (Appendix A).

Due to the thin layers, the cell is supported on the electrolyte, metallic substrate, cathode, or anode side. Electrolyte-supported cells are used for high temperatures (~ 1000 °C). For low temperature applications (500-600 °C), the support can be made of a metal sheet allowing for faster temperature cycling. Anode-supported cells made of yttria-stabilized zirconia (YSZ) and nickel as a catalyst perform best in intermediate-temperature applications (700-800 °C). Typically, the anode is manufactured with nickel oxide that is reduced to nickel by hydrogen during the first cell operation [23]. Because of the presence of nickel, the anode electrical conductivity is improved, leading to lower ohmic losses within the cell. Another advantage of the anode-supported cell is the decreased expense in material and manufacturing compared to the electrolyte- and cathode-supported configurations. When the support is on the anode side, the electrolyte can be extremely thin, on the order of 10 μm, which leads to lower overall ohmic resistance. Normally, the electrolyte is made of a YSZ / cerium gadolinium oxide (CGO) double layer, whereas the cathode material is a composite of lanthanum strontium cobaltite ferrite (LSCF) / CGO. An interconnect collects the current at the anode and cathode [24, 25]. Usually, these interconnects are manufactured as metallic ribs that also distribute the gas to the anode and cathode. The stack pressure loss is limited, due to the rib size being a few millimeters.

### 2.1.3 Fuel reforming

Since the SOFC system is normally not directly fueled with hydrogen or carbon monoxide, a number of processes can be used to produce these fuels from more complex molecules:

## 2.1. Solid oxide fuel cell system

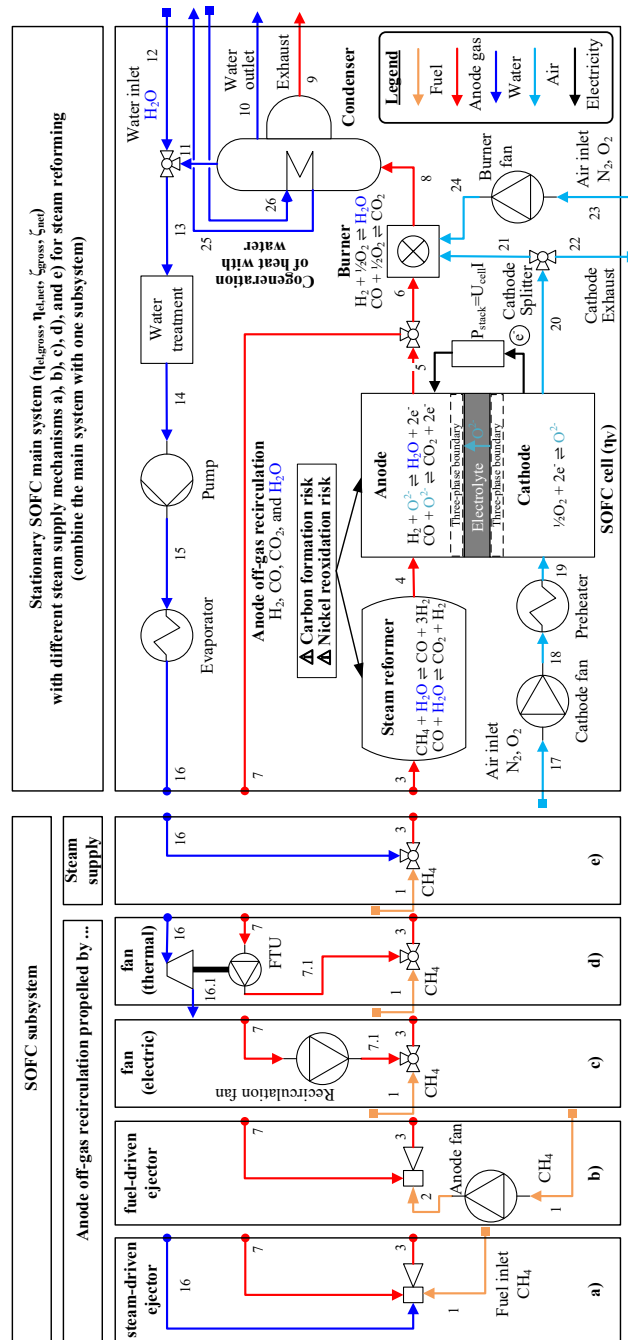


Figure 2.1 – Stationary SOFC systems with steam reformer, schematic SOFC cell, burner, condenser, evaporator, and anode off-gas recirculation propelled by a) a steam-driven ejector, b) a fuel-driven ejector, c) an electrically-driven fan, d) a patented thermally-driven fan, as well as e) direct steam supply for the steam reforming.

gas reforming, gasification of coal and biomass, water electrolysis, water splitting, photoelectrolysis, biological processes, etc. The most common production method is reforming from hydrocarbons such as biogas or natural gas. For applications that operate with natural gas from the distribution network, there are three main methods available: steam reforming (SR), catalytic partial oxidation (CPOX), and auto-thermal reforming (a combination of SR and CPOX). SR is "the oldest and most vital" [26] process and can be divided into two consecutive reactions: the steam reforming reaction (2.6) and the water-gas shift reaction (2.7). Methane ( $\text{CH}_4$ ) reacts with water vapor to form carbon monoxide and hydrogen. This carbon monoxide then reacts with steam to form carbon dioxide and hydrogen [26].



With a high reaction enthalpy at standard state ( $\Delta H^0 = 206.2 \text{ kJ mol}^{-1}$ ), the steam reforming reaction is strongly endothermic. According to le Chatelier's principle, the equilibrium of the steam reforming reaction is shifted to the right by adding a catalyst (mostly nickel based), increasing the temperature, or increasing the water vapor concentration. The water vapor concentration is generally considered by the steam-to-carbon ratio (S/C),

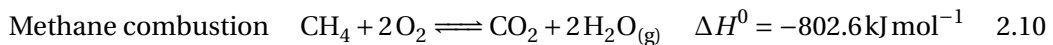
$$S/C = \frac{\gamma_{\text{H}_2\text{O}}}{\gamma_{\text{C}}} = \frac{\gamma_{\text{H}_2\text{O}}}{\gamma_{\text{CH}_4} + \gamma_{\text{CO}} + \gamma_{\text{CO}_2}} \quad 2.8$$

where the water vapor molar fraction ( $\gamma_{\text{H}_2\text{O}}$ ) is divided by the total carbon molar fraction ( $\gamma_{\text{C}}$ ). In the case of a methane-fueled SOFC, the denominator consists of the molar fractions of methane, carbon monoxide, and carbon dioxide.

For example, at a temperature of  $500^\circ\text{C}$ , standard pressure, and an S/C of one, the SR reactions convert 20 % of the methane to hydrogen, whereas all the methane is converted at a temperature of  $800^\circ\text{C}$ . If the S/C is increased to two, the full methane conversion is possible already at  $700^\circ\text{C}$  [26]. By comparing the enthalpy of reaction 2.4 to that of reactions 2.6 and 2.7, it is clear that the oxidation of hydrogen provides 5.8 the heat necessary for the SR. Therefore, part of the methane is commonly reformed inside the SOFC stack, thus cooling the stack. Using internal reforming, the cathode excess air ratio (EAR), also known as the air-fuel equivalence ratio,

$$\lambda_{\text{cathode}} = \frac{(\dot{n}_{\text{O}_2})_{\text{cathode,in}}}{(2\dot{n}_{\text{CH}_4} + 0.5\dot{n}_{\text{CO}} + 0.5\dot{n}_{\text{H}_2})_{\text{anode,in}}} \quad 2.9$$

can be reduced. It represents the ratio of the actual oxygen molar flow rate at the cathode inlet to the minimum oxygen molar flow rate necessary for anode reactions 2.4, 2.5, and methane combustion.





Considering a hydrogen-fueled SOFC system, the EAR can be lowered to four with internal reforming and can be as high as 10 with external reforming. Typically, the support plates or the metallic ribs of the stack interconnects are coated with a catalyst of a nickel basis. Direct internal reforming uses a catalyst directly on the anode [25]. Although complete internal reforming would be beneficial for the overall SOFC system efficiency, it is not feasible due to the reoxidation of the nickel catalyst within the anode. With 100 % internal reforming, no hydrogen being reformed at the anode inlet, remains a risk. If no hydrogen is supplied, the oxygen ions from the cathode will reoxidize the nickel in the anode leading to an increased aging rate of the fuel cell [27, 28].

### 2.1.4 Stack and its efficiency

An SOFC's cell potential is lower than 1 V and typically 0.75-0.85 V, whereas the current density is 0.2-0.5 A cm<sup>-2</sup> [29]. In order to increase the power output,  $n$  similar planar SOFC cells are stacked together and connected in series. The first anode is connected via the external circuit with the  $n_{th}$  cathode, the first cathode is connected to the second anode, the second cathode is connected to the third anode, etc. The interconnect collects the current and connects the cells in series. These stacked and connected cells form one SOFC stack with a power that is determined by the current ( $I$ ) and the sum of the cell potentials ( $U_{n,cell}$ ).

$$P_{stack} = \sum^j U_{j,cell} I = U_{stack} I \approx j U_{cell} I \quad 2.11$$

Assuming  $j$  similar SOFC cells that operate under the same conditions, the sum of cell potentials ( $U_{stack}$ ) can be simplified to a product ( $j U_{cell}$ ). For a steady adiabatic reactor with a constant volume and no external work input, the thermoneutral potential,

$$U_{HV} = \frac{HV}{z_e F} = \frac{-\Delta H}{z_e F} \quad 2.12$$

is calculated with the fuel's heating value (HV) (commonly the lower heating value (LHV) is used) or the reaction enthalpy ( $\Delta H$ ), the number of electrons exchanged within the reaction ( $z_e$ ), and the Faraday constant ( $F$ ). According to reaction 2.1, the parameter  $z_e$  is two for a hydrogen-fueled SOFC. The thermoneutral potential is calculated as 1.23 V at standard state (25 °C and 1 bar). For a methane-fueled SOFC with SR, the parameter  $z_e$  is eight. As shown in reactions 2.6 and 2.7, one methane molecule reacts to four hydrogen molecules which in turn react with eight electrons. The thermoneutral potential is therefore calculated as 1.04 V at standard state. The reversible potential,

$$\text{General} \quad U_{rev} = \frac{HV - T\Delta S}{z_e F} = \frac{-\Delta G}{z_e F} \quad 2.13$$

is calculated by subtracting the product of the reaction entropy difference ( $\Delta S$ ) with the temperature ( $T$ ) from the HV, which also corresponds to the Gibbs energy of the reaction ( $\Delta G$ ).

For an SOFC at ambient pressure, the Nernst potential,

$$\text{SOFC at 1 bar} \quad U_{Nernst} = \frac{1}{z_e F} \left( -\Delta G^0 + RT \ln \frac{\gamma_{O_2}^{0.5} \gamma_{H_2}}{\gamma_{H_2O}} \right) \quad 2.14$$

can be expressed using the Gibbs free reaction energy at standard conditions ( $\Delta G^0$ ), the universal gas constant ( $R$ ), and the molar fractions ( $\gamma$ ) of oxygen, hydrogen, and water vapor. Since  $\Delta S$  is very low for a methane-fueled SOFC, the Nernst potential is very close to the thermoneutral potential, even at elevated temperatures. For example, the reversible potential is still 1.035 V at 1000 K for a methane-fueled SOFC, but is reduced from 1.23 V to 0.94 V for a hydrogen-fueled SOFC with pure oxygen at the cathode inlet ( $\gamma_{H_2} = \gamma_{O_2} = 1$ ). Thus, in theory, the maximum achievable SOFC cell efficiency is given by the thermodynamic efficiency.

$$\eta_{therm} = \frac{U_{rev}}{U_{HV}} \quad 2.15$$

It is the fraction of the reversible potential (eq. 2.13) to the thermoneutral potential (eq. 2.12). The thermodynamic efficiency is nearly 100 % for a methane-fueled SOFC, even at high temperatures. For a hydrogen-fueled SOFC, it drops from 94 % at standard state to 77 % at 1000 K. These values are calculated with fluid properties provided by the United States (US) National Institute of Standards and Technology (NIST) [30].

The actual cell potential is less than the reversible potential, mainly due to three loss mechanisms: activation losses at the cathode and anode, ohmic losses due to ionic and electrical resistance within the cell, and mass transportation losses due to low hydrogen or oxygen partial pressure. The SOFC voltage efficiency,

$$\eta_V = \frac{U_{cell}}{U_{rev}} \quad 2.16$$

is the fraction of the actual cell potential to the reversible potential from eq. 2.13 and is typically 80 %. The cell potential drops to 0 V at 100 % fuel utilization (FU) due to Nernst and mass transportation losses which is a result of the increased anodic concentration overvoltage. The SOFC fuel utilization,

$$f_u = \frac{\dot{n}_{fuel,in} - \dot{n}_{fuel,out}}{\dot{n}_{fuel,in}} = \frac{\dot{n}_{fuel,reacted}}{\dot{n}_{fuel,in}} = \frac{I}{z_e F} \quad 2.17$$

is the fraction of the fuel molar flow rate that reacted within the fuel cell ( $\dot{n}_{fuel,reacted}$ ) to the fuel molar flow rate at the cell inlet ( $\dot{n}_{fuel,in}$ ). The reacted fuel molar flow rate is directly linked to the cell current ( $I$ ); hence, the FU is also referred to as current efficiency. Typically, the FU is between 80 % and 90 % [29]. An operation higher than 90 % is not recommended, due to an increased aging rate of the anode as a result of nickel reoxidation. In summary, the cell efficiency,

$$\eta_{cell} = \eta_{therm} \eta_V f_u \quad 2.18$$

is the product of the thermodynamic efficiency (eq. 2.15), the voltage efficiency (eq. 2.16), and the FU (eq. 2.17). It is typically 60 % for an anode-supported intermediate-temperature SOFC fueled by steam-reformed natural gas [29].

### 2.1.5 Stationary systems

Besides the stack, an SOFC system consists of various subsystems that are combined into one BoP. A typical system is composed of an air preparation unit, an electrical unit with the SOFC stack itself, an off-gas treatment unit including possible cogeneration of heat, and a fuel preparation unit. Figure 2.1 shows a typical stationary methane-fueled SOFC system with SR. Five different mechanisms can provide the steam for the SR process:

- anode off-gas recirculation propelled by:
  - a steam-driven ejector (option a in Figure 2.1)
  - a fuel-driven ejector (option b in Figure 2.1)
  - an electrically-driven fan (option c in Figure 2.1)
  - a thermally-driven fan (option d in Figure 2.1)
- direct steam supplied by an evaporator (option e) in Figure 2.1)

The **air preparation unit** is located upstream of the SOFC cathode and consists of an air preheater and cathode fan. Typically, the SOFC uses ambient air to feed the cathode. Although pure oxygen ( $\gamma_{O_2} = 1$ ) would decrease the Nernst losses and therefore increase the Nernst potential (eq. 2.14), it is not used in commercial applications, since the supply of pure oxygen is costly and energy-intensive. The stack temperature gradient is limited (typically on the order of 100 °C) to protect the cell layers and seals from thermal stress. A possible leakage of oxygen into the anode could lead to nickel reoxidation [31, 19]. It is therefore necessary to preheat the cathode inlet air with a preheater. The pressure loss in the piping and in the air preheater are typically on the order of several mbar, whereas the pressure loss within the stack air distribution system is on the order of 10s of mbar. To compensate for this pressure loss, a cathode fan increases the air pressure at the inlet. As a result of the required stack cooling, the EAR (eq. 2.9) is very high. Thus, the cathode fan generally represents the highest electrical auxiliary power consumption in the SOFC system.

The **electrical unit** consists of the SOFC stack itself, as described in sections 2.1.1 and 2.1.2, and various electrical equipment. The SOFC direct current (DC) potential depends on the number of cells, the cell efficiency, and the operational conditions. It is typically below the required system voltage (in Europe 230 V at 50 Hz). The DC voltage is therefore increased by a DC/DC converter. The alternating current (AC) network supply includes a DC/AC converter with a typical efficiency of 95 %. Other auxiliary losses are the electrical consumption of the fans (cathode, anode, burner, and anode off-gas recirculation), as well as the pumps. Additionally, the SOFC BoP requires controllers, measurements, and typically a communication

interface for remote operation monitoring. All these auxiliary power requirements ( $P_{aux}$ ), as well as the converter efficiency ( $\eta_{DC/AC}$ ), must be taken into account for the net values (eqs. 2.21 and 2.23).

The **off-gas treatment unit** consists of a burner, a condenser, various heat exchangers (HEXs), and if necessary, water treatment, pump, and evaporator. As stated before in section 2.1.4, the stack FU ratio (eq. 2.17) is typically 85%. The non-reacted anode exhaust gas is therefore burned to improve the overall heat recovery and thus the system utilization ratio (eqs. 2.22 and 2.23). Additionally, the burner is an important safety measure; carbon monoxide is extremely toxic and must be removed from the exhaust. HEXs recover the burner off-gas heat, which is used within the SOFC system, specifically for the anode and cathode preheater, reformer, or evaporator. Part of the water vapor is condensed in the condenser. The deaerated water leaves the system in stream 10 in Figure 2.1. The exhaust gases consisting of water vapor, carbon dioxide, nitrogen, and oxygen (stream 9) are discharged to the chimney. The condenser is cooled with water for cogeneration. Typical temperatures for cogeneration are 20 °C to 30 °C for domestic heating, but 20 °C to 60 °C for hot water supply. The cogeneration streams are denoted 25 and 26 in Figure 2.1. If required, an evaporator can produce pressurized steam from the condensed and deaerated water. For this, treatment of the condensed water is mandatory for two reasons. Firstly, the condensed water contains impurities from BoP equipment, the cathode, or the anode, which could block channels in the reformer or damage the stack. Secondly, carbon dioxide dissolves with water to form carbon acid, whereas oxygen dissolves to form hydroxide. Both are very corrosive. A typical water treatment unit filters and neutralizes the water. Additionally, fresh deionized water (12) is added to the system to regenerate the water supplied to the evaporator.

Concerning the **cathode exhaust** (stream 20 in Figure 2.1), there are three options:

1. Burning the combined cathode off-gas (21) and anode off-gas (6) in the burner. Stream 22 and the burner fan are therefore not active.
2. Separating the cathode off-gas and the anode off-gas. The cathode off-gas (22) leaves the system and the burner fan provides air at ambient conditions (23) to burn the anode off-gas (6). Stream 21 is therefore not active.
3. A combination of the previous two options, i.e., part of the cathode off-gas (22) leaves the system and part of (21) is mixed with the anode off-gas (6). The burner fan is therefore not active.

Option 1 is the state-of-the-art approach. However, it has several disadvantages, if compared to patented option 2 [32]. Firstly, the cathode outlet oxygen molar ratio is lower than  $\gamma_{O_2} = 0.21$ , since part of the oxygen ions travel through the electrolyte to the anode and react with hydrogen. Since the burner fuel inlet molar flow ratio is decreased in comparison to the anode

fuel inlet molar flow ratio, the burner air-fuel equivalence ratio,

$$\lambda_{burner} = \frac{(\dot{n}_{O_2})_{burner,in}}{(2\dot{n}_{CH_4} + 0.5\dot{n}_{CO} + 0.5\dot{n}_{H_2})_{burner,in}} \quad 2.19$$

is therefore greater than the previously mentioned cathode EAR (eq. 2.9). In Section 2.1.3, this cathode EAR is more than four. However, a forced-air burner with a high degree of combustion (i.e., 99 %) uses an air-fuel equivalence ratio of 1.1. As a result, the burner and the condenser are oversized, leading to increased pressure losses. Another disadvantage is that the water vapor molar ratio ( $\gamma_{H_2O}$ ) is reduced, yielding a lower heat recovery in the condenser. Option 2 tackles these issues. A higher condenser heat recovery, due to a higher burner exhaust dew point is feasible. For example, stoichiometric combustion of hydrogen (eq. 2.4) with air ( $\gamma_{O_2} = 0.21$ ) has the dew point at 72.5 °C, whereas the dew point is at 49 °C for an air-fuel equivalence ratio of four. Additionally, the burner flame temperature control is better with a burner fan. Option 3 combines the two advantages of a high flame temperature and high condenser heat recovery, but requires a high-temperature valve (cathode splitter in Figure 2.1).

The **fuel preparation unit** consists of a fuel treatment, an anode fan, a fuel reformer, and several HEXs. Poisonous elements, such as chromium [33] or sulfur [34], must be removed from the fuel to prevent an increased SOFC aging rate. The European low-pressure gas network ranges from 20-100 mbar. If this pressure is not sufficient, an anode fan is necessary to overcome the pressure loss. The losses occur in the piping, HEXs, reformer, stack gas distribution system, and burner. Figure 2.1 shows the SR process as described in section 2.1.3 for pure methane. This process requires water vapor that can be supplied in various ways. Firstly, it can be directly provided by the off-gas treatment unit (option e in Figure 2.1) or by the so-called AOR that contains deionized, non-acidic, and non-corrosive water vapor (option a, b, c, and d in Figure 2.1). A PRU must compensate for the pressure loss in the HEXs, the reformer, and the stack in order to realize the AOR. Section 2.2 provides a more detailed overview of the PRUs, which can be either an ejector or a fan. The ejector can be steam-driven (option a in Figure 2.1); hence, the SOFC system requires a water treatment unit, a pump, and an evaporator. Alternatively, it can be fuel-driven (option b in Figure 2.1); hence, the system requires an anode fan to increase the inlet fuel pressure, but no water treatment, pump, and evaporator are required. These components are also not required for option c in Figure 2.1, where only a recirculation fan is added to the system. This fan could either be electrically-driven by a motor (option c) or thermally-driven by a turbine (option d). As shown in Appendix A and sections 2.1.9 and 2.2.2, only electrically-driven AOR fans are available. The thermally-driven fan propelled by a steam turbine is therefore patented [35].

### 2.1.6 System efficiency

The SOFC system efficiency is measured by the electrical gross and net efficiency, as well as the gross and net utilization ratio. The SOFC electrical gross and net efficiency,

$$\eta_{el,gross} = \frac{P_{el}\eta_{DC/AC}}{\dot{n}_{fuel}HV_{fuel}} \quad 2.20$$

$$\eta_{el,net} = \frac{P_{el}\eta_{DC/AC} - P_{aux}}{\dot{n}_{fuel}HV_{fuel}} \quad 2.21$$

are calculated using the electrical output ( $P_{el}$ ), the fuel inlet molar flow rate ( $\dot{n}_{fuel}$ ), and the fuel heating value ( $HV_{fuel}$ ). These equations take into account the DC/AC converter efficiency ( $\eta_{DC/AC}$ ). Normally, the efficiency calculation uses the LHV instead of the higher heating value (HHV), such that the gross and net utilization ratio,

$$\zeta_{gross} = \frac{P_{el}\eta_{DC/AC} + \dot{Q}}{\dot{n}_{fuel}HV_{fuel}} \quad 2.22$$

$$\zeta_{net} = \frac{P_{el}\eta_{DC/AC} - P_{aux} + \dot{Q}}{\dot{n}_{fuel}HV_{fuel}} \quad 2.23$$

can be higher than one if heat ( $\dot{Q}$ ) is recovered from the water condensation. The net efficiencies are calculated by subtracting the electrical consumption ( $P_{aux}$ ) from the electrical output. This thesis uses the definitions from eqs. 2.20 to 2.23 based on the LHV and the electrical DC power (thus without the DC/AC converter efficiency), as these “efficiency” definitions are used within the SOFC community and among commercial SOFC companies.

**Important information on the efficiency and utilization ratio definitions:** From a thermodynamic perspective, the utilization of the fuel LHV for the calculation of the Gibbs free energy ( $G$ ), cell potentials in eq. 2.12, and the “efficiencies” in eqs. 2.20 to 2.23 is incorrect for the application of fuel cells. The author wants to emphasize that the utilization of the HHV is the only valid thermodynamic option. The use of the LHV for the efficiency calculation was introduced before 1900 by a “majority vote” for use with steam machines, such as steam turbines [36]. Currently, the definition of electrical efficiency and utilization ratio are part of international norms, for example the European norm 62282-3-201 [37] or the ASME PTC 50 [38] norm. SOFC manufacturers typically state the normed efficiencies, i.e., based on the fuel LHV. For methane, the LHV is only 90 % of the HHV at standard conditions.

The author also wants to emphasize that the word “efficiency” is not appropriate for the utilization ratio. The exergetic value of electric power is not comparable to the exergetic value

of heat. The exergetic gross and net efficiency,

$$\epsilon_{gross} = \frac{P_{el}\eta_{DC/AC} + \dot{Q}\left(1 - \frac{T_{in}}{T_{lm}}\right)}{\dot{n}_{fuel}EX_{fuel}} \quad 2.24$$

$$\epsilon_{net} = \frac{P_{el}\eta_{DC/AC} - P_{aux} + \dot{Q}\left(1 - \frac{T_{in}}{T_{lm}}\right)}{\dot{n}_{fuel}EX_{fuel}} \quad 2.25$$

are more appropriate definitions. These efficiencies use the fuel exergy ( $EX$ ), the inlet and outlet temperature of the cold source for the heat recovery ( $T_{in}$  and  $T_{out}$ ), and the logarithmic mean temperature.

$$T_{lm} = \frac{T_{out} - T_{in}}{\ln \frac{T_{out}}{T_{in}}} \quad 2.26$$

For the sake of coherence and comparability to industrial SOFC systems, the author uses in this thesis the LHV for the efficiency and utilization ratio definitions in eqs. 2.20 to 2.23. The values based on the HHV would be therefore 90 % of the values stated within this thesis.

### 2.1.7 Off-gas recirculation

Within an SOFC system, either the anode or cathode off-gas can be recirculated. Figure 2.1 shows only the option for the AOR (stream 7 in Figure 2.1) and not for the cathode off-gas recirculation (COR). A COR uses the hot cathode exhaust (stream 20) and recirculates it to the cathode inlet (stream 19), whereas the AOR recirculates the anode off-gas (stream 5) to the reformer inlet (stream 3). This subsection discusses the advantages and disadvantages of both off-gas recirculation options.

The **cathode off-gas recirculation** uses the hot cathode off-gas to preheat the cathode inlet air stream (19 in Figure 2.1). As a result, the air mass flow rate at the inlet stream (stream 17) is decreased. This results firstly in a decreased cathode fan size and thus decreased auxiliary power, along with increased electrical net efficiency. Secondly, due to the lower molar flow rate at the air inlet, the air preheater has a smaller size, which leads to lower capital costs for the entire SOFC system. As a disadvantage, the cathode off-gas oxygen molar ratio (stream 20) is decreased ( $\gamma_{20,O_2} < 0.21$ ), since oxygen ions diffused through the electrolyte to the anode side. This leads to a decreased Nernst potential in the cell (eq. 2.14) and lowers electrical efficiencies (eq. 2.21). Since the Nernst potential is lower, the losses, and thus the heat generation in the anode increase, which leads to an increased cooling requirement. Additionally, the lower oxygen partial pressure also increases the diffusion losses. Due to the lower oxygen partial pressure gradient between cathode and anode, less oxygen ions diffuse through the electrolyte, resulting in a decreased cell potential and power output.

From the viewpoint of an SOFC designer, the optimal COR recirculation ratio is a trade-off between decreased HEX cost and increased COR PRU cost (for example an ejector or recircula-

tion fan), increased efficiency due to lower air inlet molar flow rate, and decreased efficiency due to Nernst potential and diffusion losses.

The **anode off-gas recirculation** is advantageous, since it can increase the system FU. As pointed out in Section 2.1.4, the FU is limited to 85 % in order to mitigate the SOFC aging rate. The non-reacted fuel is burned in the burner and increases the system heat recovery, and therefore, its utilization ratio (eqs. 2.22 and 2.23). A low FU in the stack is therefore beneficial for a system with high heat recovery, and consequently, high utilization ratio. Conversely, a high FU is beneficial for a system with high electrical power output and high electrical efficiencies (eqs. 2.20 and 2.21). The AOR can increase the global FU without increasing the local FU, and thus, increases the system electrical efficiency without compromising the SOFC stack lifetime.

Another advantage of the AOR is the reuse of the water vapor in the anode exhaust. This water vapor is already deionized and non-corrosive, as the water vapor is not condensed. Thus, it can be used directly for the steam reformer at the anode inlet. Figure 2.1 option b and c show this concept. Since steam supply 16 is not available in these two concepts, the evaporator, pump, water treatment unit, and additional tap water supply (stream 12) are not required. For options b and c, the condensed water leaves the system in stream 10. The streams 11, 12, 13, 14, 15, and 16 are not necessary. The entire SOFC system is thus less complex, since only an ejector and anode fan (option b) or a recirculation fan (option c) are added. Another advantage of the SOFC system with AOR is the reduced maintenance cost, due to the absence of a water treatment unit. The water treatment unit requires regular replacement of filters and bases for water neutralization.

The AOR can be completely described with two of the following four parameters: the local and global FU, the recirculation ratio, and the oxygen-to-carbon ratio (O/C) before the reformer which is described in more detail in the next Section 2.1.8. The local FU is calculated with the molar flow rate of the streams directly before and after the anode (stream 4 and 5 in Figure 2.1), whereas the global FU is calculated with the streams directly before and after the AOR loop (stream 3 and 6).

$$\text{Local fuel utilization} \quad f_{u,local} = \frac{\dot{n}_{fuel,4} - \dot{n}_{fuel,5}}{\dot{n}_{fuel,4}} \quad 2.27$$

$$\text{Global fuel utilization} \quad f_{u,global} = \frac{\dot{n}_{fuel,1} - \dot{n}_{fuel,6}}{\dot{n}_{fuel,1}} \quad 2.28$$

The local and global FU are directly linked to the recirculation ratio (RR).

$$\text{Recirculation ratio} \quad RR = \frac{\dot{n}_7}{\dot{n}_5} = \frac{f_{u,global} - f_{u,local}}{f_{u,global}(1 - f_{u,local})} \quad 2.29$$

The RR is calculated with the molar flow rates of the anode recirculation loop (stream 7 in



Figure 2.1) and the anode off-gas (stream 5). Since the local FU is fixed due to the limited stack aging rate, an additional variable (either global FU, RR, or O/C) must be fixed to fully constrain the AOR.

There is an optimal RR in terms of electrical net efficiency. Since the RR determines the amount of water vapor that is recirculated in stream 7, it also determines the O/C before the reformer. A low RR translates to a low water vapor molar flow rate in the recirculation loop, and thus a low O/C. As discussed in Section 2.1.8, a low O/C is favorable for carbon deposition, which leads to an increased aging rate of the steam reformer and the anode in the case of internal reforming. For example, an O/C of one leads to carbon deposition for temperatures above 1000 °C and likely also for lower temperatures (depending on the hydrogen content). An increased O/C therefore mitigates the carbon deposition risk. Conversely, a higher O/C, and thus higher RR, leads to increased water vapor molar fraction ( $\gamma_{H_2O}$ ) at the steam reformer inlet and thus to increased  $\gamma_{H_2O}$  at the anode inlet (stream 4 in Figure 2.1). However, an increased  $\gamma_{H_2O}$  leads to a lower Nernst potential (eq. 2.14), and thus a lower electrical gross efficiency (eq. 2.20). The electrical net efficiency (eq. 2.21) is further decreased, due to increased auxiliary power, as already explained in the COR section passage. Since the Nernst potential is lower, the losses and thus the heat generation in the anode increases, which leads to increased stack cooling requirement and air inlet (stream 17) flow rate. A higher air inlet flow rate implies higher pressure losses in the cathode preheater and the cathode itself. A higher pressure loss and higher flow rate leads to a higher cathode fan power consumption and thus to a lower electrical net efficiency.

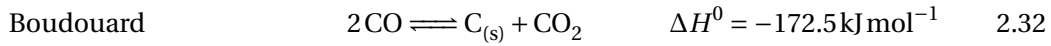
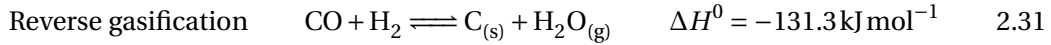
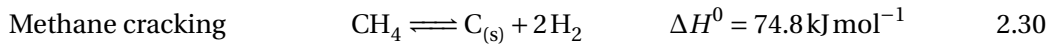
Consequently, from the viewpoint of an SOFC designer, the local FU is a compromise between the SOFC aging rate and electrical efficiency. The RR is a compromise between carbon deposition risk and electrical efficiency.

Autissier [18] optimized a 1 kW<sub>el</sub> SOFC cogeneration system with different combinations of AOR, COR, SR, and CPOX. SR instead of CPOX was found to be beneficial for the electrical efficiency of the system. Internal SR was preferred over external SR in terms of efficiency and cost reduction. In terms of cost, the AOR was preferred. Autissier pointed out that this result strongly depended on the heat exchanger and PRU (i.e., fan or ejector) cost and changes in these parameters could be beneficial for a solution with COR. This 1 kW<sub>el</sub> SOFC system could achieve 54 % electrical net AC efficiency based on the LHV, and an 85 % utilization ratio. The local ideal FU was 73 %, the global FU was 87 %, the RR was 61 %, and the S/C was 2.5.

As a **conclusion** of Autissier's results [18], this work will further develop a system with AOR and a combination of internal and external SR.

### 2.1.8 Carbon deposition

Section 2.1.3 describes the reforming process, which decomposes hydrocarbons to hydrogen and carbon dioxide. Especially in the case of higher hydrocarbons, coke in form of solid carbon can be formed during the reforming process. Coke can damage the external reformer, but also the SOFC anode or interconnects in the case of internal reforming. The coke blocks the gas channels and increases the pressure loss in the reformer and the SOFC stack [25, 39]. It can also deactivate the nickel catalyst by encapsulating it or swell the nickel catalyst, which leads to decreased porosity and thus higher electrical and ionic resistance [40]. The three main reactions for a methane-fueled SOFC are methane cracking, reverse gasification, and the Boudouard reaction.



Whether these reactions are thermodynamically possible depends on the temperature, pressure, and gas composition. For a hydrocarbon-fueled SOFC stack with SR, only three elements are involved: carbon, oxygen, and hydrogen. The sum of the molar ratios is therefore one ( $\gamma_C + \gamma_H + \gamma_O = 1$ ). Thus, the O/C and the hydrogen-to-carbon ratio (H/C) are sufficient to describe the gas composition.

$$\frac{O/C}{\gamma_C} = \frac{\gamma_O}{\gamma_C} = \frac{\gamma_{CO} + 2\gamma_{CO_2} + \gamma_{H_2O} + 2\gamma_{O_2}}{\gamma_{CH_4} + \gamma_{CO} + \gamma_{CO_2}} = \frac{\gamma_O}{1 - \gamma_O} (1 + H/C) \quad 2.33$$

$$\frac{H/C}{\gamma_C} = \frac{\gamma_H}{\gamma_C} = \frac{2\gamma_{H_2O} + 2\gamma_{H_2} + 4\gamma_{CH_4}}{\gamma_{CH_4} + \gamma_{CO} + \gamma_{CO_2}} = \frac{\gamma_H}{1 - \gamma_H} (1 + O/C) \quad 2.34$$

Sasaki and Teraoka [1] created an easy-to-read C-H-O ternary diagram based on thermodynamic calculations (without considering the kinetics of the reaction), which is valid for ambient pressure and ideal gases. Figure 2.2 shows the carbon deposition limits for temperatures between 100 °C and 1000 °C for different C-H-O reforming mixture compositions. For an O/C of two, without involving any hydrogen ( $\gamma_H = 0$ ), the carbon composition is thermodynamically impossible at all temperatures. This point is equivalent to  $\text{CO}_2$  and is marked in Figure 2.2. The blue dotted line shows all C-H-O compositions with an O/C of exactly two. For temperatures higher than 600 °C, carbon deposition is not possible for an O/C of two or higher. For temperatures below 600 °C carbon deposition is possible for hydrogen contents below 73 % ( $\gamma_H = 0.73$ ). A hydrogen content of 73 % and an O/C of two is indicated with a red circle in Figure 2.2. This red circle is also the C-H-O composition of the stoichiometric methane SR reaction. This reaction has an H/C ratio of eight (eqs. 2.6 and 2.7), which corresponds to the green-dotted line in Figure 2.2. In general, the red dashed-dotted line represents all non-stoichiometric C-H-O possibilities for methane SR. For methane reforming, carbon deposition is only possible if insufficient water is supplied (especially at high temperatures). Natural gas from the distribution network normally also consists of higher hydrocarbons (the solid square

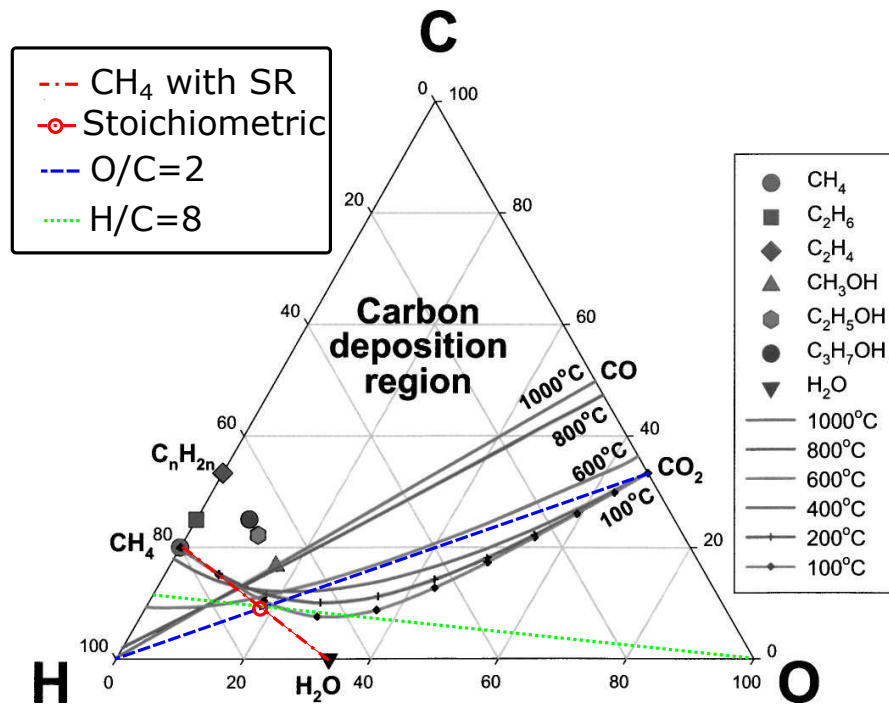


Figure 2.2 – Carbon deposition limit lines in the C-H-O ternary diagram for different constant temperatures and ambient pressure shown with solid lines. The steam reforming of methane is marked with a dotted-dashed red line. Dotted green and dashed blue lines show constant O/C and H/C ratios, respectively (adapted from [1]).

for  $C_2H_6$  and the solid diamond for  $C_nH_{2n}$ ), which increases the C molar fraction and shifts the C-H-O composition towards the carbon deposition region. To decrease the C molar fraction, it is common practice to add excess steam to the SR process. An operation with an O/C higher than two and an H/C higher than eight always leads to carbon-free operation. Excess steam also shifts the full methane conversion by SR towards lower temperatures, as pointed out in Section 2.1.3. Unfortunately, excess steam also increases the water vapor partial pressure and decreases the hydrogen partial pressure, resulting in a decreased Nernst potential (eq. 2.14). This leads to a decreased SOFC electrical efficiency (eqs. 2.20 and 2.21).

If the steam reformer is fed with steam from the AOR, the C molar fraction is increased due to the presence of  $CO_2$  and  $CO$ . Thus, the risk for carbon deposition is increased, as Figure 2.2 shows. Although an O/C of two for methane SR is safe to operate, with a AOR it can lead to carbon deposition. It is therefore important to check not solely the O/C, but also the H/C.

### 2.1.9 Research systems

SOFC systems are already commercially available and offer excellent efficiencies and high lifetime. Appendix A introduces commercial systems of several companies, such as Bloom Energy, SOLIDpower, and Kyocera. However, the main limitation of these commercial systems

is the capital, as well as service and maintenance costs. The AOR offers a solution to this problem. This chapter summarizes past and current research projects in which the hot anode off-gas is used for steam reforming of methane.

Powell et al. [41] from the **Pacific Northwest National Laboratory** conducted 24 tests with a planar SOFC between 1.67 kW<sub>el</sub> and 2.15 kW<sub>el</sub>. 63 % and 57 % electrical gross DC efficiency were reached. This correlates to 57 % and 49 % electrical net DC efficiency. The RR was varied between 83 % and 90 %, which led to global FU of 86 % and 93 %. The off-the-shelf, oil-free fan from AirTech West (USA) for the AOR had a nominal power of 300 W<sub>e</sub>, a total efficiency of 8 %, and an inlet temperature of 145 °C. This low inlet temperature was achieved by mixing the off-gas with the cold natural gas, pre-reforming, and finally cooling with an anode recuperator. Powell et al. found that the net efficiency could be further improved to over 60 % with properly sized fans (i.e., cathode and anode recirculation fans were oversized).

A project team of four German research institutes ( **CUTEC Institut, Zentrum für Brennstoffzellen, TU Braunschweig, and TU Clausthal**) were operating an SOFC with 0.87 kW<sub>el</sub> gross power and 55 % electrical gross DC efficiency. The system used a CPOX reformer and a AOR. The AOR was realized with a fuel-driven ejector, i.e., the fuel at the SOFC inlet was pressurized and served as motion fluid to increase the pressure of the non-cooled anode off-gas, the suction fluid. 85 % global fuel utilization was achieved. Within the experiment, only the “recycle ratio” and the global FU were measured; hence, the local FU was estimated with a simulation. The local FU was estimated as 73 %-78 %. The recycle ratio, which is defined as the ratio between the recycled anode off-gas mass flow rate ( $\dot{m}_{AOR}$ , stream 7 in Figure 2.1) and the inlet fuel mass flow rate ( $\dot{m}_{fuel}$ , stream 1 in Figure 2.1),

$$RR = \frac{\dot{m}_{AOR}}{\dot{m}_{fuel}} \quad 2.35$$

was varied between 8.5 and 5 [42, 43]. A direct conversion to the definition of the RR used in this thesis (eq. 2.29) is therefore not possible. However, considering a constant global FU of 85 % and a local FU of 73 %-78 %, the RR is estimated as 37 %-52 %.

In the framework of the **RealDemo-project**, the Technical Research Centre of Finland (VTT) operated a 10 kW<sub>el</sub> planar cross-flow SOFC with 66 % electrical gross AC efficiency and 54 % net efficiency, for over 10,000 hours. A 100 W<sub>el</sub> electrically driven fan was used for AOR at high-temperatures. Halinen stated that an ejector-based AOR could further decrease complexity of the recirculator equipment. The 800 W<sub>el</sub> cathode fan was the dominant parasitic effect [44]. In a previous report, an EAR of about four and a global FU of 80 % were reported [45].

Peters et al. [46] from the German research institute “**Forschungszentrum Jülich GmbH**”

demonstrated a 4 kW<sub>el</sub> SOFC with AOR at 64 % electrical gross AC efficiency and 59 % electrical net AC efficiency. The global FU was 90 % and the RR 74 %. In general, the highest electrical net efficiencies can be reached with high global FU and low RRs. Peters et al. stated that “all tests [...] were performed with a used and already aged stack; with a new stack, the achievable efficiencies are more than five percentage points higher.” Thus, efficiencies of up to 64 % were deemed feasible. A “hermetic side-channel blower” from AirTech West was used to recirculate the anode off-gas at temperatures of 160 °C to the steam reformer. An external steam supply was therefore not necessary. The housing with the electrical motor and the fan domain with anode off-gas were hermetically-sealed due to the magnetic drive. The fan nominal speed was 15 krpm.

The Austrian company **AVL List GmbH** is developing an auxiliary power unit, which is used as a range extender for automotive applications, as well as a stationary cogeneration SOFC. Recently, the company tested an SOFC with a 6.3 kW<sub>el</sub> DC power rating. 60 %-62 % electrical DC efficiency was achieved. It is not clear whether that efficiency is a net or gross value. AVL also developed an “anode gas recirculation concept using an electrically-driven hot gas recirculation blower with hydrodynamic [author’s note: oil] bearings”. This fan recirculated the anode off-gas to the steam reformer at temperatures up to 600 °C [47, 48, 49].

The US Department of Energy (DoE) started the SOFC program (formerly named the Solid State Energy Conversion Alliance (SECA) program) in 2000 to commercialize SOFC systems that were 200 kW<sub>el</sub> to 3000 kW<sub>el</sub>. Since 2000, many companies, such as Siemens ceased participation in this program along with all SOFC research. Currently, three companies are involved in SOFC system development: LG Fuel Cell Systems, Inc. (formerly Rolls-Royce Fuel Cell Systems, Inc.), Redox Power Systems, and FuelCell Energy, Inc.

**LG Fuel Cell Systems, Inc.** is developing a 250 kW<sub>el</sub> pressurized SOFC system with planar cells. For the AOR a fuel-driven ejector is used. The burned cathode and anode off-gas feeds a high- and low-pressure turbine within an in-house designed “two shaft turbo-generator”. This unit generates electricity and compresses the cathode airflow to high pressures of about 4 to 7 bars within a low and high-pressure compressor stage. The cathode off-gas recirculation is realized with an air-driven ejector. LG tested a preliminary blog test rig with 15 kW<sub>el</sub>, which did not include the two shaft turbo-generator. The report states an “anode loop electrical efficiency” of 60 %. It does not state the exact definition of the “anode loop electrical efficiency”. The author suspects that this is the electrical net DC efficiency. The project has been on-going since 2009 and is expected to run until the end of 2019 [50, 51, 52, 53].

The US company **FuelCell Energy, Inc.** sells MCFC in the multi-megawatt size range. In 2012, the company acquired Versa Power Systems, Inc. to expand the SOFC research and development program. FuelCell Energy tested a 50 kW<sub>el</sub> SOFC system with AOR. The stack used planar cells and operated at ambient pressure. The anode off-gas was mixed with fresh incoming methane. An “anode recycle blower” compressed this mixture and sent it to the steam reformer and to the SOFC anode. The “anode recycle blower” from the New York Blower

Company had a diameter of 690 mm and a rotational speed of 3.75 krpm. Its pressure rise was 37 mbar, the power was 1.8 kW, and the overall efficiency was 12 %. The advantage of this AOR is that an external water supply is only necessary during system startup. The report states a 61 % electrical net AC efficiency for the SOFC system. Although the current demonstrator has no heat recovery, the estimated utilization rate could be as high as 84 % [54, 55].

More recently, **Bosch** announced a “plug and play” 10 kW<sub>el</sub> SOFC with AOR reaching a DC efficiency of 70 %. Whether this referred to a net or gross efficiency value was not stated. The startup time was less than four hours, and only half an hour after a twelve-hour break. Bosch claims a return on investment in less than five years [56].

**Conclusion:** Except from projects from the former Rolls-Royce Fuel Cell Systems, Inc. and AVL List GmbH, the SOFC system and the necessary turbomachinery components were designed by independent companies. This leads to sub-optimal configurations of the SOFC system and AOR fan. Off-the-shelf components cannot satisfy the specific system requirements (i.e., relatively low mass flow rate and relatively high pressure rise). An integrated design and optimization procedure that takes the AOR fan and the entire SOFC system into account, could lead to better component and system efficiencies. Therefore, this work considers a high-level integrated simulation and optimization procedure.

Although many SOFC systems with AOR were previously demonstrated, to the best of author’s knowledge none used a thermally-driven AOR fan. Thus, such a system would be a novelty within AOR field.

## 2.2 Pressure rise units for off-gas recirculation

As mentioned in Section 2.1.9, state-of-the-art PRUs are ejectors, fans, blowers, or compressors. Each option is discussed below.

An **ejector** is fed with a high-pressure motive fluid that is either steam (steam-driven option a in Figure 2.1), fuel in the case of the AOR (fuel-driven option b), or air in the case of the COR (not shown in Figure 2.1). A steam-driven option for the COR is not discussed in the literature, since the steam increases the aging rate of the cathode. Within a convergent nozzle, the motive fluid is accelerated and then mixed with the suction fluid, in this case the cathode or anode off-gas. The mixture is then accelerated and decelerated within a Laval nozzle. The low pressure in the convergent part of the nozzle ingests the SOFC recycled gas, whereas in the divergent part, the mixture is decelerated and pressure is regained. The ejector has no rotating parts and no electric power supply, which favors it for high-temperature applications. The electric and rotating parts required to drive the ejector system are placed upstream of the ejector itself at ambient conditions. These parts include the anode fan for the fuel-driven AOR, the cathode fan for the air-driven COR, or the pump in the case of the steam-driven AOR. This

## 2.2. Pressure rise units for off-gas recirculation

---

technology has been used since the early 1990s to drive a AOR or COR [57].

A **fan, blower, or compressor** is a dynamic machine with a rotating bladed impeller. It increases the total pressure and therefore the total specific enthalpy of a continuous gas stream. These machines increase the fluid velocity, which can be recovered as pressure by diffusing the fluid. Common fan types are axial or radial. The fluid enters and leaves an axial machine along the axial direction, whereas it enters the machine in the axial direction and leaves it in the radial direction in the case of a radial machine. This change in direction in the radial machine also leads to a change of diameter, which increases the fluid acceleration due to centrifugal forces. Radial machines are therefore preferred for relatively low volumetric flow rates ( $\dot{V}_{in}$ ) and relatively high pressure rises, and vice versa for axial machines. The specific speed is calculated using the volumetric flow rate, the total-to-static isentropic specific enthalpy difference ( $\Delta h_{i,s,tst}$ ), and the impeller rotational speed ( $\omega$ ).

$$n_s = \frac{\omega \sqrt{\dot{V}_{in}}}{\Delta h_{i,s,tst}^{3/4}} \quad 2.36$$

For radial machines, the specific speed is typically between 0.2 and 1. Axial machines have higher specific speeds, and thus higher rotational speeds ( $\omega$ ) [2]. In COR and AOR, this would lead to very high rotational speeds. In order to mitigate the high speeds, the enthalpy increase is usually split into several stages in axial machines.

In this thesis, dynamic fans, blowers, and compressors are distinguished by the total-to-total pressure ratio,

$$\Pi_{tt} = \frac{p_{t,out}}{p_{t,in}} \quad 2.37$$

which is the ratio of total outlet pressure ( $p_{t,out}$ ) to total inlet pressure ( $p_{t,in}$ ). Fans have a pressure ratio of up to 1.11, blowers between 1.11 and 1.2, and a compressor has a pressure ratio greater than 1.2. It should be noted that various other definitions exist and that the nomenclature in the literature is not always coherent.

Besides the dynamic machines, such as fans or blowers, there are also positive displacement reciprocating machines (e.g., piston or diaphragm compressors) and positive displacement rotary machines (e.g., scroll, vane, or screw compressors). The effect of pulsation, which naturally occurs when using volumetric compressors within an SOFC, is not well studied. In addition, dynamic machines generally have higher efficiencies and can operate oil-free. Hence, the literature only reports the latter as PRUs for the use in AOR and COR.

### 2.2.1 Specifications of the pressure rise unit

With respect to Section 2.1, the PRUs (ejector, fan, blower, or compressor) have to fulfill various specifications. The specifications for the AOR are more restrictive than for the COR, due to the toxic and explosive nature of the gas, as well as aging rate problems.

#### **Pressure rise unit specifications for cathode and anode off-gas recirculation:**

- Oil and grease-free: Oil and grease can block channels in the reformer, anode, or cathode, but can also damage these components and increase the respective aging rate.
- Long lifetime: Typically, SOFC stacks are designed to operate between five and 10 years with regular inspection intervals, whereas an SOFC systems operate between 20 and 30 years. The ideal PRU would not require inspection, maintenance, or replacement. If this is not possible, these actions should coincide with the maintenance interval (typically every year).
- Low cost: Currently, the SOFC technology is a promising option in countries with subsidy programs, such as Japan, Germany, or the USA. Reducing costs is therefore essential for market entry in countries without any subsidy programs.
- Low complexity: Generally, low complexity leads to lower manufacturing and maintenance costs. Less complex systems are generally also more reliable.
- High flexibility: The operation of the PRU should be flexible and independent of the state of the SOFC system.
- High component and system efficiency: A high PRU efficiency can increase the SOFC system efficiency.

#### **Pressure rise unit specifications for anode off-gas recirculation:**

- Air-tightness: The oxygen in the air in combination with the hydrogen in the anode off-gas can lead to explosions. It can also lead to nickel reoxidation in the reformer and anode, which leads to an increased aging rate.
- No off-gas leakage: The anode off-gas is toxic (carbon monoxide) and also explosive (hydrogen); hence, leakage to the environment has to be prevented.
- Temperature resistant: Due to increased corrosion potential, the anode off-gas temperature should not fall below the dew point. This minimum temperature depends on the off-gas mixture and pressure, as well as the required safety margin.
- Explosion-proof: Since absolute air-tightness over a long time period can never be guaranteed, the PRU should be explosion-proof, i.e., have no components that could possibly ignite a hydrogen / oxygen mixture.



### 2.2.2 Commercial and research recirculation fans

Companies that offer off-the-shelf and custom-made recirculation fans include Creative Applications Co., Ltd (Japan), Domel (Slovenia), Ametek (USA), AirTech West (USA), Phoenix Analysis & Design Technologies, Inc (USA), R&D Dynamics Corporation (USA), Mohawk Innovative Technology, Inc. (USA), Barber-Nichols Inc. (USA), and AVL List GmbH (Austria).

The company **Creative Applications Co., Ltd** [58] claims to have the “first technology in the world” that offers a 70 mm electrically-driven radial fan based on a three-dimensional impeller geometry and designed for a 10 kW<sub>el</sub> SOFC system. The achieved pressure rise is 80 mbar and the mass flow rate is 14.75 kg h<sup>-1</sup> at a rotational speed of 50 krpm. The overall efficiency is 26 % at inlet temperatures of up to 650 °C [59]. Current fans operate on ball bearings, but the company is investigating dynamic gas film bearings.

Within the DoE-funded SOFC program (formerly named SECA program), there are two US companies investigating AOR fans: R&D Dynamics Corporation and Phoenix Analysis & Design Technologies, Inc. Mohawk Innovative Technology, Inc. (MITI) is currently designing a novel concept.

**Phoenix Analysis & Design Technologies, Inc.** developed a multi-stage, low-cost radial fan based on cantilevered prismatic blades with constant blade span and a shrouded impeller with a diameter of 90 mm. The pressure rise was up to 50 mbar (within several stages) and the “aerodynamic efficiency” was nearly 70 %. Although it was not specifically stated, the author estimates the rotational speed to be 20 krpm. By constraining the rotational speed to such low values, several stages were required, which increased the complexity of the system and therefore the cost. The recirculation fan was designed for SOFCs with an output of up to 50 kW<sub>el</sub> and recirculation temperatures of up to 80 °C. The company states that “single stage devices cannot achieve these high pressures unless rotational speeds are very high (up to 150,000 RPM). In this case, gas bearings are the only alternative but they are expensive and not readily available” [60]. Single row angular contact ball bearings were used instead.

**R&D Dynamics Corporation** developed a high-speed radial fan supported on dynamic gas film bearings, and more specifically foil bearings for recirculation at temperatures of up to 850 °C. The impeller diameter was 32 mm and it rotated up to 100 krpm. The pressure rise was between 10 mbar and 25 mbar, reaching a mass flow rate up to 0.43 kg h<sup>-1</sup>. An overall efficiency of 45.6 % was reported [61]. This system is also patented [62].

More recently, the US company **MITI** designed an “ultra high temperature anode recycle blower” that recirculates uncooled anode off-gas. As the off-gas temperatures of an intermediate-temperature SOFC are on the order of 700 °C, recirculation fan design is very challenging. In a first step, MITI decided to cool the AOR to 180 °C with two HEXs. The advantage is that the recirculation of a “cold” fluid at 180 °C requires less power, and thus the auxiliary power and net efficiencies were increased. As a disadvantage, the two additional HEXs increased capital cost, but also increased pressure and thermal losses. The first prototype was a radial backward

curved fan. Only the design parameters have been published, and no measured data has been released. At the nominal point, the mass flow is  $119 \text{ kg h}^{-1}$ , the pressure rise is 72 mbar, the fan diameter 50 mm, and the rotational speed is 55 krpm [63].

Within the scope of the SOFC20, in the framework of the EU-funded Fuel Cells and Hydrogen Joint Technology Initiative, a  $5 \text{ kW}_{\text{el}}$  SOFC with AOR was developed. The company **AVL List GmbH** designed a AOR radial fan with oil-lubricated bearings for temperatures of up to  $600 \text{ }^\circ\text{C}$ . Rotational speeds were up to 120 krpm and efficiencies exceeded 50 %. Although not explicitly stated, the reported efficiency was the overall, not isentropic [47].

### 2.2.3 Comparison of different pressure rise unit technologies

Section 2.2.2 as well as Section 2.1.9 summarize different PRUs. Six different state-of-the-art archetypes can be identified, as well as the novel patented concept developed within this thesis:

- Fuel-driven ejector (option b in Figure 2.1)
- Steam-driven ejector (option a in Figure 2.1)
- Low-speed (below 50 krpm) electrically-driven radial fans (option c in Figure 2.1)
  - with ball bearings connected to the electric motor by a magnetic coupling (hermetic)
  - with ball bearings directly coupled to the electric motor
- High-speed (above 50 krpm) electrically-driven radial fans (option c in Figure 2.1)
  - with dynamic gas film bearings directly coupled to the electric motor
  - with hydrodynamic oil bearings directly coupled to the electric motor
- High-speed thermally-driven radial fan (novel patented option d in Figure 2.1)

All of these PRU types are listed and captured in Table 2.1. This table rates how well each of these PRUs can fulfill the specifications stated in Section 2.2.1. A full circle (●) indicates that the PRU can fulfill the specification, whereas a blank circle (○) indicates poor fulfillment.

As stated before, ejectors can operate at high temperatures, and the driving parts can be located upstream of the ejector at ambient temperature. The lifetime of ejector systems is therefore limited only by these rotating parts. For an oil- and grease-free operation, however, it is important that upstream rotary parts, such as fans or pumps, also operate oil- and grease-free.

One limiting component of electrically-driven fans in terms of lifetime and temperature is the motor itself. It cannot tolerate intermediate-temperature SOFC off-gas temperatures that are in the order of  $700 \text{ }^\circ\text{C}$ . Dicks and Martin [64] stated that recirculation fans tended towards

## 2.2. Pressure rise units for off-gas recirculation

Table 2.1 – Comparison of different pressure rise units for anode off-gas recirculation. A full circle indicates best performance, whereas a blank circle indicates poor performance.

Coupling	Ejector		Electrically-driven fan				Thermally-driven fan
	Fuel driven	Steam driven	Ball bearings Magnetic	n/a	Dynamic gas bearings n/a	Dynamic oil bearings n/a	Dynamic gas bearings n/a
Oil and grease-free	●	●	◐	◐	●	○	●
High lifetime	●	●	◐	◐	◐	◐	◐
Temperature-proof	●	●	◐	◐	◐	◐	◐
Low complexity / cost	●	◐	◐	◐	◐	◐	◐
High flexibility	○	◐	●	●	●	●	◐
High efficiency	◐	◐	◐	◐	◐	◐	●
Air-tightness	●	●	◐	◐	◐	◐	◐
Leakage-proof	●	●	◐	◐	◐	◐	◐
Explosion-proof	●	●	●	◐	◐	◐	●
<b>Average</b>	◐	◐	◐	◐	◐	◐	◐

leakage and were “required to overcome a relatively high pressure drop with relatively small process gas flow rates. This combination of process requirements is particularly difficult to meet”. Many AOR fans were therefore oversized. Liu [65] stated that the main disadvantages of recirculation fans with ball bearings are the limited lifetime and not being able to “compensate for a larger fluid pressure drop”. This specification is contradictory to the compensation of high pressure drop, since higher fan pressure rises imply higher fan rotational speeds at elevated temperatures, which leads to decreased bearing lifetime.

Thus, many SOFC systems with an electrically-driven fan recirculate the off-gas at “cold temperatures” of 150 °C, well above the anode off-gas dew point. Cold recirculation can be achieved with an additional HEX in the recirculation loop and/or by mixing the recirculated cathode off-gas with the cold incoming air or mixing the recirculated anode off-gas with the cold incoming fuel. On the anode side, it is possible to cool the recirculated flow within the endothermic reformer. Higher recirculation temperatures are only achieved by more complex designs with an integrated heat shield that protects the electric motor and the bearings from elevated temperatures. Although a magnetic coupling is an excellent solution in terms of an explosion-proof and hermetic design, it complicates the system, limits the operational temperature and the rotational speeds, and thus limits the pressure rise and component efficiency. The ball bearings used for such PRU are oil-free, but not grease-free. These ball bearings are normally sealed and use high-vacuum grease, but the lifetime is limited.

**Dynamic gas film bearings**, which have a high lifetime even at elevated temperatures and rotational speeds, are better suited for AOR. These bearings generate an extremely thin cushion of air (i.e., several micrometers) that lifts and supports the rotor while operating at high speeds. The advantage of the dynamic gas film bearing is that it is passive and self-acting, i.e., it does not require auxiliary equipment. The wear of the bearing is extremely low and occurs only during startup until lift-off speed is achieved: the speed at which the rotor can lift off

due to the pressure built within the air cushion. These types of bearings feature a lifetime expectation that coincides with that of an SOFC stack. Due to the high rotational speeds, low clearances, and low tolerances for shaft misalignment, it is extremely challenging to couple dynamic fluid bearings with a magnetic coupling. One disadvantage of this type of bearing is designing an explosion-proof unit that hermetically separates the explosive anode off-gas from the electric motor. The housing being supplied with purge gas, such as nitrogen, is a commonly used method. The Japanese company CAP uses this technique, for example. This method has the disadvantage of decreasing the system efficiency by diluting the anode off-gas. Additionally, the auxiliary power is increased, since nitrogen must be available and compressed. The dynamic gas bearing design requires high manufacturing tolerances, which is challenging, even though these types of bearings have been in use for several decades.

**Dynamic oil bearings** are less challenging to design, since the lubricant is incompressible. Note, however, that the bearing properties, i.e., the bearing stiffness and damping, are negatively influenced at higher temperatures, which must be taken into consideration. Like the dynamic gas film bearings, these bearings have low wear and thus a high lifetime. In contrast to externally-pressurized bearings, these bearings do not require any auxiliary equipment. The main disadvantage of this type of bearings is that oil-tightness must be guaranteed in order to protect the SOFC components.

Evaluating the exact **cost of each PRU** system is difficult, however, evaluating the complexity in terms of number of components is more straight-forward. The following list evaluates the systems in order of increasing complexity with respect to component temperatures, manufacturing tolerances, and number of components.

- Fuel-driven ejector at hot conditions (2 components): Anode fan at ambient temperature and ejector at high temperature (●).
- Electrically-driven fan with ball bearings, dynamic oil, or gas film bearings at hot conditions (1 component): Fan at high temperatures with a heat shield or similar protections (◐, ◑, ◒).
- Electrically-driven fan with ball bearings, dynamic oil, or gas film bearings at “cold” conditions (2 components): Fan and a HEX (◓, ◔, ◕).
- Electrically-driven fan with ball bearings and magnetic coupling (2 components): Fan at “cold” off-gas temperatures and a HEX (◖).
- Steam-driven ejector (4 components): water treatment, pump at ambient temperature, evaporator, and ejector at high temperature (◗).
- Thermally-driven fan (4-5 components): water treatment system, pump at ambient temperature, evaporator, HEX and “cold” off-gas temperature fan-turbine unit (FTU) or hot off-gas temperature FTU (◘).

Regarding the **efficiency and flexibility** of the different PRUs, the literature provides several

theoretical comparisons.

Peters et al. [66] compared a nominal system layout for a 3 kW<sub>el</sub> SOFC without AOR to several layouts with AOR driven by a high-temperature fan, or an intermediate-temperature fan (<200 °C), as well as fuel-driven and steam-driven ejectors. The electrical net AC efficiency was up to 16 % higher than the nominal design without AOR. The layout itself, i.e., fan or ejector, had a minor influence; other criteria such as number of components or system complexity were more important. However, the "fuel blowers and ejectors [...] are not available on the shelf and have to be developed" [66].

Engelbracht et al. [67] compared a fuel and steam-driven ejector system for an SOFC with AOR. Special focus was placed on the SOFC part-load behavior. A steam-driven ejector showed strongly improved part-load behavior and slightly improved electrical net AC efficiency, but the number of components increased (i.e., condenser, pump, evaporator, and two additional HEX). The higher electrical net efficiency for the steam-driven ejector was logical, since the density of water is more than 1000-times higher than natural gas, which leads to significantly lower power consumption of the pump in comparison to the anode fan.

In terms of flexibility, an electrically-driven fan offers the best option. These fans can be operated between zero and the nominal mass flow rate. Thus, fans can provide and control the optimal RR for the respective SOFC state. Fans only depend on an input from the electrical grid, which is independent of the SOFC system and its current state. Additionally, the electric motor reacts directly and does not have delays, such as in a pump / evaporator system. Steam-driven ejectors depend on the availability of condensed water (for a system without additional water input), whereas fuel-driven ejectors are regulated by the fuel and thus change the reformer inlet composition. Engelbracht et al. [67] pointed out that this can favor carbon deposition for both cases.

In **conclusion**, the thermally-driven AOR fan is a promising option, since it is oil-free and highly efficient. It can also withstand high temperatures, offers a high lifetime, and is explosion-proof and flexible. Overall, the flexible operation is an advantage with respect to the ejector systems.

## 2.3 Fan

This section outlines a general overview of fans and components, introduces the concept of the mean-line analysis, and states the fan efficiency and power definition. It also provides an overview of the fan design process, as well as important decisions a fan designer must make.

### 2.3.1 Nomenclature

Figure 2.3 summarizes important sections and components within a fan, consisting of the fan inlet (fan section 1 to 3), the fan impeller (3 to 4), and the fan outlet (4 to 8).

**Fan inlet (fan section 1 to 3):** The first domain, the inlet domain that is typically a tube with a constant diameter. The fluid enters the domain at the machine inlet (section 1 in Figure 2.3) and leaves it at the nozzle inlet (1.1). A nozzle is located downstream of the inlet, which accelerates the flow to the optimal inlet velocity to minimize the losses. The flow further accelerates within the transition region towards the fan inducer. Ideally, this region features an aerodynamic fan nose cone that minimizes the pressure loss, but because absolute velocities, and thus losses, are low in this region, this fan nose cone is optional. Two main radial fan geometries can be distinguished: fan impellers with inducer and without inducer. Within the inducer, the flow changes direction from axial to radial. Figure 2.3 shows an inducer-less fan impeller, i.e., the fan main blade leading edge (LE) is shifted downstream of the inducer inlet (2) towards the radial section of the fan.

**Fan impeller (fan section 3 to 4):** Typically, the highest relative velocities (Section 2.3.2) occur at the fan LE; hence, this part requires careful design (Section 2.3.5). Fan designs with an inducer generally feature three-dimensional blades that require more complex manufacturing methods, whereas inducer-less fan designs often have two-dimensional prismatic blades, which simplifies manufacturing and thus reduces cost.

It is common practice to add one or more splitter blades next to the main blades with higher LE radii. Downstream of the main blade LE is the splitter blade LE (3.1) that is shown by a dashed line in Figure 2.3. The rotating wall of the fan impeller, shown with a solid red line, is named the hub, whereas the non-rotating wall is named the shroud. Two main fan designs can be distinguished: shrouded and unshrouded impellers. The shrouded impeller features a wall with a shroud on the top of the blades. The blade tip clearance is therefore zero and no blade tip leakage occurs. Due to manufacturing and assembly tolerances, the rotating unshrouded impeller requires axial clearance to the non-rotating shroud. This leads to a blade tip clearance and leakage flow from the blade pressure side (PS) towards the blade suction side (SS) (see Figure 2.4).

The same applies for the outlet of the impeller domain at the fan trailing edge (TE). The fan impeller always has a certain radial clearance at the stationary wall, dictated by manufacturing and assembly tolerances. This can lead to a negative leakage flow from the fan impeller TE to the fan housing, or a positive leakage flow from the fan housing to the fan impeller in the case of a pressurized housing. Another axial clearance is located between the impeller backface and the stationary parts. Typically, a seal, for example a labyrinth seal, is placed between the impeller backside and the fan housing to limit this leakage flow.

**Fan outlet (fan section 4 to 8):** Commonly, compressors use a vaned or vaneless diffuser to diffuse the flow, recuperate pressure, and limit the velocities, and thus losses within the volute. Fans operate at a much lower pressure ratio and thus at lower velocities; hence, a diffuser is not mandatory. After the diffuser or after the fan TE in the case of a diffuser-less fan, the volute collects the flow. Figure 2.3 shows an easy-to-manufacture rectangular cross-section volute. The volute features a coordinate system with the angle  $\phi$  indicating the position within the

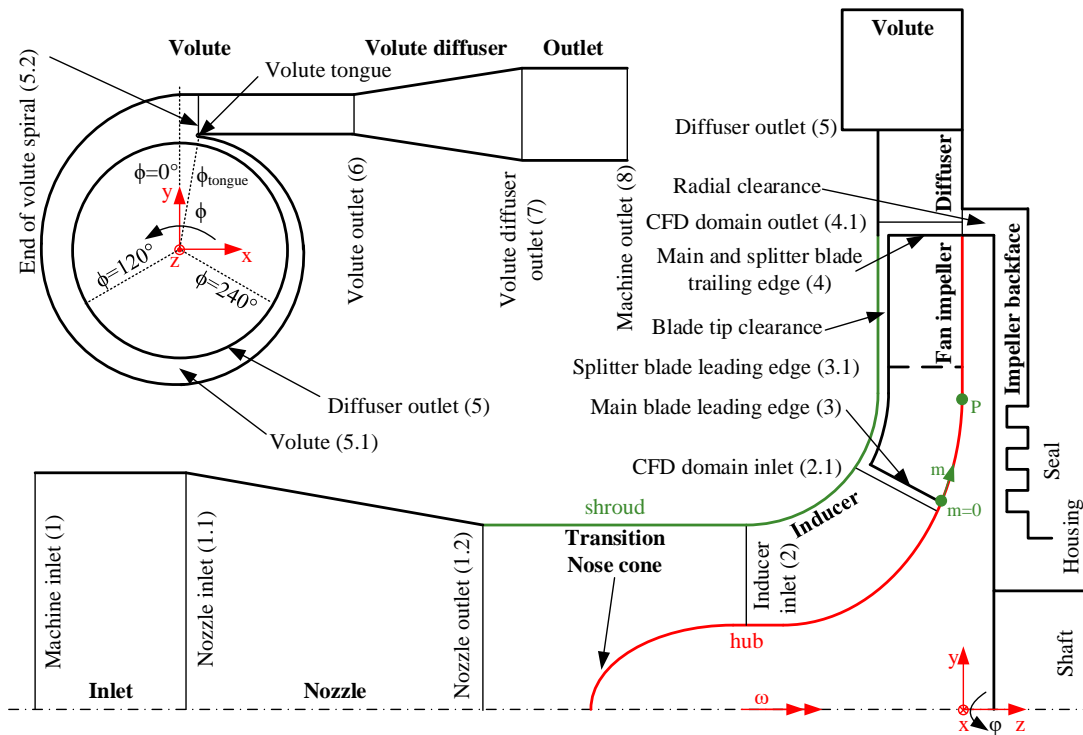


Figure 2.3 – Meridional view of a schematic inducer-less radial fan with splitter blades, diffuser, and volute, as well as the nomenclature of the different sections and important components.

volute. This angle is zero near the outlet of the volute (Figure 2.3) and increases to  $360^\circ$  with the positive angle pointing upstream. After the volute outlet (6), an additional diffuser can be installed to further recuperate pressure.

### 2.3.2 Velocity triangles and mean-line analysis

Figure 2.4 shows the top view (from the  $z$ -direction) of the impeller in Figure 2.3. The backward-curved main blades are visible between the LE hub radius ( $r_{3h}$ ) and the constant TE radius ( $d_4$ ). The splitter blades are visible between the constant splitter blade LE radius ( $r_{3.1}$ ) and the TE radius ( $r_4$ ). The circumferential velocity in cylindrical coordinates ( $[r \ \varphi \ z]$ ) at a specific point,

$$\vec{u} = \begin{bmatrix} 0 \\ c_u = -\omega r \\ 0 \end{bmatrix} \quad 2.38$$

is the product of the angular velocity in  $\text{rad s}^{-1}$  and the radius ( $r$ ). It should be noted that within this thesis, the fan turns counter-clockwise (as viewed from top) and thus has a negative angular velocity in Figure 2.4. The blade surface normal vectors point in the direction of the

circumferential velocity, and are termed the PS, since here the pressure is higher than on the opposite blade surface, the SS. In general, a velocity vector in cylindrical coordinates can be expressed via its radial, circumferential, and axial velocity components.

$$\vec{c} = \begin{bmatrix} c_{rad} = c_x \cos \varphi + c_y \sin \varphi \\ c_u = c_y \cos \varphi - c_x \sin \varphi \\ c_{ax} = c_z \end{bmatrix} \quad 2.39$$

The meridional velocity vector in cylindrical coordinates is the sum of the radial and axial velocity vector.

$$\vec{c}_m = \begin{bmatrix} c_{rad} \\ 0 \\ c_{ax} \end{bmatrix} \quad 2.40$$

The meridional coordinate follows the main blade. Wu [68] was the first to describe this surface. This coordinate for a specific point, P, is marked with a dark green dot in Figures 2.3 and 2.4,

$$m = \int_0^P \sqrt{\left(\frac{dr}{d\bar{m}}\right)^2 + \left(\frac{dz}{d\bar{m}}\right)^2} d\bar{m} \quad 2.41$$

and is calculated with the radial infinitesimal element ( $dr$ ), the axial element ( $dz$ ), and the normalized distance (from zero to one) along the meridional curve ( $d\bar{m}$ ). Figure 2.3 shows the direction of the meridional coordinate as a dark green arrow. This direction starts at the main blade hub LE with  $m = 0$ . A green dot marks this point in Figures 2.3 and 2.4. If the fan blades are exclusively radial and have no axial components ( $dz = 0$ ), the meridional coordinate at the fan TE is the difference between the fan blade TE radius ( $r_4$ ) and the fan blade hub LE radius ( $r_{3h}$ ). Another commonly used coordinate is the blade wrap angle ( $\theta$ ). This angle is zero at the main blade LE and decreases for forward-curved fan blades, remains zero for strictly radial fan blades, and increases for backward-curved fan blades. As shown in Figure 2.4, the backward-curved fan blades have a positive wrap angle at point P with respect to the introduced nomenclature. The meridional view and the  $m - \theta$  plane are widely used in turbomachinery design.

The relative velocity vector,

$$\vec{w} = \vec{c} - \vec{u} \quad 2.42$$

is the velocity relative to the rotating fan impeller domain. It is the difference between the absolute velocity vector ( $\vec{c}$ ) and the circumferential velocity vector from eq. 2.38. Considering a swirl-free flow at the fan inlet, i.e., the circumferential velocity component is zero ( $c_{u,1} = 0$ ), the absolute velocity vector at the fan LE has only a radial and axial component. The relative



velocity at the fan blade hub LE is therefore as follows.

$$\vec{w}_{3h} = \vec{c}_{3h} - \vec{u}_{3h} = \vec{c}_{3h,m} - \vec{u}_{3h} = \begin{bmatrix} c_{3h,rad} \\ \omega r_{3h} \\ c_{3h,ax} \end{bmatrix} \quad 2.43$$

At the fan TE, the axial velocity component is nearly zero and mainly driven by the pressure gradient between the fan hub to shroud, as well as circulations within the fan volute. The relative and absolute velocities therefore only contain a circumferential component, as well as a meridional component that is very close to the radial component. Figure 2.4 also shows the angle definition used within this thesis. The relative velocity angle,

$$\beta = \pi - \arccos\left(\frac{\vec{u} \cdot \vec{w}}{|\vec{u}||\vec{w}|}\right) \quad 2.44$$

is defined as  $\pi$  minus the angle between the relative velocity vector and the circumferential velocity vector. The absolute velocity angle,

$$\alpha = \arccos\left(\frac{\vec{u} \cdot \vec{c}}{|\vec{u}||\vec{c}|}\right) \quad 2.45$$

is the angle between the absolute velocity vector and the circumferential velocity vector. The definitions of  $\alpha$  and  $\beta$  with respect to the meridional direction are also widely used. The two different definitions can be converted by subtracting the respective angle from  $\pi/2$ .

In turbomachinery design, the  $m - \theta$  and  $m - \beta_{blade}$  definitions are widely used to define the exact blade geometry. For three-dimensional blades, the  $m - \theta$  and  $m - \beta_{blade}$  values are defined for different constant blade span layers, where a blade span of zero is equal to the hub and a blade span of one is equal to the shroud. For two-dimensional blades, these definitions are only defined on one span layer, for example at the hub. The blade angle at a specific point P,

$$\beta_{blade} = \arctan \frac{dm}{rd\theta} \quad 2.46$$

can be calculated from the wrap angle and the radius of point P.

It is common practice to complete the preliminary design of a turbomachine with the help of the presented velocity triangles at different fan sections, such as the blade LE and TE. Generally, the first design is made on the mean-line. The mean-line divides the flow channel into two sections with a similar area. In the case of the blade TE section in Figure 2.3, this would be at a blade span of 0.5 ( $r_{4h} = r_{4s} = r_{4,m}$ ). In the case of the inducer inlet 2, this depends on the hub radius ( $r_{2h}$ ) and the shroud radius ( $r_{2s}$ ).

$$r_{2m} = \sqrt{\frac{r_{2s}^2 + r_{2h}^2}{2}} \quad 2.47$$

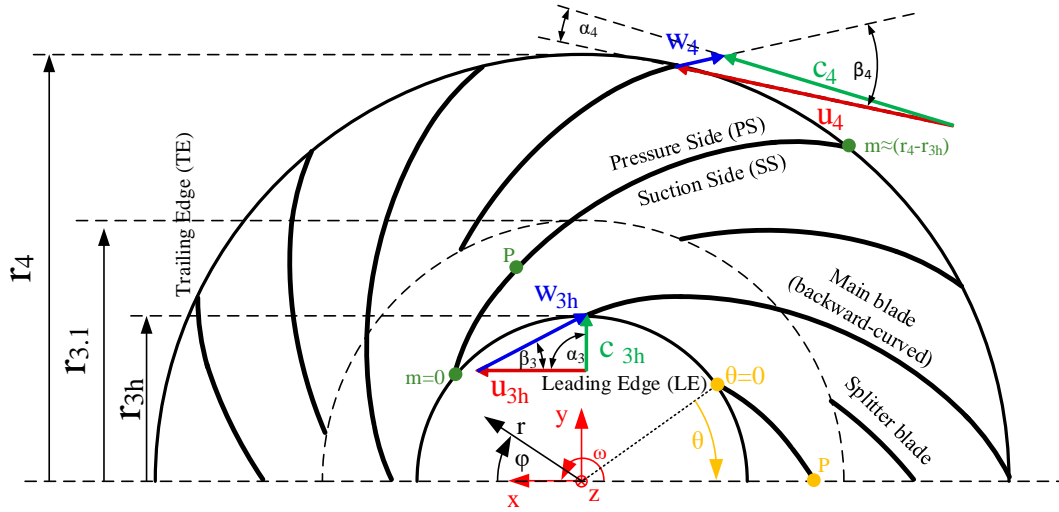


Figure 2.4 – Top view of a schematic fan with backward-curved blades and splitter blades, as well as the velocity triangles at the leading and trailing edge.

### 2.3.3 Efficiency and power

The fan drive, either an electrical motor or a turbine, provides a shaft torque ( $M_{drive}$ ) at a certain angular velocity. The provided drive power,

$$P_{drive} = M_{drive}\omega \quad 2.48$$

is the product of the drive torque and the angular velocity. For experimental power measurement, the ISO 5801 norm [69] suggests to measuring the torque with either a reaction dynamometer or a torsion meter. The shaft bearings, e.g., ball or dynamic gas film bearings, cause losses ( $P_{bearings}$ ) that decrease the shaft torque. Additionally, windage losses between the shaft and the stator ( $P_{windage}$ ), within a possible seal ( $P_{seal}$ ), as well as at the fan impeller backface ( $P_{backface}$ ) occur. In total, the torque provided to the fan, and correspondingly, the power provided to the fan,

$$P_{fan} = [M_{drive} - (M_{bearings} + M_{windage} + M_{seal} + M_{backface})] \omega = [M_{drive} - M_{loss}] \omega \quad 2.49$$

is decreased by all previously mentioned losses ( $M_{loss}$ ). These losses can be expressed as the mechanical efficiency.

$$\eta_{mech} = \frac{M_{drive} - M_{loss}}{M_{drive}} \quad 2.50$$

The exact calculation of each loss is challenging. The ISO 5801 norm [69] suggests measuring the shaft torque without the fan impeller. Thus, the sum of all losses at a specific angular

velocity ( $M_{loss}(\omega)$ ) can be experimentally measured and later subtracted from the provided shaft torque. According to the ISO 5801 norm [69], the theoretical total-to-total pressure rise within the fan impeller depends on the volumetric flow rate at the fan inlet ( $\dot{V}_3$ ) and the correction factor for compressibility effects ( $k_p$ ).

$$\Delta p_{tt,fan,theo} = \frac{P_{fan}}{\dot{V}_3 k_p} \quad 2.51$$

This correction factor for compressibility effects is based on an analytical function with respect to the pressure ratio (eq. 2.37) and the fluid's compressibility factor. Since this factor is nearly one for air and for the hot anode off-gas,  $k_p$  is assumed to be one within this work. The Euler equation multiplied by the fan inlet mass flow ( $\dot{m}_3$ ) can be used to express the fan power. It is important to note that the shroud surface causes momentum around the z-axis ( $M_{z,shroud}$ ), which decreases the total-to-total pressure rise within the fan. For most applications, this torque is neglected, which results in the classical form of the Euler equation (eq. 2.52). This equation is further simplified, if the inlet flow has negligible swirl.

$$\Delta p_{tt,fan,theo} \approx \frac{\dot{m}_3 (c_{u,4} u_4 - c_{u,3} u_3) - \overbrace{M_{z,shroud} \omega}^{\approx 0}}{\dot{V}_3 k_p} \quad \text{Negligible shroud torque} \quad 2.52$$

$$\approx \frac{\rho_3 c_{u,4} u_4}{k_p} \quad \text{Negligible inlet swirl} \quad 2.53$$

The actual total-to-total pressure rise in the fan impeller is lower due to the following frictional losses:

- **Leading edge losses:** Losses at the blade LE occur due to blunt or thick edges, which generate increased flow distortions. Next to the hub, a thick LE can trigger a secondary flow phenomena termed horseshoe vortex. Ideally, the relative flow angle at the LE ( $\beta_3$ ) should be equal to the blade angle ( $\beta_{3,blade}$ ). Thus, the incidence,

$$i = \beta_{3,blade} - \beta_3 \quad 2.54$$

is zero. In the case of off-design operation, the incidence loss increases. A positive incidence favors flow separation on the blade SS. At the nominal point, the incidence is typically a few degrees negative to enable a wide operational range. A three-dimensional fan impeller can adapt the blade angle to maintain a constant incidence. Considering a blade LE at the inducer inlet section 2, due to the increasing inducer inlet radius ( $r_2$ ), the circumferential velocity also increases, which leads to decreased blade angles with increasing radius. Since two-dimensional blades have a constant blade angle, the incidence, and thus the LE losses, vary in the span-wise direction.

- **Tip leakage losses:** The tip leakage is a secondary flow phenomena within unshrouded fan impellers. Its driving force is the pressure difference between the blade PS and SS, as well as the actual relative tip clearance, which is the local tip clearance divided by

the local channel width ( $s(m) / b(m)$ ). The tip leakage forms a vortex that interacts with the shroud boundary layer. This vortex stretches through the entire fan impeller and increases blockage.

- **Secondary flow losses:** In addition to the mentioned horseshoe vortex at the blade LE, the tip leakage loss, and the negative jet at the blade TE, the wake jet effect within a radial fan impeller can be observed. The particles in the wake have a low relative velocity, whereas the particles in the jet, the main impeller flow, have a high relative velocity. The wake forms typically at the shroud SS, whereas the jet forms at the hub PS. The separating effect of centrifugal and Coriolis forces cause this flow phenomena. This leads to a non-uniform flow distribution at the blade TE [70]. The literature states that a minimal blade tip clearance can be useful in terms of equalizing this jet wake effect at the blade TE by accelerating the low relative velocity particles within the wake, and thus reducing losses and increasing efficiency [71].
- **Endwall frictional losses:** The endwalls, such as hub, shroud, or blades have a certain roughness, which increases the boundary layer thickness, and thus the pressure losses, as well as the blockage effect. These effects increase with decreasing Reynolds number or increasing relative roughness, which is the actual roughness divided by the hydraulic diameter. Increased relative roughness therefore leads to reduced turbomachine efficiencies, as well as lower mass flow rates [72].
- **Trailing edge losses:** In the ideal case, the relative velocity at the blade TE should follow the blade, and thus have a similar angle ( $\beta_4 = \beta_{4,blade}$ ). In reality, a so-called slip velocity occurs, which reduces the relative blade angle. The deviation,

$$\Delta = \beta_{4,blade} - \beta_4 \quad 2.55$$

is the difference between the relative velocity angle and the blade angle at the fan TE, and is always greater than zero. The higher the deviation, the lower the fan pressure rise, and thus efficiency. Other losses that occur at the blade TE are secondary flows, such as the negative jet, also called blade wake, which adds losses to downstream components, such as diffusers or volutes.

Considering the total-to-total pressure rise between the fan LE and TE ( $\Delta p_{tt,34}$ ), the hydraulic efficiency or fan impeller efficiency can be calculated.

$$\eta_{hyd} = \frac{\dot{V}_3 k_p \Delta p_{tt,34}}{P_{fan}} \quad 2.56$$

Within the fan impeller, some fluid particles are recirculated to the inlet, which leads to a recirculation mass flow rate ( $\dot{m}_{fan,rec}$ ). The mass flow rate that the fan must compress ( $\dot{m}_3$ ) is

therefore higher than the inlet mass flow ( $\dot{m}_1$ ). This results in the volumetric efficiency.

$$\eta_v = \frac{\dot{m}_1}{\dot{m}_1 + \dot{m}_{fan,rec}} \quad 2.57$$

The overall fan efficiency consists therefore of the drive efficiency ( $\eta_{drive}$ ), the mechanical efficiency (eq. 2.50), the hydraulic efficiency (eq. 2.56), and the volumetric efficiency (eq. 2.57).

$$\eta_{fan} = \eta_{drive}\eta_{mech}\eta_{hyd}\eta_v \quad 2.58$$

Assuming a steady adiabatic system, the fan power can also be expressed with the first law of thermodynamics.

$$P_{fan} = \dot{m}_4 h_{t,4} - \dot{m}_3 h_{t,3} \quad 2.59$$

$$\approx \dot{m}_3 (h_{t,4} - h_{t,3}) \quad 2.60$$

This definition of the fan power is used to calculate the isentropic efficiency, which is similar to the inner efficiency ( $\eta_v\eta_{hyd}$ ) from eqs. 2.56 and 2.57.

$$\eta_{is} = \frac{h_{t,is,4} - h_{t,3}}{h_{t,4} - h_{t,3}} \quad 2.61$$

It is the ratio of the specific enthalpy difference of an isentropic compression compared to the actual specific enthalpy difference within the fan impeller. This efficiency correlation can also use the static isentropic specific enthalpy at the fan TE,

$$\eta_{is,tst} = \frac{h_{st,is,4} - h_{t,3}}{h_{t,4} - h_{t,3}} \quad 2.62$$

which results in a lower efficiency in the case of a fan and a higher efficiency in the case of a turbine. This corresponds to the total-to-static pressure rise ( $\Delta p_{tst,34}$ ) in eq. 2.56.

### 2.3.4 Similarity concepts and scaling laws

**Similarity concepts** are commonly used in turbomachinery pre-design. These can be based on the non-dimensional specific speed (eq. 2.36) and the specific diameter.

$$d_s = \frac{d_4 \Delta h_{is,tst}^{1/4}}{\sqrt{\dot{V}_{in}}} \quad 2.63$$

Balje [2] conducted exhaustive analytical calculations for turbomachines and derived the turbomachine efficiency for a certain  $n_s$  and  $d_s$  value. Figure 2.5 shows such an  $n_s$   $d_s$  performance map for radial and mixed-flow impellers with the corresponding total-to-static isentropic machine efficiency, as stated in eq. 2.62. This map is valid for air as the fluid and a

## Chapter 2. State of the Art

Reynolds number of  $4 \cdot 10^6$  based on the TE blade diameter.

$$Re_D = \frac{\rho_1 u_4 d_4}{\mu_1} \quad 2.64$$

For a fan, the Reynolds number is calculated using the dynamic viscosity ( $\mu_1$ ) and the density ( $\rho_1$ ) at the machine inlet. The Laval number for a fan,

$$La = \frac{u_4}{c_{crit,1}} \quad 2.65$$

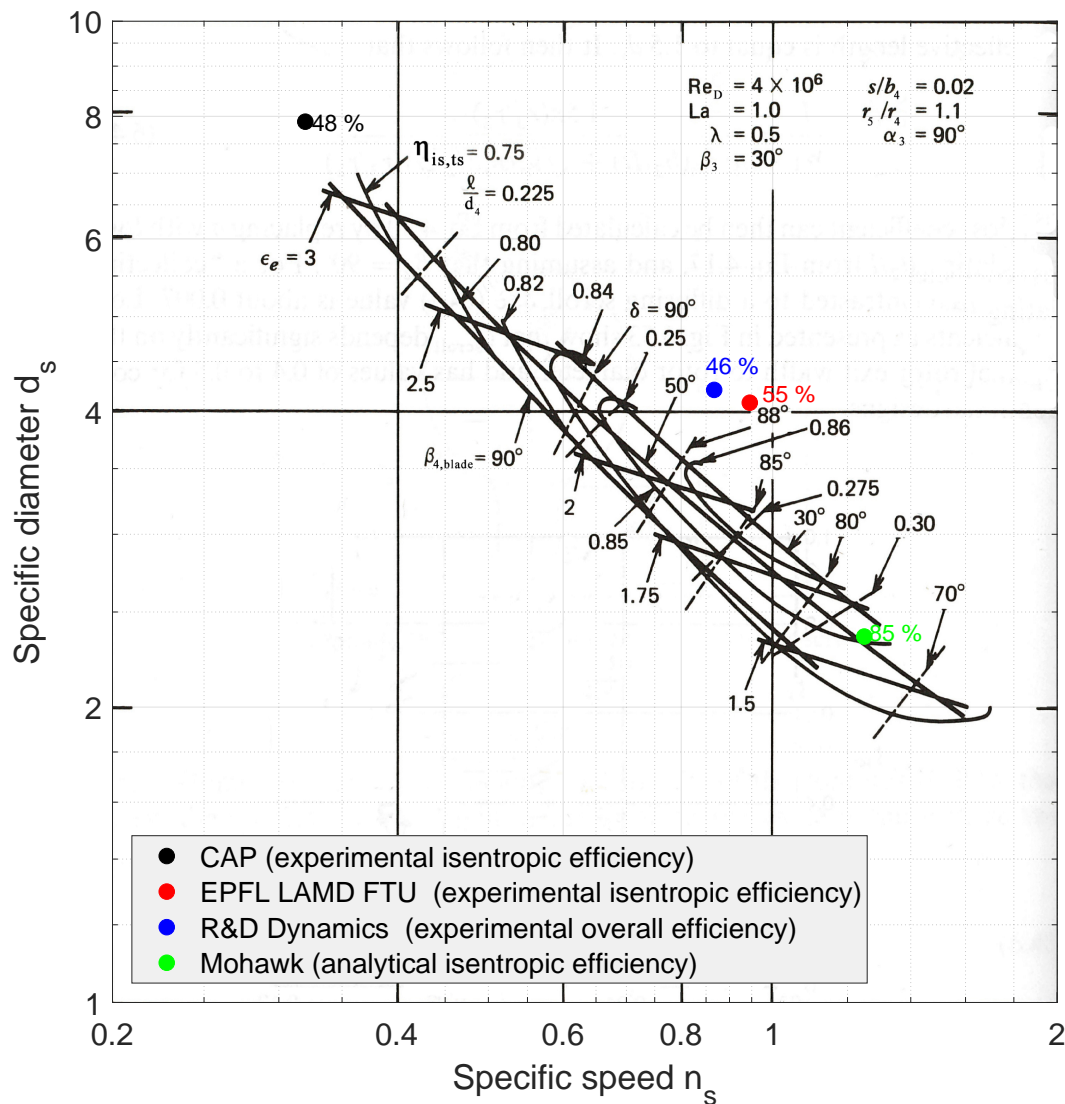


Figure 2.5 – Specific speed ( $n_s$ ) and specific diameter ( $d_s$ ) diagram showing the total-to-static isentropic radial turbomachine efficiency ( $\eta_{is,tst}$ ). Four anode off-gas recirculation fans with respective efficiencies are shown on the performance map (adapted from [2]).

is calculated using the circumferential velocity at the blade TE and the critical velocity of sound at the machine inlet ( $c_{crit,1}$ ), whereas the Mach number,

$$Ma = \frac{u_4}{c_{t,1}} \quad 2.66$$

is calculated with the velocity of sound based on the total parameters at the machine inlet ( $c_{t,1}$ ). The efficiencies calculated in Figure 2.5 are based on a Laval number of one, an inducer inlet hub radius to shroud radius,

$$\lambda = \frac{r_{2h}}{r_{2s}} \quad 2.67$$

of 0.5, a relative velocity angle at the fan LE ( $\beta_3$ ) of  $30^\circ$ , a blade tip clearance to blade TE channel width ratio ( $s/b_4$ ) of 0.02, a diffuser outlet radius to blade TE radius ( $r_5/r_4$ ) of 1.1, and swirl-free flow at the inlet ( $\alpha_3 = 90^\circ$ ). Besides the optimal  $n_s$  and  $d_s$  value, the diagram provides the optimal blade TE angle ( $\beta_{4,blade}$ ), the optimal impeller length to blade TE diameter ( $l/d_4$ ), the optimal ratio of blade TE mean diameter to blade LE mean diameter ( $\epsilon_e = d_{4m}/d_{2m}$ ), and tilt angle ( $\delta = 90^\circ$  for a radial machine and  $0^\circ$  for an axial machine). Parameters other than those stated in Figure 2.5 result in an efficiency decrease. A lower Reynolds number leads to increased viscous losses, and thus lower efficiencies. According to eq. 2.64, a lower Reynolds number is obtained by either decreasing the fan impeller diameter or increasing the machine inlet temperature, which leads to a lower density and higher dynamic viscosity. Balje based the calculations on conventional radial turbomachines with a blade TE diameter on the order of 200 mm. A decreased Laval number, and thus lower rotational speed, is beneficial for the machine, since secondary losses (e.g., LE losses, blade tip losses, and the jet wake effect due to centrifugal and Coriolis forces) are reduced.

According to eq. 2.53, a reduced circumferential velocity also leads to a lower pressure rise. Balje states that at low Laval numbers, such as 0.01, the maximum isentropic efficiency is increased by a few percentage points at low specific speeds, and thus high specific diameters. The inducer inlet hub to shroud ratio of 0.5 ( $\lambda$ ) and the inducer relative velocity angle at the fan LE of  $30^\circ$  ( $\beta_3$ ) are nearly-ideal for many conventional radial turbomachines. However, Javed et al. [73] found out that a lower  $\lambda$  value is beneficial for small-scale radial turbochargers. In general,  $\beta_3$  is selected so as to reduce the relative velocity at the blade LE. Eck [74] mentioned that  $\beta_3$  should be below  $36^\circ$  and the optimal value depends on the fan inlet geometry. A higher tip clearance ratio than 0.02 ( $s/b_4$ ) always leads to increased losses, due to secondary flows.

**Comparison:** Table 2.2 summarizes the main parameters of three electrically-driven radial AOR fans and the novel patented FTU that was designed and tested by the author. Section 2.2.2 provides a more detailed overview of these three electrically-driven fans. The fan from Creative Applications features ball bearings and is thus limited in maximum rotational speed. The two prototypes from MITI and R&D Dynamics feature foil journal and thrust gas film bearings. All parameters were obtained from experiments with air as the fluid at the temperatures stated ( $T_{t,1}$ ).

## Chapter 2. State of the Art

Table 2.2 – Comparison of the main parameters for three radial anode off-gas recirculation fans (electrically-driven) and the patented thermally-driven fan-turbine unit (FTU) developed within this thesis.

	$d_4$ mm	$n_{rot}$ krpm	$\Delta p_{tt,8,1}$ mbar	$\dot{m}_1$ $\text{kg h}^{-1}$	$T_{t,1}$ $^{\circ}\text{C}$	$\eta_{is}$ %	$n_s$	$d_s$	$Re_D$ $\cdot 10^6$
MITI [63] <sup>a,e,g</sup>	50	55	72	119	101	n/a	1.26	2.36	0.893
R&D Dynamics [61] <sup>c,e,g</sup>	31.6	99	25	5.54	850	46 <sup>b</sup>	0.87	4.21	0.068
EPFL LAMD <sup>c,f,h</sup>	19.2	168	55	4.91	200	55	0.95	4.09	0.175
CAP [58] <sup>c,d,g</sup>	70	50	80	14.75	650	48	0.32	7.90	0.235

<sup>a</sup> No experimental results published (pressure rise and mass flow rate calculated for AOR)

<sup>b</sup> Overall fan efficiency

<sup>c</sup> Experimentally measured with air

<sup>d</sup> Ball bearings

<sup>e</sup> Dynamic gas film bearings: foil journal and thrust bearings

<sup>f</sup> Dynamic gas film bearings: Herringbone-grooved journal and spiral-grooved thrust bearing

<sup>g</sup> Electrically-driven by a motor

<sup>h</sup> Thermally-driven by a steam turbine

No experimental results have been published thus far for the fan from **MITI**: The total-to-total pressure rise ( $\Delta p_{tt,18}$ ) and the machine inlet mass flow ( $\dot{m}_1$ ) are therefore theoretical values corresponding to the initial fan design. MITI designed the fan on two lines: 85 % efficiency and a blade TE angle of  $50^{\circ}$ , shown as a green dot in Figure 2.5. Because the inlet temperature is high ( $101^{\circ}\text{C}$ ) and the fan blade TE diameter is relatively small, the resulting Reynolds number is more than four-times lower than that used by Balje ( $0.893 \cdot 10^6$ ). Additionally, the blade tip clearance ( $s$ ) has to be on the order of  $60\ \mu\text{m}$  to comply with the value stated by Balje. Such a small clearance is difficult to achieve, due to the foil bearing clearance, which is typically already on the order of several 10s of  $\mu\text{m}$ , as well as manufacturing and assembly tolerances. Because of the non-optimal tilt angle ( $\delta = 90^{\circ}$  instead of the optimal  $75^{\circ}$ ), the increased viscous losses, as well as increased tip leakage, would result in an isentropic efficiency well below 85 %, although MITI claims efficiencies higher efficiencies. The author expects that the mass flow rate ( $\dot{m}_1$ ) achieved at the nominal fan pressure rise ( $\Delta p_{tt,17}$ ) is lower than expected, and thus the green point should shift to higher  $d_s$  and lower  $n_s$  values.

**CAP** designed the fan with the second-highest Reynolds number. It is more than one order of magnitude lower than that used by Balje. This is mainly resulting from the high temperatures ( $650^{\circ}\text{C}$ ). As shown in Figure 2.5,  $n_s$  values from 0.6 to 1.4 lead to optimal designs for radial turbomachines. The AOR fan from CAP has a very low  $n_s$  value of 0.37. In this region, optimal isentropic efficiencies of 70 % can be expected. Thus, the efficiency of CAP's fan is reduced by 20 % from the optimal value. As already stated, increased viscous losses due to a low Reynolds



number and increased secondary losses due to a relatively large blade tip clearance can further explain this high difference between measured and optimal isentropic efficiency. CAP likely did not design the recirculation fan in the optimal  $n_s$  region, since this would result in rotational speeds more than twice as much as the current 50 krpm, which would result in a reduced bearing life time (less than half of the current lifetime).

The AOR fan by **R&D Dynamics** has the lowest Reynolds number. It is nearly 60-times lower than that used by Balje. The overall fan efficiency is stated as 46 %. Assuming an efficiency of the electrical motor ( $\eta_{drive} = 0.9$ ) and a mechanical efficiency of the foil bearings ( $\eta_{mech} = 0.75$ ), the isentropic efficiency can be estimated to 68 % which is 17 percentage points lower than the optimal efficiency in this region. With this fan design, R&D Dynamics achieved extremely high temperatures of 850 °C, which certainly covers all intermediate-temperature SOFCs systems. The recirculated mass flow of 5.54 kg h<sup>-1</sup> is sufficient for SOFC systems up to 10 kW<sub>el</sub>. However, the pressure rise ( $\Delta p_{tt,18}$ ) of 25 mbar seems low for a 10 kW<sub>el</sub> system. The pressure rises of the other fans in Table 2.2 are three-times higher, which is more adequate. Achieving this order of pressure rise at these high temperatures, would require a rotational speed of 170 krpm (assuming a constant blade TE diameter of 31.6 mm).

**Scaling laws** can be used to scale a current fan to other geometries or one operational point to another. These scaling laws assume similar geometries (geometrical ratios are constant), similar kinematics (velocity triangles at the blade LE and TE are similar), as well as similar dynamics (ratio of impeller forces are constant). Assuming, that full similarity is achieved, the overall fan efficiency is also constant. As mentioned previously, the scaling is limited, due to various effects, such as viscous losses, compressible effects, manufacturing and machining tolerances, etc. The ISO 5801 norm [69] provides conversion rules. The following section states the simplified scaling laws for pressure rises between of up to 20 mbar for two scaled fans and a correction factor for compressibility effects ( $k_p$ ) nearly-one.

The volume flow rate through a fan impeller,

$$\dot{V}_4 = \pi d_4 b_4 c_{4,m} \quad 2.68$$

$$\dot{V} \propto \frac{1}{2} d_4^3 \omega = d_4^2 u_4 \quad 2.69$$

is directly proportional to the rotational speed and the cube of the blade TE diameter (or any other geometrical fan parameter). As stated in eq. 2.53, the total-to-total pressure rise,

$$\Delta p_{tt,fan} \propto \rho_{t,1} \frac{1}{4} \omega^2 d_4^2 = \rho_{t,1} u_4^2 \quad 2.70$$

is directly proportional to the total density at the machine inlet, the square of the blade TE diameter, and the angular velocity or the square of the circumferential velocity. Equation 2.51

shows the proportionality of the fan power.

$$P_{fan} \propto \dot{V} \Delta p_{tt, fan} = \frac{1}{8} \rho_{t,1} \omega^3 d_4^5 = \rho_{t,1} d_4^2 u_4^3 \quad 2.71$$

The power is directly proportional to the volume flow rate and the total-to-total pressure rise, which is consequently proportional to the total density at the machine inlet, the cubic of angular velocity, and the fifth power of the blade TE diameter.

The scaling laws above are commonly used in coefficients to describe a turbomachine. The flow coefficient at the machine inlet is the ratio of mass flow rate to the cube of the blade TE diameter, the angular velocity, and the density based on the total machine inlet conditions.

$$\Phi_{t,1} = \frac{2\dot{m}_1}{d_4^3 \omega \rho_{t,1}} \quad 2.72$$

The work coefficient is the ratio of total-to-total specific enthalpy difference to the square of circumferential velocity at the blade TE diameter ( $u_4 = \omega \frac{d_4}{2}$ ).

$$\psi = \frac{4\Delta h_{tt}}{d_4^2 \omega^2} \quad 2.73$$

In addition to the Reynolds number definition from eq. 2.64, there is also a definition based on the TE channel width.

$$Re_b = \frac{\rho_1 u_4 b_4}{\mu_1} \quad 2.74$$

### 2.3.5 Design procedure and concepts

The literature provides detailed design procedures for turbomachines, such as fans (for example [74, 75, 76]), compressors ([2, 77, 78, 79]), and turbines ([2, 78, 80]). The design of a turbomachine incorporates several different steps that follow in sequence. Each step increases the complexity of the model, and thus the time-consumption for the calculation itself. In order to achieve a mature turbomachine design, a designer must repeat these steps several-times. As this is time- and cost-intensive, companies have several “mother turbomachines” that can be scaled up or down using the scaling laws. This allows for fast and inexpensive design with proven results.

If no adequate “mother turbomachine” is readily available, the design must go through the specified design steps. The input parameters for the turbomachine model are as follows:

- Fluid at the machine inlet and its composition ( $\gamma_i$ )
- Total temperature at the machine inlet ( $T_{t,1}$ )

- Total pressure at the machine inlet ( $p_{t,1}$ )
- Volume flow rate or mass flow rate at the machine inlet ( $\dot{m}_1$  or  $\dot{V}_1$ , respectively)
- Total-to-static pressure rise over the entire machine ( $\Delta p_{tst,18}$ )
- Constraints of volume, weight, cost, materials, sound level, etc.

With these input parameters, the designer has all the necessary information for the turbomachine. Figure 2.6 shows the six different steps that a turbomachine designer generally follows.

**0D, similarity concepts:** With the help of the turbomachine input parameters and the zero-dimensional similarity concepts introduced in Section 2.3.4, the designer can evaluate different design options, such as axial or radial fan. This first design step outlines the overall machine parameters, such as blade TE diameter ( $d_4$ ), relative blade angle at the TE ( $\beta_{4,blade}$ ), rotational speed ( $\omega$ ), and expected isentropic efficiency ( $\eta_{is}$ ).

**1D, mean-line analysis:** In the next step, the designer calculates the velocity triangles at the mean-line and defines the blade LE and TE geometry in more detail. The designer can use one-dimensional models to evaluate the turbomachine performance in more detail. Because the blade tip leakage or the flow deviation at the blade TE, for example, are based on complex three-dimensional flow phenomena, the designer uses empirical-based models. The accuracy of these models relies on well-adjusted coefficients. However, these coefficients can greatly vary from one turbomachine to another. The designer should therefore take great care in this step and adjust the empirical coefficient with the help of more complex models, as stated in

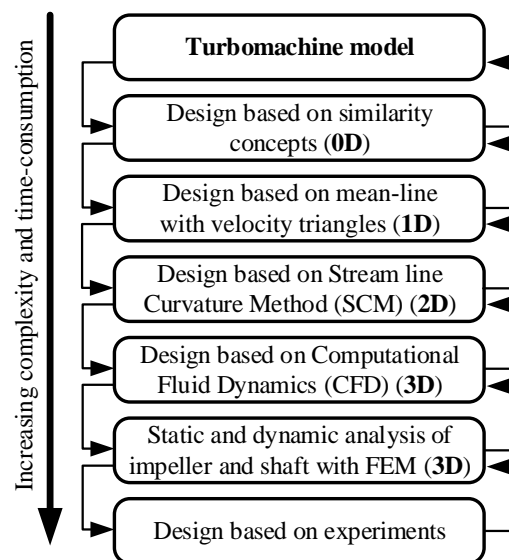


Figure 2.6 – Design procedure for a turbomachine.

the following steps.

**2D, streamline curvature method (SCM):** The next step is the quasi-three-dimensional SCM that is based on the previously introduced meridional surface described by Wu [68]. The through-flow method divides this meridional surface into several stream lines and quasi-orthogonals along the blade LE and TE that form the grid for computation. The SCM solves the conservation of momentum, conservation of mass, the previously described Euler equation, and the second law of thermodynamics for each computational node. The disadvantages of this method are that the specific entropy for each computational node must be specified, the isentropic efficiency must be available a priori, or the SCM uses empirical loss correlations to estimate the specific entropy for each node, along with the isentropic efficiency. The SCM can therefore not directly model complex three-dimensional secondary flow phenomena such as the blade tip leakage or the jet wake effect.

**3D, computational fluid dynamics (CFD):** The final aerodynamic design step uses three-dimensional CFD methods that are generally based on Reynolds-averaged Navier-Stokes equations (RANS). The RANS equations assume that the velocity and pressure are composed of a time-averaged part and a fluctuating part. This assumption introduces further unknown variables that are solved with additional turbulence models, which in turn also rely on empirical coefficients. For example, the commonly used  $k-\omega$  model relies on the specification of five empirical closure coefficients for the turbulent kinetic energy ( $k$ ) and the specific dissipation rate ( $\omega$ ) equations [81]. More accurate methods, such as detached eddy simulation, large eddy simulation, or direct numerical simulation, have been used within research projects. These methods are not a widely-used industry standards, due to the intensive computational power requirements.

**3D, finite element method (FEM):** The last design step is the selection of materials for the turbomachine impeller, shaft, and other components. A static and dynamic structural analysis ensures the mechanical integrity of the impeller with its blades, the shaft, and bearings. Finally, the designer specifies the entire turbomachine concept, including shaft, bearings, and drive, as well as its manufacturing and assembly processes. If a specific sound level is required, an acoustic analysis is necessary.

**Experiments:** Because the analytical and numerical methods rely on empirical inputs, only an experiment can validate these methods, as well as the final fan design. It has to be emphasized that these experiments always contain certain uncertainties imposed by the measurement methods and equipment. A good turbomachine designer therefore uses all the previously described methods when evaluating the results and design.

**Design decisions:** During the previously described design process, the designer must make several decisions. In general, these decisions are trade-offs between aerodynamic efficiency, sound level, static and dynamic structural integrity, as well as material, manufacturing, and assembly costs. Some of these decisions are discussed in the following section. Some design decisions are compared to AOR fans found in the literature.

- **Single-stage and multi-stage:** Multi-stage turbomachines can achieve higher pressure rises, but are also more complex to manufacture. If technically feasible, a single-stage machine is therefore preferred in terms of efficiency and cost. Only Phoenix Analysis & Design Technologies, Inc. uses several stages (up to five) in the AOR fan design [82].
- **Radial, mixed-flow, and axial design:** Axial machines are preferred for a relatively high volume flow ( $\dot{V}_1$ ) and relatively low pressure rise ( $\Pi_{tt,18}$ ), and vice versa for radial machines. Mixed-flow impellers are a trade-off between axial and radial machines and can reach the highest efficiencies. As these machines are complex to build due to the tilt angle, mixed-flow compressors are not as common as radial and axial machines. Axial machines reach the highest specific speeds, whereas radial machines have the lowest specific speeds. All commercial and research AOR fan geometries found on the market and in the literature use a radial fan, except for the side-channel fan used by Peters [46].
- **Forward- and backward curved blades:** Equation 2.53 can be rewritten with respect to the relative velocity angle at the blade TE and its meridional component.

$$\Delta p_{tt, fan, theo} = \frac{\rho_3}{k_p} u_4^2 \left( 1 - \frac{c_{m,A}}{u_4} \cot \beta_4 \right) \quad 2.75$$

It becomes clear that a forward-curved impeller ( $\beta_4 > 90^\circ$ ) can achieve higher pressure rises at a similar rotational speed than to a back-ward curved impeller ( $\beta_4 < 90^\circ$ ). However, back-ward curved impellers show better efficiency. All commercial and research radial AOR fan geometries found on the market and in the literature use backward-curved blades.

- **Inducer and inducer-less impeller:** The flow coefficient (eq. 2.72) is an indicator as to whether an inducer is required. An impeller with a low flow coefficient of up to 0.03 is favorable for an inducer-less design. Impellers with low flow coefficients usually yield higher end wall friction losses within the blade channels, due to an increased hydraulic surface, therefore achieving lower efficiencies. Shifting the blade LE downstream can limit the frictional losses in the inducer. Radial impellers with high flow coefficients feature an inducer with three-dimensional blades. Impellers with flow coefficients higher than 0.06 feature high curvature loss and are usually designed as mixed-flow impellers [83].
- **Three-dimensional and two-dimensional blades:** The radius at the inducer inlet ( $r_2(y)$ ) changes with the blade span. As a result, the circumferential velocity ( $u_2(y) = \omega r_2(y)$ ) is

a function of the blade span, and thus of  $y$ . Thus, the relative angle ( $\beta_2(y)$ ) is also a function of  $y$ . Fans with an inducer therefore feature three-dimensional blades. Inducer-less fans can feature two-dimensional blades, since the LE is at a constant radius. Only the AOR fan from Phoenix Analysis & Design Technologies, Inc. features a two-dimensional inducer-less impeller [82].

- **Constant and variable blade thickness:** From an aerodynamic viewpoint, the optimal blade thickness would be as low as possible. Blades are sometimes tapered, featuring a decreasing blade thickness with increasing blade span to support mechanical integrity. This leads to increased manufacturing cost in comparison to a blade with constant blade thickness.
- **Shrouded and unshrouded impeller:** Shrouded impellers have no blade tip leakage, but increased friction between the blade shroud and the casing shroud. Shrouded designs have a decreased volumetric efficiency, due to the recirculation mass flow from the blade TE to the LE. It is therefore common to place seals between the casing shroud and the blade shroud to limit this leakage. Unshrouded impellers feature lower friction, and thus a lower shroud torque, but increased secondary flows due to the tip leakage. Unshrouded impellers are also easier to manufacture.
- **Impeller with and without splitter blades:** The deviation at the blade TE is decreased with an increased number of blades. However, an increased number of blades leads to an increased hydraulic surface, and thus increased losses. The optimal number of blades is therefore a trade-off between a low deviation and a low frictional loss. Splitter blades do not block the inducer, which results in less frictional losses of the main blades and decreased deviation loss. Impellers often feature one or more splitter blade.
- **Blade leading edge geometry:** Considering the aerodynamic performance, the elliptical blade LE is superior to the round and blunt options. However, a blunt LE is easier to manufacture.
- **Blade trailing edge geometry:** The blade TE can be manufactured as round, elliptical, or cut-off. Since the cut-off blade TE is the easiest option in terms of manufacturing, and differences in performance are negligible, this is the most common blade TE geometry.
- **Vaned diffuser, vaneless diffuser, and no diffuser:** A fan impeller with no diffuser has increased losses in the fan volute due to increased velocities. However, the diffuser can also have high pressure losses if separation occurs. In order to limit the separation due to high circumferential velocities at the blade TE, the diffuser is often tapered at the hub, shroud, or on both sides. Thus, the channel width ( $b_4$ ) is decreased. Vaned diffusers generally have a higher peak efficiency, but a lower efficiency at non-nominal points. A diffuser complicates the fan design and thus increases manufacturing cost.
- **Volute tongue:** For maximum aerodynamic efficiency, the volute tongue, also known as the cut water region, should be placed as close as possible to the diffuser outlet and the

blade TE for a diffuser-less fan. However, apart from the number of blades, the tongue radius and the distance between the tongue and the diffuser, as well as the blade TE, significantly contribute to the intensity of the rotary sound. Generally, a high distance between the volute tongue and the diffuser and consequently the blade TE, leads to lower noise emissions. A higher volute tongue radius is also beneficial in terms of noise. Aerodynamically, a tongue radius is more beneficial than a sharp tongue. The exact placement of the volute tongue is therefore a trade-off between aerodynamic efficiency and sound level [84].

- **Volute cross section:** The volute cross section can be round, horseshoe shaped, trapezoidal, rectangular, etc. Volute with a round cross section have less secondary flows than, for example, volutes with a rectangular cross section. Less secondary flows results in a lower pressure loss. However, the difference in performance is very small; hence, design considerations in terms of manufacturability are more important [85].
- **Volute diffuser design:** Very long diffusers have no flow separation, but high pressure loss due to an increased hydraulic surface. The optimal diffuser design is therefore an aerodynamic trade-off between diffusing and frictional pressure losses.

Due to considerations of the AOR fan efficiency and cost, this work presents a single-stage, radial, backward-curved, inducer-less, unshrouded impeller with main and splitter blades that are constant-height and two-dimensional with constant thickness, a blunt LE, and a cut-off TE. This fan has no diffuser; hence, the fluid directly enters the rectangular volute after the blade TE.

## 2.4 Turbine

Since this work focuses on a radial-inflow partial-admission turbine, Figure 2.7 shows a schematic of the same. A turbine expands the fluid from high to low pressure and drives, via its momentum, the turbine impeller, and thus the shaft. The nomenclature is similar to that presented in Section 2.3.1 in a fan. The main difference in nomenclature is the reversed flow direction and the additional turbine stator. A turbine usually features non-rotating stator blades that give the flow pre-swirl to maximize the total-to-total specific enthalpy difference over the turbine impeller, thus maximizing the turbine power output. This specific enthalpy difference is equal to the Euler equation when neglecting the shroud torque (the blade angle definitions are the same, as defined in eqs. 2.44 and 2.45).

$$\begin{aligned}\Delta h_{tt} &= c_{u,8}u_8 - c_{u,7}u_7 & 2.76 \\ &= u_8c_{m,8} \cot \alpha_8 - u_7c_{m,7} \cot \alpha_7 & 2.77\end{aligned}$$

Thus, a relative angle at the blade LE higher than 90° and an absolute angle at the blade TE lower than 90° maximizes the turbine power output. The stator LE is at plane 5, whereas the TE is at plane 6. The turbine LE is at plane 7, whereas the TE is at plane 8.

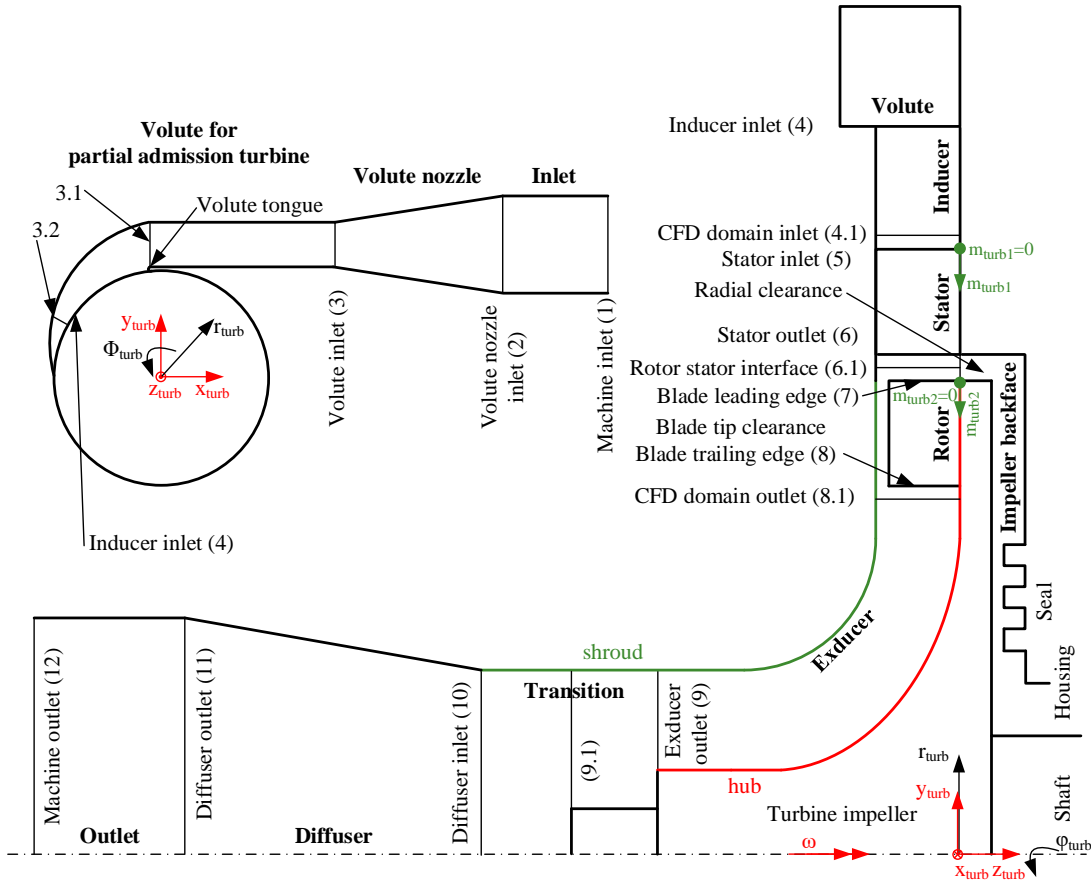


Figure 2.7 – Meridional view of a schematic partial-admission radial-inflow turbine, as well as the nomenclature of the different sections and important components.

Assuming a steady adiabatic system, the turbine power can also be expressed with the first law of thermodynamics.

$$P_{turb} = \dot{m}_8 h_{t,8} - \dot{m}_7 h_{t,7} \quad 2.78$$

$$\approx \dot{m}_8 (h_{t,8} - h_{t,7}) \quad 2.79$$

This definition of the turbine power is used to calculate the isentropic total-to-total efficiency of the rotor,

$$\eta_{is,rotor} = \frac{h_{t,8} - h_{t,7}}{h_{t,is,8} - h_{t,7}} \quad 2.80$$

while the total-to-static efficiency is calculated with  $h_{st,is,8}$ . The total-to-total isentropic efficiency of the entire turbine, including the stator and rotor can be defined, as below.

$$\eta_{is} = \frac{h_{t,8} - h_{t,5}}{h_{t,is,8} - h_{t,5}} \quad 2.81$$



All previously presented non-dimensional numbers in eqs. 2.64, 2.65, 2.72, and 2.74 are also valid for a turbine, but using the parameters at the turbine outlet (12), which are normally available. Similarly, the definitions of specific speed and diameter (eqs. 2.36 and 2.63) use the volumetric flow rate at the machine outlet and the turbine tip diameter ( $d_7$ ), respectively. An additional non-dimensional number used for turbine design, is the degree of reaction.

$$\delta_h = \frac{\Delta h_{rotor}}{\Delta h_{stage}} \quad 2.82$$

It is the fraction of the static-to-static specific enthalpy difference of the rotor ( $\Delta h_{rotor}$ ) to the static-to-static specific enthalpy difference of the stage ( $\Delta h_{stage}$ , rotor and stator). The reaction is always between zero and one, but turbines with a reaction of exactly zero or one are not achievable, since there is always some frictional, and thus pressure, losses within the rotor and stator. Turbines with the highest efficiencies are built at a degree of reaction of 0.5. In this case, the turbine stator and rotor have a similar shape, which facilitates easier manufacturing. Due to the increased static pressure between the rotor and stator, a high-reaction turbine is not capable of partial admission. The power density of a low reaction turbine is higher (twice a 0.5 reaction turbine with similar mass flow rate). The  $\alpha_8$  and  $\beta_7$  are favorable, as the change of direction of the absolute velocity is higher. A higher change of velocity also involves higher aerodynamic losses; hence, low-reaction turbines have an inferior efficiency. Additionally, losses occur due to the increased velocities, which are higher at the stator outlet and rotor inlet, as compared to the 0.5 reaction turbine design.

## 2.5 Intellectual property

The concept of a thermally-driven AOR fan was introduced in 2012 to the Technology Transfer Office (TTO) of the EPFL by Zacharie Wullemin, Daniel Favrat, Jürg Schiffmann, and Jan Van herle. In 2013, the doctoral student, Vaibhav Singh [86] and the Master's student Isha Shukla [87], further developed this concept by conducting various system simulations and optimizations. Within the “unité de cogération à pile à combustible SOFC avec recirculation” (RECOGEN) project, the RECOGEN team, including the author, finalized the SOFC concept with a thermally-driven AOR fan. The author designed, manufactured, and tested the thermally-driven fan, designated FTU between 2014 and 2018. The author contributed to the coupling of the FTU with a 6 kW<sub>el</sub> SOFC system.

The final result of the RECOGEN project was filing the patent “SOFC System With Anode Off-Gas Recirculation” [35].



## 3 SOFC System Design

This chapter describes the investigated SOFC system. It outlines the optimization and design methodology of the entire system, as well as the FTU that increases the pressure within the AOR loop. The SOFC system simulation model with its BoP components is introduced. A system with an electrically-driven AOR fan [88] is compared to a system with a thermally-driven AOR fan that is protected by an European patent [35]. This chapter concludes with presenting the baseline SOFC system and HEX network design.

### 3.1 SOFC system with thermally-driven anode off-gas recirculation fan

Section 2.1 introduces different SOFC systems and respective components, including descriptions of the advantages and disadvantages. Figure 3.1 shows the investigated SOFC system, which has the following specifications:

- Intermediate-temperature SOFC with Ni-YSZ planar anode, YSZ / CGO double layer electrolyte, LSCF / CGO composite cathode, and FeCr metal interconnect / plates as bulk material (Section 2.1.2).
- The feed gas is methane that is reformed via steam to form hydrogen (Section 2.1.3).
- The steam for the reforming is provided via a steam-driven AOR fan with gas film bearings (Section 2.1.7).
- No implemented COR (Section 2.1.7).
- The anode off-gas and the cathode off-gas are not mixed. The anode off-gas burner is provided with fresh incoming air (Section 2.1.5).
- The AOR fan is propelled by a steam turbine. The pressurized steam is evaporated from the condensed water of the anode exhaust.

This setup has several advantages that the European patent [35] explains in detail:

- High electrical net DC efficiencies based on the LHV (eq. 2.21) on the order of 65 % due to higher global fuel utilization. The efficiency is therefore increased by 5 percentage points compared to a system without AOR.
- The SOFC system can operate at a lower local fuel utilization, and thus has an increased lifetime compared to a system without AOR and similar electrical power output.
- The AOR fan has a high lifetime and is temperature-proof due to the gas film bearings. The steam-turbine-driven fan is explosion-proof, oil-free, flexible, and low-cost (Section 2.2.3).
- No external water source required, since the AOR provides deionized and pH-neutral steam for the reforming process.
- Simplified water treatment required (filtering for small particles), as compared to the state-of-the-art direct steam supply system (system e in Figure 2.1).
- Pump and evaporator are 30 % smaller than the state-of-the-art direct steam supply system
- Separation of the anode and cathode off-gas allows for higher condensing temperatures, and thus, higher cogeneration, as well as a smaller condenser, and thus, lower pressure losses compared when the anode and cathode off-gas is mixed.

The stack of the baseline 10 kW<sub>el</sub> SOFC system has several layers of three 220 cm<sup>2</sup> cells. Within one layer, these three cells are electrical in parallel and the different layers are electrical in series. Looking at the gas flows, all layers are in parallel but in each layer the gas distribution within the three cells is in series.

However, during the project, a 6 kW<sub>el</sub> SOFC system with 80 cm<sup>2</sup> cells was realized. Therefore, this chapter compares the electrically-driven and thermally-driven AOR fan based on the experimentally tested 80 cm<sup>2</sup> cells for a 10 kW<sub>el</sub> system, which corresponds to the project objective. These two systems are compared to the baseline SOFC system design. The designed, manufactured, and tested FTU is based on this baseline.

### 3.2 Methodology

The system flowsheet which includes models for BoP components, an experimentally-validated SOFC stack model, and a zero-dimensional fan and turbine model based on similarity concepts, is solved using the commercial software VALI by Belsim S.A. The design variables identified for this system are listed in Table 3.1.

As shown in Figure 3.2, the implemented design procedure is composed of two subtasks: (1) the multi-objective optimizer (MOO) of the SOFC system using the “optimisation multiobjectif de systemes énergétiques intégrés” (OSMOSE) platform (Section 1.2) and (2) the observation-based iterative fan and turbine modeling and design.

The first subtask consists of four steps. Firstly, a process flowsheet with models of the individual components, including a zero-dimensional fan and turbine model based on similarity

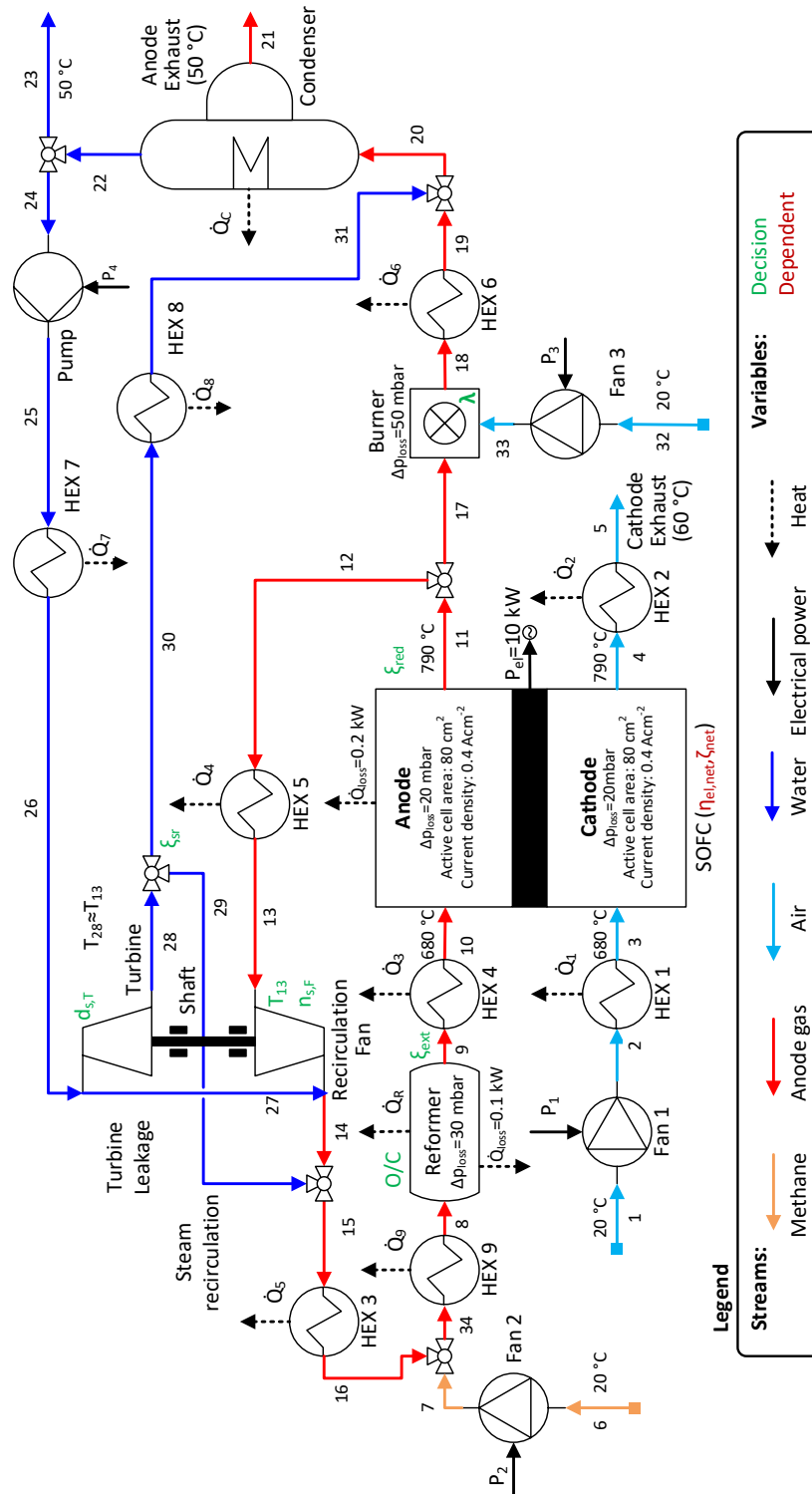


Figure 3.1 – Process flow diagram of the steady co-flow SOFC systems with 10 kW<sub>e1</sub>.

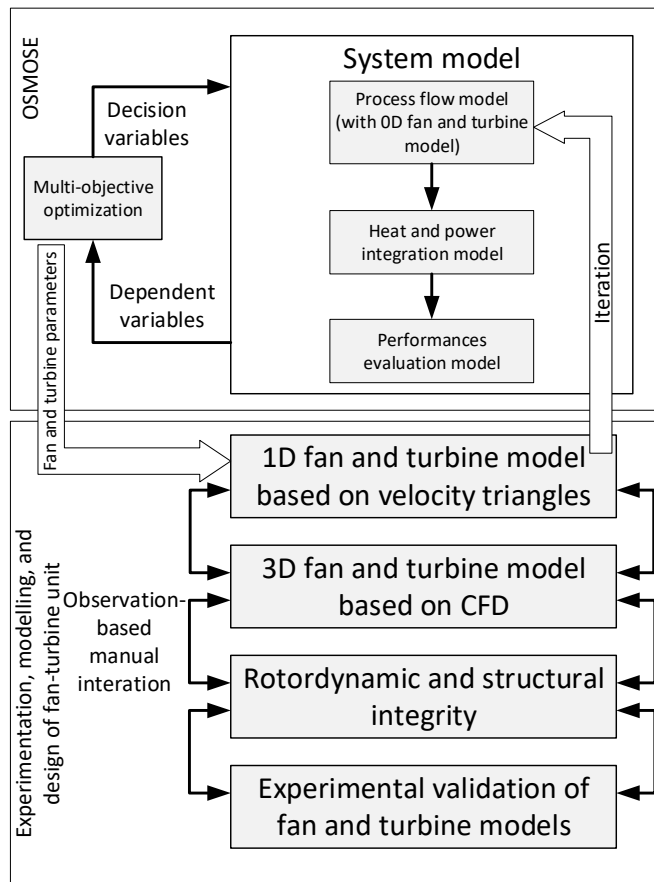


Figure 3.2 – Methodology of the SOFC system optimization.

concepts, is built. The flowsheet is solvable once the values of the previously mentioned design variables (Table 3.1) are specified. Secondly, using energy integration techniques, internal heat recovery within the system is maximized. Thereafter, performance of the system is evaluated with respect to the desired objectives (electrical net efficiency and net utilization ratio). Lastly, an iterative optimization procedure is followed, using an evolutionary algorithm, where a physically-bounded variable space are scanned. Successive generations of populations are obtained by reproduction and mutation of the existing population. Following the “survival of the fittest” rule, the iterations are stopped when a non-dominated solution set, represented by a Pareto-optimal front, is obtained. A similar methodology was used by Facchinetti et al. [89] for the optimization of an SOFC combined with a small-scale gas turbine.

The second subtask is a manual and observation-based process, which consists of four steps. Based on the fan and turbine parameters from the optimization routine, a basic fan and turbine geometry is designed by calculating the velocity triangles on the mean-line (Sections 4.4.3 and 4.5.3). The results are verified with a more detailed three-dimensional CFD simulation using Ansys CFX (Sections 4.4.4 and 4.5.4). The rotordynamic stability of the gas-film-bearing-supported FTU is investigated using an in-house model (Section 4.3.2), whereas the structural

Table 3.1 – Decision variables and the ranges for the multi-objective optimization.

Design variable	Range of values	Comments / constraints
Oxygen-to-carbon ratio in external reformer (O/C)	2-3	Fuel dilution vs. carbon deposition
External-to-total reforming fraction ( $\xi_{ext}$ )	0.2-0.5	Carbon deposition in anode vs. auxiliary power consumption
Reducing species fraction at anode exhaust ( $\xi_{red}$ )	0.1-0.2	Oxidation of the Ni-YSZ anode
Air-fuel equivalence ratio in burner ( $\lambda$ )	1.1-4.45	System energy balance and maximum temperature in burner
Fan inlet temperature ( $T_{13}$ )	200-790 °C	Cold vs. hot recirculation
Fan specific speed ( $n_{s,F}$ )	0.4-3	Fan isentropic efficiency vs. mechanical shaft losses
Turbine specific diameter ( $d_{s,T}$ )	3-35	Small vs. large turbine wheel
Steam recirculation fraction ( $\xi_{sr}$ )	0-1	Fuel dilution vs. carbon deposition

integrity of the FTU is verified with an FEM simulation using Ansys mechanical. Finally, the performance of the fan and turbine, the rotordynamic stability, and the mechanical efficiency and integrity are validated with experiments.

### 3.3 Modeling

The SOFC system modeling consists of the energy flow model, the small-scale turbomachinery model, heat and power integration, and the performance objective evaluation; i.e., maximizing the system electrical net efficiency and net utilization ratio.

#### 3.3.1 Energy flow model

The SOFC system is composed of a stack, HEXs, reformer, burner, condenser, thermally-driven recirculation fan, pump, evaporator, and auxiliary fans. The process schematic for the co-flow stack arrangement analyzed in this work is represented in Figure 3.1. In this particular configuration, both air and fuel enter the stack at a temperature of 680 °C and exit at a temperature of 790 °C. The heat fluxes  $Q_j$  can be positive or negative depending on the optimization results.

Methane (6) and air (1 and 32) at a temperature of 20 °C are the feed gases to the system. The mass flow rates are adapted to reach the targeted 10 kW<sub>el</sub> with all SOFC system configurations. The fuel (7) mixes with the recirculated anode exhaust gas (16) and is preheated to the reformer temperature (8) determined by the external-to-total reforming fraction ( $\xi_{ext}$ ) and the O/C. Within the isothermal reformer, a fraction of the methane is converted to hydrogen and carbon monoxide. The reforming reaction is completed within the stack (internal reforming). Oxygen

Table 3.2 – SOFC stack parameters.

Parameter	Fixed values
Pre-exponential factor anode	433 033 S cm <sup>-1</sup>
Pre-exponential factor cathode	4584515.9 S cm <sup>-1</sup>
Pre-exponential factor electrolyte	372.33 S cm <sup>-2</sup>
Anode activation energy	106 000 J mol <sup>-1</sup>
Cathode activation energy	101 205 J mol <sup>-1</sup>
Electrolyte activation energy	79 535 J mol <sup>-1</sup>
Current collection correction factor	4
Contact loss interconnect-anode	0.02 Ω cm <sup>-2</sup>
Contact loss interconnect-cathode	0.03 Ω cm <sup>-2</sup>
Electrolyte thickness	10 μm

from the air feed is consumed in the electrochemical reaction at the cathode (eq. 2.3). The amount of fuel utilized in the stack is determined by the reducing fuel (H<sub>2</sub>, CO) species fraction ( $\xi_{red}$ ) at the anode exhaust. The cathode exhaust (4) is cooled to 60 °C, thus providing thermal energy ( $\dot{Q}_2$  in Figure 3.1) to the system. A non-recirculated fraction of the anode exhaust (17) is sent to the burner, where it undergoes complete combustion with incoming fresh air at 20 °C (32). HEX 6 ( $\dot{Q}_6$ ) recovers heat to satisfy the energy balance for the remaining endothermal processes in the system. The other anode exhaust fraction (12), determined by the O/C before the reformer, is recirculated. The anode off-gas is condensed in a condenser at ambient pressure. The non-condensed gases (21) and condensed water (23) leave the system at 50 °C. Another portion of the condensed acid water (24) is pumped, preheated, evaporated, and superheated in HEX 7 ( $\dot{Q}_7$ ). This water vapor propels the turbine, and thus the AOR fan. 1 % of the turbine inlet mass flow rate (26) is assumed to leak towards the fan outlet (27). This leakage enters the AOR through stream 14. The steam recirculation ratio ( $\xi_{sr}$ ) determines the water vapor fraction that is transferred from the turbine steam loop to the AOR loop via stream 29. The turbine exhaust water vapor is injected before the condenser (31).

**SOFC stack.** In order to reduce the computational cost of evolutionary optimization algorithms, a zero-dimensional model adapted from Van herle [90] is used. The model parameters are summarized in Table 3.2. It accounts for non-ohmic (diffusion losses and polarisation) and ohmic losses. The non-ohmic losses “are obtained from empirical expressions, fitted to experimental current overpotential data measured individually on the cathode and anode materials” [90]. The ohmic losses “are obtained as a sum of the in-house empirically measured loss at the metallic interconnect-anode contact and interconnect-cathode contact, as well as the specific ohmic single cell resistance. The first two vary little as a function of temperature and are thus taken as constant. The third is taken from the known (and in-house measured) Arrhenius relation of the YSZ electrolyte resistivity corrected by a current collection factor” (4) [90].

The model was validated using the performance maps of a natural-gas-fueled SOFC short



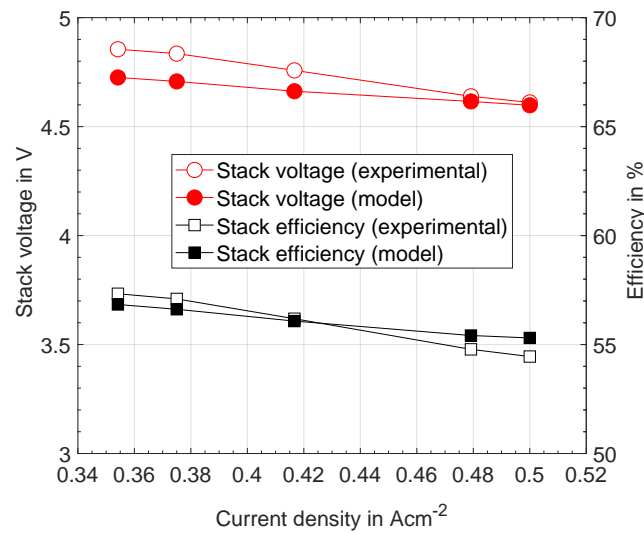


Figure 3.3 – Comparison of experimental and simulated results for a short SOFC stack (six cells), cell area  $80 \text{ cm}^2$ , and 75 % fuel utilization.

stack from industrial partner SOLIDpower. This resulted in a maximum deviation between model prediction and experimental data of  $\pm 1.6\%$  for the efficiency and  $\pm 2.7\%$  for the stack voltage within the tested boundaries, as shown in Figure 3.3. Electrical gross DC efficiency based on the LHV is reported. Both a constant stack pressure drop of 20 mbar and a stack heat loss of  $200 W_{\text{th}}$  based on experimental measurements are included in the model. An additional heat loss of  $100 W_{\text{th}}$  for piping elements is also implemented.

**Pre-reformer.** The recirculated anode exhaust (16) mixes with the incoming fuel supply (7) just upstream of the reformer. The extent of external methane reforming (eq. 2.6) and water gas shift reaction (eq. 2.7), considered at equilibrium, is determined by the operating temperature in the reformer, which is part of the optimization variables. The pressure drop in the reformer is set to 30 mbar and a constant heat loss of  $100 W_{\text{th}}$  is included corresponding to the experimental measurements.

**Burner.** In the burner, the unused fuel from the SOFC stack (17) mixes with fresh air (33) and undergoes complete combustion under adiabatic conditions. The heat released in the process is either used for the system energy balance or recovered for cogeneration. The steam in the burner exhaust can be easily condensed due to its higher partial pressure, leading to improved cogeneration efficiencies. A pressure drop due to thermodynamic and aerodynamic losses of 50 mbar is considered in the burner. The equations for methane, carbon monoxide, and hydrogen combustion are shown in eqs. 2.4, 2.5, and 2.10, respectively.

Table 3.3 – Constraints on minimum approach temperature in the heat exchangers.

Stream	Minimum approach temperature/2 in °C
Gas	25
Liquid, condensing, or evaporating	15
Reformer	50

**Heat exchangers.** Typical counter-flow HEXs are modeled. For system compactness and cost reductions, minimum approach temperatures in HEXs are restricted to the values summarized in Table 3.3. Note that modeling an HEX using a fixed approach temperature does not offer an optimization of the HEX size or cost.

**Auxiliary fans and pump.** The pump, air fan for the burner, as well as the cathode and anode fans are modeled at a constant efficiency of 22 % and the pump is modeled at a constant efficiency of 18 %. This results in an isentropic fan and pump efficiency of 60 % and 50 %, respectively. A mechanical efficiency of 40 % and an electric motor and drive efficiency of 90 % were assumed for the pump. Note that Powell et al. [41] reported cathode fan efficiencies between 12 % and 15 %, stating that the fans were not properly sized.

### 3.3.2 Small-scale turbomachinery model

Since the focus of this work is on the AOR, the thermally-driven fan and the mechanical shaft losses are modeled in detail.

#### Fan model

Analytically-derived zero-dimensional similarity concepts from Balje [2] are used to predict the fan isentropic efficiency ( $\eta_{is}$ ) and the specific diameter ( $d_{s,F}$ ), which depend on the specific speed ( $n_{s,F}$ ). Section 2.3.4 provides more details on these similarity concepts and Figure 2.5 shows the correlations used for the fan. These classical similarity concepts, however, are only valid for large-scale turbomachinery, implying high Reynolds numbers on the order of  $Re_D = 10^6$ . Since the recirculator for this 10 kW<sub>el</sub> system is operating at significantly lower Reynolds numbers of  $Re_D = 10^5$ , additional aerodynamic losses occur. The additional efficiency penalty is taken into account by the actual Reynolds number based on the TE channel width,

$$Re_b = \frac{\rho_1 u_4 b_4}{\mu_1} = \dot{m}_1 \frac{\omega}{2\pi c_{m,4} \mu_1} \propto \dot{m}_1 \quad 3.1$$

using the density ( $\rho_1$ ) and dynamic viscosity ( $\mu_1$ ) at the fan inlet, fan rotational speed ( $\omega$ ), fan TE diameter ( $d_4$ ), recirculated mass flow rate of stream 13 in Figure 3.1 corresponding to the fan inlet mass flow rate ( $\dot{m}_1$ ), TE blade height ( $b_4$ ), and the meridional velocity at the

TE ( $c_{m,4}$ ). A priori, the optimized AOR mass flow rate ( $\dot{m}_1$ ), the recirculation gas temperature (of stream 13 in Figure 3.1,  $T_{13}$ ), and the composition ( $\gamma_j$ ) are not available. Hence, an initial optimization is required to obtain a first estimate of these values. Each point on the Pareto front shown in Figure 3.6 corresponds to a specific system configuration with specific values of  $\dot{m}_1$ ,  $T_{13}$ , and  $\gamma_j$ . The mean solution values of cluster #1 and #2 for both cases (electrically and thermally-driven fan), marked with a black square in Figure 3.6, are used to design a nominal fan geometry. Section 4.4.3 describes this procedure in detail.

This one-dimensional fan model accounts for the additional losses resulting from scaling effects, such as reduced Reynolds numbers, roughness effects, TE deviation, and increased relative tip clearance. The model also provides a zero-dimensional fan model: correlations for adjusted isentropic efficiencies ( $\eta_{is} = f(n_{s,F}, Re_{b,n})$ ) and fan specific diameters ( $d_{s,F} = f(n_{s,F}, Re_{b,n})$ ) as a function of specific speed and Reynolds number (Section 4.4.3). These simplified correlations are used within the SOFC system optimization (Figure 3.2). Note that within the different system designs along the Pareto front shown in Figure 3.6, the recirculation mass flow rate, and therefore the fan diameter, vary significantly (higher mass flow implies higher fan diameters and vice versa). Consequently, the Reynolds numbers differ by up to  $\pm 30\%$  within the different clusters, in comparison to the nominal fan geometry based on the mean value of each cluster (marked with a black square in Figure 3.6). Since designing a new fan geometry for each iteration of the optimization process would result in a prohibitively high computational time, the values of the nominal impeller geometry are corrected as follows [91].

$$\eta_{is} = 1 - [1 - \eta_n(n_{s,F}, Re_{b,n})] \left( \frac{\dot{m}_{1,n}}{\dot{m}_1} \right)^{a_4} \quad 3.2$$

Within the different Pareto front clusters, the meridional velocity ( $c_{m,4}$ ) at the fan TE and the dynamic viscosity ( $\mu_1$ ) vary by  $\pm 3\%$  and  $\pm 1\%$ , respectively. These parameters are therefore considered constant along the Pareto front. For a constant specific speed, the rotational speed is kept constant and the diameter is adjusted; hence, the Reynolds number in eq. 3.1 is only a function of the fan inlet mass flow ( $\propto \dot{m}_1$ ). The experience coefficient ( $a_4$ ) in Equation 3.2 normally varies from 0.1 to 0.3 [91] and has to be specified to fit all the different fan designs on the Pareto.

Figure 3.4 compares the prediction of the zero-dimensional model that is used for the integrated optimization to the one-dimensional model for design refinement. The zero-dimensional model is Reynolds number corrected according to eq. 3.2. The nominal zero-dimensional models are based on the solutions of the two mean values of cluster #1 and #2 for the electrically-driven AOR fan (shown as black squares in Figure 3.6). They zero-dimensional model agrees with the one-dimensional model, in particular for the solutions around cluster #2, where the relative difference is less than 1%. For the solutions around cluster #1, the maximum difference between the zero-dimensional and one-dimensional model is less than 3%. This justifies the use of a simplified zero-dimensional model for the integrated system optimization.

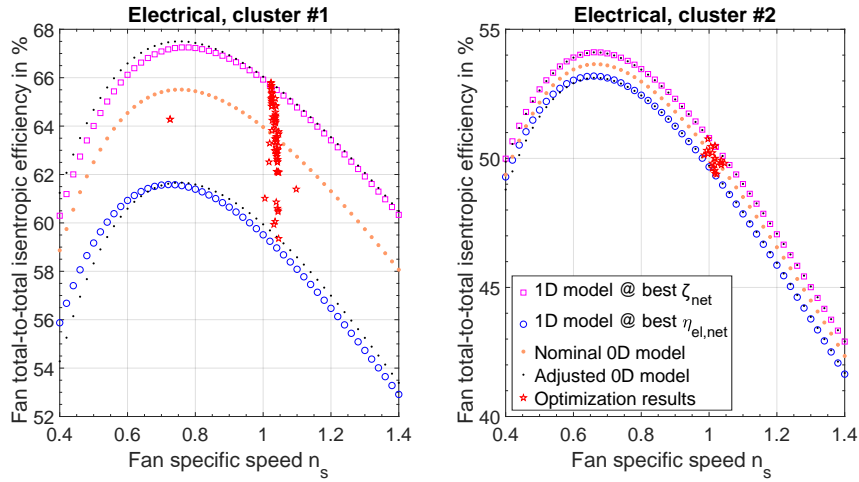


Figure 3.4 – Fan efficiencies for the SOFC system with electrically-driven AOR fan, calculated with the zero-dimensional model (similarity concepts) and one-dimensional model (mean-line analysis) for different specific speed values. Optimized specific speed values are indicated with red stars.

### Turbine model

The turbine is modeled assuming partial-admission. Similarity concepts from Balje [2] (figure 5.44) predict the turbine isentropic efficiency ( $\eta_{is}$ ) and the specific diameter ( $d_{s,T}$ ) depending on the specific speed ( $n_{s,T}$ ), similar to the fan zero-dimensional correlations. The Reynolds number based on the turbine tip diameter for these correlations ( $Re_D > 10^5$ ) is comparable to the manufactured FTU. However, the turbine blade tip clearance to turbine blade height ratio of these correlations (0.02) is lower than to the manufactured turbine (0.24), which leads to a decreased isentropic efficiency. According to figure 5.31 in [2], the correction factor for a turbine blade tip clearance to turbine blade height ratio of 0.24 is 0.725 ( $1.025 - 1.25 \cdot 0.24$ ) for a turbine specific speed of 0.08. Another limiting parameter of these correlations is the turbine blade edge thickness to blade height ratio (0.02) that is also lower than the manufactured turbine (0.15). Since the turbine blade edge thickness is at its limit with the current manufacturing method (milling), no significant improvements are possible. According to figure 5.32 in [2], the correction factor for a turbine blade edge thickness to blade height ratio of 0.15 is 0.87 ( $1.02 - 1 \cdot 0.15$ ) for a turbine specific speed of 0.08. Thus, the total correction factor is 0.63 ( $0.87 \cdot 0.725$ ). However, the turbine blade tip clearance could be realistically further reduced. A total correction coefficient of 0.75 for the turbine isentropic efficiency, calculated with Balje's similarity concepts, is thus considered for the system simulation. This factor corresponds to a turbine blade edge thickness to blade height ratio of 0.15 (0.15 in the demonstrated prototype) and a turbine blade tip clearance to blade height ratio of 0.13 (0.24 in the demonstrated prototype). This would result in a turbine blade tip clearance of 80  $\mu\text{m}$  for the designed turbine (143  $\mu\text{m}$  in the demonstrated prototype at design conditions).

Section 4.5.3 further compares Balje's similarity concepts to a one and three-dimensional model.

The turbine outlet temperature (stream 28 in Figure 3.1) is set as equal to the fan inlet temperature (stream 13). Because of this, the temperature gradient within the FTU is low, which helps to mitigate the risk of a bearing failure. The turbine operates choked within the throat, which determines the pressure ratio. The turbine total-to-total pressure ratio,

$$\Pi_{tt,T} = \left(1 + \frac{\kappa - 1}{2}\right)^{\frac{\kappa}{\kappa - 1}} + \frac{\rho_{out} \Delta h_{is} (1 - \eta_{is})}{p_{t,28}} \quad 3.3$$

is thus a function of the turbine outlet density ( $\rho_{out}$ ), the turbine isentropic efficiency ( $\eta_{is}$ ), the heat capacity ratio ( $\kappa$ ), the total-to-total isentropic specific enthalpy difference ( $\Delta h_{is}$ ), and the total pressure at the turbine outlet ( $p_{t,28}$ , stream 28 in Figure 3.1).

### Shaft model

The mechanical fan losses are modeled by assuming dynamic gas film journal and thrust bearings. In contrast to conventional ball bearings, the fan lifetime is increased, even at high rotor speeds and operational temperatures. Simplified loss correlations as proposed by Schiffmann [12] are used,

$$P_{rad} = \frac{1}{4} \pi d_{sh, fan}^3 \omega^2 \frac{\mu l_{rad}}{s_{rad}} \quad 3.4$$

$$P_{ax} = \frac{1}{32} \pi \omega^2 \left(d_4^4 - d_{sh, fan}^4\right) \frac{\mu}{s_{tb}} \quad 3.5$$

using the journal bearing length ( $l_{rad}$ ) and clearance ( $s_{rad}$ ), the thrust bearing clearance ( $s_{tb}$ ), and the shaft diameter ( $d_{sh, fan}$ ). The bearing dimensions are directly scaled with rotor speed (ndm number). The fluid film is water vapor at the turbine inlet temperature (stream 26 in Figure 3.1). This is a reasonable assumption since the water vapor from the turbine provides the gas film for the bearings. Table 3.4 states the bearing and shaft design variables.

Table 3.4 – Design parameters for the fan shaft and bearings.

Variable	Value	Description
$\frac{l_{rad}}{d_{sh, fan}}$	1	Ratio of length to shaft diameter
$\frac{s_{rad}}{d_{sh, fan}}$	0.0007	Ratio of radial clearance to shaft diameter
$\frac{s_{tb}}{d_{sh, fan}}$	0.0025	Ratio of thrust bearing clearance to shaft diameter
ndm number	$1.5 \cdot 10^6$ rpm mm	Rotational speed multiplied by shaft diameter

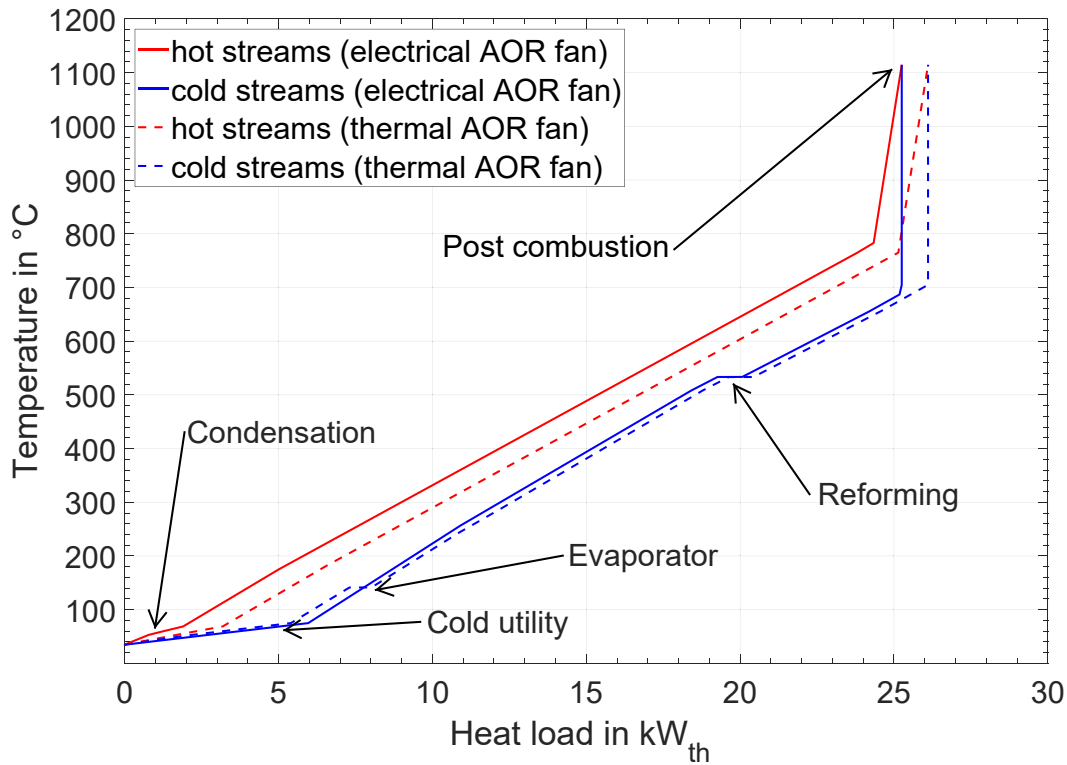


Figure 3.5 – The composite curves of the SOFC systems with the best electrical net efficiency for the electrically-driven AOR (full line [88]) and the thermally-driven AOR (dashed line).

### 3.3.3 Heat and power integration

In addition to the stack and recirculator modeling, the complete HEX network of the SOFC system is included in the optimization loop in order to favor internal heat exchange over external heat input. Excess heat produced in the system is recovered for domestic heating. This cold utility (water) heats from 20-60 °C. Figure 3.5 shows two composite curves for the systems with the highest electrical net efficiency for both the electrically-driven AOR fan (full lines) and the thermally-driven AOR fan (dashed lines). Cold sources requiring heat input are the isothermal reformer, HEX 1 (air heater), HEX 3 and HEX 9 (AOR loop heater), HEX 4 (fuel heater), and HEX 7 (steam generator). Hot sources are available in HEX 2 (stream 4, air exhaust cooling), HEX 6 (stream 17, fuel exhaust cooling), HEX 8 (stream 30, water vapor from turbine), and the condenser.

### 3.3.4 Performance objectives and multi-objective optimization

The previously introduced OSMOSE platform (Section 1.2), a queueing MOO based on an evolutionary algorithm, is used for system optimization. Starting with an initial population of randomly assigned design variables, the flowsheet is solved for each individual dataset.

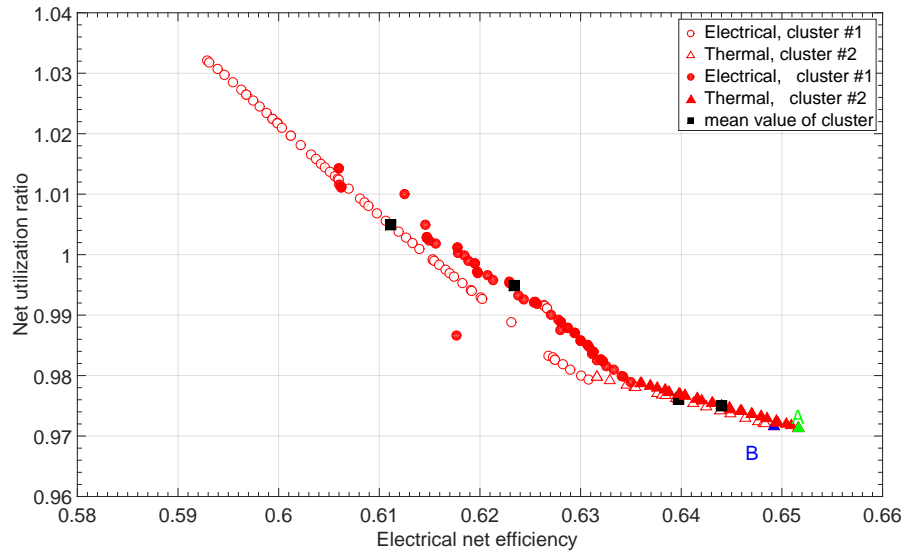


Figure 3.6 – Pareto front of the optimized SOFC systems with electrically-driven AOR fan (non-filled markers) and thermally-driven AOR fan (filled markers).

The initial population size is chosen to be 100. The individual solutions are evaluated based on the system electrical net DC efficiency according to eq. 2.21 and the net DC utilization ratio according to eq. 2.23 using the SOFC electrical output ( $P_{el} = 10\text{kW}_{el}$ ), the auxiliary equipment electrical consumption ( $P_{aux} = P_1 + P_2 + P_3 + P_4$ ), and the sum of heat flows ( $\dot{Q} = \sum_{j=1}^7 \dot{Q}_j + \dot{Q}_C + \dot{Q}_R$ ) as shown in Figure 3.1. The Pareto front is considered converged, as it changes less than 0.1 % from one design variable generation to the next. In this particular case, this is achieved after 5000 iterations.

### 3.4 Results and analysis

Figure 3.6 shows the Pareto curves obtained from the evolutionary algorithm for a co-flow stack configuration ( $10\text{kW}_{el}$  output) with both an electrically-driven AOR fan (non-filled markers) and a thermally-driven AOR fan (filled markers). Figure 3.1 shows the process flow diagram of the latter. For the SOFC system with electrically-driven AOR fan, the streams 24 to 31 are not present and the turbine is replaced with an electric motor [88].

Firstly, the curves clearly identify a trade-off between high net utilization ratio and high electrical net efficiency. Secondly, clusters of different solutions appear for both cases (electrically and thermally-driven AOR fan). The formation of these clusters is a consequence of a switch between operation with lower to higher O/C ratio (black squares in Figure 3.10). Stack operation with a thermally-driven AOR fan offers better performance, since the pump that drives the turbine consumes less electricity than the motor of the electrically-driven AOR fan. Net electrical DC efficiencies of 65 % and utilization ratios of 97 % (based on the LHV) are sug-

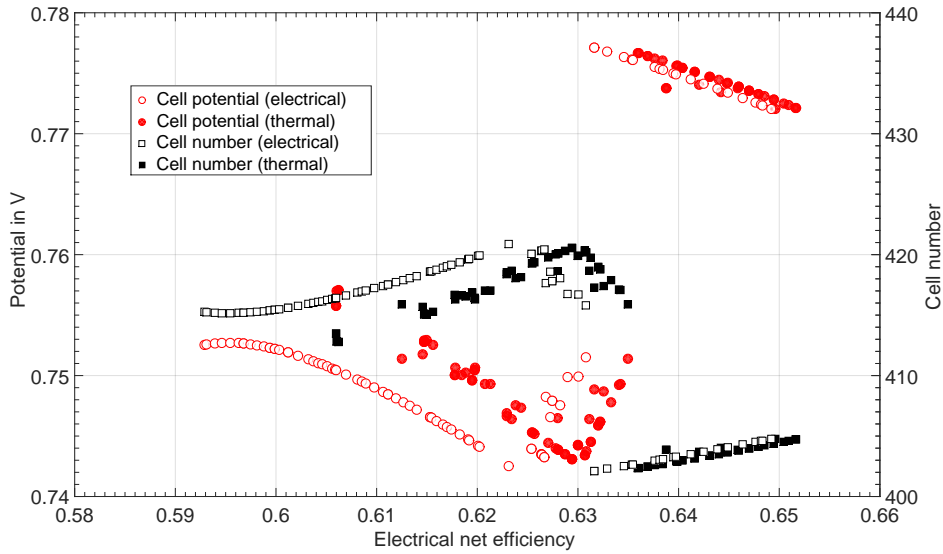


Figure 3.7 – Evolution of the fuel cell parameters along the Pareto front (constant current density of  $0.4 \text{ A cm}^{-2}$ ).

gested achievable. Such high utilization ratios are possible, since the efficiency calculation is based on the LHV, as stated in eq. 2.23 (Section 2.1.6). In addition, part of the water vapor is condensed in the condenser, as shown in Figure 3.1. The anode off-gas is burned with fresh incoming air at a low air-fuel equivalence ratio, which leads to higher partial water vapor pressure in stream 18, and thus to higher condensation and heat recovery compared to the case of anode and cathode stream mixing (4 and 11 in Figure 3.1). The utilization ratio is not constant at 111 % ( $\frac{\text{HHV}}{\text{LHV}} = 1.11$ ) for all cases on the Pareto front, because of: (1) mechanical and electrical losses in the fans, (2) constant heat losses to the environment (in total  $300 \text{ W}_{\text{th}}$ ), (3) outlet streams are not cooled to the inlet temperature of  $20 \text{ }^\circ\text{C}$ , but to  $50 \text{ }^\circ\text{C}$  (anode stream) and  $60 \text{ }^\circ\text{C}$  (cathode stream), and (4) partial condensation of the water vapor in the burner exhaust stream.

Additionally, the SOFC system with the thermally-driven fan is not viable for a system with a maximized utilization ratio above 101.5 % (left side of the Pareto front in Figure 3.6). The SOFC system with the electrically-driven AOR fan can achieve net utilization ratios up to 103 %. At such high utilization ratios, the AOR is high, leading to a high fan power, and thus to a high steam mass flow rate through the turbine. A hot source, for example burning additional natural gas in the burner, would therefore be necessary to deliver the heat to the evaporator, and thus the water vapor mass flow rate to the turbine. However, such an operational mode is not considered reasonable.

Highest electrical efficiency is reached at the highest fuel utilization, where cell potential drops due to Nernst and mass transfer losses. It follows that the number of cells in the stack has to increase to achieve the targeted electrical output power of  $10 \text{ kW}_{\text{el}}$ ; given a constant



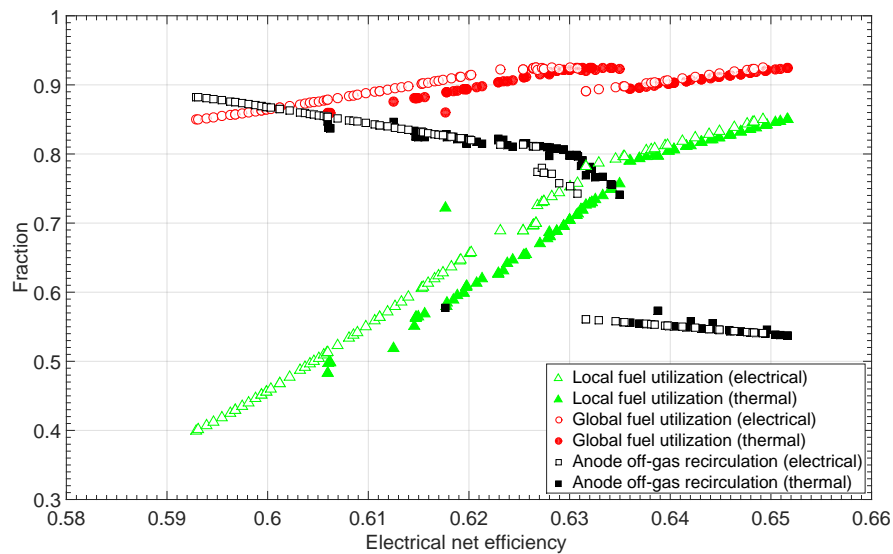


Figure 3.8 – Evolution of anode off-gas recirculation ratio, as well as local and global fuel utilization along the Pareto front.

current density of  $0.4 \text{ Acm}^{-2}$  (Figure 3.7). Figure 3.8 shows the local fuel utilization, i.e., the fuel consumed between stream 10 and 11 (Figure 3.1), the global fuel utilization, i.e., the fuel consumed between stream 7 and 17, and the anode off-gas recirculation ratio. A discontinuity is observed at 63 % (electrically-driven AOR fan) and 63.5 % (thermally driven AOR fan) electrical net efficiency, where the system switches from a lower local fuel utilization and higher recirculation operation (cluster #1) to a higher local fuel utilization and lower recirculation operation (cluster #2), including a drop in global fuel utilization. This accounts for the sudden potential jump. Note that electrical efficiencies above 60 % can be achieved with AOR, while keeping low local fuel utilization, which is beneficial for the SOFC stack lifetime (Figure 3.8).

At increased system electrical net efficiencies, the global fuel utilization is generally high, and thus more fuel is converted. Since this is an exothermic reaction, more heat is also generated in the stack. In order to limit the stack temperature gradients, the cathodic air flow increases (black squares in Figure 3.9). As less fuel is available for the system energy balance, the adiabatic flame temperature in the burner decreases, with an exception around the kink, corresponding to lower global fuel utilization (red circles in Figure 3.9). The reformer temperature tends towards lower values, in agreement with the required lower external reforming limit of 20 %, based on an isothermal equilibrium model (green triangles in Figure 3.9).

Results in Figure 3.9 indicate an improved electrical efficiency both for the fraction of reducing species (i.e.,  $\text{H}_2$  and  $\text{CO}$ ) at the anode exhaust and for the external reforming fraction, each reaching lower limits of 10 % and 20 %, respectively. This is a result of higher endothermic internal reforming neutralizing the stack heat, and thus reducing cathodic fan losses. An O/C ratio of three in the reformer corresponds to higher AOR recirculation and lower local fuel

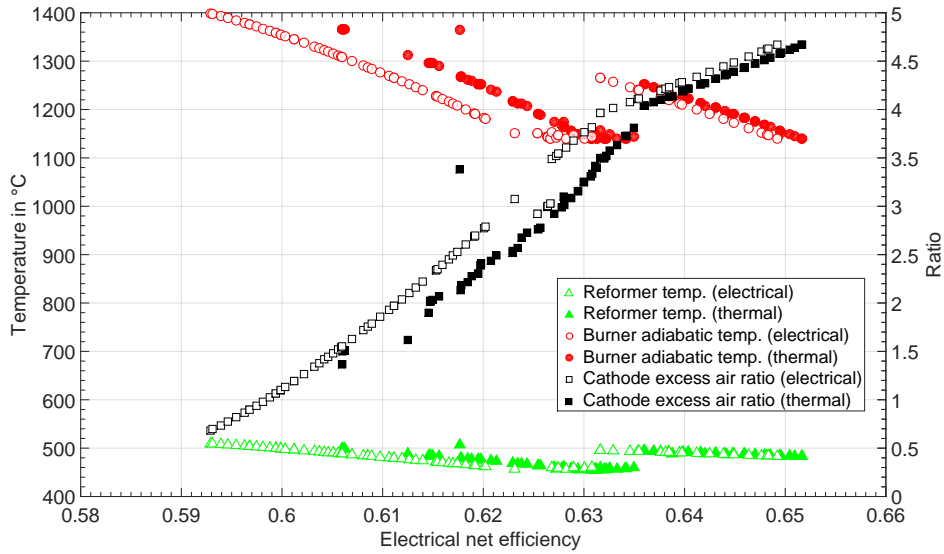


Figure 3.9 – Evolution of system temperatures (left y-axis) and cathode excess air ratio (EAR) along the Pareto front (right y-axis).

utilization. As the operation mode switches, the O/C ratio in the reformer also switches to a lower value of two.

The air-fuel equivalence ratio ( $\lambda$ ) in the burner always converges to the lower value of 1.1, which favors a high flame temperature, and thus a higher utilization ratio, as well as a higher vapor pressure, higher condensation, and thus higher heat recovery. The fan inlet temperature converges to the lower bound of 200 °C, since the volumetric flow rate is lower and the pressure rise higher for a cold fluid; hence, the fan power increases with the temperature. Wagner et al. [88] discuss the difference between cold and hot AOR in detail. The steam recirculation fraction ( $\xi_{sr}$ ) converges to zero for all SOFC systems with a thermally-driven AOR fan, since a dilution of the AOR loop decreases the Nernst potential, and thus the stack efficiency (Section 3.6). Thus, this is one of the key advantages of FTU, as compared to a steam-driven ejector that inevitably dilutes the AOR loop.

In terms of fan design, the specific speed converges to 0.98-1.05 (electrically-driven) and to 1.06-1.48 (thermally-driven). According to Balje, the highest fan efficiencies are reached at specific speeds of 0.7-0.75. The optimizer therefore sacrifices some isentropic fan efficiency points to obtain higher rotational speeds resulting in smaller fans and rotors. Thus, lower mechanical losses and better overall performance is obtained. Higher rotational speeds also enables higher turbine isentropic efficiencies; hence, the specific speed values, and thus rotational speeds are increased further for the thermally-driven fan (green up-pointing triangles in Figure 3.12). This clearly shows the importance of a holistic approaches, when designing complex, interdisciplinary systems.

Figure 3.11 shows the evolution of the isentropic fan, mechanical, and total efficiencies, which

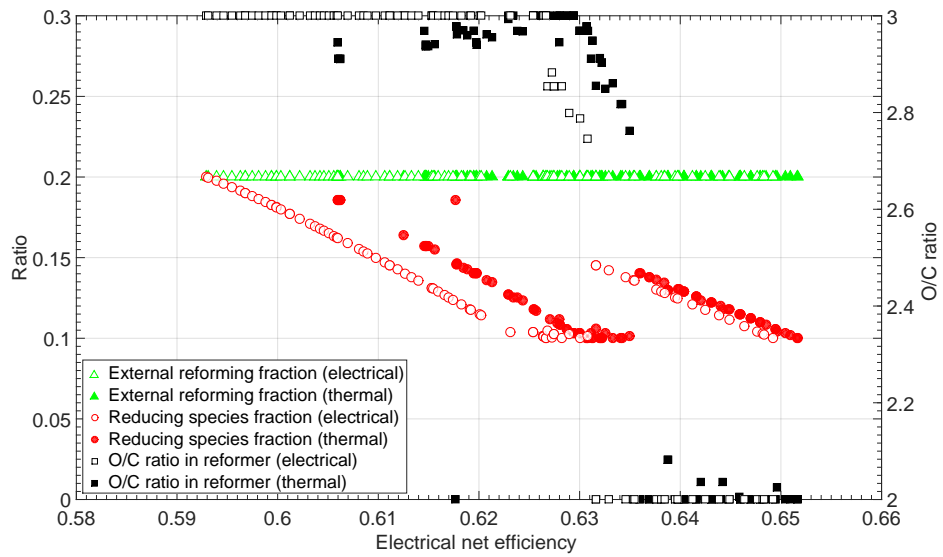


Figure 3.10 – Evolution of three design variables along the Pareto front.

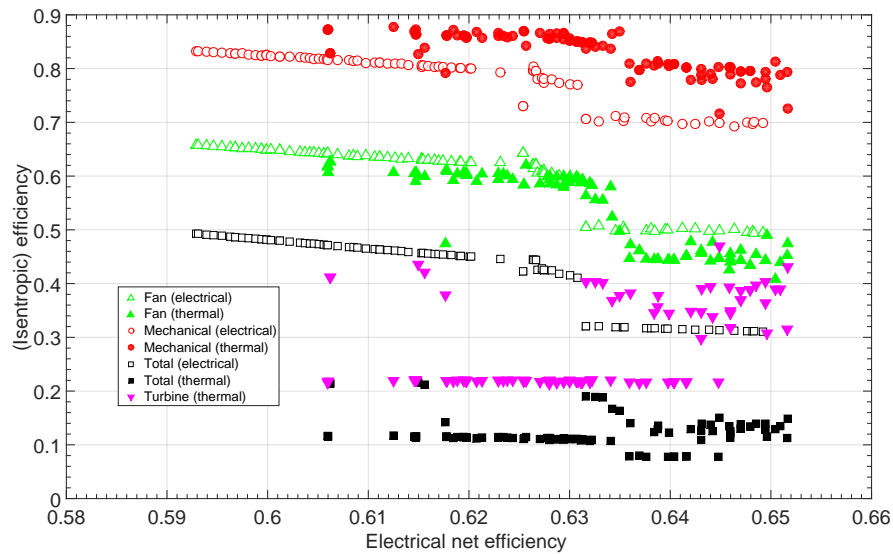


Figure 3.11 – Evolution of isentropic fan, mechanical, turbine, and total efficiencies along the Pareto front.

include an electric driving efficiency of 90 % (electrically-driven) or the turbine isentropic efficiency (thermally-driven). For both the fan and turbine, an 80  $\mu\text{m}$  blade tip clearance is assumed. At the highest electrical net efficiency point on the Pareto front, the fan achieves an overall isentropic total-to-total efficiency of 49 % (electrically-driven) and 47 % (thermally-

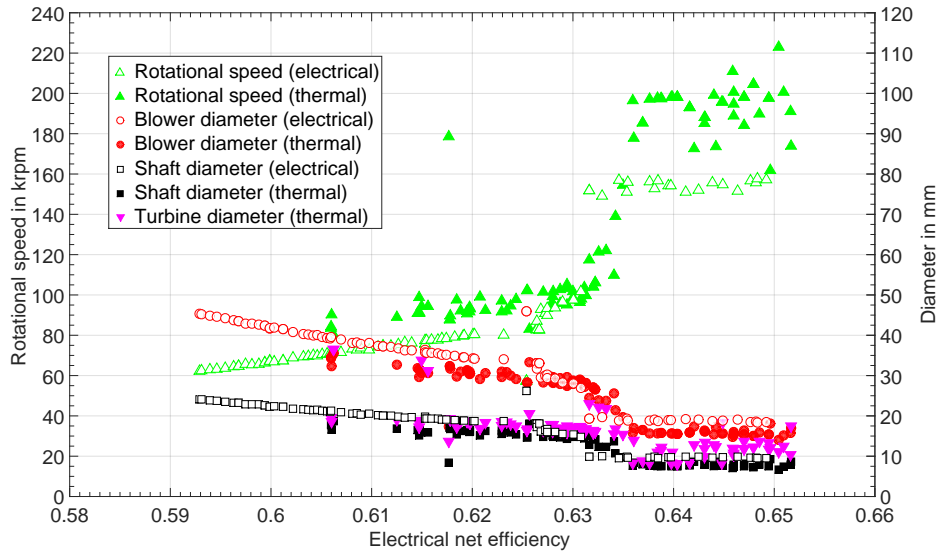


Figure 3.12 – Evolution of rotor speeds, as well as fan, shaft, and turbine diameters along the Pareto front.

driven). The difference between the two cases is the specific speed value. The higher the specific speed, the lower the fan diameter (red circles in Figure 3.12) and the lower the efficiency.

The fan power input for the thermally-driven AOR is from 25 W to 100 W, whereas it is from 24 W to 127 W for the electrical case (black squares in Figure 3.13). The main mechanical losses occur in the journal bearings: 7 W to 18 W for the electrically-driven case and 4 W to 10 W for the thermally-driven case. The mechanical efficiency increases with increasing fan diameter and with decreasing SOFC system electrical net efficiency.

As shown in Figure 3.12, for a higher AOR rate (i.e., lower electrical net efficiencies), the fan diameters are greater and the rotational speeds are lower than for lower AOR rate (i.e., higher net electrical system efficiency). Rotational speeds of up to 220 krpm and 160 krpm are required for the thermally-driven, and electrically-driven case, respectively, to achieve the pressure rise of 50 mbar. The corresponding fan diameters are between 14 mm and 45 mm and the shaft diameters are between 7 mm and 24 mm, which is feasible in terms of manufacturing and assembly.

The operational characteristics of the system, at the point of maximum electrical net efficiency (i.e., point A for the thermally-driven case and point B for the electrically-driven case as shown in Figure 3.6) are summarized in Table 3.6. The difference in electric net efficiency is rather low (0.3 %), although the electrically-driven and thermally-driven case do not represent the same system layout. Note that the optimal recirculator design varies between the two concepts.

Table 3.6 also contains the results of the baseline SOFC system design based on the same

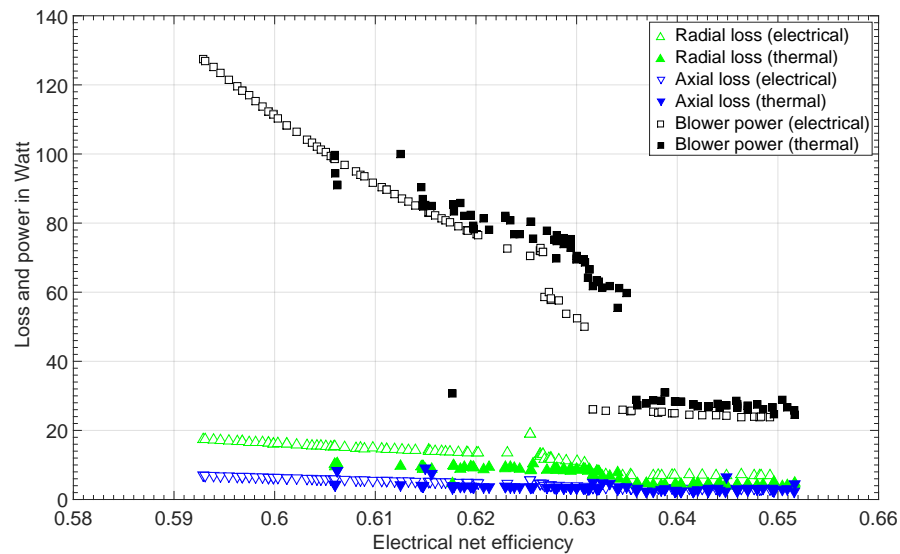


Figure 3.13 – Evolution of the fan power and the mechanical losses of the journal and thrust bearing.

process flow diagram as in Figure 3.1. However, the baseline system features another stack, as it uses three  $220 \text{ cm}^2$  serial cells that operate at lower current densities ( $0.31$ ,  $0.35$ , and  $0.25 \text{ A cm}^{-2}$ ). With this stack, a theoretical electrical net efficiency of  $65.7\%$  is possible. The corresponding AOR fan yields a  $70 \text{ mbar}$  pressure rise (an initial estimation of  $50 \text{ mbar}$  for SOFC stack and reformer,  $10 \text{ mbar}$  for components within the AOR loop, and  $10 \text{ mbar}$  as a safety margin). The tested  $6 \text{ kW}_{\text{el}}$  SOFC stack (Chapter 6) has a measured pressure loss on the order of  $60 \text{ mbar}$ , including the AOR loop. This would not significantly increase for the  $10 \text{ kW}_{\text{el}}$  versions, since only additional cells would be added. At the design point, the fan has a specific speed of  $0.8$ , resulting in a rotational speed of  $175 \text{ krpm}$ . During the experimental campaign, this fan was tested with air at  $200^\circ \text{C}$  and achieved an isentropic efficiency of  $55\%$  and a pressure rise of  $55 \text{ mbar}$  at the design point. However, the fan had a higher blade tip clearance (increased from  $0.05 \text{ mm}$  to  $0.15 \text{ mm}$  for a  $1.82 \text{ mm}$  fan blade height); hence, the isentropic efficiency and pressure rise were reduced. An a priori predicted isentropic efficiency of  $66\%$  is within a feasible range for the design fan blade tip clearance. The major difference between the optimized baseline FTU and the actual manufactured FTU is the turbine design. The initial full-admission turbine that has the same diameter as the shaft was not feasible in terms of manufacturing, since the fan blades would be too high. The author has chosen therefore to design a partial-admission turbine with a diameter of  $15 \text{ mm}$ . The following three chapters (Chapters 4 to 6) describe the shaft, fan, and turbine design (Chapter 4), the experiments (Chapter 5), and the final coupling of the AOR fan with the SOFC (Chapter 6).

### Chapter 3. SOFC System Design

Table 3.5 – Heat exchanger network (HEX) for the baseline SOFC system with thermally-driven anode off-gas recirculation fan, the minimum approach temperature ( $\Delta T$ ), the inlet (in) and outlet (out) temperatures for the hot (h) and cold (c) sources, the exchanged heat ( $\dot{Q}$ ), and HEX effectiveness ( $\epsilon_{HEX}$ ) for the respective HEXs.

Nr.	Name	HEX sources		$\Delta T^a$ in °C	Hot source		Cold source		Heat $\dot{Q}$ in kW <sub>th</sub>	$\epsilon_{HEX}^b$
		Hot	Cold		$T_{in,h}$ in °C	$T_{out,h}$ in °C	$T_{in,c}$ in °C	$T_{out,c}$ in °C		
1	HEX #1	HEX 2	HEX 1	50	800	145	53	680	10.8	0.88
2	HEX #2	HEX 5	HEX 9	50	800	365	166	480	1	0.50
3	HEX #3	HEX 5	HEX 1	50	365	200	32	53	0.34	0.06
4	HEX #4	HEX 6	HEX 4	50	1151	920	480	680	0.74	0.34
5	HEX #5	HEX 6	Ref. <sup>c</sup>	75	920	699	480	480	0.68	0.50
6	HEX #6	HEX 6	HEX 7	40	699	153	70	221	1.5	0.85 <sup>d</sup>
7	HEX #7	Cond. <sup>f</sup>	CU <sup>e</sup>	30	153	70	20	60	2.5	0.625
8	HEX #8	HEX2	CU <sup>e</sup>	40	145	60	20	60	1.3	0.68

<sup>a</sup> The minimum approach temperature ( $\Delta T$ ) is calculated with the hot and cold source values from Table 3.3

<sup>b</sup> The heat exchanger effectiveness is calculated with the temperature difference ratio  $\frac{T_{in,h} - T_{out,h}}{T_{in,h} - T_{in,c}}$  if the heat capacity rate of the cold source is higher than that of the hot source ( $\dot{m}_c c_{p,c} > \dot{m}_h c_{p,h}$ ), for example an evaporating fluid. Otherwise  $\frac{T_{out,c} - T_{in,c}}{T_{in,h} - T_{in,c}}$ , for example for a condensing fluid

<sup>c</sup> The reformer (Ref.) is modeled as isothermal at equilibrium

<sup>d</sup> The evaporator consists of one preheater (effectiveness of 0.37), the evaporator at 121 °C (0.85), and the super-heater (0.06)

<sup>e</sup> The cold utility (CU) is considered as water that heats from 20 °C to 60 °C

<sup>f</sup> The condenser (Cond.) consists of a pre-cooler to a temperature of 85 °C for stream 20 in Figure 3.1 and the condenser with a slighting partial pressure and temperature to 70 °C. The uncondensed water vapor mass fraction in the exhaust (stream 21) is 18 %

### 3.5 Heat exchanger network design (baseline SOFC system)

The SOFC systems with the electrically-driven and thermally-driven AOR fan from Table 3.6 have no specific HEX network included. The stated net utilization ratio is thus the maximum achievable value with an ideal HEX network. However, such an HEX network would lead to increased system cost. The baseline SOFC system in Table 3.6 features a HEX network based on a heuristic trade-off between maximum utilization ratio and minimum cost using on seven HEX. Thus, it has a lower utilization ratio by 9 percentage points, as compared to the ideal HEX network.

Table 3.5 lists these seven HEXs that are based on Figure 3.1. The first heat exchanger (HEX #1) is on the cathode side and connects HEX 1 and HEX 2. This is also the HEX with the highest heat exchange (10.8 kW<sub>th</sub>), the highest effectiveness of 88 %, and thus the highest heat exchange area, size, and cost. The second HEX (HEX #2) cools the recirculated anode off-gas

### 3.6. Sensitivity of steam leakage (baseline SOFC system)

and then heats it after the recirculation fan. It consists of HEX 3 and HEX 9. The third heat exchanger (consisting of HEX 5 and HEX 1) cools the recirculated anode off-gas to the fan inlet temperature of 200 °C. Thus, the minimum approach temperature of 50 °C for of HEX #2 is obtained. HEX 6 is split into three serial HEXs that are connected: HEX 4 (HEX #4), the reformer (HEX #5), and the evaporator HEX 7 (HEX #6). The final real application of these three HEXs could be implemented as one unit that features burner, reformer, evaporator, and fuel preheating. The last HEX is the condenser that is connected to the cold utility (water from 20-60 °C) for domestic heat cogeneration. It is possible to add an eighth HEX for cogeneration of domestic heat at the cathode outlet (HEX #8); hence, the utilization ratio would be nearly the ideal one. However, this would imply an additional HEX, and thus additional cost. Hot recirculation at high electrical net efficiency is also promising, since it eliminates two HEXs (HEX #2 and #3). This saves capital cost. A clearer picture could be obtained with the implementation of a cost objective for the multi-objective optimization.

### 3.6 Sensitivity of steam leakage (baseline SOFC system)

For the baseline system with the baseline HEX network (Tables 3.5 and 3.6), a steam leakage rate through the FTU to the AOR loop of 12 % was assumed. This corresponds to stream 27 in Figure 3.1, the so-called turbine leakage. During the design of the FTU, the author paid special attention to minimizing this leakage rate from the turbine rotor blade LE through the FTU housing to the fan TE, since it has a significant impact on the SOFC system efficiency. The FTU features an inward-pumping thrust gas film bearing that has a clearance on the order of 10 µm. This clearance is the only fluid path from the turbine to the AOR loop. The attempt to measure this leakage mass flow rate was not successful (Figure 5.8). An analytical leakage model based on the measured pressures and Laval nozzle theory suggest a maximum leakage rate on the order of 0.2 kg h<sup>-1</sup>, and thus 9 % of the turbine water vapor mass flow rate of the baseline system (2.2 kg h<sup>-1</sup>). The author assumes this leakage rate to be negligible. Numerical investigations of the specific FTU thrust bearing geometry by Nibourel [92] suggest a leakage mass flow rate near-zero, due to the inward-pumping effect of the thrust bearing.

Figure 3.14 shows a sensitivity analysis of the baseline system with the actual measured turbomachine efficiencies (55 % for the fan and 39 % for the turbine), as well as the indirectly measured mechanical shaft losses via a run-out test (12.5 W). The black dashed line at 0.12, with an electrical net DC efficiency of 65.6 %, corresponds to the baseline design with the actual measured FTU parameters. Note that the electrical net efficiency is decreased by 0.1 % with respect to the values in Table 3.6, since the turbomachine efficiencies of the baseline model are estimated higher (66 % for the fan and 47 % for the turbine) than those measured. With a turbine leakage rate of 1 % (stream 27 in Figure 3.1), the SOFC system electrical net DC efficiency increases by 0.3 percentage points to 65.9 % (red point in Figure 3.14), whereas it decreases by 0.9 percentage points to 64.7 % for a turbine leakage rate of 40 %. For an increased turbine leakage rate, the AOR recirculation rate decreases and the local fuel utilization increases; however, the global fuel utilization decreases (for a constant O/C=2 at the reformer,

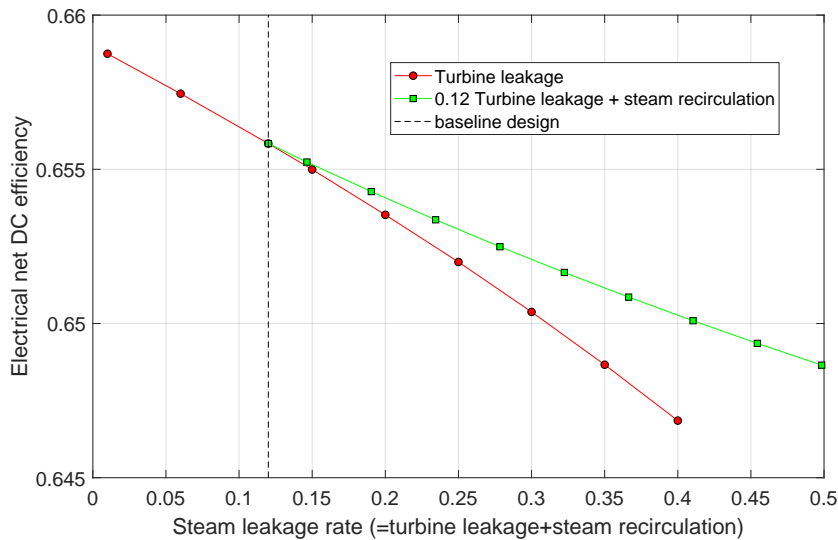


Figure 3.14 – Sensitivity analysis of the baseline system for different total steam leakage rates from the turbine to the anode off-gas recirculation.

external-to-total reforming fraction of 0.2, and reducing species fraction at anode exhaust  $\xi_{red}=0.1$ ). Figure 3.14 also shows a second sensitivity analysis (green squares) that corresponds to a constant turbine leakage rate of 12 % and an increased steam leakage via the so called steam recirculation loop (stream 29 in Figure 3.1) with  $\xi_{sr} = 0 - 43$  %. The total steam leakage rate corresponds to the mass flow rate of stream 27 and 29 divided by 26 ( $\frac{\dot{m}_{27}+\dot{m}_{29}}{\dot{m}_{26}}$ ), resulting in 12-50 %. The drop in electrical net efficiency is less significant (65.1 % at 40 % total steam leakage rate). Thus, it is beneficial for the system to first expand the steam in the turbine and then recirculate it to the AOR loop; for example, to increase the water vapor content. In conclusion, the overall FTU efficiency should be maximized, whereas the turbine leakage rate to the AOR loop should be minimized, to obtain the highest SOFC system efficiencies.

### 3.7 Chapter conclusion

This chapter presents the simulation and optimization (with genetic algorithms) of a patented [35] SOFC system with AOR. The novelty of this system is the pressure rise unit: a radial fan with oil-free and long-lifetime gas film bearings (herringbone-grooved and spiral grooved) driven by a steam turbine. The system allows for high global fuel utilization (92 %), while maintaining a local fuel utilization of 85 %, and thus a reasonable stack aging rate. Electrical net DC efficiencies based on the LHV on the order of 65 % and utilization ratios (cogeneration of electricity and heat) on the order of 97 % are feasible according to the system optimization for a AOR rate of 54 %. Optimal parameters with respect to boundaries were proposed, including the O/C in the external reformer (2), the external-to-total reforming fraction (0.2),



the reducing species fraction at the anode exhaust (0.1), the air-fuel-equivalence ratio in the burner (1.1), the fan inlet temperature (200 °C), and the steam leakage rate from the steam turbine to the AOR loop (0). The maximum cogeneration efficiencies (up to 103 % based on the LHV) are obtained for an O/C of three and for a reducing species fraction at the anode exhaust of 0.2.

Since the focus of this work is the design, manufacturing, and testing of the novel AOR fan, this FTU was considered within the system simulation and optimization. The radial-inflow partial-admission turbine is simulated according to similarity concepts proposed by Balje [2] with a correction factor of 0.75 accounting for the thick turbine blade edges and an increased blade tip clearance (80 μm). These parameters are limited, due to the assembly and manufacturing of the FTU. The fan is simulated with adapted similarity concepts proposed by Balje [2] accounting for a blade tip clearance of 80 μm and the actual Reynolds number based on the fan diameter, which is one order of magnitude lower than that used in classical concepts, resulting in lower fan efficiencies. The mechanical losses of the gas film bearings are considered with a simplified analytical model.

For a 10 kW<sub>el</sub> SOFC system with the highest electrical net efficiency, the optimal specific speed for the AOR fan is found to be 1.1 leading to a rotational speed of 174 krpm and a fan tip diameter of 17 mm, which is comparable to the turbine tip diameter. Such a small AOR fan is not readily available off-the-shelf. In literature, the AOR fans coupled with the SOFC system were oversized and operated off-design at low mass flow rates, resulting in poor efficiencies. Thus, the integrated simulation and optimization approach results in an appropriate design of the turbomachinery components.

In the optimized system, the turbine operates with 1.7 kg h<sup>-1</sup> of steam at a pressure ratio of 2.2, while the AOR fan recirculates 2.4 kg h<sup>-1</sup> of water vapor, leading to an increase of the supplied steam by the factor of 1.4. Components, such as the water treatment (particle filter and neutralization), the pump, and the evaporator, are therefore downsized compared to the classical direct-steam-supply SOFC system.

A sensitivity analysis of the steam leakage rate from the turbine to the AOR loop proposes a significant impact on the system electrical net efficiency: it decreases almost linearly by up to 1.2 percentage points, considering an increase of the leakage rate from 1 % to 40 %. Therefore, the minimization of this leakage rate is a target specification of the FTU.

### Chapter 3. SOFC System Design

Table 3.6 – Operational characteristics of the SOFC system with electrically and thermally-driven AOR fan, as well as the baseline design (three serial 220 cm<sup>2</sup> cells) at the best electrical net efficiency (LHV DC) point, assuming a blade tip clearance of 80 μm for turbine and fan.

	Electrical <sup>a</sup>	Thermal <sup>b</sup>	Baseline
SOFC stack electrical DC output in kW <sub>el</sub> ( $P_{el}$ )	10	10	10
Electrical gross DC efficiency (LHV) in %	68.7	68.7	70.0
Electrical net DC efficiency (LHV) in % ( $\eta_{el,net}$ )	64.9	65.2	65.7
Net utilization ratio (LHV DC) in % ( $\zeta_{net}$ )	97.2	97.1	91.7
Number of cells in stack ( $j$ )	405	405	3 · 64 = 192
Cell potential in V ( $U_{cell}$ )	0.772	0.772	0.789
Current density in A cm <sup>-2</sup> ( $\frac{I_{cell}}{A_{cell}}$ )	0.4	0.4	0.31, 0.35, 0.25
Cell area in cm <sup>2</sup> ( $A_{cell}$ )	80	80	3 · 220
Fan specific speed ( $n_{s,F}$ )	1.02	1.12	0.8
Fan rotational speed in krpm ( $n_{rot}$ )	157	174	175
Fan diameter in mm ( $d_4$ )	18.4	17.0	20.0
Fan inlet temperature in °C ( $T_{13}$ )	200	200	200
Recirculation mass flow rate in kg h <sup>-1</sup> ( $\dot{m}_{13}$ )	5.8	5.7	4.78
Fan pressure rise in mbar ( $\Delta p_{tt,fan}$ )	50	50	70
Fan isentropic efficiency in % ( $\eta_{is}$ )	49	47	66
Fan efficiency in % ( $\eta_{is}\eta_{mech}$ )	34	34	40
Overall efficiency in % ( $\eta_{is}\eta_{mech}\eta_{drive}$ )	31	15	18.9
Fan power consumption in W ( $P_{fan}$ )	24	25	21
Recirculation unit power consumption ( $P_{total}$ )	38 W <sub>el</sub>	34 W	34 W
Turbine specific diameter ( $d_{s,T}$ )	-	13.8	5.46
Turbine specific speed ( $n_{s,T}$ )	-	0.05	0.09
Turbine diameter in mm ( $d_8$ )	-	17.4	9.5
Turbine efficiency in % ( $\eta_{is}$ )	-	43	47
Turbine pressure ratio ( $\Pi$ )	-	2.2	1.8
Turbine mass flow rate in kg h <sup>-1</sup> ( $\dot{m}_{26}$ )	-	1.7	2
AOR water vapor mass flow rate kg h <sup>-1</sup>	2.4	2.4	2.2
Shaft diameter in mm ( $d_{sh,fan}$ )	9.5	8.6	9.5
Mechanical efficiency of shaft in % ( $\eta_{mech}$ )	70	73	61
O/C ratio at reformer inlet (O/C)	2.0	2.0	2.0
H/C ratio at reformer inlet (H/C)	4.0	4.0	4.5
Reducing species fraction ( $\xi_{red}$ )	0.1	0.1	0.1
External-to-total reforming fraction ( $\xi_{ext}$ )	0.2	0.2	0.2
Methane mass flow rate in kg h <sup>-1</sup> ( $\dot{m}_1$ )	1.05	1.05	1.03
Cathode excess air ratio (EAR)	4.67	4.67	3.04
Local fuel utilization in % ( $f_{u,local}$ )	85.0	85.0	85.4
Global fuel utilization in % ( $f_{u,global}$ )	92.5	92.5	92.0
Recycle ratio in % ( <b>RR</b> , eq. 2.35)	552	547	465
Anode off-gas recirculation ratio in % (RR)	54.1	53.8	51.5

<sup>a</sup> AOR fan driven by electrical motor, data published in [88]

<sup>b</sup> Similar system as in [88], but AOR fan driven by a steam turbine

## 4 Fan-Turbine Unit Design

This chapter introduces the overall concept of the FTU and its shaft and bearing design. It also details the fan and turbine design of the FTU, as well as the one-dimensional and three-dimensional turbomachinery design tools used within this thesis.

### 4.1 Small-scale turbomachinery

With respect to conventional turbomachines, small-scale turbomachinery has increased losses as follows (chapter 2.2 in [12]):

- Higher viscous losses due to decreased Reynolds number.
- Higher frictional losses due to decreased hydraulic diameter.
- Higher tip leakage losses due to increased relative tip clearance.
- Higher losses due to decreased manufacturing and assembling capability (for example thick blade edges or misalignment).
- Higher heat losses due to increased area-to-volume ratio.

Small-scale turbomachinery, therefore, has inferior isentropic efficiencies compared to conventional machines. In addition, the mechanical efficiency decreases with reduced machine size, since the power is relatively low in comparison to the mechanical losses [85].

### 4.2 Design procedure of the anode off-gas recirculation unit

The system simulation and optimization that Chapter 3 describes provides the basic turbomachinery parameters, such as fan and turbine tip diameters, shaft diameter, rotational speed, and efficiencies. With these parameters, it is possible to find a shaft and bearing geometry that allows for stability over the entire operational range. In the next step, the fan and turbine impellers are designed following a procedure that Section 2.3.5 describes. In this step, the parameters from the system optimization serve as a basis. However, adjustments to the tip di-

ameters and/or rotational speed may be applied to enhance the turbomachine's performance. This design step is based on a manual observational method. The system is thus not optimized, and further efficiency increases are viable by performing a more detailed system simulation and optimization. In the final step, the author integrated the shaft and turbomachinery design into a three-dimensional model considering materials, manufacturing, and assembling. The focus is an easy-to-manufacture and easy-to-assemble system with low cost.

### 4.3 Fan-turbine unit concept and bearing design

This section describes the overall design concept of the FTU including all of its components, as well as the gas film bearing design.

#### 4.3.1 Concept of the fan-turbine unit

Since the FTU recirculates the anode off-gas to the reformer and SOFC stack, the FTU features materials that are compatible with these gases. Figure 4.1 features an overview of the FTU and its components with respective part numbers on the right side. The shaft features a diamond-like carbon (DLC) coating (part 01 in Figure 4.1) that has a low static friction coefficient (measured as 0.06). This is beneficial for startup and shutdown. For operation with water vapor at 220 °C, the turbine starts at a measured inlet gauge pressure of 0.23 bar.

**Parts:** All the components of the FTU are manufactured by milling, turning, or drilling operations exclusively. Only the diffuser at the fan volute outlet (rectangular to round) is machined with a wire using the electric discharge method. Some parts, such as the shaft (part 01) and the journal bearing (part 02), feature surface finishing (i.e., grinding and/or honing) to achieve tight tolerances. The fan impeller (part 03) is mounted on the shaft (part 01). The shaft screw (part 04) ensures the fan impeller positioning. This screw passes through the entire hollow shaft and the hollow turbine impeller (part 05). A custom-made nut (part 06) tightens the shaft screw, and thus the turbine impeller and the fan impeller. The design fan blade tip clearance is 0.05 mm, which is not solely achievable with manufacturing and assembly tolerances. A shim (part 07), referred to as the “journal bearing blockage”, adjusts the desired position of the fan volute (part 08) and, therefore, the fan blade tip clearance. The housing (part 09) aligns the journal bearing (part 07), fan volute (part 08), seal (part 10), and turbine volute (part 11). The turbine volute also features the partial-admission turbine stator (part 12). A shim (part 14) between the shaft and the turbine impeller adjusts the turbine backface clearance and the turbine blade tip clearance.

**Measurement positions:** The housing features connections for 2x2 LionPrecision C3S capacitive displacement probes (Figure 4.1 shows two), two thermocouples that measure the temperature on the journal bearing (at the position of the two red dots in Figure 4.1 at differ-

### 4.3. Fan-turbine unit concept and bearing design

ent angular positions), and one Philtec D20 optical displacement probe for rotational speed measurement (at the position of the green dot in Figure 4.1). Other connections included a connector to measure the housing pressure ( $p_{ho}$ , shown in the middle left), a connector to measure the seal static pressure ( $p_{st,seal}$ ), and a connector to supply pressurized air to the housing (not shown). On the bottom left, Figure 4.1 shows the static pressure tap at the rotor-stator turbine interface. The PTFE o-ring (15) decouples this pressure measurement from the turbine volute. O-rings (16 and 17) decouple the seal static pressure measurement from the housing and the turbine volute. The seal static pressure tap features four holes in between the seal teeth (Figure 4.1 on the left in the middle) that measure the pressure within the seal. O-rings 18 and 20 ensure gas-tightness of the FTU to the environment, whereas o-ring 19 ensures tightness between the fan volute and the housing, thus allowing for the housing pressure measurement. At the top of Figure 4.1, one of the three pressure taps used to measure the fan TE static pressure ( $p_{st,4}$ ) is shown at an angular position of  $\phi = 0^\circ$ . The fan

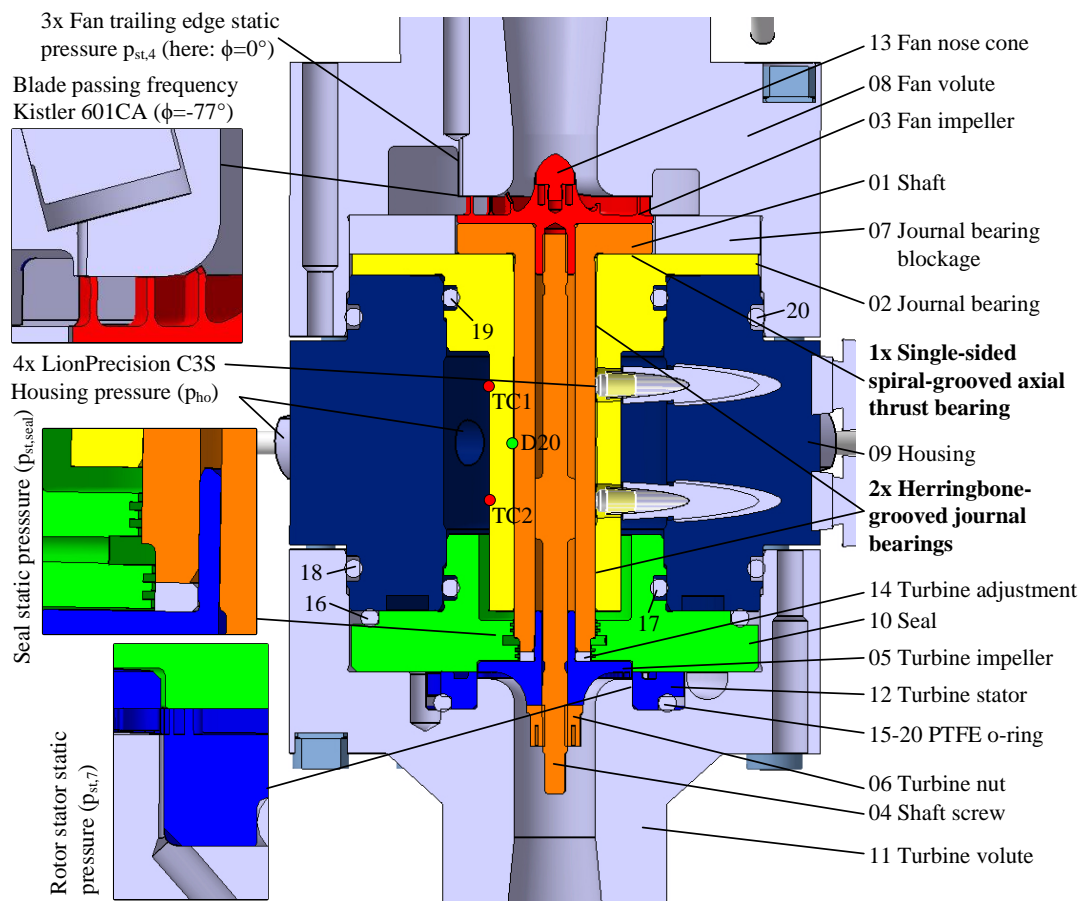


Figure 4.1 – Concept of the fan-turbine unit with all parts (right side), some static pressure measurement positions (left side), temperature measurement positions (red dots), and rotational speed measurement with an optical sensor (green dot).

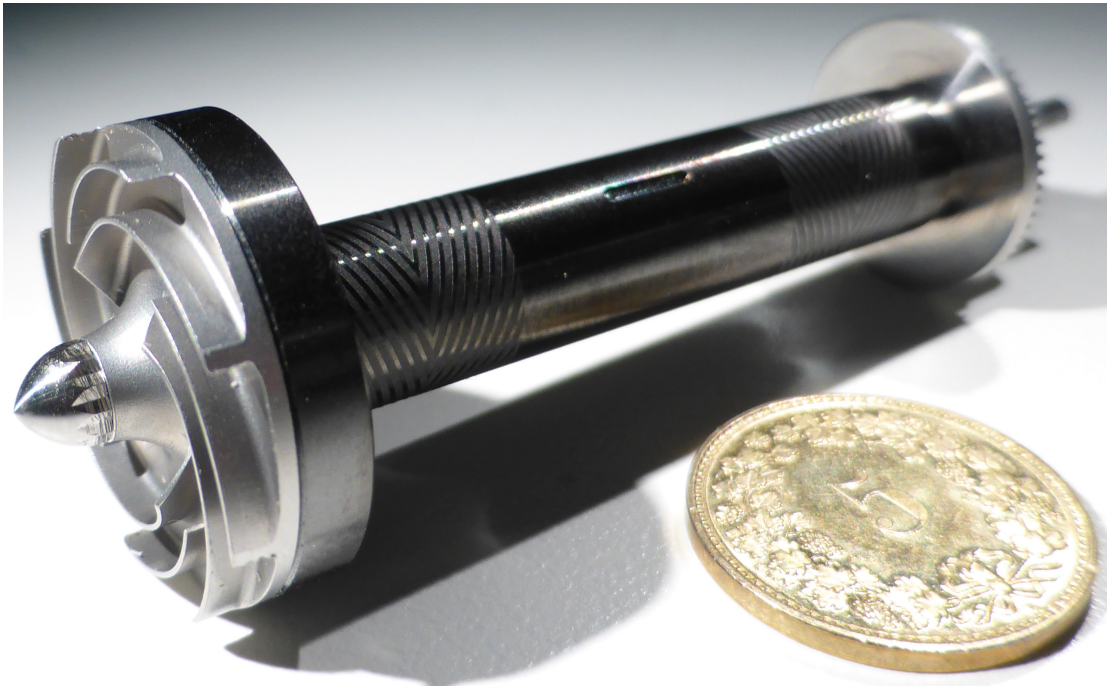


Figure 4.2 – Side view of the radial anode off-gas recirculation fan with mounted spinner (left), the diamond-like carbon (DLC) coated shaft with an 8 mm diameter featuring two herringbone-grooved journal bearings, and the radial-inflow turbine (right). The Swiss five centime coin diameter is 17.15 mm.

volute features two other taps at angular positions of  $120^\circ$  and  $240^\circ$ . At a position of  $\phi = -77^\circ$ , there is the static pressure tap for the blade passing frequency measurement with the Kistler 601 CA piezo-electric pressure transducer (shown in the top left of Figure 4.1).

### 4.3.2 Gas film bearing and shaft design

The AOR fan uses self-acting herringbone-grooved journal and a spiral-grooved thrust gas film bearings, which operate in the pump-in mode. Schiffmann [12] implemented a similar bearing concept. Figure 4.2 shows the fan and its 8 mm shaft with the two herringbone-grooved patterns at the journal bearing locations. Since rotors supported on gas film bearings tend to be unstable, the designer must verify the stability over the entire operational range. The approach used here is similar to the validated procedure implemented by Schiffmann [12] (chapter 3 and 4). A modal FEM simulation of the rotor using the commercial Ansys software suggests that the first bending frequency is 280 krpm. Since the shaft nominal speed is 175 krpm, and thus below this first bending frequency, a rigid-body model is used. The rotor has five degrees-of-freedom, including axial and radial displacements and two tilting motions around the center of gravity. The resulting set of second-order differential equations are an eigenvalue problem. The ratio of the real part of these eigenvalues ( $\gamma_j$ ) to the imaginary part

### 4.3. Fan-turbine unit concept and bearing design

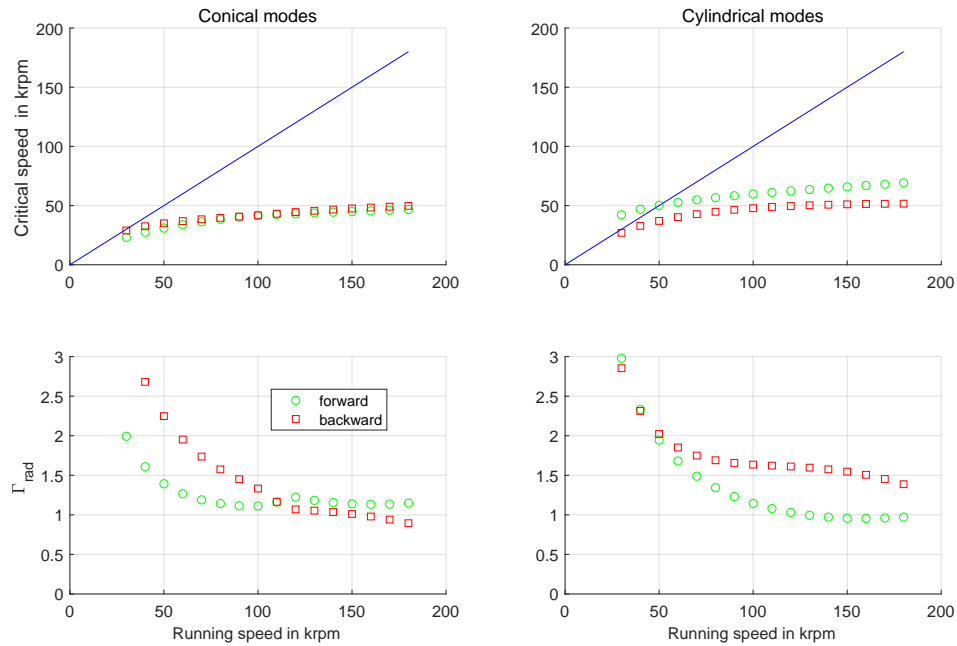


Figure 4.3 – Whirl map for the anode off-gas recirculation fan journal bearings with a diameter of 8 mm operated with water vapor at 220 °C corresponding to the design point.

$(\omega_j)$  is described using the logarithmic decrement,

$$\Gamma = -2\pi \frac{\gamma_j}{\omega_j} \quad 4.1$$

as a criteria for rotor stability. If this number is higher than zero ( $\Gamma > 0$ ) over the complete operational range, the rotor is stable. In addition to the system mass inertia matrix, the bearing damping and stiffness matrices are required to formulate the rotor differential equations of motion. The flow within the journal and thrust bearings are governed by the Reynolds equation. Using the narrow groove theory [93], a modified Reynolds equation is obtained that is linearized by applying the perturbation method. This allows for the aerodynamic fluid film bearings' properties to be calculated, which not only depend on the rotor rotational speed but also on the excitation frequency.

Figure 4.3 shows the whirl map for the conical and cylindrical modes of the AOR fan. The green circles correspond to a forward whirl, whereas the red squares indicate a backward whirl. During the rampup to the design speed of 175 krpm, a cylindrical mode (at 50 krpm) is passed. Due to the high damping ( $\Gamma > 1$ ), the operation is safe within this regime. Within the operational range, the logarithmic decrement is above 0.9; hence, the rotor is stable.

The spiral-grooved thrust bearing design uses a similar methodology. Section 4.6 introduces

an analytical model to calculate the thrust force. The knowledge of the exact thrust force is important, since the thrust gas film bearing is unstable if the thrust is elevated. At the design rotational speed of 175 krpm with the water vapor at 220 °C, the thrust bearing is capable of compensating for 11 N before becoming unstable. Since the rotor shows very stable operation with different fluids (i.e., air, pure nitrogen, and water vapor) at different temperatures (ambient and up to 220 °C) and up to a rotational speed of 220 krpm, the author assumes the bearing design procedure validated.

A static structural FEM simulation with Ansys investigates the impeller deformation and equivalent stresses to ensure the mechanical integrity of the entire system. Since the fan rotor tip speed is  $176 \text{ ms}^{-1}$ , the static structural integrity is not critical. However, the author did not investigate time-dependent mechanical deformation, such as creep.

### 4.4 Radial fan

This chapter introduces the baseline fan impeller that was designed, manufactured, simulated, and experimentally tested within this thesis. The experiments and numerical simulation show good agreement at the fan nominal point. The results obtained are therefore used to adjust the one-dimensional analytical mean-line model. This section also presents the CFD setup and results for the single passage, as well as for the full passage fan model.

#### 4.4.1 Fan specifications

The baseline fan impeller is designed for a total inlet pressure of 1.05 bar, a total inlet temperature of 200 °C, an inlet mass flow rate of  $4.78 \text{ kg h}^{-1}$ , and anode off-gas composed of water vapor, hydrogen, carbon monoxide, and carbon dioxide (61.4 %, 7.4 %, 2.6 %, and 28.6 % molar ratio, respectively). The design total-to-total pressure rise is 70 mbar. The pressure drop in the SOFC stack and in the reformer are determined based on experience: 30 mbar and 20 mbar, respectively. The author estimates the overall pressure drop in the heat exchangers upstream and downstream of the reformer (Figure 3.1) and within the anode loop to be 10 mbar. In total, the AOR fan compensates for 70 mbar at the design point, thus accounting for a safety margin of an additional 10 mbar of pressure drop in valves, bends, and piping.

#### 4.4.2 Fan design summary

The fan TE diameter ( $d_4$ ) is 19.2 mm and the fan design rotational speed of 175 krpm corresponds to a specific speed of 0.8, as defined by Balje [2]. Since the actual hot anode off-gas is toxic and explosive, the author tested the fan consecutively with ambient air (Section 5.3), hot air at 200 °C (Section 5.5), and finally with the actual SOFC (Chapter 6). A constant Mach number from eq. 2.66 defines the rotational speed for each of these tests. For example, instead



Table 4.1 – Geometrical parameters of the radial anode off-gas recirculation fan (fan sections 1 to 8 as defined in Figure 2.3).

<b>Inlet (1) and inlet nozzle (1.1, round)</b>				<b>Blade tip clearance (s)</b>			
$d_1 = d_{1.1}$	12.00 mm	$l_{1.2,1.1}$	21.00 mm	$s_{design}$	0.05 mm (design)		
				$s_{shim}$	0.05 mm+0.1 mm (shimmed)		
<b>Inducer inlet (2) at hub (h) and shroud (s)</b>				<b>Fan backface / thrust bearing clearance (s)</b>			
$d_{2h}$	4.08 mm	$d_{2s}$	8.22 mm	$s_{tb}$	0-0.010 mm zero to nominal speed (movement of the thrust bearing)		
<b>Impeller (3-4)</b>				<b>Volute (5-6, square)</b>			
Blade leading edge (3) at hub and shroud				End of logarithmic spiral (5.2)			
$d_{3h}$	7.32 mm	$d_{3s}$	10.02 mm	$h_{5.2} \times b_{5.2}$	6.77×6.77 mm		
$\beta_{3,blade}$	30°(s)-36°(h) (blunt leading edge)			Cut water region at volute tongue			
$z_{main}$	4			$d_{tongue}$	0.4 mm	$\phi_{tongue}$	-59°
Splitter blade leading edge (3.1)				Volute outlet (6)			
$\beta_{3.1}$	22°	$d_{3.1}$	12.70 mm	$h_6 \times b_6$	9.93×6.77 mm		
$z_{splitter}$	4	$z$	4 + 4 = 8	<b>Volute diffuser (6-7, rectangular to round)</b>			
$r_s$	2.04 mm	(shroud radius)		$d_7$	16.00 mm	$l_{7,6}$	40.00 mm
Blade trailing edge (4)				<b>Outlet (8)</b>			
$d_4$	19.20 mm	$t_{blade}$	0.25 mm	$d_8$	16.00 mm		
$b_4$	1.82 mm+0.15 mm (shimmed)						
$\beta_{4,blade}$	17° (cut-off trailing edge)						

of 175 krpm, the rotational speed for hot air is 168 krpm, and therefore, very similar. The fan design is based on a trade-off between efficiency and low manufacturing cost. Table 4.1 lists the main geometrical fan parameters, while Figure 4.4 shows the top view of the radial AOR fan and its volute.

**Fan inlet (fan section 1 to 3 as defined in Figure 2.3):** At the machine inlet, the flow is accelerated within the inlet nozzle to the fan inducer. The fan spinner is designed as a tangent Haack profile, as shown in Figure 4.2. The fan flow coefficient based on the total machine inlet conditions ( $\Phi_{t,1}$  as defined in eq. 2.72) at the design point is very low (0.033). A low flow coefficient favors an inducer-less fan design, since the end wall frictional losses within the blade channels increase due to a decreased hydraulic diameter. Therefore, the fan LE is shifted from the inducer inlet towards the radial impeller section. This also allows for a two-dimensional prismatic blade design that is easier to manufacture. The fan shroud changes direction from axial to radial with a radius of 2.04 mm. At the shroud the flow accelerates, whereas the fluid decelerates at the fan hub. This velocity gradient between hub and shroud leads to large incidence angles at the blade LE, even if designed at a constant radius, and thus at a constant angular velocity. This flow phenomena is addressed by decreasing the blade LE radius at the hub, which resulted in lower circumferential velocities, and vice versa for the shroud. The blade LE relative angle at the hub ( $\beta_{3h,blade} = 36^\circ$ ) and at the shroud ( $\beta_{3s,blade} = 30^\circ$ ), as

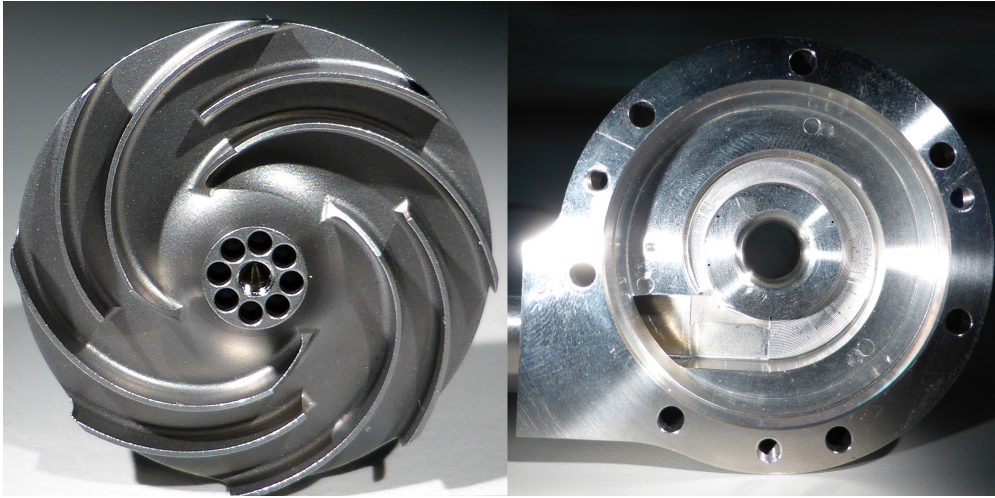


Figure 4.4 – Top view of the radial anode off-gas recirculation fan without mounted spinner featuring holes for balancing (left) and the logarithmic fan volute (right) featuring four pressure taps with a diameter of 0.4 mm at the fan trailing edge, respectively volute inlet.

well as diameters ( $d_{3h}$  and  $d_{3s}$ ) are designed to minimize the relative velocity, and thus the losses as stated in eqs. 4.9 and 4.10 [74]. The fan blade LE channel width is designed for a constant velocity between the axial-oriented fan inducer inlet and the radial-oriented blade LE.

**Fan impeller (fan section 3 to 4):** The fan features four main blades and four splitter blades. The splitter blades are placed towards the radial impeller section at a radius of 12.70 mm. The first 22 % of the main blades with respect to the meridional coordinate are fully unloaded. Thus, that the Euler work in this region is zero. The pressure therefore does not increase and the pressure difference between the blade suction and pressure sides is kept within a few millibar. This low pressure difference reduces the formation of the tip leakage vortex. As the design relative blade tip clearance ( $s_{design}/b_4 = 0.0275$ ) is high, this leakage flow is dominant within the impeller. The minimum feasible blade tip clearance is limited due to manufacturing and assembly tolerances, as well as the clearance within the dynamic gas film bearings.

This thesis presents the results for the shimmed version with a 0.15 mm blade tip clearance, which corresponds to a safety margin of 0.1 mm with respect to the design value. The single-sided spiral-grooved inward-pumping dynamic thrust gas film bearing is located at the fan backface. During operation, the running clearance decreases by 0.010 mm at design speed, since the thrust bearing generates pressure, lifting the fan towards the shroud. The blades are non-tapered and have a thickness of 0.25 mm, limited by mechanical stress induced during the milling process. A blade thickness of 0.20 mm is possible, but requires extremely careful milling operations and is therefore not favored. The manufacturing tool limits the radius between the blade and fan hub to 0.2 mm. The manufacturing process of the fan, volute, and impeller is simplified by keeping the blade height at a constant value of 1.82 mm.

Since a constant channel width and blade height may cause excessive diffusion within the impeller, highly backward-curved blades can be used to limit the diffusion. The blade angle at the TE with respect to the circumference is  $17^\circ$ , and thus very low. The fan must then spin relatively fast to obtain a certain pressure (eq. 2.75). A high shaft rotational speed leads to a higher circumferential velocity at the turbine inlet (diameter of 15 mm). Since the turbine inlet absolute velocity is slightly higher than Mach 1 at the design point, and therefore much higher than the circumferential velocity, the turbine inlet relative velocity is also high, which leads to elevated losses. A high rotational speed can therefore limit the losses on the turbine side and increase the overall FTU efficiency, since highly-backward curved fan impellers offer good efficiency.

**Fan outlet (fan section 4 to 5):** Due to the low blade angle at the TE, the flow exits the fan impeller with a high circumferential velocity component, which calls for a pinched diffuser design. A diffuser in general, but especially a pinched design complicates the fan. In addition, the Mach number with respect to the design total inlet conditions and the angular velocity at the blade TE is 0.39; hence, a diffuser-less design is viable. However, the frictional pressure losses due to a high volute inlet velocity ( $c_{u,4}$ ) are increased. The author decided to eliminate the diffuser and to collect the fluid directly in a well-designed volute right after the fan blade TE (at the design point without acceleration or deceleration of the fluid).

**Fan volute and diffuser (fan section 5 to 7):** The volute has an easy-to-manufacture square shape, is designed for constant angular momentum, and is entirely manufactured through classical milling and turning operations (except for the rectangular-to-circular volute outlet diffuser). At the end of the logarithmic spiral, the volute features a quadratic surface ( $6.77 \times 6.77$  mm), which increases towards a rectangular surface at the volute outlet ( $9.93 \times 6.77$  mm). According to Leidel [84], the placement of the volute tongue is a trade-off between the sound level and aerodynamic efficiency. The tongue radius angle ( $\phi_{tongue}$ ), defined as the angle between the end and the start of the logarithmic spiral, is  $-59^\circ$  (Figure 2.3), leading to a distance between the fan TE and the tongue of 2.5 mm. After the volute, a rectangular-to-circular diffuser recovers pressure.

#### 4.4.3 One-dimensional simulation

Figure 4.6 shows the mean-line design procedure, as introduced in Section 2.3.2. The preliminary fan design uses similarity concepts by Balje, as introduced in Section 2.3.4. A previously published paper by the author [88] proposes a procedure adopting Balje's preliminary design method to small-scale turbomachinery with elevated losses.

With the machine inlet conditions and the design total-to-static fan pressure rise, the similarity concepts calculate the fan diameter ( $d_4$ ), the fan angular velocity ( $\omega$ ), and its isentropic total-to-static efficiency ( $\eta_{is,tst}$ ) as defined in eq. 2.62). Since the velocity at the machine outlet

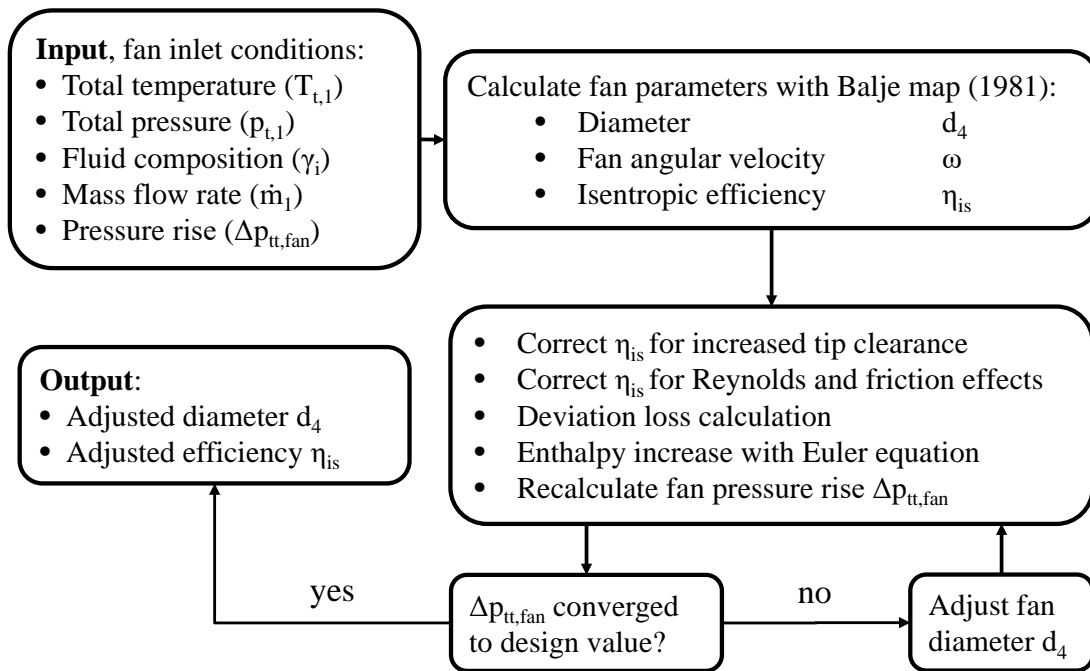


Figure 4.5 – Schematic of the one-dimensional fan calculation procedure based on mean-line design.

is low, the difference in total-to-static and total-to-total isentropic efficiency ( $\eta_{is} \approx \eta_{is,tst}$ ), along with the total and static pressure is very low ( $p_{t,8} \approx p_{st,7}$ ). At the design point of the FTU, the experimentally measured difference between the two isentropic efficiency definitions is 0.4 percentage points in the case of a fan outlet tube with a diameter of 16 mm. Thus, this procedure assumes no difference between the total-to-static, as well as total-to-total values of efficiency ( $\eta_{is} \approx \eta_{is,ts}$ ) and pressure rise ( $p_{t,8} \approx p_{s,8}$ ).

As introduced in Section 4.1, small-scale turbomachinery feature elevated losses; hence, the isentropic efficiency given by Balje’s similarity concepts is overestimated. Thus, a small-scale fan designed with the original Balje similarity concepts yield a decreased fan total-to-total pressure rise at the design rotational speed and mass flow rate.

In order to account for the reduced fan size, the efficiency and pressure rise predicted by Balje are corrected by evaluating four loss mechanisms: (1) increased tip leakage losses due to higher manufacturing and assembly tolerances, (2) increased viscous losses due to decreased Reynolds number, (3) increased frictional losses due to increased relative surface roughness, and (4) the deviation loss at the fan TE.

**(1) Tip clearance:** Pfleiderer [94] suggested a correlation for efficiency correction with respect

to the relative blade TE clearance ( $s/b_4$ ).

$$\eta_{is} = \eta_{is,n} \left( -a_1 \frac{s}{b_4} + 1.011 \right) \quad 4.2$$

The value of  $a_1$  depends on the machine and is based on experience. Pfleiderer proposes 1.5-3 for this value. Based on a CFD investigation of several relative blade tip clearances (0, 0.022, 0.047, 0.071) for a previously introduced fan impeller geometry, the experience coefficient  $a_1$  is determined to be 2.3 for anode off-gas and air at 200 °C . Section 4.4.4 provides more details on these numerical simulations.

**(2) Reynolds and (3) frictional loss:** The equation from Wiesner [91] is used to account for the frictional and Reynolds effect.

$$\eta_{is} = 1 - (1 - \eta_{is,n}) \frac{\log \left( 3.18 \cdot 10^{-6} + \frac{13.67}{Re_b} \right)}{\log \left( RMS + \frac{13.67}{Re_b} \right)} \left( 0.06606 + 0.9394 \left( \frac{Re_{b,n}}{Re_b} \right)^{\frac{0.9879}{Re_b^{0.24336}}} \right) \quad 4.3$$

The equation calculates the isentropic efficiency ( $\eta_{is}$ , eq. 2.61) as a function of the root mean squared surface roughness (RMS), the actual Reynolds number based on the channel TE ( $Re_b$ , eq. 2.74), and the nominal Reynolds number ( $Re_{b,nom}$ ). It is important to note that Balje uses the Reynolds definition based on the blade tip diameter ( $Re_D$ , eq. 2.64), which is  $4 \cdot 10^6$  in Figure 2.5. This Reynolds number therefore requires a conversion to the  $Re_b$  definition. Wiesner states that this equation is accurate up until  $Re_{b,nom}/Re_b = 100$ .

**(4) TE deviation loss:** Pfleiderer [94] suggests a method to account for the deviation loss at the blade TE,

$$c_{u,4} = \left( u_4 - \frac{c_{m,4}}{\tan \beta_4} \right) \left( 1 + 2a_2 \frac{1 + \frac{3\beta_{4,blade}}{\pi}}{z \left( 1 - \left( \frac{d_3}{d_4} \right)^2 \right)} \right)^{-1} \quad 4.4$$

with the variables as defined in Sections 2.3.1 and 2.3.2. Pfleiderer states that for a LE to TE diameter ratio ( $d_3/d_4$ ) greater than 0.5, there is no significant change, therefore the  $\frac{d_3}{d_4}$  ratio is kept constant at 0.5. The value of  $a_2$  is experience-based and ranges between 0.65 and 0.85 for a fan without a diffuser, where the fluid enters the volute directly after the fan TE. This experience coefficient is determined to be 0.6 to best fit the experimental results (Figure 4.6). The experience values of Pfleiderer are based on conventional machines with a high TE tip diameter, operating with ambient air, and thus having high Reynolds numbers. The fan within this thesis operates at elevated temperatures (200 °C), thus the viscosity is increased. Consequently, and in addition to the reduced size, the Reynolds number is relatively low ( $Re_D = 0.18 \cdot 10^6$ ). Due to the increased viscosity, the deviation loss is relatively low compared to large-scale machines.

For the correlation in eq. 4.4, the meridional velocity at the blade TE must be known.

$$c_{m,4} = \frac{\dot{m}_1}{\pi d_4 (b_4 - s_4) \rho_4} \frac{\pi d_4}{\pi d_4 - \frac{t_4}{\cos \beta_4} z} \quad 4.5$$

The density ( $\rho_4$ ) calculation uses the static pressure and temperature at the blade TE. Classical gasdynamic correlations are used to calculate the static values with respect to the total values for temperature and pressure. Water vapor at ambient pressure and 200 °C has a compressibility number of 0.995 leading to a 0.5 % error for the assumption of ideal gas. The ideal gas assumption is valid for carbon monoxide, carbon dioxide, and hydrogen (all gases are part of the AOR).

Assuming no inlet swirl, the fan total-to-total specific enthalpy increase is directly linked to the circumferential velocity ( $u_4$ ) and the circumferential component of the absolute velocity ( $c_{u,4}$ ) at the fan TE, as stated in eq. 2.53.

$$\Delta h_{tt, fan} = c_{u,4} u_4 \quad 4.6$$

The NIST fluid data base is used to calculate the total pressure at the fan outlet, since it is a function of the total specific entropy at the fan inlet ( $s_{t,1}$ ) and the fan outlet total isentropic specific enthalpy ( $h_{t,is,8} = h_{t,1} + \Delta h_{tt, fan} \eta_{is}$ ). The total temperature at the machine outlet ( $T_{t,8}$ ) is determined using the total specific enthalpy ( $h_{t,8} = h_{t,1} + \Delta h_{tt}$ ) and the total pressure ( $p_{t,8}$ ). For an adiabatic machine, the total temperature at the machine outlet is equal to the total temperature at the fan blade TE ( $T_{t,4} = T_{t,8}$ ). The model assumes a constant pressure loss coefficient of  $\frac{2}{3}$  for the fan volute frictional pressure loss, which is a result of the full passage CFD simulation at the design point (10 mbar pressure loss within the volute) and a total loss of the meridional velocity component ( $c_{m,4}$ ), due to swirl generation. The total blade TE pressure is therefore equal to the fan outlet total pressure minus the volute pressure loss.

$$p_{t,4} = p_{t,8} - \frac{1}{2} \rho_4 \left( \frac{2}{3} c_{u,4}^2 + c_{m,4}^2 \right) \quad 4.7$$

Due to the high channel width ( $b_4 = 1.97$  mm), the meridional velocity is three-times lower than the absolute circumferential velocity component; hence, the sudden expansion loss is inferior to the volute frictional loss. Equations 4.4 and 4.5 use the blade number ( $z$ ), which is defined with the blade chord length to channel depth ratio of five.

$$z = \left\lceil 5 \frac{d_4 \pi \sin \beta_{4, blade}}{l_{chord}} \right\rceil \quad 4.8$$

The optimal ratio is a trade-off between deviation losses and frictional losses within the blade channels. A high ratio leads to increased frictional losses and decreased deviation losses and vice versa for a low ratio. Since the blade TE angle ( $\beta_4$ ) is low, the optimal ratio is relatively high compared to values found in the literature (Eck [74] recommends two). The blade chord

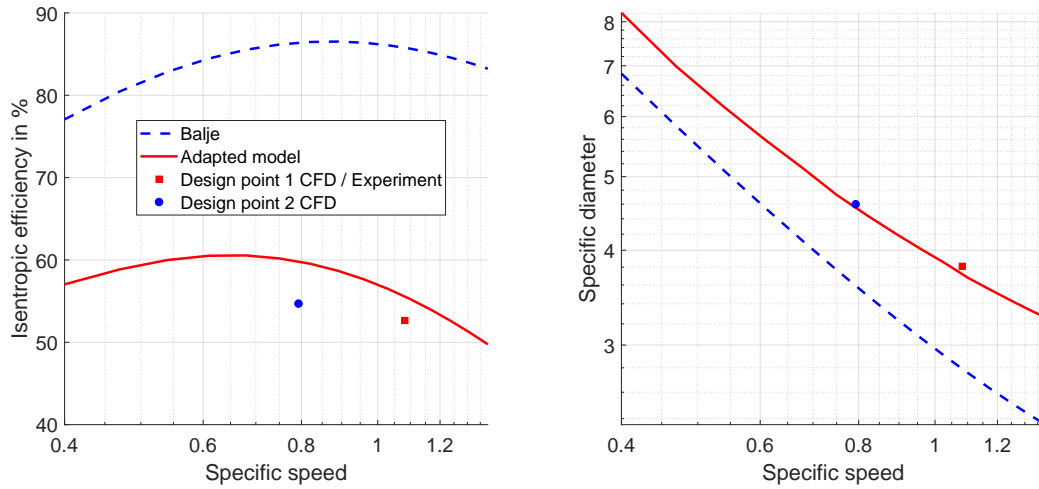


Figure 4.6 – Original Balje correlations, adapted model, and comparison to measurements and CFD simulations.

length ( $l_{chord}$ ) is predicted assuming circular blades.

The calculation procedure determines the optimal blade LE angle ( $\beta_3$ ) and blade LE diameter ( $d_3$  in eq. 4.4) to minimize the relative velocity ( $w_3$ ), and thus the losses [74]. Typically, the relative velocity at the LE is the highest within the fan impeller; hence, the losses are elevated in this region.

$$\beta_{3,blade} = \arctan\left(\frac{1}{3\sqrt{2}}\left(1 + 2e^{-\frac{\beta_3}{2r_s}}\right)\right) \quad 4.9$$

$$d_3 = \left(8 \frac{\pi d_3}{\pi d_3 - t_3 \frac{z}{2}} \frac{\dot{m}_1}{\rho_3 \pi (1 - \lambda^2) \omega \tan \beta_{3,blade}}\right)^{\frac{1}{3}} \quad 4.10$$

This calculation takes the fluid deceleration at the hub and the fluid acceleration at the shroud due to the inlet shroud radius ( $r_s$ ) into account. This radius indicates how abruptly the shroud changes from the axial to the radial direction. The higher this radius, the lower the fluid acceleration at the fan shroud and the lower the blade LE angle (and vice versa). According to eq. 4.9, the optimal  $\beta_3$  for a sharp edge ( $r_s = 0$ ) is  $35.3^\circ$ .

**Comparison to experiments:** Figure 4.6 shows the relation between the specific speed ( $n_s$ ) and the total-to-static isentropic efficiency, as well as the specific diameter ( $d_s$ ), according to Balje, with a blue dashed line. Peak compressor isentropic total-to-static efficiencies can reach up to 86 % at a specific speed of 0.85. Figure 4.6 also shows the experimentally validated computational results of FTU design point 1 (red square) with a  $150 \mu\text{m}$  blade tip clearance instead of the design  $50 \mu\text{m}$  (middle point on the 168 krpm speed line in Figure 5.12). Due to the increased blade tip clearance, the fan cannot achieve the design total-to-total pressure rise

of 70 mbar. However, the fan achieves this design pressure rise at a lower mass flow rate (left point on the 168 krpm speed line in Figure 5.12). This off-design point is referred to as design point 2 in Figure 4.6 (blue circle in Figure 4.6). The graph shows the efficiency and specific diameter evolution predicted by the model that is adapted to the experiments and the CFD simulations (red line). The tuned variables are the experience coefficient ( $a_1 = 2.3$ ) in eq. 4.2 and the experience coefficient ( $a_2 = 0.6$ ) in eq. 4.4. Due to the increased Reynolds and blade tip losses (relative blade tip clearance of  $s/b_4 = 0.082$ ), a higher fan diameter is favored, thus shifting the best efficiency point to a specific speed of 0.65.

For these input parameters (mass flow rate of  $5.3 \text{ kg h}^{-1}$ , fan pressure rise of 48.2 mbar, and air at 0.96 bar and  $200^\circ\text{C}$ ), the adapted model shows reasonable agreement (within 3 %) with measured efficiency. The measured total-to-total isentropic efficiency is 52.5 % (red square) and the adapted model predicts 55.5 % at this point. With this geometry, the specific diameter absolute value is increased by 1.6 at low specific speeds and by 1.0 for specific speeds above 0.8.

However, these results should be treated with care, since the model is adjusted at this point with the experimental measurements and the CFD simulations. A simple analytical model based on similarity concepts cannot predict the fan efficiency and pressure rise accurately; hence, a three-dimensional CFD simulation is necessary to adjust the final fan geometrical parameters, as described in the next subsection.

### 4.4.4 Three-dimensional single passage simulation

The estimation of the fan isentropic efficiency and pressure rise with similarity concepts and simple one-dimensional models is limited, due to the highly non-uniform and three-dimensional flow within the impeller (formation of jet and wake). Additionally, the relatively high blade tip clearance has a significant impact on the estimation. An adiabatic and steady CFD simulation is therefore performed in order to determine the fan performance and to design the exact fan blade shape. This subsection also presents a numerical tip clearance investigation that uses the anode off-gas and air at  $200^\circ\text{C}$ .

#### Simulation setup

ANSYS BladeGen uses the geometric data from the one-dimensional model to construct a three-dimensional model. Figure 4.7 shows the geometric model, consisting of an inlet duct (section 1.1 to 1.2 in Figure 2.3), the transition region to the fan inducer inlet with the tangent Haack fan nose cone (section 1.2 to 3), the fan impeller (section 3 to 4), and an additional diffuser (section 4 to 5). The addition of the virtual diffuser helps the simulation achieve a better convergence. The fan diffuser is therefore a numerical virtual domain that does not represent the real system. It is important to note that the diffuser hub and shroud walls are free-slip walls.

**Geometry generation:** The simulation only models one single passage, including one main



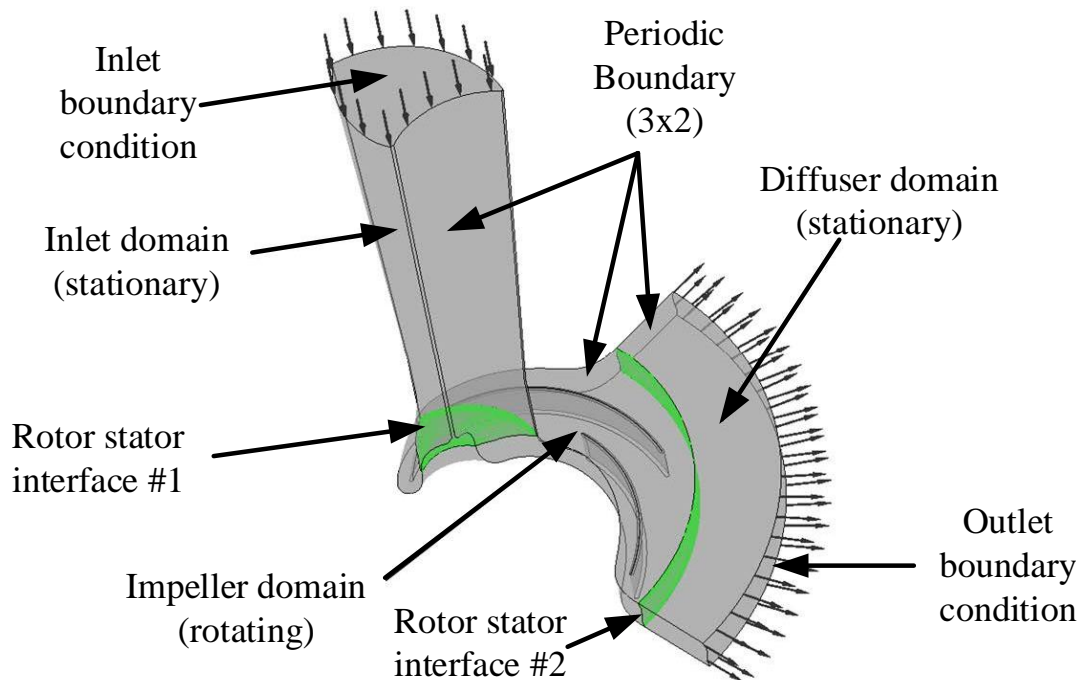


Figure 4.7 – Domain regions: inlet, rotating fan impeller, and diffuser from left to right. The fluid-to-fluid interfaces between the stationary and rotating domain are marked green.

and one splitter blade. The fan blade shape is controlled by the blade angle distribution ( $\beta_{blade}$ ) at the hub profile. The spanwise distribution type is set to “axial element” to obtain prismatic blades. Both LE and TE have an elliptic ratio of 2.0 and 1.0, respectively, which simplifies the grid generation. Figure 4.7 shows the splitter blade LE and TE, whereas Figure 4.4 shows the real fan geometry with a blunt LE and a cut-off TE (as implemented in the full passage CFD simulation, Section 4.4.5). As already mentioned, the blade thickness is constant in the span-wise (hub-to-shroud) and streamwise (LE to TE) directions. The hub fillets caused by manufacturing (radius of 0.2 mm) are not included in the single passage simulation. However, the influence is negligible; the fan TE area would be decreased by 0.1 %, which leads to less diffusion and therefore a lower static pressure on the order of 0.1 %.

**Grid generation:** The “ATM Optimized” topology in ANSYS TurboGrid creates a structured grid based on hexahedral elements. Figure 4.8 shows the mesh for the fan hub, the fan main and splitter blades, and the diffuser. For all cases (different fluids and different blade tip clearances), the first element height is 0.0005 mm, which corresponds to a  $y^+$  value of 1.0. Appendix B presents the details on the mesh sensitivity analysis and shows that a computational mesh with  $10^6$  elements is adequate. The design blade tip clearance of 0.04 mm features 13 elements in the span-wise direction. This study investigates a design blade height ( $h_4$ ) of 1.82 mm with the design running tip clearance of 0.04 mm at the design speed, a zero tip clearance (ideal

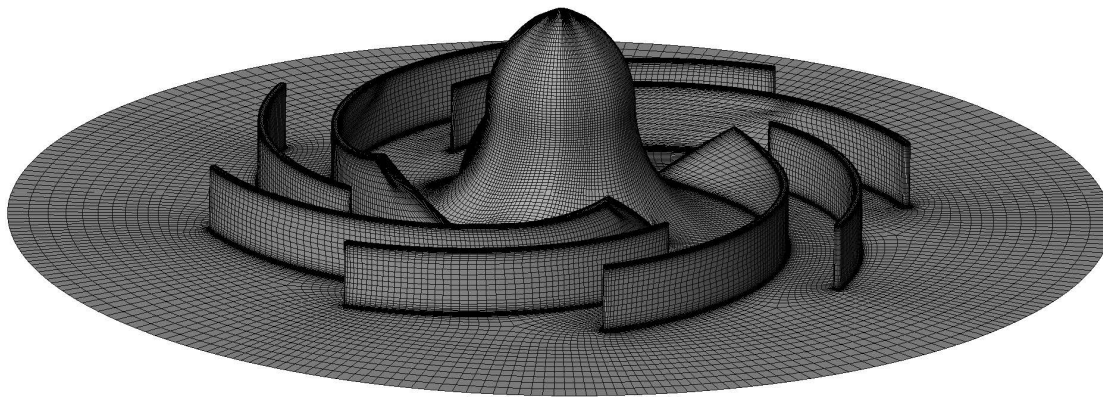


Figure 4.8 – Generated mesh for the fan hub, blades, and diffuser for all four blade passages.

case), and two additional blade tip clearances ( $s_4$ ) that are realized with a shim of 0.05 mm and 0.1 mm thickness, respectively. For all four different cases with the two different fluids (air and anode off-gas), the mesh is the same, except that the number of cells within the blade tip clearance increase linearly from nine to 29. Thus, the total mesh element number is not constant for all investigated cases. Table 4.2 lists the parameters of the four different tip clearance cases.

This maximum  $y^+$  value of the first cell (1.54) occurs for the simulation with a blade tip clearance of zero and the anode off-gas, whereas it is 1.26 for hot air. For all other cases, the maximum  $y^+$  value is below 1.2. However, the maximum  $y^+$  value only occurs locally; for example, at the main and splitter blade LE. Figure 4.9 provides an overview of the  $y^+$  values for the anode off-gas case (fluid composition of water vapor, hydrogen, carbon monoxide, and carbon dioxide) with a blade tip clearance of zero.

**Boundary conditions:** Figure 4.7 shows the simulation boundary conditions, which are as follows. At the nozzle inlet (section 1.1 in Figure 2.3), the total temperature (200 °C), the total pressure (0.96 bar), and the gas composition are defined. Two different gases are investigated: hot air at 200 °C and the anode off-gas at 200 °C (molar ratios of water vapor, hydrogen, carbon monoxide, and carbon dioxide are 61.4 %, 7.4 %, 2.6 %, and 28.6 %, respectively). The

Table 4.2 – Relative blade tip clearance and mesh data for the four different cases.

Running clearance	Relative clearance ( $s_4/b_4$ )	Number of elements within the clearance	Total mesh elements in million
0 mm	0/1.82=0	0	0.79
0.04 mm	0.04/1.86=0.022	9	1.00
0.09 mm	0.09/1.91=0.047	19	1.24
0.140 mm	0.14/1.96=0.071	29	1.55

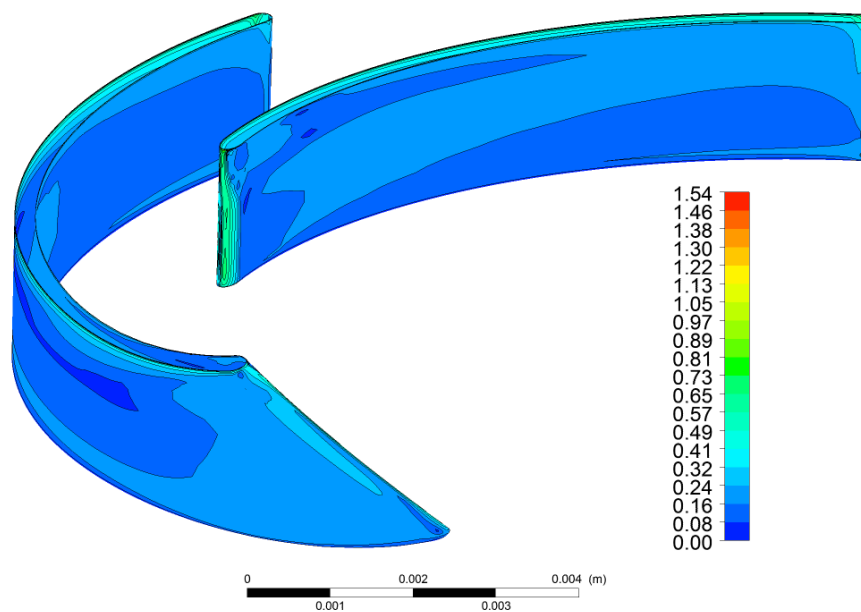


Figure 4.9 –  $y^+$  values for the anode off-gas simulation with a zero blade tip clearance.

numerical tip clearance study uses the conditions of the experiment with hot air (Section 5.5). The rotational speed is 168 krpm and the mass flow rate is  $5.29 \text{ kg h}^{-1}$ . Based on a constant Mach number (eq. 2.66) and a constant flow coefficient ( $\Phi$ , eq. 2.72), the conditions for the anode off-gas are 175.5 krpm and  $4.71 \text{ kg h}^{-1}$ . Table 4.3 summarizes the investigated operating conditions. Note that the simulation assumes a leakage-free operation ( $\dot{m}_1 = \dot{m}_8$ ). Further boundary conditions are as follows:

- The fan inlet nozzle hub and shroud are non-slip walls.
- The rotor-stator interfaces #1 and #2 is a fluid-to-fluid frozen rotor interfaces.
- The impeller domain rotates at the rotational speed specified in Table 4.3.
- The fan hub and the fan blades are rotating no-slip walls, whereas the fan shroud is a counter-rotating no-slip wall to account for the relative motion of fan blades and hub (no surface roughness defined).
- All sides of the fluid domain are rotational periodicities (in total 3x2) to account for the interaction of the different single passages.
- The blade clearance interfaces are a fluid-to-fluid interface.

Table 4.3 also shows the predicted (on the basis of measurements with ambient air) thrust gas film bearing axial clearance at running conditions, discussed in Section 4.4.4. This thrust bearing is located at the fan backface.

**Solver setup:** The CFD simulation uses compressible fluids with constant heat capacity and

## Chapter 4. Fan-Turbine Unit Design

Table 4.3 – Operational conditions for the experiment and numerical simulation with air. The machine inlet total pressure is 0.96 bar and the total temperature is 200 °C, which is the reference case (marked in **bold**) for the numerical simulation with the anode off-gas (constant Mach number and constant flow coefficient  $\Phi$ ). The thrust bearing axial clearance, which corresponds to the fan impeller blackface clearance, in the case without mounted fan volute is measured at ambient conditions, whereas the other values are predictions (pred.) assuming constant thrust force.

Fluid	Total inlet temp. in °C	Total inlet pressure in bar	Rotational speed in krpm	Mass flow rate in $\text{kg h}^{-1}$	Axial clearance in $\mu\text{m}$
Conditions for the experiment and the numerical tip clearance study with air					
<b>Air</b>	<b>200</b>	<b>0.96</b>	<b>168</b>	<b>5.29</b>	14.1 (pred.)
Conditions for the numerical tip clearance study with the anode off-gas (AO) based on a constant Mach number and a constant $\Phi$ with respect to the experiment					
AO	200	0.96	175.5	4.71	12.5 (pred.)

viscosity at 200 °C. The heat transfer model accounts for the fluid total energy. The advection scheme is high resolution for all differential equations. The shear stress transport model with a low turbulence intensity of 1 % at the inlet boundary accounts for the fluid turbulence. This model is the commonly used industry-standard for turbomachinery simulation. As mentioned before, a first cell  $y^+$  value of one for all simulation cases is selected, so as not to rely on wall functions to accurately simulate the boundary layer and possible separations.

A multiphase fluid model accounts for the composition of the anode off-gas. The fluids share the same static pressure and velocity field, but each fluid has a separate static temperature field. The simulation does not account for the heat exchange between the different fluids. The assumption of adiabatic mixing defines the fan outlet temperature. However, the anode off-gas consists of a mixture with very different gas densities:  $0.05 \text{ kg m}^{-3}$  for hydrogen,  $0.44 \text{ kg m}^{-3}$  for water vapor,  $0.68 \text{ kg m}^{-3}$  for carbon monoxide, and  $1.08 \text{ kg m}^{-3}$  for carbon dioxide at 200 °C and 0.96 bar. Thus, the Coriolis and centrifugal forces acting on the fluid particles are different, which the simulation does not account for (simulation considered a bulk fluid). In the case of the multi-phase anode off-gas simulation, each fluid features an independent static temperature field; hence, each fluid has different isentropic efficiency ( $\eta_{is}$ , eq. 2.61). In general, the lighter the fluid, the higher the isentropic total-to-total efficiency which is above 90 % for hydrogen at the design point.

Equation 2.61 calculates the isentropic efficiency with the mass-flow-averaged total inlet specific enthalpy, the total blade TE specific enthalpy, and the total blade TE isentropic specific enthalpy. The anode off-gas specific enthalpy,

$$\bar{h}_{off-gas} = \sum_j^4 \xi_j h_j \quad 4.11$$

is the sum of all four fluid enthalpies with respect to the mass ratios. The mass-flow-averaged

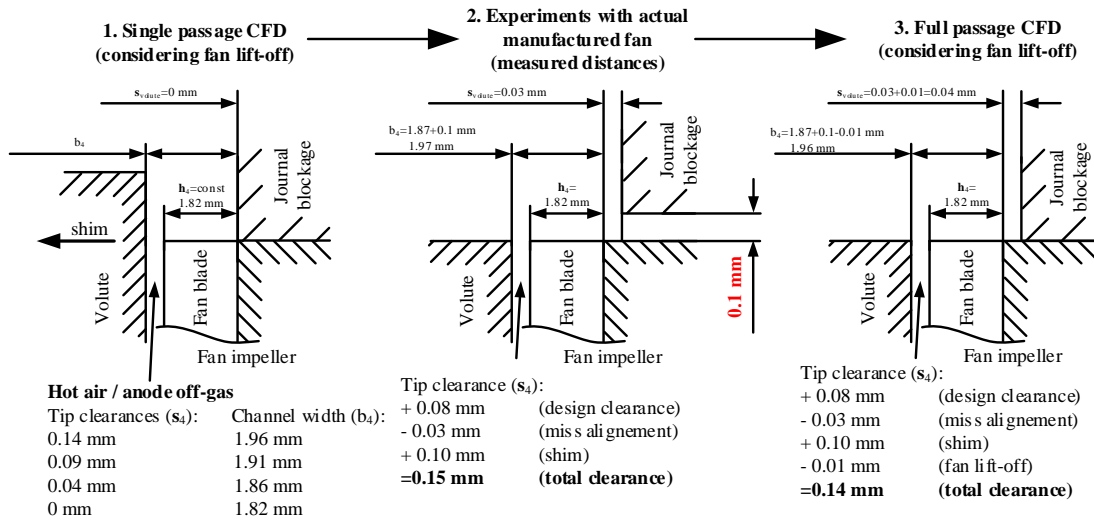


Figure 4.10 – Comparison of the blade and channel heights for (1) the single passage CFD simulation, (2) the experimentally investigated fan, and (3) the full passage CFD simulation.

enthalpies,

$$\eta_{is} = \frac{\bar{h}_{t,is,A} - \bar{h}_{t,in}}{\bar{h}_{t,A} - \bar{h}_{t,in}} \quad 4.12$$

evaluate the isentropic efficiency for both cases (hot air and anode off-gas).

**Pressure rise for hot air and anode off-gas:** Although the Mach number of both cases (hot air and anode off-gas) are the same, the pressure rise is lower for the anode off-gas case due to the lower heat capacity ratio ( $\kappa$ ). For hot air it is 1.4, whereas it is 1.3 for the anode off-gas. With the definition of the work coefficient ( $\psi$  in eq. 2.73), the total-to-total fan specific enthalpy increase can be calculated ( $\Delta h_{tt,fan} = \psi u_4^2 = \psi Ma^2 \kappa RT_t$ ), as can the total pressure at the fan outlet (section 8).

$$p_{t,8} = p_{t,2} \left[ 1 + (\kappa - 1) \psi Ma^2 \right]^{\eta_{is} \frac{\kappa}{\kappa-1}} \quad 4.13$$

With respect to this equation, a fan with a constant work coefficient ( $\psi$ ), a constant isentropic total-to-total efficiency ( $\eta_{is}$ ), and a constant Mach number ( $Ma$ ) achieves a higher pressure rise with a higher heat capacity ratio ( $\kappa$ ), and vice versa.

### Geometry comparison with the manufactured prototype

Figure 4.10 shows a comparison of the geometries used for the tip clearance analysis: (1) single passage CFD simulation, (2) the experimentally investigated fan, and (3) the full passage CFD

simulation that Section 4.4.5 describes in more detail. The design channel width at the blade TE is 1.9 mm and the design blade tip clearance is 0.08 mm. After the manufacturing and assembly process of the FTU, a “TESA Micro-Hite Plus M” measures all important dimensions. The fan impeller hub and the volute have a misalignment of 0.03 mm; hence, the actual channel width is reduced from 1.9 mm to 1.87 mm and the design blade tip clearance from 0.08 mm to 0.05 mm.

**Thrust gas film bearing axial clearance:** During operation, the channel width further decreases, due to the axial clearance of the thrust gas film bearing. Section 5.2 describes the measurement of this thrust bearing axial clearance in detail in the case of air at ambient conditions. Table 4.3 provides an overview of the predicted thrust bearing clearances for hot air and the anode off-gas. Due to size and temperature restrictions, this measurement is only possible without the mounted fan volute. During nominal operation with the fan volute, the thrust force increase (Section 4.6); hence, the thrust bearing clearance decreases. The bearing clearances listed in Table 4.3 are therefore the maximum expected values. At similar thrust force and rotational speed, the axial clearance of the thrust bearing is the lowest for the anode off-gas (lowest dynamic viscosity) and the highest for hot air. The difference in dynamic viscosity of air at ambient temperature ( $1.82 \cdot 10^{-5}$  Pa·s) and the anode off-gas at 200 °C ( $1.79 \cdot 10^{-5}$  Pa·s) is small. The thrust bearing clearance for ambient air without the mounted fan volute is therefore a good indication of the maximum axial clearance at design conditions with the anode off-gas. The maximum expected thrust bearing clearance for air at 200 °C is approximately 10 % higher than the measured thrust bearing clearance for ambient air (assuming similar thrust force and similar rotational speed). Both simulations are performed with an estimated thrust bearing axial clearance of 0.01 mm. Both the single passage, as well as the full passage, CFD simulations account for a blade tip clearance reduction of 0.01 mm. It is important to note that neither the full passage nor the single passage simulation account for the radial clearance between the fan impeller and the journal bearing blockage (0.1 mm, thick red value in the middle of Figure 4.10), which should be modeled as a free-slip wall section. At this location, a leakage flow, much lower than  $0.2 \text{ kg h}^{-1}$  at the design point, enters the fan impeller fluid domain. Section 5.4 provides more details on this leakage flow from the turbine through the housing towards the fan impeller fluid domain.

**Shimming versus trimming:** There are two different “philosophies” to investigate the blade tip clearance influence. The first, is the trimming approach. The channel width ( $b_4$ ) is constant, whereas the blade height ( $h_4$ ) changes from the perfect shrouded case ( $h_4 = b_4$ ) towards higher blade tip clearances ( $h_4 < b_4$ ). This approach is certainly the more choice, since the channel width is constant and, therefore, the fluid diffusion is also constant. However, this approach is costlier to implement experimentally, since for each new test case, an additional fan impeller is necessary. Another disadvantage of this approach is that the fan impeller manufacturing tolerance can lead to perturbation of the investigated tip clearance effect. Another possibility is the misalignment between the different fan impeller hubs and the volute, as Figure 4.10

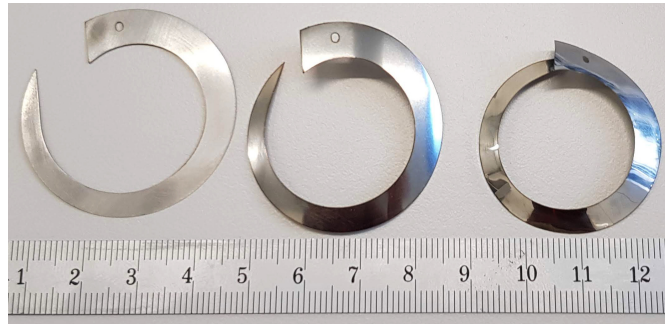


Figure 4.11 – The three different laser-manufactured shims available for the fan volute: 0.1 mm (left), 0.05 mm (middle), and 0.02 mm (right) with a slotted hole for shim and volute alignment.

shows. A precise alignment is challenging for small-scale machines and this can lead to different channel widths ( $b_4$ ).

A more effective way to investigate the blade tip clearance effect is the shimming approach. The experiments use the same fan impeller with a constant blade height ( $h_4$ ) and the volute moves further away, increasing the blade tip clearance, but also the channel width ( $b_4$ ) and therefore the impeller diffusion. Figure 4.10 shows the volute displacement on the left side, and the arrow marked with “shim” points in the negative  $z$ -direction. The volute moves further away with the help of thin, laser-cut shims. Figure 4.11 shows three of these shims with thicknesses of 0.1 mm, 0.05 mm, and 0.02 mm. Within this thesis, the fan volute uses the 0.1 mm shim. The actual running blade tip clearance is therefore  $0.08 - 0.03 + 0.10 - 0.01 = 0.14$  mm. This is a composition of the design blade tip clearance (0.08 mm), the fan hub-to-volute misalignment (-0.03 mm), the 0.1 mm shim, and the thrust bearing clearance at nominal conditions (-0.01 mm). The nominal relative blade tip clearance is therefore  $0.14/1.96 = 0.071$ .

### Blade shape design

The next subsection discusses the results of the blade clearance analysis in detail. A clearance of 0.04 mm, instead of the tested 0.14 mm, leads to a higher simulated total-to-total isentropic efficiency at the blade TE by 15 percentage points. The tip leakage losses are therefore dominant for this small-scale fan impeller. Suppressing and lowering these losses is beneficial for the fan efficiency. The tip leakage forms at the blade LE and the vortex stretches through the entire impeller domain. As mentioned in Sections 2.3.5 and 4.4.2, this blade tip clearance vortex forms due to the pressure difference between the blade SS and PS. A reduction of this pressure difference at the blade LE where the most dominant vortex starts reduces the intensity of the tip leakage vortex.

The fan total pressure rise over a certain blade length at the point (P) is zero, if the Euler work,

$$\Delta h_{tt,3,P} = c_{u,P} u_P - c_{u,3} u_3 \stackrel{!}{=} 0 \quad 4.14$$

is also zero. A blade that follows eq. 4.14 has therefore no total pressure rise. Assuming conservation of momentum ( $c_u r = \text{const.}$ ) and conservation of mass ( $2\pi r b c_m = \text{const.}$ ), the blade wrap angle ( $\theta$ ) for a zero-Euler-work blade,

$$\theta(r) = \frac{1}{2} \frac{u_3}{c_{m,1}} \left[ \left( \frac{r}{r_3} \right)^2 - 1 \right] - \frac{c_{u,3}}{c_{m,3}} \ln \frac{r}{r_3} \quad 4.15$$

is a function of the inlet conditions ( $c_{m,3}$ ,  $c_{u,3}$ ,  $r_3$ , and  $u_3$ ) [74]. In the case of no inlet swirl ( $c_{u,3} = 0$ ) and near-to-radial blades ( $dr \gg dz \rightarrow dm \approx dr$ ), the relation for the blade angle is obtained with eqs. 2.46 and 4.15 [74],

$$\beta_{blade}(r) \approx \arctan \frac{dr}{rd\theta} = \arctan \left[ \frac{r_3 c_{m,3}}{u_3 r} \left( \frac{2\theta c_{m,3}}{u_3} + 1 \right)^{-0.5} \right] \quad 4.16$$

and thus is only a function of the radius ( $r$ ), the LE radius ( $r_3$ ), the meridional velocity at the blade LE ( $c_{m,3}$ ), and the circumferential velocity at the blade LE ( $u_3$ ).

**Blade shape:** Figure 4.12 shows the blade angle ( $\beta_{blade}$ ) distribution at the fan hub that is equal to a blade span of zero (blue line with squares), at a blade span of 0.5 (blue line with dots), and at the shroud that is equal to a blade span of one (blue line with circles). The blade angle distribution of the first 22 % with respect to the meridional coordinate follows eq. 4.16 (blue line with squares in the lower graph of Figure 4.12). Within this region, the Euler work is therefore zero, and as a result, the total pressure rise is approximately zero.

The blue line with the hexagrams shows the blade angle distribution at the main blade LE. The blade angle varies therefore between  $36^\circ$  at the hub (radius of 3.7 mm) and  $30^\circ$  at the shroud (radius of 5 mm). The vertical black dotted lines mark the main blade LE at the hub and at the shroud, the splitter blade LE (with a constant  $\beta_{blade}$ ), as well as the main and splitter blade TE.

**Blade loading:** Figure 4.12 shows single passage CFD results of the fan impeller in the case with hot air at  $200^\circ\text{C}$  and a relative blade tip clearance of 0.071. The static pressure at the main blade, as well as at the splitter blade suction and pressure side (commonly referred to as the blade loading) are represented by red dots. At the hub surface (zero span) and at a span of 0.5, the static pressure is near-constant until the splitter blade LE at a radius of 6.35 mm (due to the zero-Euler-work blade design). Between the splitter blade LE and the blade TE, the pressure rises linearly within the fan impeller, which leads to a pressure difference between the blade suction and pressure side that is pronounced at a span of 0.5. The pressure difference at a span of 0.92 (relative blade tip clearance of 0.071) is within a few mbar at the radius of 5.5 mm. Figure 4.12 provides indications of the fluid flow at the main blade and splitter blade LE. Because of the blade LE thickness of 0.25 mm, the flow decelerates at the blade stagnation point leading to a high static pressure. On the blade suction surface a local separation forms with a low static pressure, since the flow cannot follow the rapid geometrical change of the



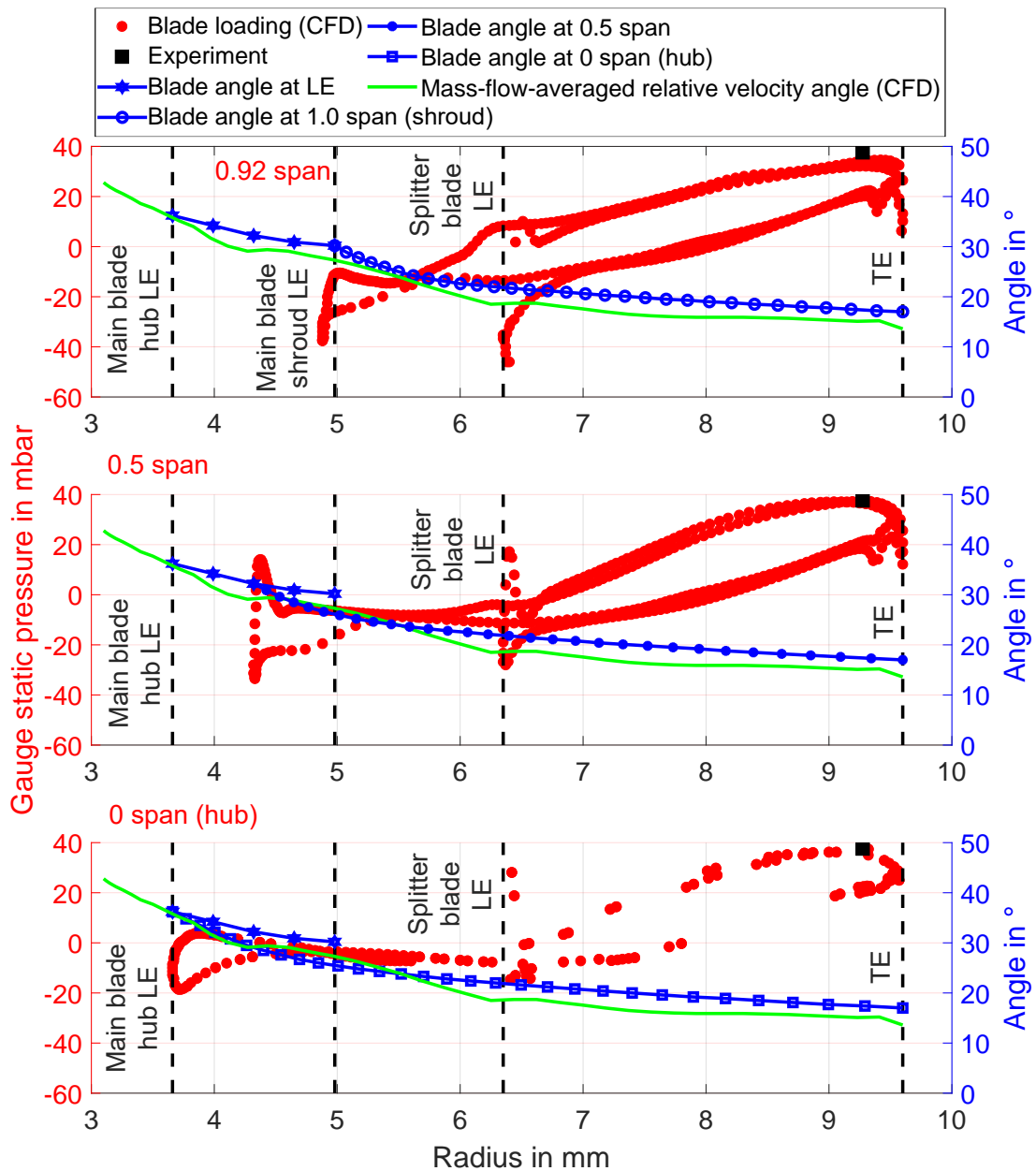


Figure 4.12 – Experimental static pressure measurement (black square) at the shroud (radius of 9.28 mm) and computational blade loading (red points) of a fan blade (the relative tip clearance is 0.071 and the tip is located at  $1 - 0.071 = 0.929$  span) at different spans: 0.92 span (upper graph), 0.5 span (middle graph), and zero span (lower graph). The blue line corresponds to the blade angle at different spans: 1.0 span (circles), 0.5 span (dots), and zero span (squares). The line with hexagrams corresponds to the blade angles at the fan leading edge (LE). The green line shows the mass-flow-averaged relative velocity angle ( $\beta$ ).

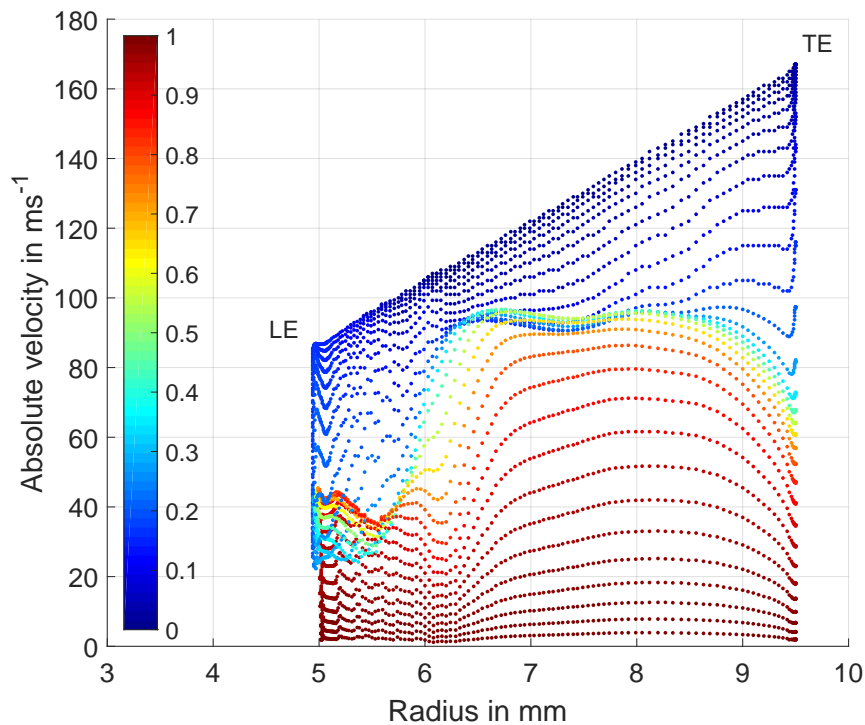


Figure 4.13 – Absolute velocity ( $c$ ) of hot air at  $200\text{ }^{\circ}\text{C}$  within the blade tip clearance at different spans (absolute blade tip clearance is  $0.14\text{ mm}$ ). At  $100\%$  blade tip clearance span, i.e., at the shroud surface, the velocity is zero because of the counter-rotating no-slip wall, whereas the velocity is equal to  $u = \omega r$  at the blade tip (i.e., at zero blade tip clearance span), because of the rotating no-slip wall.

blade LE. Figure 4.14 provides a comparison of this flow for: a) the single passage and b) the full passage simulation. Since the LE in the full passage simulation is blunt, this effect is more pronounced. On the blade PS, the pressure rises; hence, the pressure difference in this region is high (up to  $15\text{ mbar}$  at a blade span of  $0.92$ , as shown in the upper graph of Figure 4.12).

**Blade tip leakage:** Figure 4.13 shows the absolute velocity in the middle of the blade tip clearance (i.e.,  $0.5$  blade tip clearance span) represented by green dots, as well as for different spans within the blade tip clearance (between zero and one). At  $0.5$  blade tip clearance span, the highest leakage mass flow rate occurs. The absolute velocity ( $c$ ) decreases from  $44\text{ ms}^{-1}$  at the main blade LE to a minimal value of  $30\text{ ms}^{-1}$  at a radius of  $5.5\text{ mm}$  (minimum pressure difference between SS and PS), and then steadily increases towards a maximum absolute velocity of  $94\text{ ms}^{-1}$  at a radius of  $8\text{ mm}$ . There is a high pressure difference between the blade SS and PS at this last point. The decrease in absolute velocity at the blade LE is a result of the zero-Euler-work blade design, and limits the tip leakage mass flow rate, increasing the fan isentropic efficiency.

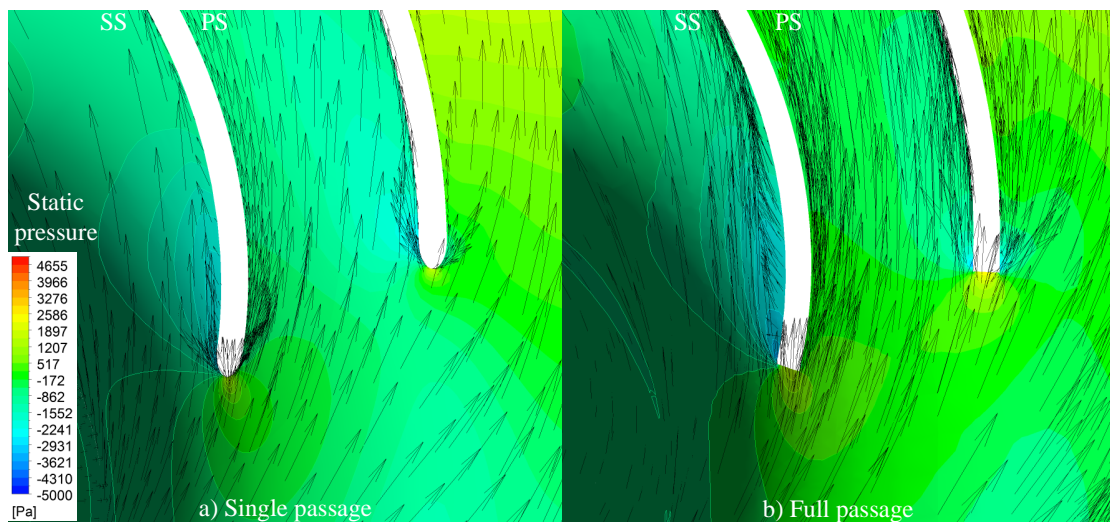


Figure 4.14 – Comparison of the static pressure and the relative velocity components (black arrows) that are tangential to the constant span surface at 0.5 span around the main and splitter blade leading edge for the a) single passage and b) full passage CFD simulation for air at 200 °C and a rotational speed of 168 krpm.

**Blade incidence and deviation:** Figure 4.12 also shows the mass-flow-averaged relative velocity angle ( $\beta$  as defined in eq. 2.44) as a continuous green line. A comparison of  $\beta$  with the blade angle leads to the incidence ( $i$  as defined in eq. 2.54) at the blade LE and the deviation ( $\Delta$  as defined in eq. 2.55) at the blade TE. At a span of 0.92 and 0.5, the incidence is thus positive and at +3°, whereas it is +0.5° at the hub. Upstream of the main blade LE at a span of 0.5 and in front of the splitter blade LE,  $\beta$  has an irregularity, since the flow conform to the blades. Downstream of the splitter blade LE, the relative velocity angle is always smaller than the blade angle, which leads towards a deviation of 3° at the blade TE.

**Comparison to the experiment:** The graph also features a comparison with experimental results. The manufactured fan volute features three pressure taps with a diameter of 0.4 mm at angular positions ( $\phi$ ) of 0°, 120°, and 240°. Figure 2.3 defines this angle  $\phi$  within the volute. Figure 4.4 shows the holes that are placed in the volute wall at a diameter of 18.55 mm. A low-frequency (3 Hz) pressure sensor measures the time-averaged static pressure at the fan shroud. The graph shows the average value of all three taps at different angular positions. The measured mean value of all three pressure taps (37.6 mbar) is 4.4 mbar higher than the line-averaged shroud static pressure at similar position (diameter of 18.55 mm), obtained from the single passage steady CFD simulation.

**Result discussion**

Table 4.4 lists the experimental results (Section 5.5), as well as the numerical results of the full passage CFD simulation (Section 4.4.5) and of the single passage CFD simulation. Both the numerical and experimental evaluations use air with an inlet total temperature of 200 °C, an inlet total pressure of 0.96 bar, an impeller rotational speed of 168 krpm, and an inlet mass flow rate of 5.29 kg h<sup>-1</sup>.

**Evaluation of parameters:** The fan inlet (section 1 as defined in Figure 2.3) and outlet temperature (section 8) are used to evaluate the experimental total-to-total pressure rise ( $\Delta p_{tt}$ ), the isentropic total-to-total efficiency ( $\eta_{is}$ ), the fan power (eq. 2.60), and the total-to-total temperature difference ( $\Delta T_{tt}$ ) with the assumption of an adiabatic system. Table 4.4 lists the respective measurement uncertainties. Appendix C provides more detail on the measurement uncertainty calculation and calibration of measurement devices. The experiment evaluates the total-to-static pressure rise between the machine inlet (1) and the fan TE (4). The single passage simulation evaluates this pressure rise between the nozzle inlet (1.1) and the fan TE

Table 4.4 – Comparison of experiment (Exp), full passage (FP) with volute, and single passage (SP) with virtual diffuser CFD simulations for hot air with a total inlet temperature of 200±0.5 °C, a total inlet pressure of 0.96±0.0005 bar, a rotational speed of 168±0.5 krpm, and a mass flow rate of 5.29±0.05 kg h<sup>-1</sup> with a TE diameter of 19.2 mm (constant  $h_4$  of 1.82 mm and  $\beta_{4,blade} = 17^\circ$ ).

	$s_4$ in mm	$b_4$ in mm	$\Delta p_{tt}$ in mbar	$\eta_{is}$ in %	$P_{fan}$ in W	$\Delta T_{tt}$ in K	$\Delta p_{tst}$ in mbar	$\Delta s^g$ in J kg <sup>-1</sup> K <sup>-1</sup>
Exp	0.14	1.96	(48.7) <sup>a</sup>	(51.7) <sup>a</sup>	18.8 ± 0.8 <sup>a</sup>	12.5 ± 0.5 <sup>a</sup>	37.6 ± 3.1 <sup>b</sup>	-
FP <sup>c</sup>	0.14	1.96	60.2 <sup>e</sup>	66.4 <sup>f</sup>	18.5 <sup>g</sup>	12.3 <sup>e</sup>	31.4 <sup>h</sup>	8.5
SP <sup>d</sup>	0.14	1.96	59.4 <sup>e</sup>	65.1 <sup>f</sup>	18.5 <sup>g</sup>	12.3 <sup>e</sup>	33.3 <sup>h</sup>	9.0
SP <sup>d</sup>	0.09	1.91	70.2 <sup>e</sup>	72.9 <sup>f</sup>	19.5 <sup>g</sup>	13.1 <sup>e</sup>	43.9 <sup>h</sup>	7.6
SP <sup>d</sup>	0.04	1.86	85.6 <sup>e</sup>	79.1 <sup>f</sup>	21.7 <sup>g</sup>	14.5 <sup>e</sup>	55.3 <sup>h</sup>	6.3
SP <sup>d</sup>	0	1.82	91.6 <sup>e</sup>	81.2 <sup>f</sup>	22.6 <sup>g</sup>	15.1 <sup>e</sup>	61.3 <sup>h</sup>	6.0

<sup>a</sup> Measured between the machine inlet (1) and machine outlet (8)

<sup>b</sup> Measured between the machine inlet (1) and fan blade TE shroud (4) at a diameter of 18.55 mm

<sup>c</sup> Evaluated between fan nozzle outlet (1.2) and fan blade TE: pressure loss inlet side test section consisting of bellmouth, inlet pipe, and fan inlet nozzle is 0.31 mbar

<sup>d</sup> Evaluated between fan nozzle inlet (1.1) and fan blade TE: pressure loss inlet test side section consisting of bellmouth and inlet pipe is 0.06 mbar

<sup>e</sup> Mass-flow-averaged parameter

<sup>f</sup> Evaluated with the mass-flow-averaged enthalpies according to eq. 4.12

<sup>g</sup> Sum of the impeller hub, impeller main and splitter blade torque around the rotational axis (z-axis) multiplied by the angular velocity ( $\omega$ )

<sup>h</sup> Mean pressure at the shroud surface at a diameter of 18.55 mm

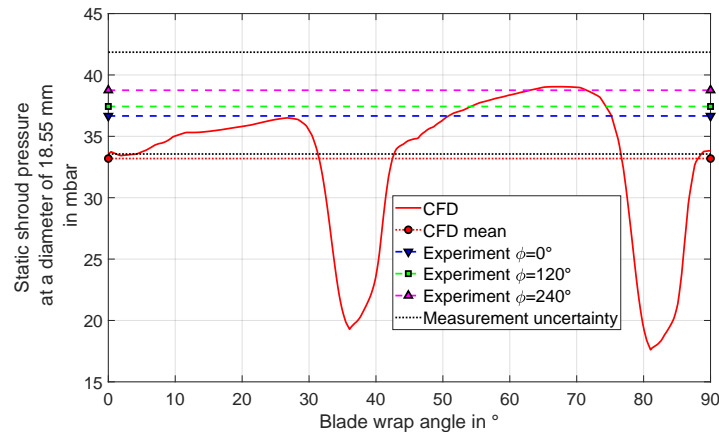


Figure 4.15 – Static pressure at the shroud wall (diameter of 18.55 mm) for air at 200 °C with a tip clearance of 0.14 mm obtained from CFD (red line), experimental measurements at a volute angle of  $\phi = 0$  (blue dotted line), 120° (green dotted line), and 240° (magenta dotted line) with a low-frequency pressure sensor (averaged value), and the mean value of the numerical pressure profile (red dotted line).

(4), whereas the full passage simulation evaluates it between the nozzle outlet (1.2) and the fan TE (4). However, the pressure loss within these sections is small: the loss from the bellmouth inlet to the nozzle inlet (1-1.1) is 0.06 mbar according to ISO 5167-3 norm [95], whereas it is 0.25 mbar within the fan nozzle (1.1-1.2) according to ISO 5801 norm [69].

**Experiment and simulation (hot air case):** Within the measurement uncertainty, the total-to-total temperature increase, as well as the fan power correlate well to the single and full passage CFD simulations. The numerical fan power calculation uses the torque sum of the fan hub, main and splitter blades around the rotational axis (z-axis). The difference in the total-to-static pressure rise ( $\Delta p_{t,st}$ ) is 6.46 mbar for the full passage CFD simulation and 4.46 mbar for the single passage simulation (accounting for the losses at the fan inlet side) and, therefore, relatively high. The full passage value is 17 % lower than the averaged experimental value. Figure 4.15 shows the wall pressure at the position of the experimental wall pressure taps at a diameter of 18.55 mm over the single passage (90°) for the experiments (dashed lines) with the minimum and maximum measurement error bands ( $p_{st,4,0^\circ} - 3.1$  mbar and  $p_{st,4,240^\circ} + 3.1$  mbar). Since the flow in the volute is accelerate, the static pressure decreases between the 240° and the 0° angular position. It also shows the numerical pressure profile (solid red line) and its average value (red dashed line). A full passage unsteady CFD simulation might capture the static shroud pressure measurement at the different angular positions more accurately.

However, the total-to-total pressure rise between the machine inlet (1) and outlet (8) ( $\Delta p_{tt,8,1}$ ) is 48.75 mbar for the experiment and 47.3 mbar for the full passage CFD simulation between the machine inlet (1) and the volute outlet (6). The volute features, therefore, a loss above 10 mbar at this point. This represents a difference of at least 1.5 mbar (measurement uncer-

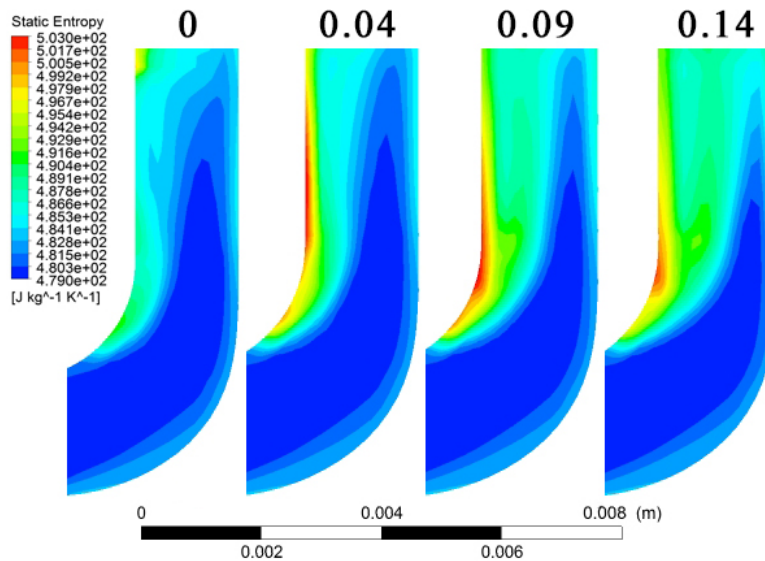


Figure 4.16 – Comparison of the entropy in the meridional view for the different cases with a 0 (left), 0.04 mm (second from left), 0.09 mm (second from right), and 0.14 mm (right) tip clearance in the case with air at 200 °C (constant blade height of 1.82 mm).

tainty is  $\pm 0.15$  mbar). The volute diffuser and outlet section (6-8) are not included in the full passage simulation. Assuming a total pressure loss of 1-2 mbar within these sections, the full passage and the experiment results are within 3 mbar.

Thus, the single passage CFD simulation is an effective tool for the preliminary fan design, since the time-consuming process of designing, meshing, and simulating the volute is eliminated. However, the pressure loss within the volute is quite significant at this low fan pressure rise. For the current design, the total pressure loss within the volute is 20 % of the total pressure at the fan TE (eq. 4.7).

**Hot air case:** Figure 4.16 shows the entropy for the different fan blade tip clearances with the imaginary case of zero and the three other cases: 0.04 mm, 0.09 mm, and 0.14 mm. The red color indicates high entropy, and thus high losses, whereas the blue color refers to the initial fluid entropy, and thus low losses. The separation at the blade LE due to the change from the axial to the radial direction is visible for all cases (green color with an entropy of  $490 \text{ J kg}^{-1} \text{ K}^{-1}$ ). The high entropy within the tip clearance is also visible (red color with an entropy of  $500 \text{ J kg}^{-1} \text{ K}^{-1}$ ). For the three tip clearance cases (0.14, 0.09, and 0.04), the recirculation from the main and splitter blade pressure side towards the main blade LE is significant.

With respect to the reference case with a blade tip clearance of 0.14 mm, the total-to-total fan pressure rise is 26.2 mbar higher for the 0.04 mm case. With the current tolerances and clearances available, the fan could theoretically operate with this tip clearance. However, a touch down of the blades at nominal speed leads to irreversible damage to the fan impeller

Table 4.5 – Comparison of single passage (SP) with virtual diffuser CFD simulations for the anode off-gas with a total inlet temperature of 200 °C, a total inlet pressure of 0.96 bar, a rotational speed of 175.5 krpm, and a mass flow rate of 4.71 kg h<sup>-1</sup> with a TE diameter of 19.2 mm (constant  $h_4$  of 1.82 mm and  $\beta_{4,blade} = 17^\circ$ ).

	$s_4$ in mm	$b_4$ in mm	$\Delta p_{tt}^g$ in mbar	$\eta_{is}^{g,l}$ in %	$P_{fan}^e$ in W	$\Delta T_{tt}^g$ in K	$\Delta p_{tst}^h$ in mbar	$\Delta s^g$ in J kg <sup>-1</sup> K <sup>-1</sup>
SP <sup>d</sup>	0.14	1.96	52.6	67.0	17.6	9.1	29.5	8.7
SP <sup>d</sup>	0.09	1.91	64.0	73.9	19.3	10.0	39.5	7.5
SP <sup>d</sup>	0.04	1.86	78.2	81.6	20.9	11.1	51.0	5.7
SP <sup>d</sup>	0	1.82	85.0	84.3	21.8	11.7	58.2	5.1

<sup>d</sup> Evaluated between fan nozzle inlet (1.1) and fan blade TE (full channel width  $b_4$ ): pressure loss inlet test side section consisting of bellmouth and inlet pipe is 0.06 mbar

<sup>e</sup> Sum of the impeller hub, impeller main and splitter blade torque around the rotational axis (z-axis) multiplied by the angular velocity ( $\omega$ )

<sup>g</sup> Mass-flow-averaged parameter

<sup>h</sup> Mean pressure at the shroud surface at a diameter of 18.55 mm

<sup>l</sup> Evaluated with the mass-flow-averaged enthalpies according to eq. 4.12

and the shaft. Within the first test campaign presented in this thesis, the author chose a tip clearance of 0.14 mm to mitigate possible risks. For the 0.09 mm tip clearance case, the total-to-total fan pressure rise is still 10 mbar than the reference value. This leads to a theoretical isentropic total-to-total fan impeller efficiency of 72.9 % and 79.1 % (0.09 mm and 0.04 mm cases, respectively).

**Anode off-gas case:** Table 4.5 provides data for the tip clearance analysis with the anode off-gas (mixture of carbon dioxide, carbon monoxide, hydrogen, and water vapor). The mesh and simulation setup are identical to the hot air case analysis. As suggested previously, the blade TE Mach number and flow coefficient are constant with respect to the simulation of the hot air case. This leads to a rotational speed of 175.5 krpm and a mass flow rate of 4.71 kg h<sup>-1</sup>. These parameters are slightly off-design, since the design mass flow rate is 4.78 kg h<sup>-1</sup> and the design rotational speed is 175 krpm. All other boundary conditions are similar (total inlet pressure of 0.96 bar and total inlet temperature of 200 °C). Equation 4.13 suggests that the total-to-total pressure rise is lower for the anode off-gas case, since the heat capacity ratio is 1.3 (and 1.4 for air). The simulated pressure rise is 52.6 mbar for the anode off-gas reference case (blade tip clearance of 0.14 mm). It is therefore 6.8 mbar lower than the hot air single passage reference case. As a result, the fan power and temperature increase are also lower. The isentropic efficiency calculated with eqs. 4.11 and 4.12 is slightly increased by 1.9 percentage points.

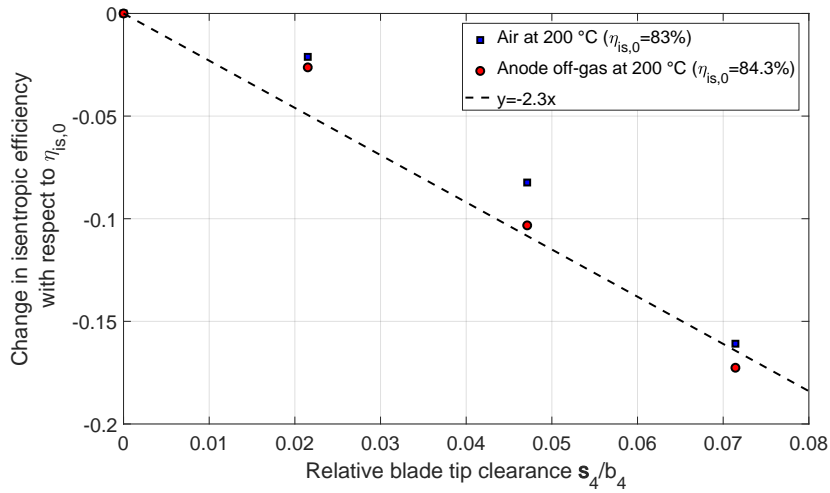


Figure 4.17 – Change of the fan isentropic total-to-total efficiency with respect to the “ideal” isentropic efficiency of a zero tip clearance fan for different relative blade tip clearances for the anode off-gas case (red dots) and the air case (blue dots), as well as a comparison to the tip clearance loss correlation from Pfleiderer with an experience coefficient ( $a_1$ ) of 2.3 (black dotted line).

**Comparison to initial fan design:** The design fan inlet total pressure is higher than the experimental value (1.05 mbar instead of 0.96 mbar). Scaling laws according to the ISO 5801 norm [69] allow for the calculation of the operating points, which are different than the actual measurements and the numerical simulations. If the difference of the pressure rise value between the two operating points is lower than 20 mbar, the simplified correlations from eqs. 2.69 to 2.71 are applicable. At the design point, the pressure rise would therefore be  $\frac{1.05}{0.96} \frac{4.71}{4.78} \left(\frac{175}{175.5}\right)^2 52.6 = 56.4$  mbar for the 0.14 mm case, and 83.8 mbar for the 0.04 mm case. However, the volute yields a pressure loss of more than 10 mbar; hence, the fan can achieve the design pressure rise of 70 mbar with a running tip clearance of 0.04 mm (design cold tip clearance is 0.05 mm) at design conditions (total inlet pressure of 1.05, rotational speed of 175 krpm, and mass flow rate of  $4.78 \text{ kg h}^{-1}$ ). Considering, that the experiment and CFD simulation with hot air show adequate correlation, the single passage CFD simulation for the anode off-gas should therefore also yield correlation. This verifies the design conditions of 70 mbar at  $4.78 \text{ kg h}^{-1}$  and 175 krpm, while considering a running tip clearance of 0.04 mm. However, the performance with the design tip clearance and with the anode off-gas were not tested experimentally; hence, the CFD simulations and design fan performance are not validated.

**Comparison hot air and anode off-gas case:** Figure 4.17 features a comparison of the change in isentropic efficiency with respect to the relative blade tip clearance ( $s_4/b_d$ ) using the nominal zero blade tip clearance case for both the anode off-gas (red points) and the hot air case (blue points). The effect of a more conventional relative blade tip clearance of 0.022 is not



as significant as for the other two investigated cases. For the 0.022 relative blade tip clearance, the experience coefficient ( $a_1$ ) in eq. 4.2 is one, whereas for the other two cases (i.e., 0.047 and 0.071), the experience coefficient is between 1.75 and 2.4. An experience coefficient of 2.3 (black dotted line) is a trade-off between the anode off-gas and hot air cases for the fan geometry that this section presents.

#### 4.4.5 Three-dimensional full passage simulation

Table 4.4 in the previous subsection summarizes the results of the experiment at nominal conditions with air at 200 °C, as well as the corresponding single passage and full passage CFD simulations. The fan power, total-to-total temperature increase, as well as the total-to-static pressure rise between the machine inlet and the fan TE correlate well. However, the pressure loss in the volute is significant (12 mbar); hence, the overall total-to-total pressure rise and, therefore, the isentropic total-to-total efficiency are not simulated accurately without considering the volute within the simulation.

A full passage simulation (consisting of all four single passages, as shown in Figure 4.7, and the fan volute) is therefore necessary to simulate the pressure losses within the fan volute. Thus, the computational domain consists of the entire fan impeller and volute domain. Since the generation of a structured mesh for the fan impeller and the fan volute is time-consuming, the author chooses to use an unstructured mesh for the same. This allows for a more flexible

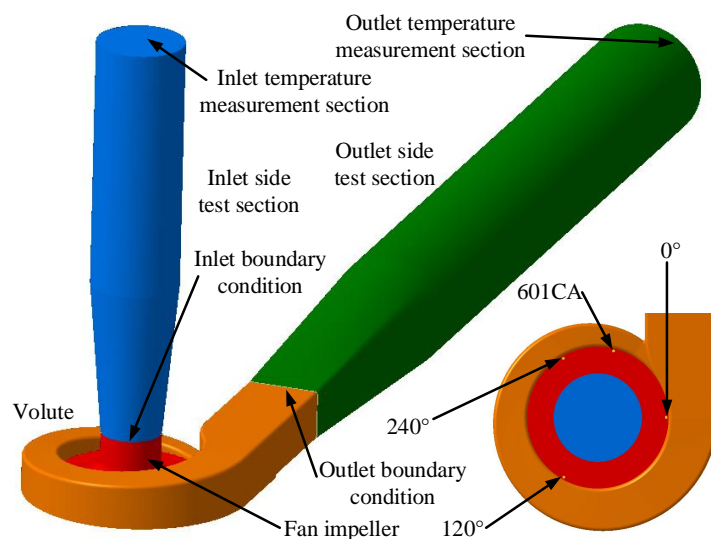


Figure 4.18 – Fluid domain of the measurement (blue, red, orange, and green), for the CFD (red and orange), and position of the pressure taps at the fan trailing edge (0°, 120°, 240°, and blade passing frequency measurement with the Kistler 601CA).

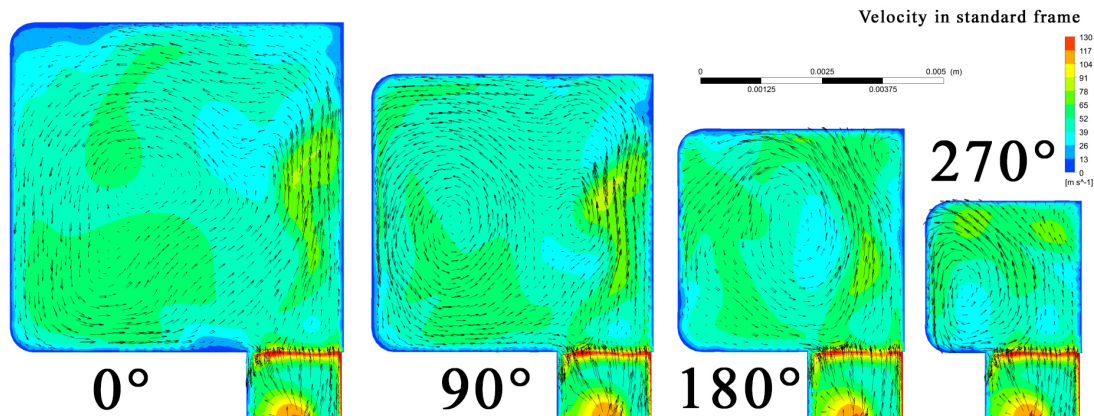


Figure 4.19 – Comparison of the velocity ( $c$ ) within the volute for different angles ( $\phi$ ) of  $0^\circ$ ,  $90^\circ$ ,  $180^\circ$ , and  $270^\circ$ .

mesh generation process. The full passage CFD simulation accounts, therefore, for several geometric details that the single passage CFD simulation does not account for, including:

- The blunt fan blade LE (instead of the elliptical LE in the single passage simulation).
- The cut-off fan blade TE (instead of the elliptical TE in the single passage simulation).
- The rotor-stator interface #2 between fan impeller and volute at exactly 19.2 mm; hence, fan section 4 and 4.1 are identical (the single passage simulation has this interface at a higher radius to facilitate the mesh generation, as shown in Figure 4.7).
- The fan impeller hub fillets with a radius of 0.2 mm caused by the manufacturing process (neglected within the single passage simulation).
- The misalignment between the fan impeller hub and the fan volute (Figure 4.10) that is on the order of 0.04 mm at the design point.
- The exact volute geometry.

Figure 4.18 shows the entire fluid domain between the fan inlet and outlet temperature measurement locations: the inlet side test section (blue), the full fan impeller (red), the fan volute (orange), and the outlet side test section (green). The CFD simulation uses an unstructured mesh with  $14.3 \cdot 10^6$  tetrahedron elements for the fan impeller and volute domain (red and orange). The geometry assumes a running clearance  $140 \mu\text{m}$  ( $150 \mu\text{m} - 10 \mu\text{m}$ ) at 168 krpm for all operating points. This  $140 \mu\text{m}$  blade tip clearance is resolved with three elements within the gap. The area-averaged  $y^+$  values of the volute, impeller hub, impeller shroud, and impeller blades are maintained below nine, seven, 12, and 5, respectively. The numerical setup is similar to the previously introduced single passage simulation with a few exceptions: no periodic boundary conditions are necessary, due to the full fan passage, the rotor-stator interface #1 is equal to the inlet boundary condition (inlet nozzle not included), and the outlet boundary condition is equal to the volute outlet (section 6 in Figure 2.3).

Table 4.4 summarizes the results at the nominal point and Section 5.5 compares the experi-

mental and numerical fan characteristic (Figure 5.12).

Figure 4.19 shows the absolute velocity within the fan volute at different positions ( $\phi$ ) as defined in Figure 2.3. The black arrows indicate the tangential absolute velocity component with respect to the cross section at  $0^\circ$ ,  $90^\circ$ ,  $180^\circ$ , and  $270^\circ$ . An anti-clock-wise recirculation forms within the fan volute that partially blocks the section at the fan TE (section 4). A classical overhung volute would decrease this blocking effect. The simple square volute allows for a manufacturing process exclusively using milling and turning operations. A casting process would allow for a more complex and efficient shape, such as an overhung volute. However, this work does not investigate such an option.

## 4.5 Radial-inflow turbine

This section introduces the turbine baseline design, the zero and one-dimensional model, as well as the three-dimensional CFD calculation based on a single passage and a full passage.

The radial-inflow turbine design is inspired by the work by Sato et al. [96, 97]. A low-reaction high-work turbine generator with a 10 mm diameter was demonstrated. At its design point and a rotational speed of 450 krpm, the turbine had a theoretical electrical power output of  $50W_{el}$  with an air supply on the order of 5-6 bar. Due to the lack of a thrust bearing, Sato et al. did not demonstrate the original design point. However, the  $30W_{el}$  off-design point at 360 krpm, with a pressure ratio of 3.35 and a mass flow rate of  $3.1 \text{ kg h}^{-1}$ , had an estimated turbine total-to-static isentropic efficiency of 47%. The prismatic blade height was 0.2 mm with an aspect ratio (span to radial chord length) of 0.2 and a non-running blade tip clearance of 0.02 mm.

### 4.5.1 Turbine specifications

**Design point:** Table 4.6 lists the design parameters of the radial-inflow turbine (case 1). The designed turbine uses water vapor with an inlet total temperature of  $220^\circ\text{C}$  and total pressure of 2.2 bar at section 4 (turbine inducer inlet in Figure 2.7) at the design conditions. The static outlet pressure at section 9 (turbine exducer outlet) is 1.0 bar, resulting in a total-to-total pressure ratio of 1.9, a mass flow rate of  $2.1 \text{ kg h}^{-1}$ , and a rotational speed of 175 krpm. The turbine provides the power for the gas film bearing mechanical losses that are 12.5 W at the design speed and the fan power of 20.9 W, considering the fan running blade tip clearance at the design point of 0.04 mm (Table 4.5). The verified analytical model (Figure 5.5) calculates the gas film bearing mechanical losses. The turbine should deliver 36 W at the design point.

**Experiments with water vapor:** During experimentation (Section 5.6), the turbine operated successfully with water vapor up to a maximum speed of 220 krpm. At a rotational speed of 173 krpm, a total-to-total pressure ratio of 1.9 and a steam mass flow rate of  $2 \text{ kg h}^{-1}$  were

## Chapter 4. Fan-Turbine Unit Design

Table 4.6 – Radial-inflow turbine parameters at the design point (CFD values in the first row) and experimentally measured parameters at off-design conditions.

Fluid	Case	Inlet total temperature in °C	Inlet total pressure in bar	Outlet static pressure in bar	Rotational speed in krpm
Water	(1)	220 <sup>a</sup>	2.2 <sup>a</sup>	1.0 <sup>c</sup>	175.0
Air	(2)	220.3 <sup>b</sup>	2.73 <sup>b</sup>	0.965 <sup>d</sup>	168.2
Fluid	Case	Turbine power in Watt	Mass flow rate in kg/h	Total-to-static isentropic efficiency in %	Type
Water	(1)	36 <sup>e,f</sup>	2.1 <sup>f</sup>	38 <sup>f</sup>	Design point
Air	(2)	39.9 <sup>g</sup>	2.86	39.2 <sup>h</sup>	Measurement

<sup>a</sup> At inducer inlet (section 4 in Figure 2.7), which leads to a pressure ratio of 1.9

<sup>b</sup> At inlet side test section (section 1)

<sup>c</sup> At exducer outlet (section 9)

<sup>d</sup> Ambient condition

<sup>e</sup> Expected turbine power with increased turbine blade tip clearance by 0.029 mm

<sup>f</sup> Expected design values

<sup>g</sup> Measured turbine power corrected with the heat dissipation of the bearing and shaft windage mechanical losses as described in Section 5.4

<sup>h</sup> Evaluated between inlet side test section (section 1) and outlet side test section (section 12)

measured between the turbine inlet at section 1 and the turbine outlet at section 12 (Table 6.1). However, the turbine outlet side test section was not insulated. A reliable turbine power and efficiency measurement using the inlet and outlet side test section total temperatures (turbine section 1 and 12, respectively) and the turbine inlet mass flow rate was only possible with a polytetrafluoroethylene (PTFE) tube that decouples the measurement section from the ambient, as well as a thick layer of glass fiber insulation. Such a measurement was conducted for a maximum rotational speed of 147 krpm (Section 5.6).

**Experiments with hot air:** A reliable measurement was conducted with hot air at a rotational speed of 168 krpm (96 % of the design speed, 175 krpm). Since the experimental and numerical turbine characteristic with hot air at a total inlet temperature of 220 °C (case 2 in Table 4.6) show reasonable agreement with the single passage CFD simulations (Section 4.5.4), Section 4.5.2 uses the verified hot air case that is close to the design rotational speed of 175 krpm to outline the design philosophy (velocity triangles) of the low-reaction radial-inflow turbine. This is case 2 in Table 4.6. Note that the turbine pressure ratio is higher due to a higher velocity of sound in the water vapor ( $545 \text{ m s}^{-1}$  at 220 °C) as compared to air ( $443 \text{ m s}^{-1}$  at 220 °C). Additionally, the dynamic viscosity of water vapor at 220 °C is  $1.70 \cdot 10^{-5} \text{ Pas}$ , whereas it is  $2.7 \cdot 10^{-5} \text{ Pas}$  for hot

air. The losses of the water-vapor-lubricated journal and thrust gas film bearings are  $1 - \frac{\mu_{\text{vapor}}}{\mu_{\text{air}}}$  lower than those for the air-lubricated bearings; hence, the design turbine power is lower for case 1 with water vapor.

#### 4.5.2 Turbine design summary

The turbine design of the FTU does not focus on achieving a high isentropic efficiency, but on achieving a high specific turbine power output with respect to the mass flow rate ( $\frac{P_{\text{turb}}}{\dot{m}_{\text{turb}}}$ ). This specific turbine power output has to be maximized, since the excess heat and, therefore, the available steam mass flow rate within the SOFC system is limited. Conversely, the pump power (pump component in Figure 3.1) is relatively low, due to the high fluid density of the water. A high turbine inlet pressure and, therefore, a high theoretically-achievable Mach number reduces the required turbine inlet mass flow rate. Such a turbine requires a carefully-designed Laval nozzle to accelerate the fluid beyond a Mach number of one. Another option is a multi-stage Parsons turbine design, such as in conventional steam turbines, a Tesla turbine design, and a Ljungström turbine design, which the author did not consider due to the complexity. The realized turbine design, therefore, uses a single convergent stator and achieves a Mach number of one within the stator throat at the design point. Due to the missing divergent part, the acceleration beyond a Mach number of one is limited. However, the wake at the stator TE acts as a diverging nozzle; hence, local Mach numbers up to 1.3 are possible. The specific turbine power increases further with a high turning angle, whereas the isentropic efficiency decreases with increasing turning angle according as in [98] (eq. 4.20), since the profile losses increase. Low-reaction turbines feature a high blade turning, and thus higher specific power, higher specific enthalpy difference, and lower isentropic efficiency compared to the nearly-optimal turbine design at a reaction of 0.5 [99].

The advantages of the **low-reaction turbine** are as follows:

- **High-power:** As mentioned before, low-reaction turbines feature a high turning angle, and thus a high specific power and a high specific enthalpy difference (but a lower isentropic efficiency).
- **Low thrust force:** Due to the low static pressure in the rotor-stator interface, the low turbine impeller hub static pressure leads to a low thrust force. For the current design, this turbine impeller thrust force is nearly-zero (Section 4.6), which is beneficial, since the FTU only features a single-sided thrust gas film bearing that is not capable of compensating for the turbine impeller thrust due to the static hub pressure (eqs. 4.32 and 4.33) and the fluid impulse of the turbine exhaust (eq. 4.37).
- **Partial-admission:** Due to the low static pressure in the rotor-stator interface, the low-reaction turbine is capable of operating as a partial-admission turbine. Advantage of the partial-admission design include increasing the turbine radius while the turbine blade height remains constant, increasing the blade height while the turbine radius remains

constant, or a combination of the two. A higher radius increases the turbine specific enthalpy (at constant rotational speed), whereas an increased blade height decreases the relative blade tip clearance, and thus increases the turbine isentropic efficiency (not considering partial-admission losses).

- **Low turbine-to-fan leakage rate:** Due to the low static pressure in the rotor-stator interface, the pressure difference between the turbine and the fan TE is lower, which leads to a lower water vapor leakage mass flow rate from the turbine side to the anode off-gas recirculation. The water vapor leakage dilutes the anode off-gas, and thus reduces the Nernst potential according to eq. 2.14, which leads to a lower stack and SOFC system efficiency (Section 3.6).
- **Low blade tip clearance leakage:** A low-reaction turbine design leads to a lower pressure difference between the blade SS and PS, which is favorable for a reduced tip leakage loss [100]. Since the turbine channel width is relatively small (0.7 mm) and the turbine blade tip clearance relatively high (0.133 mm), the relative blade tip clearance is high; hence, the tip leakage loss is the most pronounced secondary flow loss.

Due to the above, the author considers a low-reaction turbine design as the ideal choice for the FTU. Since the experiments measured only the turbine rotor-stator interface static pressure but not the total temperature (due to size constraints), the turbine reaction is estimated with the measured rotor-stator interface static pressure ( $p_{st,7}$ ) and the turbine inlet static pressure ( $p_{st,1}$ ).

$$\delta_p = \frac{p_{st,7} - p_{amb}}{p_{t,1} - p_{amb}} \quad 4.17$$

A high-specific-power turbine design uses a high blade turning and features, therefore, an elevated turbine rotor pressure loss. Thus, the objectives of minimizing the turbine reaction and maximizing the turbine specific power conflict.

**Classical turbine design:** Lewis [99] provides correlation for optimal turbine design in terms of the stage loading factor ( $\psi$ , eq. 2.73), the turbine reaction ( $\delta_h$ , eq. 2.82), and the stage flow factor ( $\Phi$ ).

$$\Psi_{opt} = 2\sqrt{\Phi^2 + 0.5 + \delta_h(\delta_h - 1)} = 2\sqrt{\left(\frac{c_{m,m,i}}{u_{m,i}}\right)^2 + 0.5 + \delta_h(\delta_h - 1)} \quad 4.18$$

Lewis defines the stage flow factor similarly to the previously defined flow coefficient (eq. 2.72) with the meridional velocity ( $c_{m,m}$ ) and the circumferential velocity on the mean radius ( $u_m$ ) at a certain turbine section (i). Assuming a reasonable flow coefficient of 0.8 (according to Lewis), and a turbine reaction of 0.15, the optimal stage loading coefficient is two; hence, the absolute velocity is half of the circumferential velocity at the rotor inlet. Water vapor at 220 °C has a velocity of sound of 545 ms<sup>-1</sup>. With respect to the fan design rotational speed of 175 krpm, a diameter of 29.7 mm could achieve a circumferential velocity of  $\frac{545 \text{ms}^{-1}}{2} = 272.5 \text{ms}^{-1}$ . Such a

high radius in comparison to the fan TE diameter (19.2 mm) leads to increased thrust forces (Section 4.6) and, therefore, to increased mechanical losses, and a low degree of admission (assuming a constant turbine power) featuring increased partial-admission losses.

**Design challenges:** The fan has a low pressure rise and relatively low blade tip Mach number, as well as a low rotational speed, which limits the turbine efficiency. The MOO of the entire system (Table 3.6) suggests operating the fan at relatively high specific speeds of 1.1, and thus low fan isentropic efficiency, in order to increase the turbine efficiency.

Therefore, the current turbine design does not operate in the optimal flow coefficient ( $\Phi_i$ ) range, which according to Lewis, is on the order of 0.5 to 0.8. Due to the low rotational speed, the flow coefficient and the stage loading coefficient are higher and the turbine isentropic efficiency is lower. The baseline design turbine has a flow coefficient of 1.3 based on the turbine rotor LE section and a stage loading coefficient of 3.2 based on the turbine rotor LE circumferential velocity for the design case with water at 220 °C and a rotational speed of 175 krpm. As mentioned before, such values are uncommon for classical turbines and result of the relatively low turbine rotor LE circumferential velocity ( $u_7$ ). The relative velocity at the turbine rotor blade LE ( $w_7$ ) is thus relatively high, which leads to increased profile losses and increased potential for flow separation. These losses are further amplified by the limits of manufacturing (i.e., relatively thick turbine rotor blade edges). Additionally, the turbine rotor blade tip clearance is relatively high and the turbine rotor blade height is relatively low (limits in manufacturing and assembling). This increases secondary flow losses, which the designer must carefully consider.

**Baseline design:** Table 4.7 lists all important turbine parameters and Figure 4.20 shows the absolute and relative velocities at different turbine sections, as defined in Figure 2.7 with respective angles defined in eqs. 2.44 and 2.45. A single passage CFD simulation (Section 4.5.4) determines all absolute and relative velocities.

**Volute (turbine section 3.1 to 4 as defined in Figure 2.7):** The absolute velocity at the turbine inducer inlet ( $c_4$ ) features a certain absolute flow angle ( $\alpha_4$ ) due to the turbine volute. The a tunnel type-volute consists of a half circle with a radius ( $R_{3,1}$ ) of 2 mm and a rectangular part with a height of  $2R_{3,1} = 4$  mm at turbine section 3.1 (Figure 4.21). The volute width is equal to the stator blade channel width ( $b_{3,1} = b_4 = b_5 = b_6 = 0.7$  mm) and is constant for the entire volute. The volute inlet area is therefore  $A_{3,1} = \frac{1}{2}R_{3,1}^2\pi + 2R_{3,1}b_4$ . The volute outlet is rectangular and features the same admission ( $\epsilon_a = \frac{13}{61}$ ) as the turbine stator. The volute outlet area is therefore  $A_4 = \epsilon_a 2r_4\pi b_4$ . In a first approximation, the absolute flow angle at the volute outlet ( $\alpha_4$ ) is independent of the fluid properties and is only a function of the volute inlet area ( $A_{3,1}$ ) and its radius ( $r_{3,1} = r_4 + R_{3,1}$ ) and the volute outlet area ( $A_4$ ) and its radius ( $r_4$ ), all radii with respect to the  $r_{turb}$  coordinate system (Figure 2.7).

$$\alpha_4 = \arctan\left(\frac{r_{3,1}}{r_4} \frac{A_4}{A_{3,1}}\right) = \arctan\left(\frac{r_{3,1}}{r_4} \frac{\epsilon_a 2r_4\pi b_4}{\frac{1}{2}R_{3,1}^2\pi + 2R_{3,1}b_4}\right) = 33^\circ \quad 4.19$$

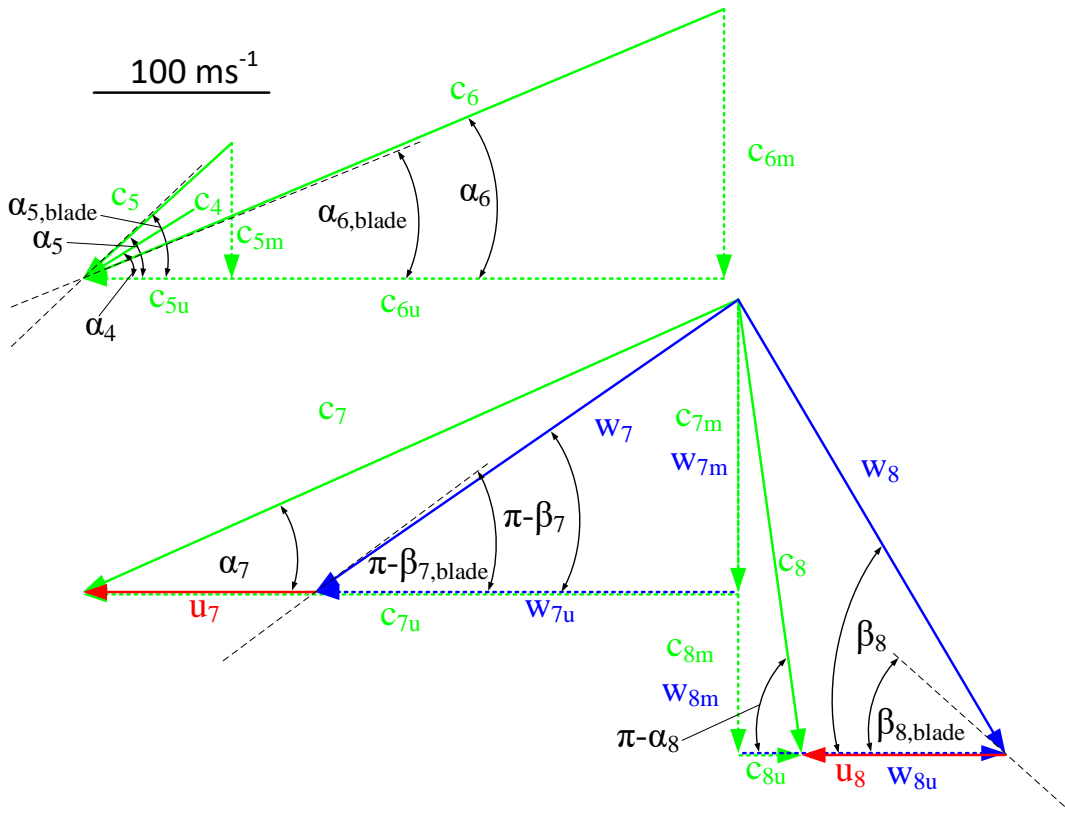


Figure 4.20 – Absolute velocity at the turbine inducer inlet (4), stator leading edge (5), and stator trailing edge (6), as well as velocity triangles with absolute velocity (green), relative velocity (blue), and circumferential velocity (red) for the turbine rotor leading edge (7) and trailing edge (8) in the case with air at 200 °C and a rotational speed of 168 krpm obtained from a single passage CFD simulation (mass-flow-averaged over entire channel width).

Numerical investigations of this turbine volute by Font [101] suggest a deviation of up to +1°; hence, eq. 4.19 is a good approximation for  $\alpha_4$ . The turbine volute is designed for constant angular momentum ( $rc_u = \text{const.}$ ) that yields a homogeneous distribution of the fluid to the turbine inducer (4). Thus, the radius of the tunnel-type volute between turbine section 3.2 and 3.1 (Figure 4.21) is a function of the volute angle ( $R(\Phi_{turb})$ ), whereas the width ( $b$ ) is constant. Figure 4.21 shows the manufactured turbine volute. The first part of the turbine volute is manufactured with a spherical milling tool. However, the size of the tool is limited to 0.5 mm, such that the last volute part (starting from section 3.2 in Figure 4.21) is manufactured with a planar milling tool and approximated linear surfaces.

**Inducer (turbine section 4 to 5):** Note that the absolute flow angle ( $\alpha$ ) is not constant between the turbine inducer inlet (section 4 in Figure 2.7) and outlet, nor at the turbine stator LE (5). Due to the relatively small channel width of 0.7 mm, the frictional losses of the turbine hub and shroud reduce the fluid momentum; hence, the absolute velocity circumferential



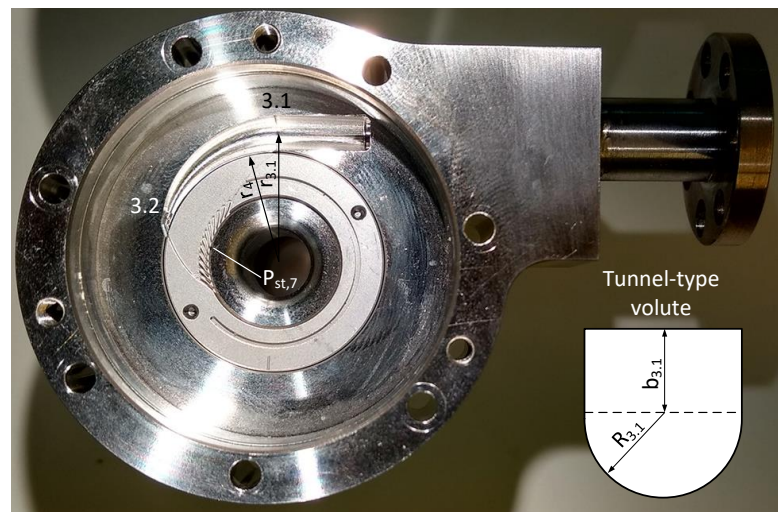


Figure 4.21 – The manufactured partial-admission turbine volute, the removable turbine stator (slightly misaligned in this photo), and the half circle static shroud pressure measurement tap at the rotor-stator interface ( $p_{st,7}$ ).

component does not strictly follow the  $rc_u = \text{const.}$  correlation. The flow angle increases between the turbine inducer inlet and the stator LE and is a function of the radius ( $\alpha(r)$ ). The turbine inducer sidewalls do not follow a logarithmic spiral. A single passage CFD simulation (Section 4.5.4) determines the exact sidewall geometry for the design point (water vapor at 220 °C). Figure 4.20 shows an example of air at 220 °C, where the absolute velocity flow angles increases from the initial 33° to 42.3° at the turbine stator LE; hence, the stator features an incidence of 1.4° at this operational point.

**Stator (turbine section 5 to 6):** The stator blade LE angle ( $\alpha_{5,blade}$ ) is 43.7°. The turbine stator turns the flow to 22.8° and accelerates it to Mach one. Since the stator TE blade angle ( $\alpha_{6,blade}$ ) is 22°, the stator features a deviation of 0.8° at this operational point. The deviation is relatively low, since the stator does not feature a blade tip clearance and the stator solidity is relatively high (2.42). The stator blade TE thickness is limited to 0.08 mm, due to manufacturing constraints. The stator blade height of 0.7 mm is also limited because of manufacturing: The 0.2 mm tool that mills the stator blades is limited to a length of 0.8 mm. The blade aspect ratio (blade height divided by radial chord length) is  $\frac{h_5}{r_5 - r_6} = 0.7$  and 0.36 using the actual blade chord length (from the blade LE and TE), which is 1.92 mm. The blade solidity based on the turbine stator TE (blade radial chord length divided by blade span at the blade TE) is  $\frac{r_5 - r_6}{2\pi r_6} 61 = 1.26$  and 2.42 using the actual chord length of 1.92 mm. The selected stator blade TE thickness and blade height are challenging to manufacture, and some stator blades show plastic deformation at the blade TE due to the manufacturing process (Figure 4.23 on the left). However, during operation, the forces (drag and lift) acting on the stator blades are negligible (<0.1 N). The turbine stator blade thickness and blade angle distribution is custom.

**Rotor (turbine section 7 to 8):** The turbine rotor blade thickness and blade angle distribution is based on the primary series National Advisory Committee for Aeronautics (NACA) profile

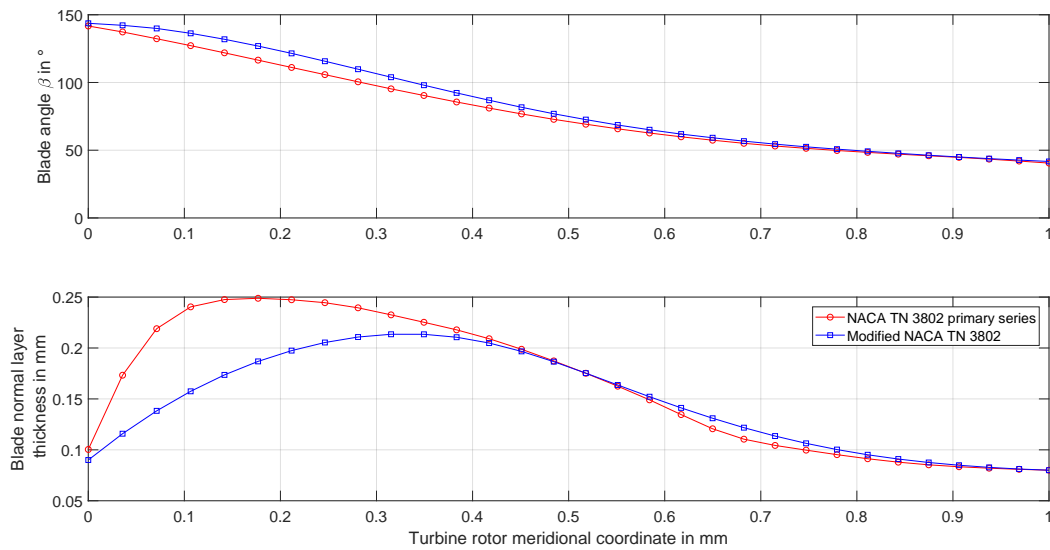


Figure 4.22 – The turbine rotor angle and thickness distribution for a blade turning of  $102^\circ$  using the NACA TN 3802 primary series and the modified NACA TN 3802.

from the technical note 3802 [102]. The technical note provides a thickness distribution on a mean chamber line, such that an infinite number of blade profiles could be generated by superimposing the thickness distribution and the chamber mean-line. The selected blade turning angle is  $102^\circ$  ( $\beta_{7,blade} - \beta_{8,blade}$ ), whereas the blade stagger angle is  $6.6^\circ$ . Figure 4.22 shows the original selected NACA profile (red dots) and the modified profile (blue squares). The original profile features the maximum normal layer thickness at the 20% chord location, whereas the maximum thickness of the modified profile is at the 35% chord location. The maximum normal layer thickness is reduced from the initial 0.25 mm to 0.21 mm. NACA technical note 3802 provides recommendations for the LE and TE radii. The LE radius divided by the chord length of 4.4% and the TE radius divided by the chord length of 1% are recommended. This would lead to a LE radius of 0.0445 mm and to a TE radius of 0.0101 mm. However, such small radii are not possible to manufacture with the selected method (milling). The forces during the manufacturing process are too high; hence, such thin blades would deform plastically (stator blade TE in Figure 4.23 on the left). Other manufacturing methods, such as laser manufacturing or chemical etching might achieve smaller radii than the selected methods. However, the author did not investigate these manufacturing methods, as the goal of the entire FTU is to design a unit with low manufacturing cost, and thus with the least possible number of different manufacturing processes. For the proposed turbine rotor blade design, the LE radius is 0.09 mm and the TE radius is 0.08 mm, nearly eight-times higher than the recommendation from the NACA technical note. The chosen radii and blade thickness are reasonable to manufacture with exclusively milling operations and without any plastic blade deformation, which is more critical for the turbine rotor than for the turbine stator, due to the centrifugal forces.

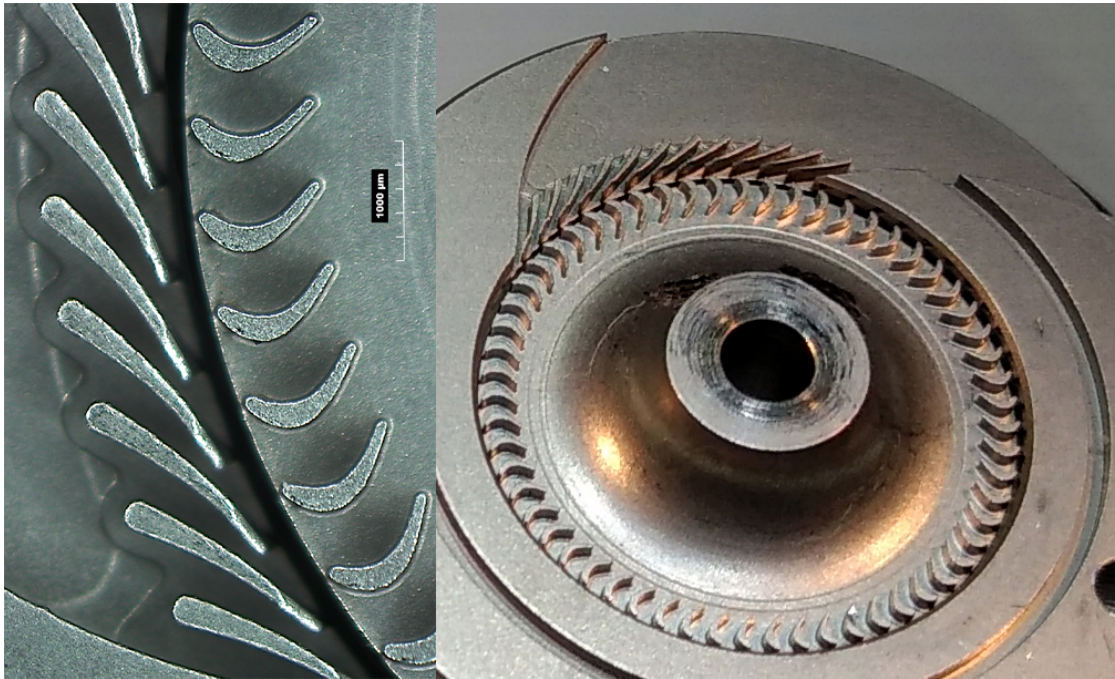


Figure 4.23 – Optical microscopy with Hirox KH-8700 (left) of the turbine stator and rotor (digitally mirrored) and overview of turbine stator and rotor (upside-down) with turbine inducer (right).

The turbine blade design is therefore challenging for three primary reasons. Firstly, the high power density requires high blade turning. Secondly, the relative Mach numbers at the rotor LE is relatively high due to a high stage loading factor. Thirdly, the acceleration at the turbine rotor LE is high due to a relatively high LE radius, which was limited due to manufacturing constraints. The original NACA primary profile from technical note 3802 [102] leads to increased separation at the rotor blade SS and PS (depending on the blade incidence), as well as to a rapid acceleration and deceleration at the blade LE. To limit these negative effects, the author shifted the maximum normal layer thickness from the initial 20 % chord location to 35 % (Figure 4.22 on the bottom). In addition the thickness was reduced from the initial 0.25 mm to 0.21 mm, and the blade turning at the turbine LE was decreased (Figure 4.22 on the top).

In the case with air at 220 °C, the mass-flow-averaged absolute velocity at the turbine rotor LE is  $409 \text{ m s}^{-1}$ , which corresponds to a Mach number of 1.03. The (mass-flow-averaged) absolute velocity flow angle ( $\alpha_7$ ) is 23.9° and, therefore, 1.1° higher than the absolute velocity angle at the stator TE ( $\alpha_6 = 22.8^\circ$ ), due to the hub and shroud frictional losses. This leads to a relative velocity flow angle ( $\beta_7$ ) of 145.4°. Figure 4.20 shows the  $\pi - \beta_7$  angle (34.6°) as 1.7° smaller than the actual turbine rotor blade LE angle ( $\pi - \beta_{7,blade} = 36.3^\circ$ ). The turbine is designed for zero incidence at a rotational speed of 175 krpm and using water vapor.

As designed, the turbine rotor blade tip clearance is 0.114 mm and the turbine blade height

## Chapter 4. Fan-Turbine Unit Design

Table 4.7 – Geometrical parameters of the radial-inflow turbine (turbine sections 1 to 12 as defined in Figure 2.7).

<b>Inlet (1) and inlet nozzle (2, round)</b>				<b>Channel width (<i>b</i>)</b>			
$d_1 = d_2$	6.00 mm	$l_{3,2}$	11.4 mm	$b_7 = b_8 = 0.7 \text{ mm} - s_{miss}$			
<b>Volute inlet (3, round)</b>				<b>Blade tip clearance (<i>s</i>)</b>			
$R_3$	2 mm	$l_{3,1,3}$	21 mm	$s_{design}$	0.114 mm		
<b>Volute (tunnel-type, 3.1-4)</b>				$s_{actual}$	0.133-0.143 mm (zero to nominal speed) (increased due misalignment)		
<b>Turbine backface clearance (<i>s</i>)</b>							
Tunnel type volute inlet (3.1)				$s_{back}$	0.115-0.105 mm (zero to nominal speed)		
$R_{3.1}$	2 mm	$h_{3.1}$	0.7 mm	<b>Turbine hub and stator hub (reference) misalignment(<i>s</i>)</b>			
Tunnel type volute outlet (3.2)				$s_{miss}$ -0.019 to -0.029 mm (zero to nominal speed)			
$R_{3.2}$	0.56 mm	$h_{3.2}$	0.7 mm	<b>Turbine rotor and stator axial clearance (<i>s</i>)</b>			
<b>Turbine inducer (4-5)</b>				$s_{axial}$	0.125 mm		
Inducer inlet (4)				<b>Exducer outlet (9) on hub (<i>h</i>) and shroud (<i>s</i>)</b>			
$r_4$	13.00 mm	$h_4$	0.7 mm	$d_{9h}$	5.6 mm	$d_{9s}$	8.00 mm
<b>Turbine stator (5-6)</b>				<b>Diffuser inlet (10)</b>			
Stator leading edge (5)				$d_{10}$	8 mm	$l_{11,10}$	20.8 mm
$\alpha_{5,blade}$	43.7°	$t_5$	0.25 mm	<b>Diffuser outlet (11) and outlet (12)</b>			
$r_5$	8.65 mm	$h_5 = b_5$	0.70 mm	$d_{11} = d_{12}$ 12.00 mm			
Stator trailing edge (6)							
$\alpha_{6,blade}$	22°	$t_6$	0.08 mm				
$r_6$	7.65 mm	$h_6 = b_6$	0.70 mm				
Chord	1.92 mm	Chamber	1.93 mm				
Stagger angle		58.6°					
$z_{stator}$	12	(out of 61)					
Admission of $\frac{12+1}{61} = 0.213$							
<b>Turbine rotor (7-8)</b>							
Rotor leading edge (7)							
$\beta_{7,blade}$	143.7°	$t_7$	0.09 mm				
$r_7$	7.50 mm	$h_7$	0.586 mm				
Rotor trailing edge (8)							
$\beta_{8,blade}$	41.7°	$t_8$	0.08 mm				
$r_8$	6.50 mm	$h_8$	0.586 mm				
Stagger angle		6.6°					
Chord	1.01 mm	Chamber	1.24 mm				
$z_{rotor}$	59						

is 0.586 mm (Table 4.7). However, the turbine side faces alignment difficulties similar to the fan side that Section 4.4.4 discusses in detail. Although the FTU uses a turbine adjustment

shim (part 14 in Figure 4.1), alignment to the micrometer is challenging. The turbine and the stator hubs feature a misalignment of -0.019 mm at zero speed and -0.029 mm at design conditions. The stator hub and rotor hub misalignment increases with increasing rotational speed, since the thrust bearing axial clearance increases. Consequently, both the turbine rotor channel width and the turbine rotor blade tip clearance increase up to 0.71 mm and 0.143 mm, respectively, with increasing speeds up to 168 krpm, which leads to a relative blade tip clearance ( $\frac{s_{actual}}{b_7}$ ) of 0.20. The high relative turbine blade tip clearance increases the turbine secondary flows, such as the tip leakage flow. This flow from the blade PS to the SS increases the turbine rotor deviation. The rotor TE mass-flow-averaged relative flow angle ( $\beta_8$ ) is 59.5° and, therefore, 17.8° higher than the blade TE angle ( $\beta_{8,blade} = 41.7^\circ$ ). The turbine rotor deviation is 12° when considering only the mass-flow-averaged velocity of the full turbine blade height and 4.3° when considering the surface between zero and 0.5 span. The selected number of turbine rotor blades (59) is a trade-off between this deviation loss, the blade profile losses, and the partial-admission losses. A high blade number is beneficial for a low deviation and for low partial-admission losses, but increases the profile losses. The selected blade solidity based on the turbine rotor TE (blade radial chord length divided by blade span at the blade TE) is  $\frac{r_7-r_8}{2\pi r_8} 59 = 1.44$  and 1.46 using the actual chord length of 1.01 mm.

**Exducer and diffuser (turbine section 8 to 11):** The turbine exducer hub and shroud are based on circular surfaces with a radius of 3.275 mm and 2.35 mm, respectively. The flow within a full-admission exducer would be accelerated, since the area at the exducer inlet ( $\pi (d_{9s} + 2.35\text{ mm}) b_8$ ) is higher than the area at the exducer outlet ( $\pi (d_{9s}^2 - d_{9h}^2)$ ). However, the partial-admission exducer ( $\frac{13}{61}$ ) expands the flow, which leads to a diffusion. The turbine rotor TE is thus designed in such way that the flow exits the rotor in a nearly 90° angle to limit the swirling motion of the flow, and thus the losses. As stated before, the circumferential velocity component  $c_{u8}$  does not follow the  $r c_u = \text{const.}$  correlation, due to the frictional hub and shroud losses. A low  $c_{u8}$  component is therefore beneficial to reduce the total pressure losses within the turbine exducer. At the exducer outlet, two sudden expansions occur: first, at the end of the turbine nut (part 06 in Figure 4.1 with a 5.6 mm diameter) and second, after the shaft screw (part 04 with a 2.27 mm diameter). Although these two sudden expansions cause a pressure loss, the concept helps to facilitate the unit assembly and balancing process. At the machine outlet (section 10 to 11), the flow diffuses in a diffuser from a 8 mm diameter to a 12 mm diameter. The diffuser length is 20.8 mm.

### 4.5.3 Zero and one-dimensional simulation

For the turbine pre-design, zero and one-dimensional models are essential to obtain the baseline geometry.

**One-dimensional model:** Soderberg [98] describes a loss correlation for turbines at optimal load coefficient according to the Zweifel criterion [103] at zero incidence, a Reynolds number based on the hydraulic diameter of the throat section ( $Re_{d_h}$ ) of  $10^5$ , an aspect ratio defined with the blade height and the radial blade chord ( $\frac{h}{r_7-r_8}$ ) of three, a blade maximum thickness to radial chord ratio ( $\frac{t_{max}}{r_7-r_8}$ ) of 0.2, and a deflection lower than 120°. The “nominal” loss

coefficient,

$$\zeta_n = 0.04 + 0.06 \left( \frac{\frac{\pi}{2} - \alpha_7 + \frac{\pi}{2} - \alpha_8}{\pi \frac{100}{180}} \right)^2 \quad 4.20$$

is a function of the blade deflection. If the aspect ratio or the Reynolds number differ from the conditions above, Soderberg provides a correlation to adapt the nominal loss coefficient for both rotor and stator.

$$\zeta_{stator} = 1 - (1 + \zeta_n) \left( 0.993 + 0.021 \frac{r_7 - r_8}{h} \right) \left( \frac{10^5}{Re_{d_h}} \right)^{0.25} \quad 4.21$$

$$\zeta_{rotor} = 1 - (1 + \zeta_n) \left( 0.975 + 0.075 \frac{r_7 - r_8}{h} \right) \left( \frac{10^5}{Re_{d_h}} \right)^{0.25} \quad 4.22$$

This Reynolds number ( $Re_{d_h}$ ) definition is equal to eq. 2.64, but with the hydraulic diameter ( $d_h$ ) instead of the turbine tip diameter ( $D$ ). This hydraulic diameter of the throat section at the rotor TE is based on the channel depth ( $\frac{\pi d_8}{z_{rotor}} \cos \beta_{8,blade}$ ) and the rotor blade height ( $h_8$ ).

$$d_h = \frac{2 \frac{\pi d_8}{z_{rotor}} \cos \beta_{8,blade} h_8}{\frac{\pi d_8}{z_{rotor}} \cos \beta_{8,blade} + h_8} \quad 4.23$$

The total-to-static isentropic efficiency is thus a function of the rotor (eq. 4.21) and stator loss coefficient (eq. 4.22), as well as the turbine total-to-total enthalpy difference ( $\Delta h_{tt}$ ).

$$\eta_{is,tst} = \frac{1}{1 + \frac{1}{2\Delta h_{tt}} (\zeta_{rotor} w_8^2 + \zeta_{stator} c_7^2 + c_8^2)} \quad 4.24$$

For the design point, water vapor with a total inlet pressure of 2.2 bar, a total inlet temperature of 220 °C, a static outlet pressure of 1 bar, and a rotational speed of 175 krpm, the CFD simulation (Section 4.5.4) predicts a total-to-static isentropic efficiency of 42.6 % at the turbine rotor TE and 37.5 % at the turbine section 9. Using the values obtained from CFD ( $Re_{d_h}$ ,  $\Delta h_{tt}$ ,  $w_8$ ,  $c_7$ , and  $c_8$ ) and the correlation from Soderberg (eq. 4.24), the isentropic total-to-static efficiency is determined to 42.4 %, indicating sufficient accuracy.

**Zero-dimensional model:** Similarity concepts by Balje [2] (figure 5.44 for partial-admission turbines with low reaction) based on the specific speed and specific diameter suggest an isentropic total-to-static efficiency of 60 %. The blade tip clearance to blade height ratio in Balje's figure 5.44 is 0.02, but is 0.244 for the actual manufactured and tested FTU. For such a high ratio, Balje suggests multiplying the efficiency with a correction factor ( $1.025 - \frac{0.10}{0.08} 0.244$ , figure 5.31 based on  $n_s = 0.08$  [2]) of 0.72, resulting in an isentropic efficiency of 43.2 %. Additional losses occur due to the thick TE and LE to blade height ratio that of 0.15. Balje suggests a correction of 0.87 ( $1.02 - 1 \cdot 0.15$ , figure 5.32 based on  $n_s = 0.08$  [2]) for thick blade edges, which results in an isentropic efficiency of 37.6 % that is on the order of the CFD (37.5 %) and (extrapolated) experimental values (Figure 5.15).

Therefore, the author concludes that the one-dimensional loss correlations by Soderberg

[98] and the zero-dimensional similarity concepts by Balje [2] with the blade tip clearance and blade edge corrections are both viable for small-scale turbine pre-design based on the mean-line analysis and similarity concepts, respectively

Another important parameter for this analysis that is difficult to determine a priori is the turbine discharge coefficient. The measured value for the nominal point with hot air at 220 °C, which is 0.76 that is relatively low, whereas the single passage CFD simulation suggests a value of 0.92. Section 4.5.4 discusses possible reasons for the relatively high blockage of the turbine stator (e.g., partial-blockage of the turbine stator with particles, plastic deformation of stator blades).

Besides the losses within the rotor and stator, additional losses occur in a partial-admission turbine.

**Pumping loss:** The non-admission arc of the steam turbine pumps the fluid towards the wall, which causes a certain loss. These pumping losses are, according to Roelke (chapter 8 in [100]),

$$P_{pumping} = a_5 \bar{\rho} u_m^3 h^{1.5} d_m (1 - \epsilon_a) \quad 4.25$$

a function of the pumping-power loss experience coefficient ( $a_5 = 5.92 \text{ m}^{-0.5}$ ), the mean density in the turbine rotor ( $\bar{\rho} = \frac{\rho_7 + \rho_8}{2}$ ), the rotational speed at the mean-line ( $u_m$ ), the diameter at the mean-line ( $d_m$ ), and the turbine degree of admission ( $\epsilon_a$ ). Since this correlation is applicable for classical axial steam turbines, it uses the mean parameters (eq. 2.47). In the case of the radial-inflow turbine, the author assumes the mean diameter to be  $d_m = \frac{d_7 + d_8}{2}$  and the mean circumferential velocity to be  $u_m = \frac{d_7 + d_8}{4} \omega$ . Roelke also states that “the effects of blade height and diameter on the pumping-power loss are quite uncertain, as evidenced by variations in the exponents on these terms” [100]. The effect of the blade number ( $z_{rotor}$ ) is also unclear [100]. Thus, no reliable analytical equation is therefore available. The full passage three-dimensional steady simulation (Section 4.5.5) with air at ambient temperature for a rotational speed of 150 krpm suggests a power of 32.2 W (13.248 W) for the admission section and a power of -0.2 W for the non-admission section, which corresponds to the pumping loss (Figure 4.27). Thus, this loss is 0.6 % of the turbine power and, therefore, significantly lower than the analytical value from eq. 4.25 (1 W). The author suspects that eq. 4.25 overpredicts the pumping loss for such a small-scale radial-inflow turbine with a low aspect ratio.

**Filling and emptying loss:** The second type of partial-admission turbine losses results from the filling and emptying effects. When the non-admission part of the turbine enters the active sector with admission, a stagnant flow is inside the rotor passage. The high-momentum fluid from the turbine stator (up to Mach 1.3 at the design point) must accelerate this stagnant flow. This scavenging continues until the full blade channel is in the active sector. After the blade channel leaves the active sector, the amount of high-momentum fluid entering one blade channel decreases, which leads to diffusion of the flow. According to Stenning [104], this loss,

$$P_{filling,emptying} = \dot{m}_1 \frac{d_7}{z_{rotor} 3 d_6 \epsilon_a} c_{u,8} u_8 \quad 4.26$$

is a function of the rotor blade pitch ( $\frac{\pi d_7}{z_{rotor}}$ ), the nozzle active arc length ( $\pi d_6 \epsilon_a$ ), and the rotor exit momentum ( $c_{u,8} u_8$ ). A low blade pitch, i.e., a high number of rotor blades ( $z_{rotor}$ ), is therefore beneficial for reducing the emptying and filling losses, but it also increase the profile losses. According to eq. 4.26, this loss is very low and on the order of 0.1 W.

### 4.5.4 Three-dimensional single passage simulation

The geometry and mesh generation, as well as the setup for the turbine CFD simulation is similar to the previously described simulation of the fan (Section 4.4.4). Figure 4.24 shows the simulation domain that consists of the turbine inducer (Figure 4.23 on the top right), the turbine stator, the turbine rotor, and the turbine exducer until the change in radius from 2.8 mm to 1.135 mm, which corresponds to the shaft screw diameter (part 04 in Figure 4.1). The turbine nut (part 06 in Figure 4.1) is modeled as round, although it features a hexagon for tightening and is partly damaged due to the balancing process (Figure D.1).

As listed in Table 4.7, the stator has 12 blades and features an admission of  $\frac{12+1}{61} = 0.21$ . The single passage simulation features a periodic boundary condition for each domain, thus in total there were  $4 \cdot 2 = 8$  periodic boundary conditions. Although the actual turbine rotor features 59 rotor blades, for the CFD simulation the rotor has 61 blades to realize a frozen rotor interface between the stator and rotor with no pitch change (rotor-stator interface #1 in Figure 4.24). The rotor pitch in the simulation is therefore 3.3 % smaller than the pitch of the actual turbine rotor.

Since the simulation accounts only for one passage, the pumping effect of the non-admission turbine blades is not taken into account. According to analytical correlations from eq. 4.25, these losses are 1.5 W at the nominal point (168 krpm) with air at a total inlet temperature of 220 °C and a total inlet pressure of 2.7 bar. Since the ideal turbine power of the single passage simulation is 48.2 W (13·3.71 W), these pumping losses correspond to 3 %. However, the author expects this loss to be lower (Section 4.5.5). Only a full passage simulation can model the non-admission blade pumping effect, and thus this loss mechanism (Section 4.5.5). Only a full passage transient simulation can model the filling and empty loss of the partial-admission turbine, which is according to eq. 4.26 0.1 W (0.2 % of the ideal power of 48.2 W) for the current geometry at the nominal point with hot air. Another limitation of the simulation is the fact that the blade row at the beginning of the admission has a lower isentropic efficiency and thus a lower power compared to the central blade rows (Figure 4.27).

The inlet boundary condition (turbine section 4) is the total pressure and the total temperature, as well as the absolute flow angle ( $\alpha_4 = 33^\circ$ ) that is a result of the turbine volute geometry. The turbine inlet from turbine section 1 to 4 is assumed to be adiabatic, and thus the total temperature is constant between the position of the turbine inlet total temperature measurement at section 1 (Figure 2.7) and section 4. The pressure loss between section 1 and 4 is taken into account with analytical correlations (9 mbar for hot air at nominal conditions). The outlet boundary condition (turbine section 9) is the area-averaged static pressure; hence, the mass flow rate through the passage is the result of the simulation. As for the inlet section, the



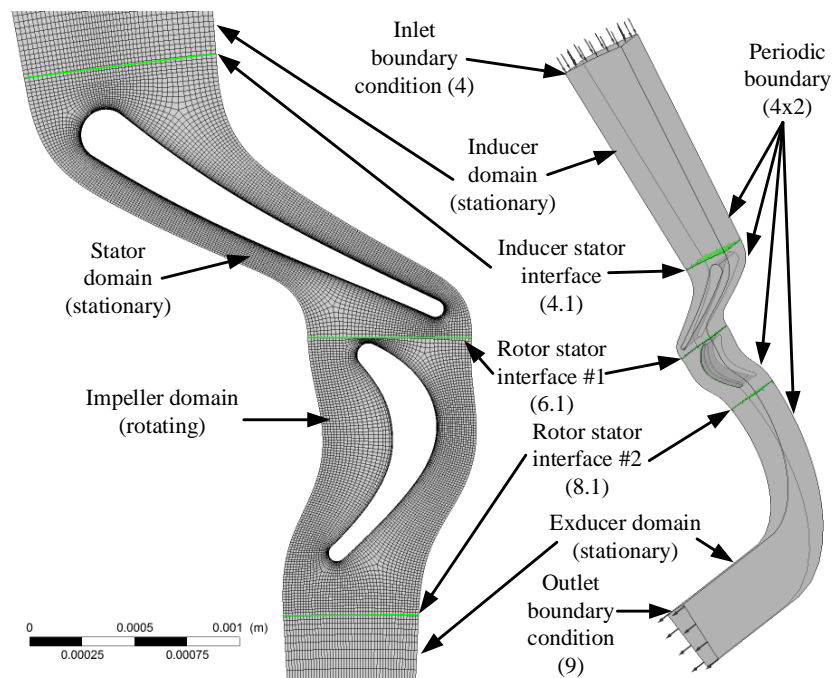


Figure 4.24 – Domain regions (right): inducer, stator, rotating turbine impeller, and exducer domain from the top to the bottom, and generated mesh (left) at the hub for each domain from the bottom view. The fluid-to-fluid interfaces are marked green.

outlet boundary condition takes the pressure loss between section 9 and 12 using analytical correlations into account (sudden expansion and frictional loss, 22 mbar for hot air at nominal conditions). The stationary exducer domain hub assumes a rotating wall with the rotational speed of the rotor domain. The simulation does not account for the axial misalignment at the design speed of  $-0.029$  mm between the turbine impeller hub and the stator hub (Section 4.5.2).

### Hot air at 168 krpm

Table 4.8 provides a comparison between the single passage CFD simulation and the experiment with a total inlet temperature of  $220.3 \pm 0.5$  °C, a total inlet pressure of  $2.73 \pm 0.003$  bar, an ambient pressure of  $0.97 \pm 0.0005$  bar, and a rotational speed of  $168.2 \pm 0.5$  krpm. The outlet total temperature is 170.5 °C within the CFD simulation, whereas it is 193.1 °C in the experiment, which corresponds to a temperature difference of 22.6 °C. The following effects contribute to this difference:

(1) Assuming a fan inlet temperature of 200 °C (oven temperature is at 200 °C) and a distance of 45 mm between the fan impeller and the turbine impeller, the theoretical maximum fan-to-turbine heat flux is 0.4 W (neglecting the heat transfer coefficients at the fan and turbine

## Chapter 4. Fan-Turbine Unit Design

Table 4.8 – Comparison of the single passage turbine CFD and the experiment (exp.) in the case with air at a total inlet temperature of  $220.3 \pm 0.5$  °C, a total inlet pressure of  $2.73 \pm 0.003$  bar, an ambient pressure of  $0.97 \pm 0.0005$  bar, and a rotational speed of  $168.2 \pm 0.5$  krpm.

	Mass flow rate in $\text{kg h}^{-1}$		Power in W		Mechanical loss in W
	Actual	Corrected	Actual	Corrected	
Exp.	$2.86 \pm 0.01$	-	$22.1 \pm 0.5^b$	$39.9 \pm 0.5^d$	17.8
CFD	$13 \cdot 0.264 = 3.43$	$2.86^a$	$13 \cdot 3.71 = 48.2^c$	$40.2 \pm 0.2^e$	-

	Outlet total temperature in °C		Isentropic efficiency in %		Rotor-stator static pressure in bar
	Actual	Corrected	Actual	Corrected	
Exp.	$193.1^f$	$171.6^g$	$21.8^b$	$39.2^d$	$1.23^j$
CFD	-	$170.5^h$	-	$38^i$	$1.36^k$

<sup>a</sup> Assuming the same mass flow rate as measured in the experiment

<sup>b</sup> Evaluated with total temperatures at machine inlet (1) and machine outlet (12) and the mass flow rate at the machine inlet (1)

<sup>c</sup> Number of stators (13) multiplied by the sum of the turbine impeller hub and impeller blade torque around the rotational axis (z-axis) multiplied by angular velocity ( $\omega$ )

<sup>d</sup> Corrected with the dissipated heat from the bearing and windage mechanical loss ( $P_{turb,exp,corrected} = 22.1 \text{ W} + 17.8 \text{ W}$ )

<sup>e</sup> Corrected with the experimentally measured mass flow rate ( $P_{turb,CFD,corrected} = 48.2 \cdot \frac{2.86 \text{ kg h}^{-1}}{3.43 \text{ kg h}^{-1}} \pm 48.2 \cdot \frac{0.01 \text{ kg h}^{-1}}{3.43 \text{ kg h}^{-1}}$ )

<sup>f</sup> Experimentally measured total temperature at the machine outlet section (12)

<sup>g</sup> Expected total temperature at the turbine rotor outlet (8) that is not measured

<sup>h</sup> Mass-flow-averaged total temperature at turbine section 9

<sup>i</sup> Mass-flow-averaged between the exducer outlet (9) and the inducer inlet (4)

<sup>j</sup> Evaluated with a half circle (radius of 0.15 mm) at a diameter of 15.3 mm at the turbine shroud (Figure 4.25)

<sup>k</sup> Line-averaged value at the shroud at a diameter of 15.18 mm, corresponding to the diameter that divides the half circle pressure tap into two equal surface areas

side).

$$\dot{Q}_{turb,fan} = \frac{\lambda_c}{d} \pi (r_{sh,fan2}^2 - r_{sh}^2) \Delta T = \frac{15}{0.045} \pi (0.004^2 - 0.002^2) (200 - 170.5) \text{ W} = 0.4 \text{ W} \quad 4.27$$

This accounts for the shaft diameter on the fan side ( $r_{sh,fan2} = 4$  mm) and the internal shaft diameter ( $r_{sh} = 2$  mm). A possible heat flux inside the shaft screw (part number 04 in Figure 4.1) with a diameter of 1.25 mm is 0.05 W. This leads to a total theoretical maximum heat flux within the shaft of 0.45 W (0.4 + 0.05 W).

(2) The heat dissipation by the shaft windage and bearing mechanical losses is 17.8 W, which consist of: turbine backface disk friction loss, shaft windage losses, losses in the two journal

bearings, losses at the fan backface, and losses in the thrust bearing. The model from Daily and Nece [105] for regime III (laminar flow, separate boundary layers) calculates the turbine backface disk friction losses. The model from Schiffmann (chapter 3.5.4 in [12]) calculates the remaining losses, assuming a fully turbulent flow for shaft windage. Section 5.4 provides more information about the exact loss calculation and Section 5.3 provides run-out tests that realize the indirect measurement of the combined losses.

For the operational point at 168.2 krpm the model suggests a mechanical power loss and thus heat dissipation of 17.8 W, which is 43-times higher than the possible heat conduction from fan-to-turbine (eq. 5.8). IT is also on the same order as the measured turbine power (22.1 W) and fan power (19.0 W). The fan power experimental measurement, full passage, and single passage CFD simulations show good correlation (Table 4.4). All pipes and FTU housing have thick insulation with glass fiber tape (Figure 5.11), and thus the heat flux to the oven environment is expected to be low. Thus, the author assumes that all the dissipated heat crosses the turbine fluid domain. The corrected experimental turbine power is thus the measured value plus the calculated value accounting for the heat dissipation, which is 39.9 W (22.1 + 17.8 W). The sum of the measured fan and calculated shaft power is 3.1 W lower than the corrected turbine power ( $P_{turb,exp,corrected} - P_{mech} - P_{fan,exp} = 39.9 - 17.8 - 19$ ). The reason for this could be the measurement uncertainty of the fan power ( $\pm 0.8$  W), the measurement uncertainty of the turbine power ( $\pm 0.5$  W), the uncertainty of the mechanical loss calculation, or heat conduction to the environment.

The measured mass flow within the experiment is  $2.86 \text{ kg h}^{-1}$  and the result of the single passage simulation is  $13 \cdot 0.264 = 3.43 \text{ kg h}^{-1}$ , which corresponds to a difference of  $0.57 \text{ kg h}^{-1}$  (16.7 % of the mass flow rate from the CFD simulation) or 2.2 of the 13 turbine stator passages ( $\frac{0.57}{0.264}$ ). The reasons for this are listed by decreasing influence below:

- The turbine stator was partially blocked by particles (ceramics from the oven and glass fibers from the insulation, which penetrated the system during the test rig assembly process).
- The actual manufactured stator blade thickness is higher, due to limitations in manufacturing (bending of the milling tool with a diameter of 0.2 mm and a length of 0.8 mm, and plastic deformation of the stator trailing edge due to the milling forces). This leads to a measured minimum distance between two stator rows of 0.18-0.23 mm, whereas it is 0.23 mm in the CFD simulation. The critical area within one stator row of the manufactured prototype is therefore 0-22 % smaller than the original geometry (Figure 4.23 on the left).
- Both turbine inducer side endwalls with a length of 8 mm (Figure 4.23) feature a boundary layer displacement thickness of 0.04 mm. This results in a partial blocking of the first and the last stator blade row on the order of 17 % and thus in an overall blockage of all stator blades on the order of 2.7 %. The single passage CFD accounts for the turbine

inducer hub and shroud end wall effects (but not for the two sidewalls).

- The manufactured stator vanes have a roughness based on the arithmetical mean deviation (Ra) of 0.002 mm, resulting in a 1.2 % lower critical area.

The four facts listed above could be the reason for a higher mass flow rate, and thus a higher power in CFD simulations. In order to compare the single passage CFD simulation to the experiment, the author uses the specific power output of the CFD simulations.

$$P_{CFD,corrected} = \frac{P_{CFD}}{\dot{m}_{CFD}} \dot{m}_{exp} \quad 4.28$$

Table 4.8 provides both the corrected power measurements for the CFD simulation according to eq. 4.28 (40.2 W) and the measured power corrected with the heat dissipation from the mechanical shaft losses of 17.8 W (39.9 W  $\pm$  0.5 W). The difference is therefore between 0 and 0.8 W. The single passage CFD simulation has the following limitations:

- The steady simulation cannot fully capture the unsteady rotor-stator interaction that results in a time-varying turbine power output, due to the turbine rotor blade and stator wake interaction (according to Font [101], the time-averaged turbine power is 1.2 W lower for the nominal point with hot air at 168 krpm).
- Partial-admission losses due to pumping, as well as blade channel filling and emptying are not considered and cause increased losses that are most likely on the order of 0.3-1.6 W (eqs. 4.25 and 4.26).
- A possible heat conduction from the fan to the turbine could lower the experimentally measured turbine power (according to eq. 5.8 on the order of 0.4 W).
- A possible heat conduction from the turbine outlet side test section piping (section 11 to 12 in Figure 2.7) to the oven environment could lower the experimentally measured turbine power on the order of 0.3 W assuming 10 layers of glass fiber tape insulation with a thickness of 0.7 mm and a thermal conductivity of 0.045 W m<sup>-1</sup> K<sup>-1</sup> (neglecting the heat transfer coefficients inside and outside the pipe, as well as the metallic tube conductivity).

$$\dot{Q}_{oven} = \frac{T_{oven} - T_{12}}{\frac{\ln \frac{D_{12} + 20t_{insulation}}{D_{12}}}{\lambda_c \cdot 2 \cdot \pi \cdot l_{12}}} = \frac{200 - 193.1}{\frac{\ln \frac{15 + 10 \cdot 0.7}{15}}{0.045 \cdot 2 \cdot \pi \cdot 0.1}} \text{ W} = 0.3 \text{ W} \quad 4.29$$

Although the corrected power and efficiency of the experiment and the CFD simulations show good correlation, it becomes clear that an exact experimental measurement or numerical simulation is challenging due to the thermal effects, the manufacturing and assembly tolerances, and the unsteady effects involved within a (partial-admission) turbine. Sato et al. [96] stated for the experimental measurement of a 10 mm diameter turbine: “Determining the adiabatic efficiency of the turbine was challenging as there is heat transfer from the generator via conduction and convection and not all thermodynamic states or the direct turbine shaft power could be measured.”

The rotor-stator static pressure from the experiment (1.23 bar) is 0.13 mbar lower than to the CFD simulation (1.36 bar). A decrease of the static outlet pressure decreases the rotor-stator static pressure and increases the turbine power. The correct determination of the outlet boundary condition (static pressure) is therefore challenging, since only the ambient pressure (at section 12 in Figure 2.7) is measured and the pressure losses between section 9 and 12 are estimated with analytical correlations.

Table 4.9 – Comparison of the single passage turbine CFD and the experiment (exp.) in the case with water vapor at a total inlet temperature of  $220.1 \pm 0.5^\circ\text{C}$ , a total inlet pressure of  $1.83 \pm 0.003$  bar, an ambient pressure of  $0.96 \pm 0.0005$  bar, and a rotational speed of  $147.0 \pm 0.5$  krpm.

	Mass flow rate in $\text{kg h}^{-1}$		Power in W		Mechanical loss in W
	Actual	Corrected	Actual	Corrected	
Exp.	$1.55 \pm 0.12$	-	$16.5 \pm 1.3^b$	$24.8 \pm 1.3^d$	8.3
CFD	$13 \cdot 0.134 = 1.75$	$1.55^a$	$13 \cdot 2.01 = 26.13^c$	$23.3 \pm 1.79^e$	-

	Outlet total temperature in $^\circ\text{C}$		Isentropic efficiency in %		Rotor-stator static pressure in bar
	Actual	Corrected	Actual	Corrected	
Exp.	$196.1^f$	$189.3^g$	$29.8^b$	$40.6^d$	$1.07^j$
CFD	-	$191.4^h$	-	$30.7^i$	$1.05^k$

<sup>a</sup> Assuming the same mass flow rate as measured in the experiment

<sup>b</sup> Evaluated with total temperatures at machine inlet (1) and machine outlet (12) and the mass flow rate at the machine inlet (1)

<sup>c</sup> Number of stators (13) multiplied by the sum of the turbine impeller hub and impeller blade torque around the rotational axis (z-axis) multiplied by angular velocity ( $\omega$ )

<sup>d</sup> Corrected with the dissipated heat from the bearing and windage mechanical loss ( $P_{turb,exp,corrected} = 16.5\text{ W} + 8.3\text{ W}$ )

<sup>e</sup> Corrected with the experimentally measured mass flow rate ( $P_{turb,CFD,corrected} = 26.13 \cdot \frac{1.55\text{ kg h}^{-1}}{1.75\text{ kg h}^{-1}} \pm 26.13 \cdot \frac{0.12\text{ kg h}^{-1}}{1.75\text{ kg h}^{-1}}$ )

<sup>f</sup> Experimentally measured total temperature at the machine outlet section (12)

<sup>g</sup> Expected total temperature at the turbine rotor outlet (8) that is not measured

<sup>h</sup> Mass-flow-averaged temperature at turbine section 9

<sup>i</sup> Mass-flow-averaged between the exducer outlet (9) and the inducer inlet (4)

<sup>j</sup> Evaluated with a half circle (radius of 0.15 mm) at a diameter of 15.3 mm at the turbine shroud (Figure 4.25)

<sup>k</sup> Line-averaged value at the shroud at a diameter of 15.18 mm, corresponding to the diameter that divides the half circle pressure tap into two equal surface areas

### Water vapor at 147 krpm

In summary, the water vapor case had several limitations in comparison to the previous hot air case (Section 5.6) and was more challenging for the following reasons:

- Control of the shaft rotational speed with the membrane pump was slower and more inaccurate.
- Membrane pump delivered pulsating flow; hence, the shaft rotational speed changed within  $\pm 1$  krpm over time.
- Less accurate turbine inlet mass flow rate measurement.
- Condensation of water vapor in the pressure lines.
- Partial blockage of the turbine stator (especially for rotational speeds higher than 150 krpm), due to a particles.

As mentioned in Section 4.5.1, a correct (with sufficient insulation) and steady turbine measurement was performed only up to a rotational speed of 147 krpm for water vapor, whereas the design rotational speed is 175 krpm. The CFD simulation is therefore compared to the measured point at 147 krpm (Section 5.6). Table 4.9 lists the results for both the experiments and the CFD simulation. The correction method is similar to Section 4.5.4 for the case with hot air.

The rotor-stator static pressure of the experiment (1.05 bar) and of the simulation (1.07 bar) show good agreement within 0.02 bar. The experimentally measured admission based on eq. 4.17 is therefore 12.5 %, while the simulated admission is 10.5 %.

For the water vapor case, the membrane pump KNF SIMDOSE 10 controlled and measured the turbine inlet mass flow rate. Since its precision is 2 % full scale, the mass flow rate and, therefore, the turbine power could not be determined as precisely as in the hot air case that used a Coriolis mass flow meter. The uncertainty of the measured mass flow rate was  $\pm 0.12 \text{ kg h}^{-1}$ . The experimental turbine power was  $16.5 \pm 1.3 \text{ W}$ . The analytical calculated bearing and shaft losses are 8.3 W; hence, the corrected experimental turbine power is 24.8 W ( $16.5 \text{ W} + 8.3 \text{ W}$ ). The corrected simulated turbine power is 23.3 W. The difference between the corrected experimental turbine power (24.8 W) and the corrected simulated turbine power (23.3 W) is thus 1.5 W. The sum of the measured fan power, the corrected turbine power, and the calculated shaft power is 4.5 W ( $P_{turb,exp,corrected} - P_{mech} - P_{fan,exp} = 24.8 - 8.3 - 12.0$ ), suggesting a higher deviation than for the previous hot air case (deviation of 3.1 W).

The exact power and efficiency measurement at off-design conditions was therefore challenging, due to the unknown heat flux towards the turbine or the fan. The water vapor case was measured at off-design conditions with respect to the rotational speed (i.e., 147 krpm instead of 175 krpm).

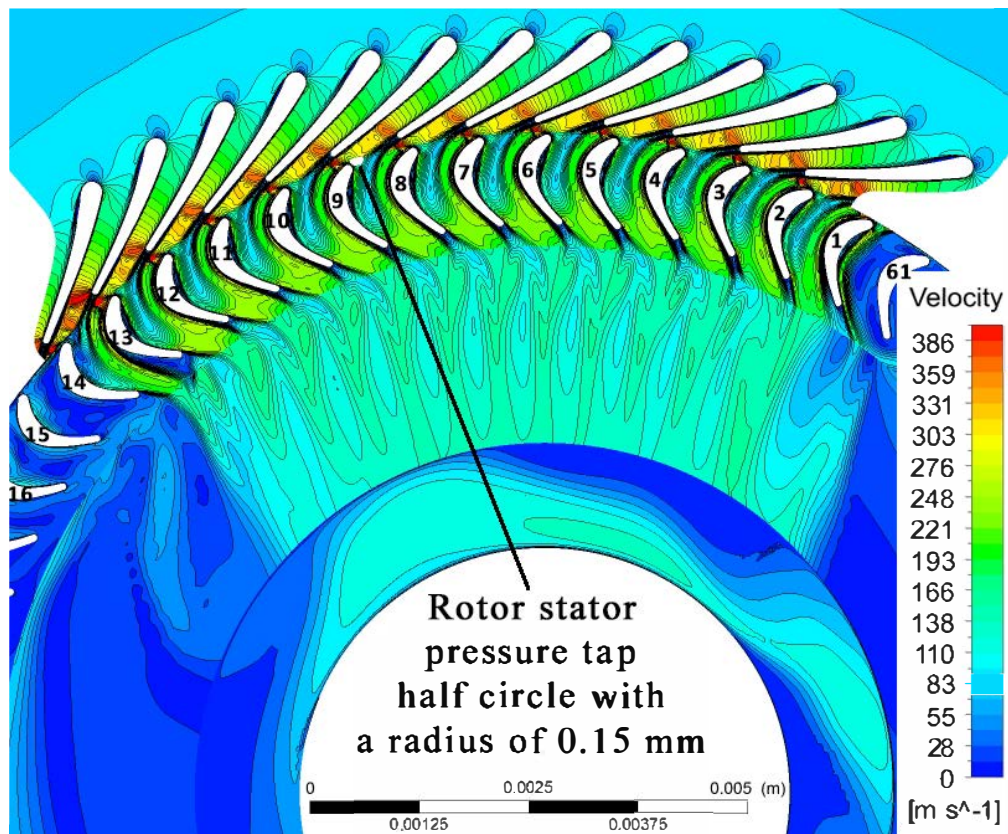


Figure 4.25 – Full passage simulation of the partial-admission turbine with the velocity (absolute in non-rotating domain and relative in rotating rotor domain) at a span of 0.5 and at the exducer outlet (turbine section 9).

#### 4.5.5 Three-dimensional full passage simulation

The full passage turbine simulation uses several single passages as Section 4.5.4 describes. In total, the simulation accounts for 13 turbine inducer and stator passages, as well as 59 turbine rotor and exducer passages. The boundary conditions are exactly the same, except for the 2x2 periodic boundary conditions at the turbine rotor and exducer, which are no longer required due to the full passage simulation. The simulation does not account for turbine inducer sidewalls (only hub and shroud), since the turbine inducer and stator still feature 2x2 periodic boundary conditions.

The steady full passage simulation is useful for determining the following: (1) the degree of admission at turbine outlet section 9, (2) the hub static pressure profile, which is used for the thrust force calculation, (3) the power of each turbine blade with respect to its position within the active zone, and (4) the determination of the blade pumping power within the non-active zone.

**(1) Degree of admission:** Since measurements at ambient conditions (Sections 5.2 and 5.3) are used to verify the thrust force model (Figure 4.28), the full passage simulation features ambient air with a total inlet temperature of 22.8 °C, a total inlet pressure of 2.2 bar, and an ambient pressure of 0.97 bar. The turbine rotational speed is 150 krpm. Figure 4.25 shows the velocity contours at a span of 0.5 and at the exducer outlet, which corresponds to section 9 in Figure 2.7. The velocity corresponds to the absolute velocity ( $c$ ) in the stationary domain and to the relative velocity ( $w$ ) in the rotating domain. The mass-flow-averaged velocity is  $150 \text{ m s}^{-1}$  at the turbine rotor exducer interface (section 8.1) and  $96 \text{ m s}^{-1}$  at the exducer outlet (9) suggesting a diffusion in the exducer domain. The initial admission at the turbine blade TE is 0.21 ( $\frac{13}{61}$ ), whereas it is  $\frac{1}{3}$  at the exducer outlet. This section corresponds to the light blue area in Figure 4.25, which also shows the position of the rotor-stator shroud static pressure measurement ( $p_{st,7}$ ) with a white half circle (radius of 0.15 mm) at a diameter of 15.3 mm in between two turbine stator blades, and thus in the main flow region (and not the stator wake). The pressure tap is located in the middle of the 13 stator blades.

**(2) Turbine hub static pressure profile:** Figure 4.26 shows the static pressure distribution along the turbine radius. The green triangle corresponds to the experimentally measured gauge value of this pressure tap (white half circle in Figure 4.25) multiplied by the degree of admission ( $\epsilon_a = 0.21$ ). Its measured value is  $233 \text{ mbar} \frac{13}{61} = 50 \text{ mbar}$ , and therefore is comparable to the value suggested by the CFD simulation ( $226 \text{ mbar} \frac{13}{61} = 48 \text{ mbar}$ ). The shroud static pressure is evaluated at a diameter of 15.18 mm. The diameter of 15.18 mm divides the half circle pressure tap (radius of 0.15 mm) into two equal surfaces ( $15.3 \text{ mm} - 2 \cdot 0.4 \cdot 0.15 \text{ mm}$ ) and is thus representative of the measured static shroud pressure. Since the total pressure and, therefore, the static pressure is higher in the center of the turbine admission, the measured gauge static pressure is higher than the simulated line-averaged value over the entire 13 stator blades. In the CFD simulation, the static pressure in the center of the turbine admission is 226 mbar, whereas the line-averaged value over the entire turbine admission at the turbine impeller shroud and hub is 150 mbar and 162 mbar, respectively. The difference of static pressure at the turbine rotor LE between the turbine hub and shroud is thus low ( $162 \text{ mbar} - 150 \text{ mbar} = 12 \text{ mbar}$ ). The measured shroud rotor-stator static pressure is thus a reasonable estimation for the (non-measured) hub rotor-stator static pressure.

The graph also features the line-averaged hub static pressure at different radii (red non-filled circles). The integral of this pressure profile over the radius ( $r_{turb}$ ) and the  $\varphi_{turb}$  angle corresponds to the thrust force in the  $z_{turb}$  direction (Figure 2.7). The simulated line-averaged hub static pressure (over the entire turbine impeller) at a diameter of 7.55 mm is 42 mbar, and lower than the experimentally measured value multiplied by the degree of admission (50 mbar).

At the turbine rotor LE the flow accelerates due to the increasing turbine blade thickness (and thus the static pressure decreases), and then decelerates due to the decreasing turbine blade thickness (and thus the static pressure rises). The maximum turbine rotor blade thickness is located at a meridional position ( $m_{turb2}$  in Figure 2.7) of 0.35, which corresponds to a radius



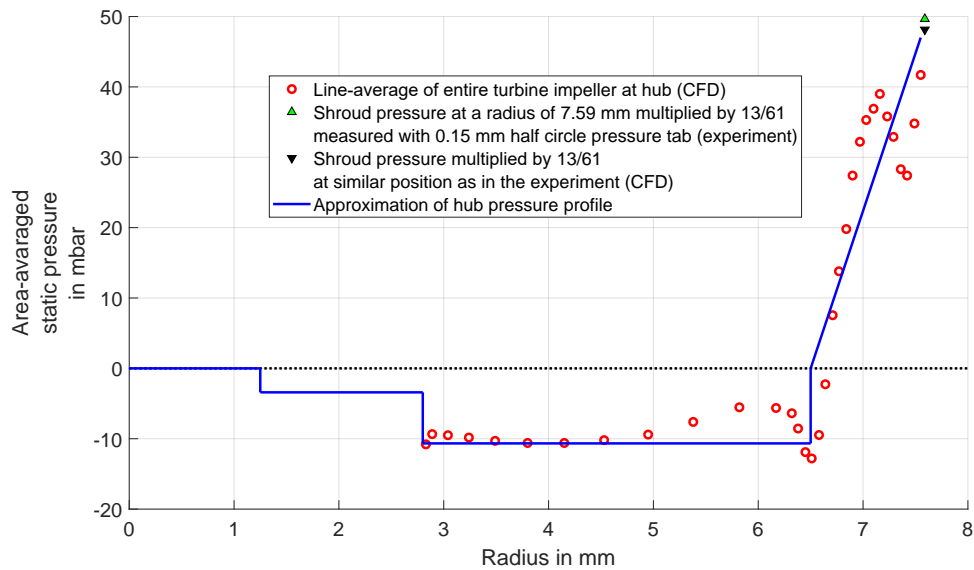


Figure 4.26 – Line-averaged hub static pressure profile for the full impeller turbine (red dots) and comparison to the approximated hub static pressure profile for the thrust force calculation with an analytical model (solid blue line), as well as to the measured value at the rotor-stator interface multiplied by 13/61 (up-pointing green triangle).

of 7.15 mm. At this point, the static pressure begins to decrease nearly-linearly. At the turbine rotor TE, there is also this acceleration and then deceleration effect.

The pressure profile is nearly-constant between a radius of 2.8 mm and 5 mm. Equation 4.32 calculates this pressure with the turbine inlet mass flow rate ( $\dot{m}_{turb} = 3.6 \text{ kg h}^{-1}$ ), the density at turbine section 9 ( $\rho_9 = 1.26 \text{ kg m}^{-3}$ ), the hub and the shroud radii at section 9 (2.8 mm and 4 mm, respectively), and the (area-averaged) absolute flow angle at the section 9 ( $\alpha_9 = 30^\circ$ ). The mass-flow-averaged absolute flow angle at section 9 is nearly- $90^\circ$ , since the author designed the turbine for low swirl at the turbine rotor TE to reduce losses in the turbine exducer, turbine transition region, turbine diffuser, and turbine outlet. However, the rotating turbine impeller hub and the rotating turbine impeller blades create a swirling flow within the non-active area. For the simulated case, this swirl has an area-averaged angle of  $30^\circ$ ; hence, the (area-averaged) absolute velocity is higher by a factor  $\frac{1}{\cos \alpha}$  and the (area-averaged) static gauge pressure lower by a factor  $\frac{1}{\cos^2 \alpha}$ . This area-averaged absolute angle can be estimated by assuming the active flow that occupies  $\frac{1}{3}$  of section 9 is non-swirling ( $\alpha = 90^\circ$ ), whereas the non-active section ( $1 - \frac{1}{3}$ ) is swirling ( $\alpha = 0^\circ$ ).

Figure 4.26 shows the correlation between this model (blue full line) and the CFD value (red non-filled circles) between a radius of 5 mm and 2.8 mm. The force in the z-direction, as defined in Figure 4.28, is 0.02 N within the CFD simulation, whereas the approximated model suggests a force of 0.007 N. This force is extremely small, since a low thrust force is beneficial for the FTU, and thus overall SOFC system efficiency.

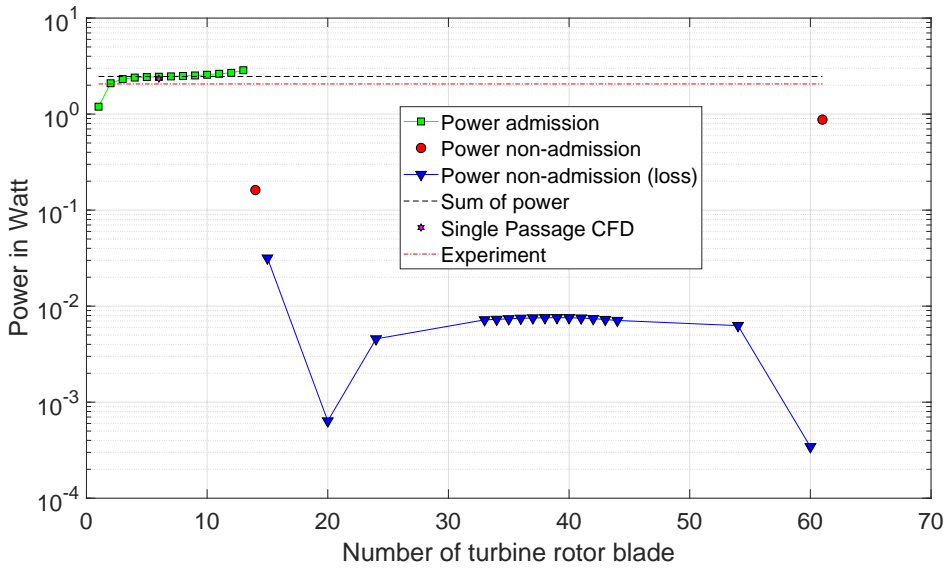


Figure 4.27 – Full passage steady CFD simulation of turbine at 150 krpm with ambient air: Power of each turbine blade (1-61) where the first blade corresponds to the first blade in the admission, i.e., the filling, and the 13th blade to the last blade in the admission, i.e., emptying (green squares). The 14th and 61st turbine blade (red dots) in the non-admission area have a positive power, whereas the blades 15 to 60 (down-pointing blue triangle) have a negative power and correspond to the pumping loss (0.18 W). The magenta hexagram corresponds to the result of the single passage simulation and the red dashed-dotted line to the experiment.

**(3) Power per turbine blade:** Figure 4.27 shows the power ( $P_{turb,blade} = M_{z,blade}\omega$ ) for each turbine blade. The numbers on the x-axis correspond to the blade number in Figure 4.25. The first blade, is the first in the admission, i.e., the position where the blade filling starts. The 13th blade is the last blade in the admission, i.e., the position where the blade emptying starts. Regarding the steady simulation, the power of the 13th blade is the highest, since there is no fluid within the next channel of the 14th blade. Due to the steady simulation, the blade emptying process is not simulated. Figure 4.26 shows the separation on the PS of the 13th blade, which leads to a low pressure on this blade PS, and thus to a higher torque and power compared to the other blades with no separation. The blades within the admission are marked with green squares in Figure 4.27. The blade before and after the admission (blade number 14 and 61) have a simulated power of 0.16 W and 0.9 W, respectively (marked with red circles in Figure 4.27). The sum of all individual blade powers in Figure 4.27 corresponds to 32 W, whereas the result of the single passage simulation (magenta hexagram in Figure 4.27) multiplied by thirteen is 30.4 W. Since the difference between the two simulations is low (1.6 W or 5%), but the wall clock computational time is on the order of two orders of magnitude higher for the full passage simulation, the single passage simulation is preferred. The experimental

value (measured power plus mechanical losses) corresponds to 26.8 W (red dashed-dotted line in Figure 4.27).

**(4) Blade pumping loss:** The turbine blades with a negative power (15-60, blue down-pointing triangle in Figure 4.27) correspond to the pumping loss, i.e., the torque is in the opposite direction to the other blades. The sum of these losses is 0.18 W and therefore significantly lower than the analytical value from eq. 4.25.

## 4.6 Thrust force model

Besides the stability of the journal bearing, the stability of the thrust gas film bearing over the entire FTU operational range is mandatory for a failure-free FTU operation. Since the thrust bearing stability depends, among other variables, on the thrust force, an accurate thrust force model is important during the FTU design phase.

The FTU features a single-sided spiral-grooved thrust gas film bearing, which operates in the pump-in mode, on the fan backface. The thrust must therefore be directed towards the positive z-direction (as defined in Figure 4.28 and Figure 2.3). A large enough thrust force in the negative z-direction would lead to a touchdown of the turbine backface towards the seal or the fan blades towards the fan volute, depending on the respective clearances. For the FTU setup presented within this thesis, the stationary turbine backface clearance is set to 0.115 mm (Table 4.7), whereas the stationary fan tip clearance is 0.150 mm (Table 4.1). For the tested FTU setup, an axial touchdown would therefore occur at the turbine backface.

Another important aspect is that a high thrust force increases the viscous friction, and thus the power loss within the thrust gas film bearing, which leads to a lower mechanical efficiency of the FTU. A lower mechanical efficiency leads to a higher turbine water vapor mass flow rate and higher turbine inlet pressure, which favors a higher water vapor leakage mass flow rate from the turbine to the fan. This water vapor leakage dilutes the anode off-gas and reduces the SOFC Nernst potential (eq. 2.14). The FTU should therefore feature a low thrust force.

Figure 4.28 shows an example of the thrust forces of the FTU unit for the tested case with air at 200 °C, while the shaft rotates at 168 krpm (Table 4.4). At this test point, the fan ingested ambient air and the turbine exhaust exited to the ambient (Figure 5.10 shows the experimental setup). The experimental setup allowed for the measurement of all pressures that are necessary to calculate the thrust force:

- $p_{st,4}$ : The static pressure at the fan TE shroud (mean of  $\phi = 0^\circ, 120^\circ, 240^\circ$ ) at a diameter of 18.55 mm (green value).
- $p_{ho}$ : The static and total housing pressure:  $p_{t,ho} \approx p_{st,ho} = p_{ho}$  (blue value).
- $p_{st,seal}$ : The static pressure within the seal at the turbine backface (dark red value).
- $p_{st,7}$ : The turbine rotor-stator static pressure at the shroud in the middle of the 13 stator

## Chapter 4. Fan-Turbine Unit Design

blades that is approximately representative for the turbine rotor hub pressure within the turbine admission (yellow value).

The maximum static pressure in the thrust bearing occurs at the end of the groove ( $p_{st,tb}$ , red value in brackets) and was not measured, since an exact measurement within the fluid film was challenging. A pressure tap at the end of the spiral groove where the maximum pressure ( $p_{st,tb}$ ) occurs, would alter the effective bearing clearance (i.e.  $14\mu\text{m}$ ), and thus the measured static pressure. An indirect estimation, or calculation of ( $p_{st,tb}$ ) is possible either with the rotor thrust bearing clearance measurement (Section 5.2) or with thrust force calculation as presented in this subsection that uses the measured static pressures along with the fan and turbine mass flow rates.

The sum of all measured pressure profiles (marked in black in Figure 4.28) is  $+1.15\text{ N}$  (for air at  $200\text{ }^\circ\text{C}$  and  $168\text{ krpm}$ ). The spiral-grooved thrust bearing compensates for this axial load (red pressure profile that was not measured). Two linear slopes (red thick full lines) approximate the pressure profile of the thrust bearing. In the case in Figure 4.28, the spiral-grooved thrust bearing maximum static pressure ( $p_{st,tb}$ ) is slightly below the housing pressure, which indicates a leakage flow rate from the FTU housing towards the fan TE. For lower rotational speeds, the maximum static pressure inside the thrust bearing ( $p_{st,tb}$ ) is higher than the housing pressure, which indicates a leakage mass flow rate from the fan TE towards the turbine due to the inward-pumping effect of the spiral-grooved thrust bearing. Figure 4.28 shows this as an example with two red thick dashed lines.

**Pressure profiles:** In general, the pressure profiles assume either a linear increase or decrease. The integral for the linear increase from a lower radius (for example  $r_{3,1}$ ) with a zero gauge pressure to a higher radius (for example  $r_4$ ) with a higher gauge pressure (for example  $1.035p_{st,4}$ )

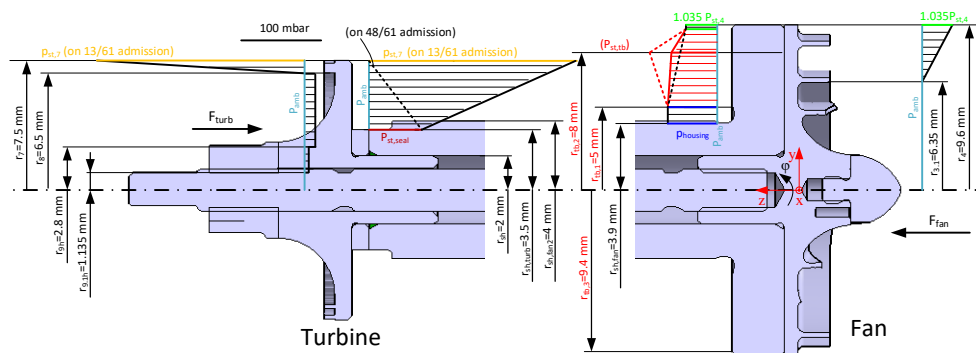


Figure 4.28 – Axial force of the FTU for the turbine (left) and the fan side (right) close to the nominal point at a rotational speed of  $168\text{ krpm}$ . All pressures were measurements except for the axial thrust bearing pressure in brackets (calculated).

is thus,

$$F_{z, fan, front} = \frac{1.035 p_{st,4}}{r_4 - r_{3.1}} \int_0^{2\pi} \int_{r_{3.1}}^{r_4} (r - r_4) r dr d\varphi \quad 4.30$$

the integral in cylindrical coordinates over the angle  $\varphi$  and the radius ( $r = \sqrt{x^2 + y^2}$ ), as defined by Figure 4.28 and Figure 2.3. The pressure profile at the turbine backface within the no-admission section ( $\frac{48}{61}\pi$ ) increases linearly from the ambient pressure at the turbine rotor LE to the measured seal static pressure ( $p_{st, seal}$ ) at a lower radius ( $r_{sh, turb}$ ). The force is thus,

$$F_{z, turb, back \frac{48}{61}} = \frac{p_{st, seal}}{r_7 - r_{sh, turb}} \int_0^{\frac{48}{61} 2\pi} \int_{r_{sh, turb}}^{r_7} (r_7 - r) r dr d\varphi \quad 4.31$$

a function of these pressures, radii, and the degree of admission ( $1 - \frac{13}{61} = \frac{48}{61}$ ).

**Static pressure profiles at the fan side:** The pressure rise in the fan impeller is in a first approximation linear (hub pressure profile in Figure 4.12 at the bottom). Until the fan splitter blade LE, the static pressure is nearly-constant due to the zero-Euler-work blades at the fan inlet. This configuration is thus not only beneficial for a reduced fan blade tip leakage mass flow rate (Figure 4.13), but also reduces the thrust force on the machine, and thus increases the overall SOFC system efficiency. A linear slope from the fan splitter blade LE at a radius of 6.35 mm to the blade TE at a radius of 9.6 mm approximates the static pressure profile at the fan hub. In the experiment, three pressure taps at a radius of 9.275 mm determine the blade TE shroud static pressure; hence, this value is multiplied by the factor  $1.035 (\frac{9.6}{9.275})$  to estimate the static pressure at the fan TE.

The thrust force calculation assumes that the inlet pressure to the spiral-grooved thrust bearing is equal to the fan blade TE pressure. The pressure profile between the 9.4 mm and 9.6 mm radii is constant, due to the chamfer from manufacturing. The inward-pumping thrust bearing increases the pressure. At the nominal conditions, the (calculated) maximum pressure inside the bearing ( $p_{st, tb}$ ) at a radius of 8 mm is close to the housing pressure  $p_{ho}$  (Figure 4.28). The shaft undercut necessary for manufacturing limits the thrust bearing surface to a radius of 5 mm. The calculation assumes a constant pressure profile equal to the housing pressure ( $p_{ho}$ ) for the undercut (between the 3.9 mm and 5 mm radii).

**Static pressure profiles on the turbine side:** The turbine backface seal features six seal teeth: three at a 4 mm radius and three at a 3.5 mm radius. The measured seal static pressure corresponds to the pressure in the middle of the seal. The calculation assumes that this pressure is equal to the turbine backface static pressure at a radius of 3.5 mm. The partial-admission turbine backface and turbine impeller hub pressure calculation features two sections:  $\frac{13}{61}$  within the turbine admission and  $\frac{48}{61}$  for the non-admission section. For the  $\frac{13}{61}$  admission section at the turbine backface, the pressure rises linearly from the static seal pressure to the measured static pressure within the turbine rotor-stator interface ( $p_{st,7}$ ). Since the pressure

difference between  $p_{st,7}$  and  $p_{st,seal}$  is very low (maximum 43 mbar at a rotational speed of 168 krpm), the model does not assume quadratic, but rather, simplified linear pressure profiles at the turbine backface. For the other  $\frac{48}{61}$  non-admission section at the turbine backface, the static pressure decreases linearly from the seal static pressure to the ambient pressure (thick dashed black line at the turbine backface in Figure 4.28).

A half-circle pressure tap (radius of 0.15 mm) at the turbine shroud in the middle of the 13 stator blades within the main flow region (and thus not in the stator wake) measures the static pressure within the turbine rotor-stator interface ( $p_{st,7}$ ). The rotor-stator static pressure decreases towards the non-admission area and is thus a function of  $\varphi$ . However, this model assumes that  $p_{st,7}$  is constant within the region of admission ( $\frac{13}{61}$ ) and that it decreases linearly from the measured static pressure ( $p_{st,7}$ ) to the ambient pressure between a radius of 7.5 mm and 6.5 mm corresponding to the turbine blade LE and TE, respectively. Within these radii, the turbine impeller hub pressure for the other  $\frac{48}{61}$  is constant at the ambient pressure.

Due to the high velocity at the turbine rotor outlet, the static pressure at the turbine hub is below the ambient pressure. The thrust force calculation assumes a constant pressure profile between the turbine rotor outlet radius ( $r_8$ ) of 6.5 mm and the exducer outlet hub radius ( $r_{9h}$ ) of 2.8 mm. A constant pressure profile is also assumed between the exducer outlet hub radius ( $r_{9h}$ ) and the end of the shaft screw ( $r_{9.1h}$ ). The area at the rotor outlet ( $\frac{13}{61}2\pi r_8 b_8 = 6.1 \text{ mm}^2$ ) is lower than the area at the exducer outlet ( $a_3\pi(r_{9s}^2 - r_{9h}^2) = 8.5 \text{ mm}^2$ ); hence, the flow decelerates. The turbine hub pressure is thus,

$$p_{amb} - p_8 \approx p_{amb} - p_9 = \frac{1}{2} \frac{\dot{m}_{turb}^2}{\rho_9 \pi^2 (r_{9s}^2 - r_{9h}^2)^2} \frac{1}{\cos^2 \alpha_9} \quad 4.32$$

$$p_{amb} - p_{9.1} = \frac{1}{2} \frac{\dot{m}_{turb}^2}{\rho_9 \pi^2 (r_{9s}^2 - r_{9.1h}^2)^2} \frac{1}{\cos^2 \alpha_{9.1}} \quad 4.33$$

a function of the (area-averaged) absolute flow angle ( $\alpha_9$  and  $\alpha_{9.1}$ ), the turbine mass flow rate, the density, and the radii at section 9 and 9.1. Since the static pressure is an area-averaged variable, the equation above does not use the discharge coefficient ( $a_3$ ), but instead uses the area-averaged flow angle that accounts for the swirl at section 9 due to rotating turbine hub and turbine impeller blades.

Figure 4.26 shows the line-averaged static pressure profile for the turbine full passage simulation (air at ambient temperature and at a rotational speed of 150 krpm). In comparison, the experimental and numerical values multiplied by the admission of  $\frac{13}{61}$  are also shown. The numerical pressure profile reveals the more complex fluid flow in the turbine rotor (accelerations and decelerations). A linear pressure profile is assumed to simplify the complex flow phenomena. At least for the investigated case, the analytical (0.007 N) and numerical (0.02 N) calculated thrust force due to the turbine impeller hub static pressure are reasonably correlated (0.013 N difference). Since this turbine hub thrust force is relatively low (3 %) with respect to the compensated thrust force (red profile in Figure 4.28), the approximated model is feasible.

**Fluid impulse on the fan side:** The force at the fan inducer inlet resulting from the fluid ( $F_{fan}$ ) assumes a constant velocity profile at the fan inducer inlet.

$$F_{fan} = \dot{m}_{fan} \bar{c}_2 = \frac{\dot{m}_{fan}^2}{\pi (r_{2s}^2 - r_{2h}^2) \rho_2} = \frac{\dot{m}_{fan}^2}{\pi (0.00411^2 - 0.00204^2) \rho_2} \quad 4.34$$

Since the flow is nearly-undisturbed at the bellmouth inlet and the inlet sides test section is short, the flow profile is not yet fully-developed; hence, this is a reasonable approximation.

**Fluid impulse on the turbine side:** However, at the turbine outflow, the velocity profile at the exducer outlet section (9) is highly non-uniform, due to the partial admission (Figure 4.25); hence, the velocity is a function of the radius ( $r = \sqrt{x^2 + y^2}$ ) and the angle ( $\varphi$ ). If the fluid does not expand after the turbine rotor TE and thus the area that the fluid occupies is constant, this would lead to a theoretical admission at the section 9 of 0.24,

$$\epsilon_{a,9,min} = \frac{\epsilon_{a,8} d_8 b_8}{(r_{9s}^2 - r_{9h}^2)} = 0.24 \quad 4.35$$

which is slightly greater than the admission at the turbine rotor TE ( $\epsilon_{a,8} = \frac{13}{61} = 0.21$ ). However, the fluid expands between section 8 and 9, such that the admission at section 9 is higher than the theoretical value of 0.24 (eq. 4.35). Section 4.5.5 introduces a full passage simulation of the partial-admission turbine with air at ambient temperature and at a rotational speed of 150 krpm. This simulation suggests that the admission at section 9 is  $\frac{1}{3}$  and thus 0.09 above the minimum admission of 0.24 (eq. 4.35). With the help of this experience coefficient, which corresponds to the admission at section 9 ( $a_3 = \frac{1}{3}$ ), the force at the turbine outlet due to the fluid impulse,

$$F_{turb} = \int_{0^\circ}^{360^\circ} \int_{r_{9h}}^{r_{9s}} \vec{c}_9 \vec{c}_9 \begin{pmatrix} 0 \\ 0 \\ 1 \end{pmatrix} \rho r dr d\varphi \approx \frac{1}{a_3} \dot{m}_{turb} \bar{c}_9 \quad 4.36$$

$$F_{turb} \approx \frac{1}{a_3} \dot{m}_{turb} \bar{c}_9 = \frac{1}{a_3} \frac{\dot{m}_{turb}^2}{\pi (r_{9s}^2 - r_{9h}^2) \rho_9} = \frac{1}{\frac{1}{3}} \frac{\dot{m}_{turb}^2}{\pi (0.004^2 - 0.0028^2) \rho_9} \quad 4.37$$

is calculated using the turbine mass flow rate ( $\dot{m}_{turb}$ ), the fluid density ( $\rho_9$ ), the shroud radius ( $r_{9s}$ ), and the hub radius ( $r_{9h}$ ) at the section 9, which is 4 mm and 2.8 mm, respectively (Figure 4.28).

## 4.7 Chapter conclusion

This chapter introduces the baseline design of the FTU that focuses on low manufacturing and assembly cost, rather than maximizing component efficiency. It consists of 14 parts that are manufactured with basic milling and turning operations, as well as surface finishing

operations (grinding and honing) for the rotor and stator. High-precision surface tolerances for the journal and thrust gas film bearings are necessary for stable operation.

The baseline fan impeller is designed with respect to the previously described baseline SOFC system: for a total inlet pressure of 1.05 bar, a total inlet temperature of 200 °C, and an inlet mass flow rate of 4.78 kg h<sup>-1</sup> anode off-gas composed of water vapor, hydrogen, carbon monoxide, and carbon dioxide (61.4 %, 7.4 %, 2.6 %, and 28.6 % molar ratios, respectively). The design total-to-total pressure rise is 70 mbar. The fan TE diameter is 19.2 mm and the fan design rotational speed 175 krpm corresponding to a specific speed of 0.8, as defined by Balje [2].

The similarity concept by Balje [2] is not adequate for a reliable fan pre-design, since the Reynolds number for the Balje maps is one order of magnitude higher than the one of the fan considered in this work. A correction procedure based on the fan mean-line analysis is therefore proposed to account for the loss mechanisms involved within small-scale turbomachinery: (1) increased tip leakage losses due to higher manufacturing and assembly tolerances, (2) increased viscous losses due to decreased Reynolds number, (3) frictional losses due to increased relative surface roughness, and (4) the deviation loss at the fan TE. The correlation of Pfleiderer [94] with an experience coefficient of 2.3 (loss mechanism 1), the correlation of Wiesner [91] (loss mechanism 2 and 3), and the correlation of Pfleiderer for fans without a diffuser [94] with an experience coefficient of 0.6 are chosen. The loss coefficient based on the fan blade TE circumferential velocity within the fan volute (without diffuser) is found to be  $\frac{2}{3}$ , whereas the meridional component is lost due to the swirling fluid motion.

This adapted fan similarity concept allows for a more adequate fan pre-design and an estimation of the fan isentropic efficiency and tip diameter within  $\pm 5\%$  (compared to the performed CFD simulation and experiments). The optimal fan specific speed is shifted towards lower values (0.65) compared to classical concepts (0.85), due to lower Reynolds-dependent and manufacturing-dependent (blade tip clearance) losses at higher specific diameters and higher blade tip diameters.

The baseline high-work low-reaction partial-admission radial-inflow steam turbine based on 61 prismatic blades has a tip diameter of 15 mm. The blade radial chord is 1 mm and the blade height is 0.6 mm. Expanding a steam mass flow rate of 2.1 kg h<sup>-1</sup> with a total inlet temperature of 220 °C, a total-to-total pressure ratio of 1.9 yields a power output of 36 W at a total-to-static isentropic efficiency of 38 %. Although the turbine dimensions are uncommon, the similarity concepts by Balje [2] with a correction factor for the increased blade tip clearance and blade edges yield reasonable results. In addition, the one-dimensional loss model based on mean-line analysis by Soderberg [98] with a correction factor for the Reynolds number and the blade height yields reasonable results.

However, zero and one-dimensional models are not sufficiently accurate for small-scale turbomachinery design with a relatively high blade tip clearance and thick blade edges. These



factors require a careful blade design for both the fan and turbine. The fan blade geometry is selected to be unloaded at the front to reduce the onset of the tip clearance vortex. The turbine rotor blade design (based on the primary series NACA profile from the technical note 3802 [102]) is adapted to the thick blade LE and high inlet velocities to avoid a flow separation (maximum normal layer thickness at 35 % of the blade chord and more gentle blade turning). The author compared single passage and full passage three-dimensional CFD simulations for both the fan and turbine. With respect to the fan, a single passage simulation captures the flow phenomena if the designer considers the elevated pressure loss in the volute. The turbine single passage simulation is preferred to a time-consuming full passage simulation, since it is a good trade-off between computational time and accurate result (deviation of 5 % towards the full passage simulation at one tested operational point).

Since the single-sided spiral-grooved thrust gas film bearing is only able to compensate a thrust force in one direction (up to 11 N at the design conditions), a careful evaluation of the thrust force is required by the designer. A thrust force model based on approximate static pressure profiles (verified with CFD simulations) is presented. Using this model, the thrust force is calculated to be 1.2 N for an operation with hot air (220 °C) at a rotational speed of 168 krpm.



## 5 Fan-Turbine Unit Experiments

This chapter provides an overview of the experimental testing of the designed FTU. Appendix C introduces the utilized measurement equipment and the respective uncertainty and calibration, if necessary. Before the FTU can operate, the rotating parts have to undergo a balancing procedure (Appendix D). Since no high-precision sensors for high temperatures were available in the laboratory and operating such a small-scale steam turbine was a delicate task, the author chose to perform the FTU test in several consecutive steps:

- Propelling the FTU with air nozzles and measuring the thrust bearing axial clearance.
- Propelling the FTU with the turbine (ambient air) and measuring the thrust bearing axial clearance.
- Propelling the FTU with the turbine (ambient air) and operating the fan with ambient air.
- Propelling the FTU with the turbine (hot air, 220 °C) and operating the fan with hot air (200 °C).
- Propelling the FTU with the turbine (hot water vapor, 220 °C) and operating the fan with hot air (200 °C).

### 5.1 Fan-turbine unit propelled by nozzles with pressurized ambient air

Figure 5.1 shows the experimental setup of the balancing procedure (Appendix D). This setup also measured the thrust bearing axial clearance of the unit without the influence of the turbine side, since the turbine and the turbine volute were not mounted. Instead, the FTU featured a “dummy turbine” wheel (Figure D.1 on the right) that held together all rotor components (fan impeller, shaft, screw inside the shaft, “dummy turbine”, and turbine nut). Two pressurized air nozzles propelled the FTU instead of the turbine impeller. There was the possibility to inject pressurized air from the local network inside the FTU housing to increase the housing pressure. Figure 5.1 does not show this connections since it was on the oppo-

site side of the housing. This setup featured the measurement of the housing pressure and the journal bearing temperature close to the fan and turbine side with two thermocouples (TCs). Two LionPrecision C3S sensors close to the fan side were used to measure the radial displacement and orbit measurements, as well as two C3S measurements close to the turbine side. It also featured the possibility to mount a Philtec D20 optical displacement sensor (in the middle of Figure 5.1) or a C3S (bottom right of Figure 5.1) to measure the thrust bearing static and dynamic axial clearance. The range of the available C3S is limited to 50  $\mu\text{m}$ -50-100  $\mu\text{m}$ , whereas the D20 is capable of measuring 140  $\mu\text{m}$ -360-100  $\mu\text{m}$  within the so called “far-side range” (linear within  $\pm 1\%$ ).

**Thrust bearing static axial clearance measurement:** Due to its superior range, the Philtec D20 (in-house calibration) measured the static thrust bearing axial clearance between 0  $\mu\text{m}$  at 0 bar(g) of housing pressure and 210  $\mu\text{m}$  at a housing pressure of 0.96 bar(g). Up until a certain housing pressure, all the leakage flow from the housing to the ambient went entirely through the outlet at the “dummy turbine”, whereas no leakage occurred on the fan side. Due to the rotor weight and the friction force between the DLC shaft and the stainless steel journal bearing (rotor inclined by 45°), the clearance at the fan backface was zero and no leakage occurred. The fan lifted off if the housing pressure ( $\Delta p_{ho}$ ) at the fan blackface could compensate the static friction force ( $\mu_0 m_{rotor} g$ ) and the weight of the rotor ( $m_{rotor} g$ ).

$$\Delta p_{ho, lift-off} = \frac{m_{rotor} g \left( \sin \frac{\pi}{2} + \mu_0 \cos \frac{\pi}{2} \right)}{\pi \left( r_{tb,1}^2 - r_{sh, fan}^2 \right) + \frac{2\pi}{r_{tb,3} - r_{tb,1}} \int_{r_{tb,1}}^{r_{tb,3}} (r_{tb,3} - r) r dr} \quad 5.1$$

$$= \frac{0.0253 \cdot 9.81 \left( \sin \frac{\pi}{2} + 0.06 \cos \frac{\pi}{2} \right)}{\pi \left( 5^2 - 3.9^2 \right) + \frac{2\pi}{4.4} \int_5^{9.4} (9.4 - r) r dr} 10 \text{ bar(g)} = 0.0155 \text{ bar(g)} \quad 5.2$$

The equation assumes a constant pressure profile for a radius from 3.9-5 mm that is equal to the housing pressure, a linear profile for a radius from 5-9.4 mm, and ambient pressure for a radius from 9.4-9.6 mm. Figure 4.28 shows the definition of the different radii and a schematic example of the rotating FTU thrust force profile with mounted turbine impeller. Replacing the fan TE static pressure ( $p_{st,4} = 0$ ) with zero provides the investigated pressure profile (black dotted line in Figure 4.28). The rotor mass was 0.0253 kg (measured with a scale) and the static frictional coefficient of the DLC stainless steel shaft was 0.06 (rotor pulling weight was 0.0015 kg  $\rightarrow \mu_0 = \frac{0.0015}{0.0253}$ ). Figure 5.2 at the top shows the measurements of the static thrust bearing axial clearance. The top left shows the entire measurement range from 0-0.96 bar(g), whereas the top right graph shows a zoomed in region of 0-0.02 bar(g). The calculated lift-off housing pressure ( $\Delta p_{ho, lift-off}$ ) from eq. 5.2 agrees with the measurements (0.0162 bar(g)  $\pm$  0.0031 bar(g)). After the impeller lifted off, the pressurized air from the housing leaked via the fan impeller and the turbine side; hence, the static pressure inside the housing decreased, although the supply pressure increased. The pressure decreased from 0.0170 bar(g) to 0.0157 bar(g), as the axial lift-off increased.

**Conclusion:** At a pressure of 0.0157 bar(g) inside the housing and an thrust bearing axial

## 5.1. Fan-turbine unit propelled by nozzles with pressurized ambient air

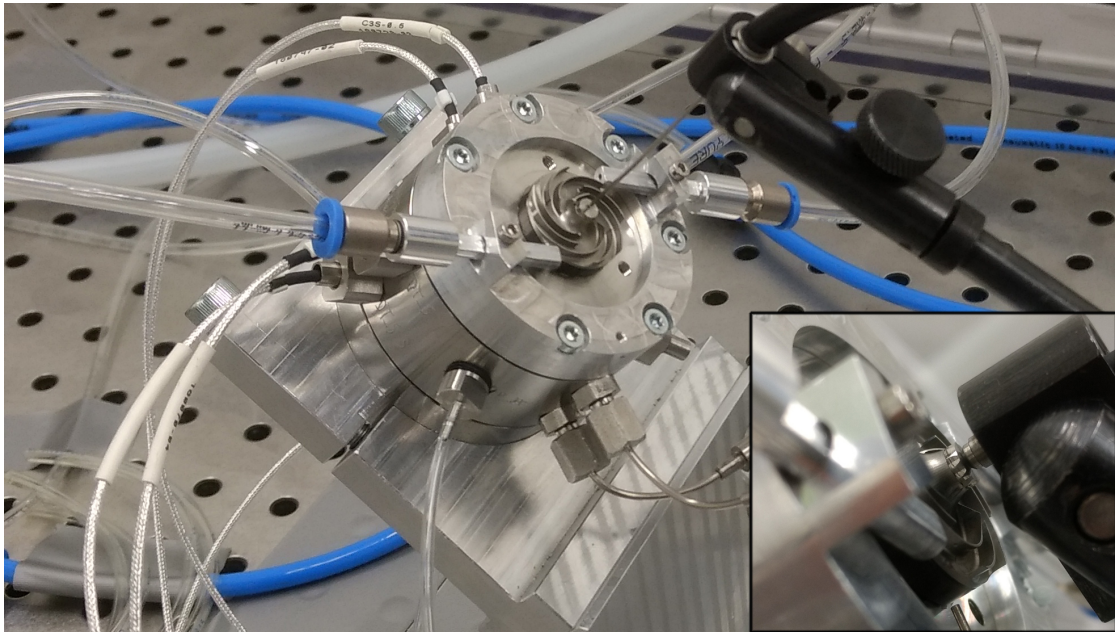


Figure 5.1 – The FTU mounted at 45° with four (two front and two back) installed LionPrecision C3S sensors for the radial displacement measurement, one Philtec D20 for thrust bearing axial clearance measurement, a C3S (lower right corner), one pressure tap for the housing pressure, and two TCs measuring the journal bearing temperature. Two pressurized air nozzles at the fan propelled the shaft.

clearance of 20  $\mu\text{m}$ , during nominal operation, the load capacity of the spiral-grooved thrust bearing was nearly-zero and the housing pressure compensated for the thrust (for this setup with inclined rotor and no turbine mounted). The dynamic thrust bearing therefore operated as a static thrust bearing fed with pressurized air.

**Dynamic thrust bearing axial clearance measurement:** Figure 5.2 also shows two examples of the dynamic thrust bearing axial clearance for both a bearing with a housing pressure of zero (green graphs in the middle) and for a bearing with a 0.1 bar(g) housing pressure (blue graphs at the bottom) in the time domain (left) and in the frequency domain (right).

In these two experiments, the rotor accelerated due to the pressurized air from the nozzles on the fan side up until a certain speed. A valve cut off the pressurized air from the nozzles and the rotor started to decelerate, due to the frictional loss within the bearings (rotor run-out) without any external influence. With respect to the time domain, the direction of the axial displacement identified two different operational modes: (1) dynamic thrust bearing in the middle and (2) static thrust bearing at the bottom.

(1) With increasing speed, the bearing stiffness of the dynamic thrust bearing increased, since the static pressure at the fan backside increased due to the inward-pumping effect of the spiral-grooved thrust bearing. The thrust bearing axial clearance increased up to a value of

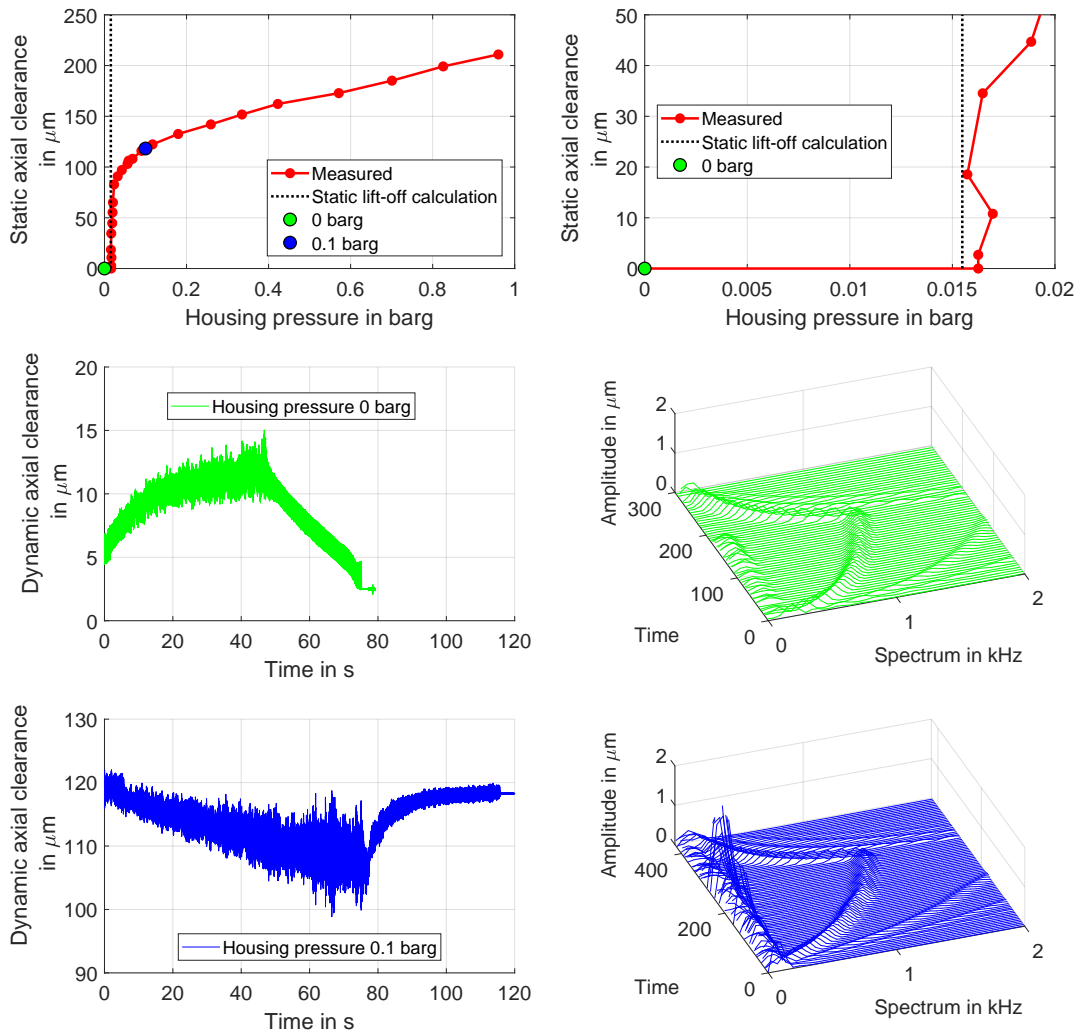


Figure 5.2 – Comparison of thrust bearing axial clearances at different housing pressures. Top: measurement of static axial clearance (rotor not rotating) between 0 and 0.96 bar(g) (left) and zoomed in view of this graph at the region of the initial fan lift-off, i.e., 0.0162 bar. Middle: dynamic axial clearance measurement with zero housing pressure up to 66 krpm in the time domain (left) and the frequency domain (right). Bottom: dynamic axial clearance measurement with 0.1 bar housing pressure up to 73 krpm in the time domain (left) and the frequency domain (right).

11  $\mu\text{m}$  at a speed of 66 krpm (1.1 kHz). After the experiment, the rotor did not return to the zero thrust bearing axial clearance position, but still had an offset of 2.5  $\mu\text{m}$ . The C3S axial displacement at zero speed was therefore important to determine, since the thrust bearing axial clearance was the difference between the zero axial displacement and the displacement measurement of the C3S sensor (Figure 5.1). The zero axial displacement was determined a priori by pushing the rotor against the stator.

## 5.2. Turbine propelled by pressurized ambient air

---

(2) For the static bearing (at the bottom), the thrust bearing axial clearance decreased with increasing speed. From an initial static axial clearance at zero speed, which was 118  $\mu\text{m}$ , the thrust bearing axial clearance decreased with increasing speed up to 11  $\mu\text{m}$  (mean value) at a speed of 73 krpm (1.2 kHz). At a speed of 66 krpm, the decrease in axial clearance was 8  $\mu\text{m}$  (mean value) and thus lower than the dynamic axial bearing increase (11  $\mu\text{m}$ ). At a constant housing pressure, the bearing load capacity decreased therefore with increasing speed, since the pressure at the fan backside decreased due to higher velocities.

**Water fall plots:** The right side in the middle and at the bottom of the figure features the waterfall plot of the respective experiment with the frequency on the x-axis, the time on y-axis (50 kHz sampling, one fast Fourier transformation (FFT) features  $2^{14}$  samples, and each FFT overlaps by 20 %), and the amplitude on the z-axis. The synchronous vibrations for each experiment were identical. However, for the experiment with 0.1 bar housing pressure, above 60 krpm, the sub-synchronous axial vibrations had an amplitude higher than 1  $\mu\text{m}$ , which increased to 3  $\mu\text{m}$  at the maximum speed (73 krpm). For the run-out without external forces acting on the rotor, the axial sub-synchronous vibrations remained (amplitudes up to 0.5  $\mu\text{m}$ ), whereas these completely disappeared for the dynamic thrust bearing with zero housing pressure. In general, the sub-synchronous vibrations caused by the two air nozzles, had a lower impact with respect to the zero housing pressure case.

**Conclusion:** As result of these two experiments, no pressurized air supply was used for the housing. The housing pressure only increased due to the influence of the turbine. The measured static pressure decreased between the turbine rotor-stator interface ( $p_{st,8}$ ), the seal at the turbine backface ( $p_{st,seal}$ ), housing ( $p_{ho}$ ), and the fan TE ( $p_{st,4}$ ).

## 5.2 Turbine propelled by pressurized ambient air

Figure 5.3 shows the setup for the thrust bearing axial clearance ( $s_{tb}$ ) measurement. The thrust bearing operates in the pump-in mode, i.e., it draws the gaseous lubricant from the blade TE into the fan housing. The thrust bearing axial clearance depends on the fluid, the axial load, and the thrust bearing geometry. For this measurement setup, ambient pressurized air propelled the turbine and thus the rotor. The turbine volute was therefore mounted but not visible in the picture. The setup was very similar to the setup from Figure 5.1 with the following changes. A LionPrecision C3S exclusively measured the thrust bearing axial clearance due to the small maximum displacement of 12.4  $\mu\text{m}$ . Since the FTU was now mounted directly on the ceramic oven (Figure 5.10 provides an overview) and no longer on an optical table, the axial clearance displacement sensor was mounted directly with a vertical holder. As discussed in Section 5.1, no pressurized air supplied the housing during operation, since the operation with zero housing pressure was more stable. However, the housing pressure still increased due to the influence of the turbine side. The measured turbine inlet total pressure was up to 2 bar, and the measured turbine rotor-stator gauge pressure was up to 0.22 bar at a speed of 150 krpm.

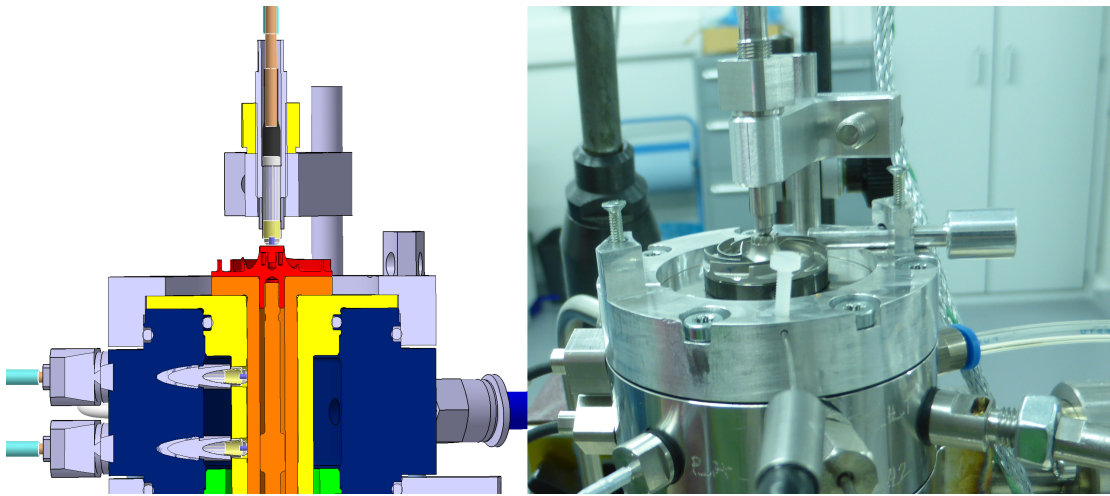


Figure 5.3 – Dynamic thrust bearing axial clearance measurement setup on the fan side (vertically mounted). Pressurized ambient air propels the turbine and thus the shaft (not shown).

The FTU was in the vertical design position with respect to gravitational force. The axial preload was thus higher, because of the increased weight of the rotor with the actual turbine (0.0013 kg heavier) in comparison to the “dummy turbine” from Section 5.1 ( $m_{rotor} = 0.0266$  kg with mounted turbine wheel). The static housing lift-off pressure must compensate for the rotor weight  $m_{rotor}g = 0.26$  N, and no frictional forces. According to eq. 5.1, the static lift-off housing pressure was 0.022 bar for this configuration. The FTU reached this pressure above a rotational speed of 80 krpm. The maximum housing pressure measured within this test campaign was 0.064 bar at a speed of 150 krpm. However, the rotor only lifted off up to 12.4  $\mu$ m, since the thrust force was increased due to the influence of the turbine wheel.

For this measurement series, the fan volute was not mounted on the FTU, since the C3S probe was too big to fit inside the fan volute to measure the thrust bearing axial clearance. The C3S sensor was only capable of withstanding temperatures of up to 50 °C; hence, the axial clearance measurement was only performed for the two cases:

- **Case 1:** Shaft with “dummy turbine” (Figure 5.1) in vertical position and zero housing pressure up to 136 krpm (ambient conditions). Only the air nozzles propelled the rotor in the case with the mounted “dummy turbine”. The pressurized air from the nozzles induced axial (sub-synchronous) vibrations (Figure 5.2 in the middle right) and an additional thrust force. The C3S sensor evaluated the (mean) axial clearance during the shaft run-out without the operational nozzles and, therefore, reduced vibrations (exclusively synchronous). No external thrust forces were acting on the rotor during the run-out.
- **Case 2:** Shaft with turbine impeller and mounted turbine volute in the vertical position



## 5.2. Turbine propelled by pressurized ambient air

---

and with zero housing pressure up to 150 krpm (ambient conditions). During operation with the turbine, no axial sub-synchronous vibrations occurred and the synchronous vibrations were on the order of  $0.4\ \mu\text{m}$  at a rotational speed of 150 krpm. The (mean) thrust bearing axial clearance was therefore evaluated at a steady state at different rotational speeds; i.e., 30 krpm, 40 krpm, ..., and 150 krpm.

**Comparison of thrust bearing axial clearance:** The axial clearance for the shaft with mounted “dummy turbine” (case 1) is on the left side of Figure 5.4 with blue squares. The axial clearance for the shaft with mounted turbine and turbine volute (case 2) is on the left side with red dots. The axial clearance for case 2 was lower, since the turbine induced a certain amount of thrust force, as compared to the free spinning “dummy turbine” in case 1. The maximum axial clearance was  $12.4\ \mu\text{m}$  at a rotational speed of 150 krpm for case 2, and  $13.4\ \mu\text{m}$  at a rotational speed of 136 krpm for case 1. The axial clearance was not measured at the operational temperature of  $200\ ^\circ\text{C}$ , since for this case no appropriate sensors with adequate measurement uncertainty and size were available in the laboratory (high-temperature-resistant, high-precision, and small-target-size-capable; the target has a diameter of 4 mm). The graph on the left, therefore, features a calculation of the axial clearance for in case with  $200\ ^\circ\text{C}$  air. This calculation utilizes the narrow-groove theory and the perturbation method [12] and assumes a constant thrust force for both cases (ambient air and air at  $200\ ^\circ\text{C}$ ). The axial clearance is on the order of 1.2-1.5  $\mu\text{m}$  higher, due to the increased air viscosity at elevated temperatures. The axial clearance for the design conditions with the anode off-gas at  $200\ ^\circ\text{C}$  is comparable to the ambient air case, since the viscosity for each fluid is very similar ( $1.82 \cdot 10^{-5}$  Pas for ambient air and  $1.79 \cdot 10^{-5}$  Pas for the anode off-gas).

The **thrust force model** is based on the procedure from Schiffmann [12] (chapter 3.4), which uses the narrow-groove theory that assumes an infinite number of grooves that with an infinite length-to-width ratio. This FTU spiral-grooved thrust bearing is located between a radius of 8 mm and 9.4 mm and features 20 grooves; hence, the length-to-width ratio is low. Nibourel [92] performed a CFD analysis of this groove geometry at a rotational speed of 100 krpm and with three different clearances ( $5\ \mu\text{m}$ ,  $9\ \mu\text{m}$ , and  $14\ \mu\text{m}$ ). A deviation of 28-31 % was found between the model based on narrow-groove theory and the numerical analysis. The experiments proposed a similar value of 0.7, since for case 1, the calculated thrust force should be equal to the rotor weight. Thus, this finite-groove effect reduces the theoretical maximum achievable pressure at the end of the spiral groove ( $p_{st,tb}$  in Figure 4.28) by 30 %. The author therefore introduces an experience coefficient of 0.7 that accounts for the finite groove number, and consequently, the finite length-to-width ratio.

**Comparison of thrust force:** The right side of Figure 5.4 features the thrust force corrected with the experience coefficient of 0.7 (red triangles) for case 2 (with mounted turbine). It was 0.3 N at a speed of 30 krpm and 0.8 N at a speed of 150 krpm. Figure 5.4 also features the corrected thrust force for case 1 (with “dummy” turbine), which was 0.26-0.36 N (blue

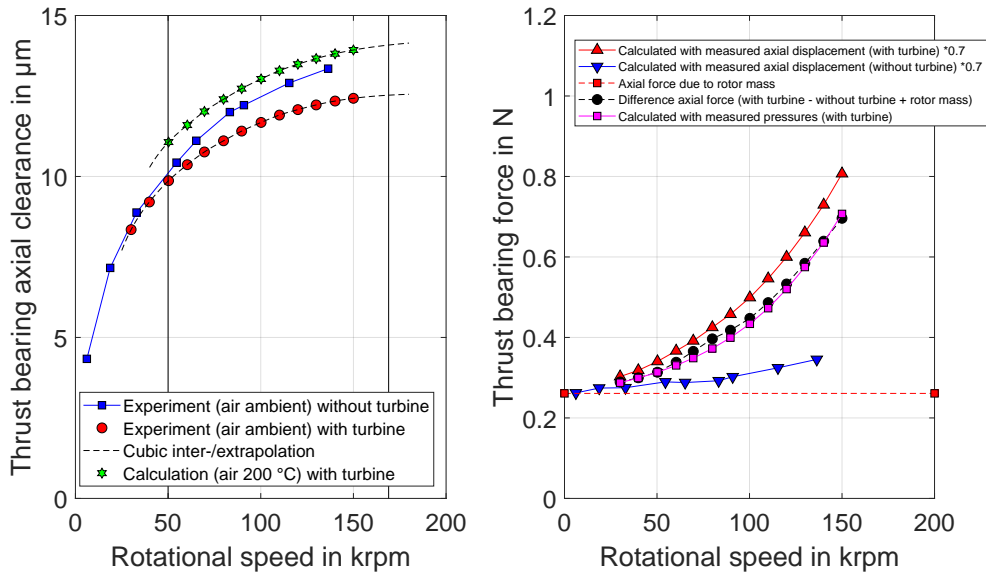


Figure 5.4 – Left: measured thrust bearing axial clearance for ambient air without turbine volute (blue squares) and with turbine volute (red circles), as well as calculated axial clearance (green hexagoms) with turbine volute and hot air, assuming constant thrust force. Right: calculated thrust forces with the measured axial clearance without turbine volute (blue down-pointing triangles) and with turbine volute (red triangles), as well as the thrust force without the effect of the fan impeller wheel (dashed line with black circles) and the calculated thrust force with measured pressures (magenta squares).

down-pointing triangles). Note that with the correction factor of 0.7, the bearing thrust force was nearly equivalent to the rotor weight for low speeds, whereas it increased for higher speeds, most likely due to the fluid impulse of the air that the fan ingested from the ambient.

The difference in the thrust force for case 2 and case 1 plus the thrust force due to the rotor weight (red squares in Figure 5.4) was the thrust force without considering the impact of the fan impeller. Figure 5.3 shows this difference with a dashed line marked with black dots. The thrust force was therefore between 0.26 N at zero speed (marked with a red square in Figure 5.3) up to 0.7 N at 150 krpm.

The graph also features a calculation of the turbine thrust force based on the measured turbine rotor-stator static pressure and on the measured turbine backface seal pressure. Section 4.6 introduces this thrust force calculation model based on the measured pressures (magenta squares in Figure 5.4). For the calculations here, the fan TE static gauge pressure ( $p_{st,4}$ ) is equal to zero and the fan TE static absolute pressure equal to the ambient pressure.

**Conclusion:** The thrust force calculations based on the measured pressures (magenta squares) and the thrust bearing axial clearance measurement (dashed line with black dots) show reasonable agreement ( $\pm 7\%$ ). This verifies both models and the experimental approach.

However, a final validation of both models and the experimental approach is still lacking. The author wishes to emphasize that a direct measurement of the thrust force was not possible due to the: (1) the size constraints for small-scale machines and (2) the low load capacity, and thus small tolerance for misalignment of the fluid film bearings.

### 5.3 Fan and turbine operated with ambient air

As mentioned previously, thrust force measurement is challenging. Additionally, shaft torque measurement of the small-scale FTU is complicated for the following reasons: (1) the shaft diameter is very small at 8 mm, (2) the dynamic gas film bearings with a radial clearance on the order of several  $\mu\text{m}$  have a low load capacity and a low tolerance to displacement or misalignment, (3) the torque is between 0 to 0.001 N m and therefore very low, (4) the temperatures are elevated up to 220 °C, and (5) the available space for any measurement device is restricted to a few millimeters. To the best of the author's knowledge, no torque measurement device that complies with the above is available.

It was therefore not possible to directly measure the power provided by the turbine (eq. 2.48) or the power provided to the fan (eq. 2.49). Thus, the fan and turbine powers were measured thermodynamically with the temperatures and pressures at the machine inlet and outlet, as well with the measured machine inlet mass flow rate (eqs. 2.60 and 2.79).

However, a run-out test can indirectly measure the shaft mechanical loss, which is the difference between the turbine and fan power  $P_{loss} = P_{drive} - P_{fan} = P_{turb} - P_{fan}$ . This loss has the same order of magnitude as the turbine and fan power, suggesting challenges for the thermodynamic turbomachinery power and efficiency measurement. The exact determination of the mechanical losses is therefore important (Section 5.4).

**Analytical mechanical loss model:** Demierre et al. [106] compared an analytical windage loss model to rotor run-out measurements of a microcompressor-turbine unit, which showed agreement within a  $\pm 10\%$  band. Chapter 3.5.4 in [12] describes this model in detail. The mechanical losses consist of:

- Bearing losses:
  - losses of the two herringbone-grooved journal gas film bearings
  - losses of the spiral-grooved thrust gas film bearing that consists of a plain part at a radius of 5-8 mm and a grooved part at a radius of 8-9.4 mm
- Windage losses (fully turbulent):
  - Fan impeller (diameter of 19.2 mm)
  - Shaft (diameter of 8 mm)
  - Seal (diameter of 8 mm and 7 mm)
  - Turbine impeller (diameter of 15 mm)

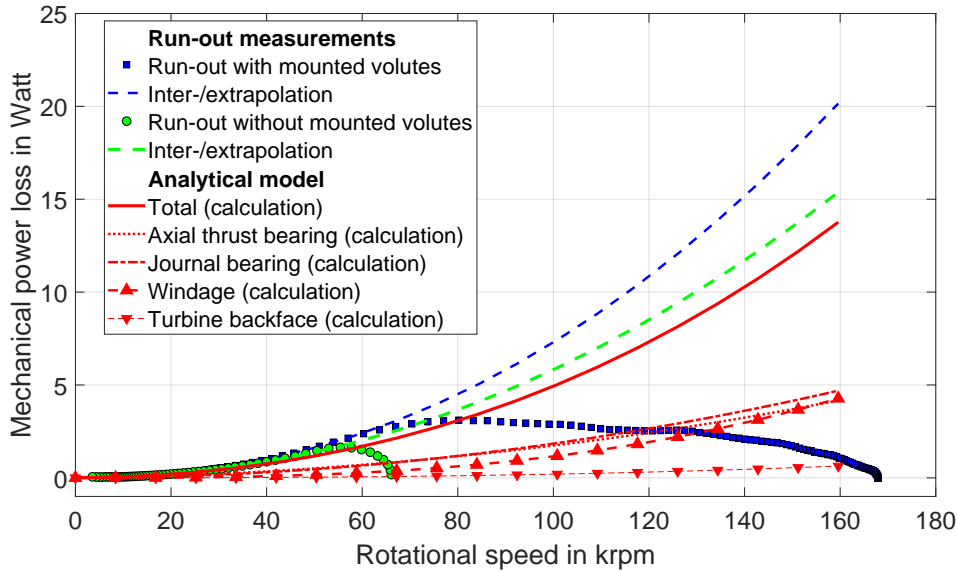


Figure 5.5 – Mechanical losses calculated using the experimental shaft run-out without mounted fan or turbine volute (green), with both fan and turbine volute mounted (blue), and the result of the analytical model (red lines).

Additionally, the turbine backface features losses. The model from Daily and Nece [105] for regime III (laminar flow, separate boundary layers) calculates this turbine backface disk friction loss.

**Experimental mechanical loss measurement:** Figure 5.5 shows two run-out tests with air at ambient conditions. One run-out test was performed without mounted volutes (both fan and turbine) and two air nozzles accelerated the shaft. The experimental setup was similar to the vertical setup in Section 5.1. The pressure inside these nozzles was slowly decreased from 66 krpm to 55 krpm and the run-out without external forces began at this speed (green circles in Figure 5.5). The green thin dashed line shows an interpolation and extrapolation of the expected losses. The second run-out was similar to the one described in Section 5.2 with both the turbine and fan volute mounted. The mass flow rate into the turbine was continuously decreased from 168 krpm to 60 krpm, at which point no external forces acted on the turbine (blue squares in Figure 5.5). The thin dashed blue line shows an interpolation and extrapolation of the expected losses. Due to risk mitigation, the author did not conduct a run-out test at a higher rotational speed.

**Comparison:** The thick red line in Figure 5.5 shows the calculated mechanical losses due to the journal and thrust gas film bearing, turbine backface, seal, and shaft windage. This corresponds to the  $M_{loss}\omega$  term in eq. 2.49. These calculated losses are lower than the (ex-

### 5.3. Fan and turbine operated with ambient air

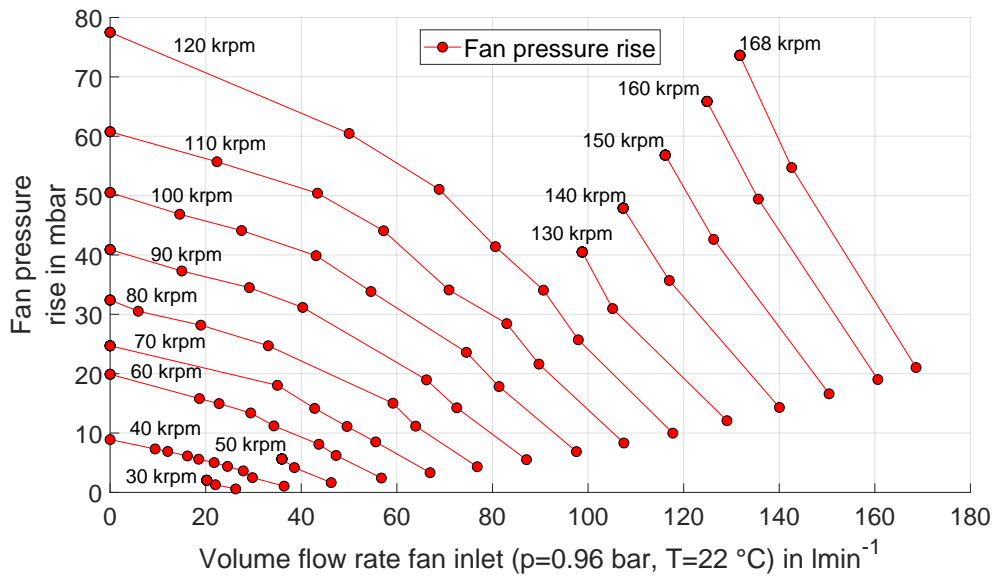


Figure 5.6 – Fan total-to-total pressure rise as a function of the fan inlet volume flow rate and the rotational speed in the case with ambient air.

trapolated) experimental predictions, since the calculation does not take into account the aerodynamic losses of the fan and turbine impeller. At a rotational speed of 168 krpm, the difference between the calculated mechanical losses and the measured extrapolated losses is 1.6 W.

The model suggests a total power loss of 15.4 W at a rotational speed of 168 krpm (red thick line), consisting of the thrust bearing loss of 4.6 W (dotted line in Figures 5.5 and 5.7), the journal bearing losses of 5.2 W (dashed-dotted line), the windage losses of 4.9 W (dashed line), and the turbine backface losses of 0.7 W (thin dashed red line).

**Assumption:** Since Demierre [106] verified and Daily and Nece [105] validated the respective models and the (extrapolated) experimental run-out tests correlate reasonably to the models, the author assumes that the mechanical loss model is applicable for the FTU loss calculation. However, a final validation is still not possible due to the lack of an exact torque measurement device.

Note that the mechanical losses increase at higher temperatures, since the air viscosity increases. Although the viscosity of ambient air and steam at 220 °C are similar (about  $1.7 \cdot 10^{-5}$  Pas), the mechanical losses for the steam-lubricated gas film bearings is lower due to the lower density of steam ( $0.44 \text{ kg m}^{-3}$  for steam and  $1.13 \text{ kg m}^{-3}$  for ambient air). The steam-lubricated bearings feature the lowest mechanical loss, and the hot air-lubricated bearings feature the highest losses.

**Fan characteristic:** For operation with the SOFC stack, it is necessary to startup the FTU with zero volume flow rate, since the FTU begins the recirculation with a closed valve at the exit

(Chapter 6). As soon as the fan outlet total pressure is higher than the total pressure at the reformer inlet, the valve at the fan outlet is gradually opened and the recirculation starts. The stable FTU operation at this point is mandatory.

Thus, this operation was tested with ambient air (22 °C and 0.96 bar). Figure 5.6 shows the measured fan total-to-total pressure rise as a function of the fan inlet volume flow rate and the rotational speed. The pressure rise was measured with an open throttle at the fan outlet (right points in Figure 5.6) and a closed throttle at the fan outlet (left points) for rotational speeds of 30 krpm, 40 krpm, ..., 110 krpm, and 120 krpm. The right points represent therefore the pressure drop of the unthrottled measurement setup (Figure 5.10) and the minimal achievable fan pressure rise at given rotational speeds. With the proposed measurement test setup, it is therefore not possible to measure points on a speed line that are less throttled, respectively have a higher volume flow rate, since the test rig has no auxiliary fan at the outlet sides test section. A maximum pressure rise of 77.5 mbar is achieved at zero volume flow rate and a rotational speed of 120 krpm which is sufficient to overcome the pressure loss of the SOFC system at working conditions (55 mbar).

**Conclusion:** The FTU operates stable at zero volume flow rate, increased pressure rise and thus increased thrust force. Since the viscosity of the hot anode off-gas is comparable to the ambient air viscosity, the FTU is capable to start the AOR while preventing the fuel from bypassing the SOFC stack.

### 5.4 Calculation of turbomachinery parameters

As pointed out in Section 5.3, the shaft torque measurement was not possible. Thus, the fan and turbine powers were measured thermodynamically with the pressures and temperatures at the machine inlet and outlet, as well with the measured machine inlet mass flow rate, according to eq. 2.60 and eq. 2.79. However, this thermodynamic measurement approach is challenging, overall for small-scale turbomachines due to: (1) high area-to-volume ratio and thus increased heat fluxes to the environment, (2) low fan and turbine power, and (3) low mechanical efficiency and thus high heat dissipation.

Figure 5.7 shows the fan impeller domain with its boundaries marked with a green dashed line. Several enthalpy streams, power, and heat fluxes cross the control volume boundaries. At the fan inlet (1) and outlet (8) the measurement of mass flow rate, temperature, and pressure allow for the determination of the enthalpy streams. When considering all energy fluxes shown in Figure 5.7, the steady energy balance is given as follows.

$$P_{fan} + \dot{m}_1 h_{t,1} - \dot{m}_8 h_{t,8} + \dot{m}_l h_{t,l} + \dot{Q}_{cond} - \dot{Q}_{amb} - \dot{M}_{z,s} \omega = 0 \quad 5.3$$

A similar equation is formulated for the turbine side, where the temperature and pressure are measured at the turbine inlet (1) and outlet (12). The mass flow rate is measured at the turbine inlet, but not at the outlet.

$$-P_{turb} + \dot{m}_1 h_{t,1} - \dot{m}_{12} h_{t,12} - \dot{m}_l h_{t,l} + \dot{Q}_{cond} \pm \dot{Q}_{amb} - \dot{M}_{z,s} \omega = 0 \quad 5.4$$

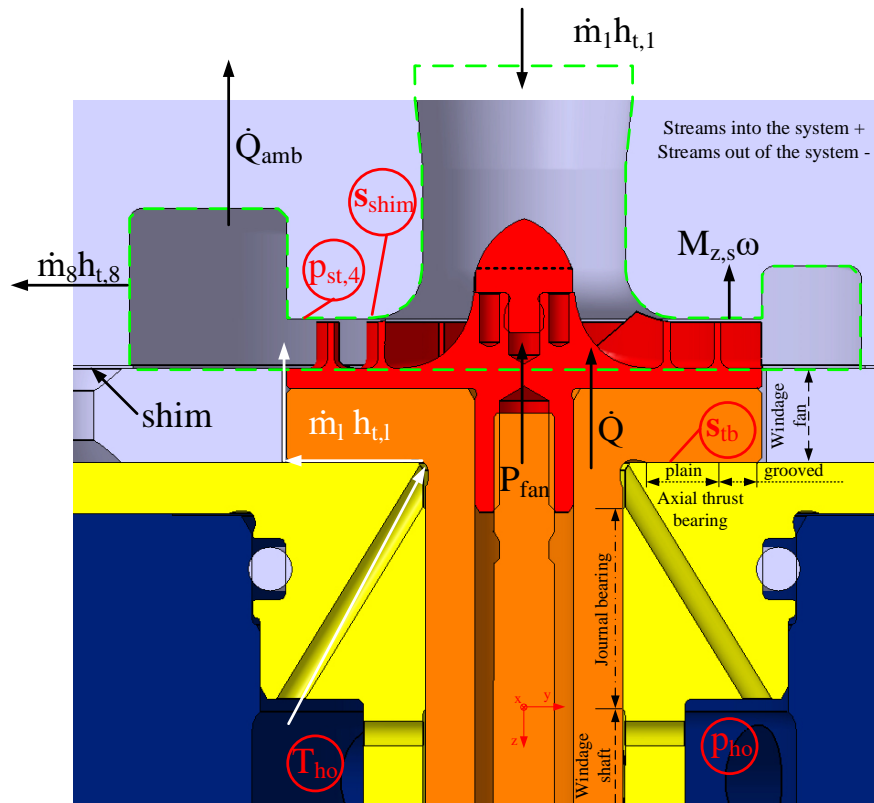


Figure 5.7 – Overview of enthalpy streams, power, and heat input and output to the fan fluid domain (green dotted line).

As Table 4.1 states, the nominal fan tip clearance is set to  $50\ \mu\text{m}$ . However, for risk mitigation, the first tests used a  $100\ \mu\text{m}$  shim (Figure 5.7), which increased the fan blade tip clearance to  $150\ \mu\text{m}$ , yielding a relative running blade tip clearance of  $0.071$  ( $\frac{s_{4,n}}{b_{4,n}} = \frac{0.05+0.1-0.01}{1.82+0.05+0.1-0.01} = \frac{0.14}{1.96}$ ) at  $168\ \text{krpm}$  (nominal conditions) with the consideration of the thrust bearing clearance at hot conditions (assumption of  $10\ \mu\text{m}$ ). Figure 5.4 shows green hexagrams that correspond to the calculated values for air at  $200\ ^\circ\text{C}$  without mounted fan volute. The turbine featured a blade tip clearance of  $133\ \mu\text{m}$ , yielding a relative running blade tip clearance of  $0.20$  ( $\frac{s_{7,n}}{b_{7,n}} = \frac{0.133+0.01}{0.719+0.01}$ ) at  $168\ \text{krpm}$ . A high relative tip clearance decreases the fan and the turbine efficiency, due to increased tip leakage, and reduces the fan efficiency (Tables 4.4 and 4.5), as well as the turbine efficiency. An increased tip clearance also reduces the shroud torque ( $M_{z,s}$ ). The efficiency calculation assumes an adiabatic fan and turbine shroud, i.e., the viscous losses due to the shroud torque only increase the temperature of the fan fluid. Hence,  $M_{z,s}\omega$  in eqs. 5.3 and 5.4 is approximately zero. The values obtained with the numerical simulations (Sections 4.4.5 and 4.5.4) suggest that the shroud torque power ( $M_{z,s}\omega$ ) may reach 5 % of the fan power for the non-throttled case (right black hexagram) of the  $168\ \text{krpm}$  speed line in Figure 5.12. For the turbine side, the shroud torque power may reach 1 % of the turbine power (non-throttled fan case at  $168\ \text{krpm}$ ).

Both the leakage mass flow rate from the turbine to the housing and from the housing to the fan fluid domain, as well as heat dissipation may significantly affect the power and efficiency measurements:

**Leakage:** Concerning the fan side, the leakage mass flow rate from the pressurized housing (due to the turbine) towards the fan TE corresponds to the difference between the fan outlet and inlet mass flow rates ( $\dot{m}_l = \dot{m}_8 - \dot{m}_1$ ). The leakage flows from the housing to the thrust bearing within four 1 mm diameter aeration holes, through the in-ward pumping thrust bearing, and enters the fan impeller fluid domain at the TE (see white arrows in Figure 5.7). This leakage flow is determined by the thrust bearing clearance ( $s_{tb}$ ) of 0-14  $\mu\text{m}$ , the shaft rotational speed ( $\omega$ ), the actual thrust bearing geometry, the housing conditions ( $p_h$  and  $T_h$ ), and the total-to-static pressure ratio between the housing and the fan TE ( $p_h/p_{st,4}$ ). Figure 5.12 shows the static housing pressure that is equal to the total pressure (fluid velocity near zero), as well as the fan TE shroud pressure at  $0^\circ$ ,  $120^\circ$ , and  $240^\circ$ . Since the fan power was deduced from the mass flow rates and temperature measurements, the leakage flow temperature had a direct impact on the measured fan power.

This leakage flow would not influence the actual measured power if it has the same temperature as the fluid at the fan inlet and the power is evaluated with the measured mass flow rate at the fan outlet ( $P_{fan} = \dot{m}_8(h_{t,8} - h_{t,1})$ ). If the leakage flow temperature is higher than the fan inlet temperature, the actual measurement overestimates the fan power, and thus underestimates the fan efficiency (and vice versa).

If the fan power is calculated with the fan inlet mass flow rate, a leakage flow would not influence the actual measurement, if the leakage flow temperature is the same as the fluid temperature at the fan TE ( $P_{fan} = \dot{m}_1(h_{t,8} - h_{t,1})$ ). If the leakage flow temperature is higher than the fan TE temperature, the actual measurement overestimates the fan power, and thus underestimates the fan efficiency (and vice versa).

**Heat dissipation:** The heat input to the fan impeller via conduction ( $\dot{Q}_{cond}$ ) has two main sources: (1) the heat conduction within the shaft, shaft screw, and the housing because of a temperature gradient between the fan and the turbine, as well as (2) the more dominant heat dissipation due to the losses of the journal bearings, the thrust bearings, the shaft windage, and turbine backface (Figure 5.5). The heat conduction to the environment ( $\dot{Q}_{amb}$ ) in eqs. 5.3 and 5.4 was approximately zero because of the glass fiber insulation (Figure 5.11). The turbine  $\dot{Q}_{amb}$  can be either negative or positive when turbine outlet temperature is higher or lower, respectively, than the oven temperature.

The influence of the leakage mass flow rate and the heat addition is evaluated more closely for the fan side. The following three different isentropic total-to-total fan efficiencies are defined and compared. The first corresponds to that one already defined in eq. 2.61, which is based on



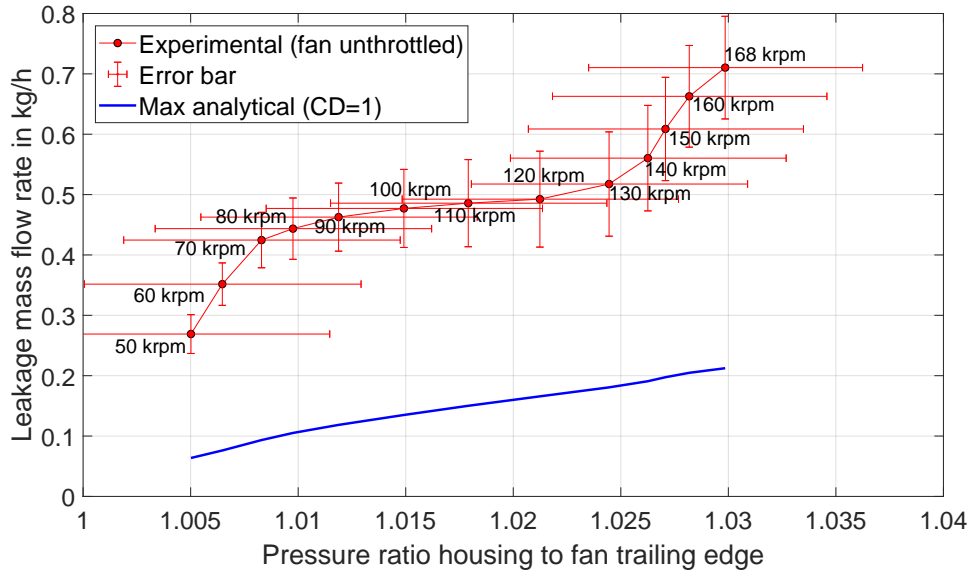


Figure 5.8 – Comparison of the experimental and analytical ( $CD=1$ ) leakage mass flow rate from turbine to fan for non-throttled operation.

an adiabatic system with no leakage mass flow rate.

$$\eta_{is,1} = \frac{\dot{m}_1 (h_{t,8,is} - h_{t,1})}{\dot{m}_1 (h_{t,8} - h_{t,1})} = \frac{P_{is}}{P_1} \quad 5.5$$

$$\eta_{is,2} = \frac{\dot{m}_1 (h_{t,8,is} - h_{t,1})}{\dot{m}_8 h_{t,8} - \dot{m}_1 h_{t,1} - \dot{m}_1 h_{t,1}} = \frac{P_{is}}{P_2} \quad 5.6$$

$$\eta_{is,3} = \frac{\dot{m}_1 (h_{t,8,is} - h_{t,1})}{\dot{m}_1 (h_{t,8} - h_{t,1}) - \dot{Q}_{cond}} = \frac{P_{is}}{P_3} \quad 5.7$$

#### 5.4.1 Evaluation of the leakage from the turbine to the fan

Figure 5.4 shows the thrust bearing axial clearance ( $s_{tb}$ ) as a function of the rotor rotational speed that was measured with a LionPrecision C3S capacitive probe for an operation with air at 200 °C (green hexagrams). Figure 5.8 shows the measured leakage mass flow rate (red line) for the non-throttled fan (right points on the speed lines in Figure 5.12). The measured leakage mass flow rate from the turbine to the fan was up to 0.7 kg h<sup>-1</sup> at 168 krpm.

The measurement is compared to an analytical calculation based on a Laval nozzle that takes into account the thrust bearing axial clearance (see green hexagrams in Figure 5.4), the total pressure and temperature in the housing ( $p_{ho}$  and  $T_{ho}$ ), and the average fan TE shroud pressure. The blue line in Figure 5.8 shows this maximum possible leakage mass flow rate with a theoretical discharge coefficient of one ( $CD = 1$ ). This maximum leakage mass flow rate for the non-throttled fan is therefore 0.2 kg h<sup>-1</sup>, which is less than 4 % of the fan inlet mass flow

rate for all measured points between 50-168 krpm.

These results clearly suggest a significant discrepancy between the measurements and the theoretical maximum leakage mass flow rates. The author hypothesizes that this discrepancy was a consequence of residual swirl within the outlet side test section (further discussion in Appendix C). Consequently, the efficiency  $\eta_{i,s,2}$  from eq. 5.6 is evaluated using the calculated maximum possible leakage flow rate (blue line in Figure 5.8) instead of the measurements. The fan outlet mass flow rate is accordingly calculated with this maximum analytical value for the leakage mass flow rate and the fan inlet mass flow rate ( $\dot{m}_8 = \dot{m}_1 + \dot{m}_l$ ).

### 5.4.2 Influence of the leakage and heat on the turbomachine power and efficiency

Figure 5.9 compares the measured isentropic total-to-total fan efficiencies and power (eq. 5.5) with the two corrected values (eqs. 5.6 and 5.7). Section 5.5 describes the experiments in detail. The experimental mean ambient pressure was  $0.965 \text{ bar} \pm 0.004 \text{ bar}$ , the total fan inlet temperature was  $200 \text{ }^\circ\text{C} \pm 2 \text{ }^\circ\text{C}$ , and the rotational speeds were 50 krpm, 70 krpm, ..., 150 krpm, and  $168 \text{ krpm} \pm 1 \text{ krpm}$ . Correlations from the ISO 5801 norm [69] adjust all experiments to a constant rotational speed, a constant ambient pressure (0.96 bar), and a constant fan inlet total temperature ( $200 \text{ }^\circ\text{C}$ ).

Isentropic efficiency 1 and power 1 (eq. 5.5) are directly evaluated based on the measured data. The fan power is calculated with the measured fan inlet and outlet temperature, as well as with the inlet mass flow rate ( $\dot{m}_1$ ).

**Influence of the leakage:** Isentropic efficiency 2 and power 2 (eq. 5.6) account for the leakage mass flow. The leakage specific total enthalpy ( $h_{t,l}$ ) is determined using the housing temperature ( $T_{ho}$ ) and the housing pressure ( $p_{ho}$ ). It is assumed that this enthalpy is constant until the leakage flow enters the fan fluid domain at the fan TE. As pointed out in Section 5.4.1, the maximum theoretically possible leakage mass flow rate ( $\dot{m}_l$ ) with a discharge coefficient of 1 (blue line in Figure 5.8) is used. The fan outlet mass flow rate is calculated with this leakage mass flow rate ( $\dot{m}_8 = \dot{m}_1 + \dot{m}_l$ ).

The influence of the leakage rate on the measured fan efficiency is between +1.4 % and +0.3 %, and is thus very small. Consequently, the effect of the leakage flow rate on the measurements for both the turbine and fan fan are neglected.

**Influence of the heat dissipation:** Isentropic efficiency 3 and power 3 (eq. 5.7) account for the heat input from the thrust bearing losses. Here it is assumed that 50 % of the dissipated heat due to the thrust bearing losses is conducted to the stator part, whereas the other 50 % of the heat is conducted to the fan impeller, and thus into the fan fluid domain. The heat dissipation ranges between 0.3 W at 50 krpm and 3.0 W at 168 krpm. With respect to the measured fan power (1.3 W at 50 krpm and 18.8 W at 168 krpm), the thrust bearing heat dissipation had significant influence on power and efficiency measurements. Heat addition to the fan flow increases the measured fan power ( $P_1$ ), and thus decreases the measured isentropic fan efficiency ( $\eta_1$ ). When taking the heat addition effect into account, the net fan power is decreased

## 5.4. Calculation of turbomachinery parameters

( $P_3$ ), and thus the isentropic fan efficiency with heat addition correction is increased ( $\eta_3$ ). The difference between  $\eta_1$  and  $\eta_3$  was 2.8 percentage points at 50 krpm and 19.0 percentage points at 90 krpm.

Note, that the heat loss to the environment ( $\dot{Q}_{amb}$ ) that is neglected within this study would have the opposite effect. It would decrease the measured power ( $P_1$ ), and thus increase the measured efficiency ( $\eta_1$ ).

Similarly, the heat addition to the turbine domain has a significant impact on the power and efficiency measurement. Heat loss to the environment would increase the power ( $P_1$ ), and

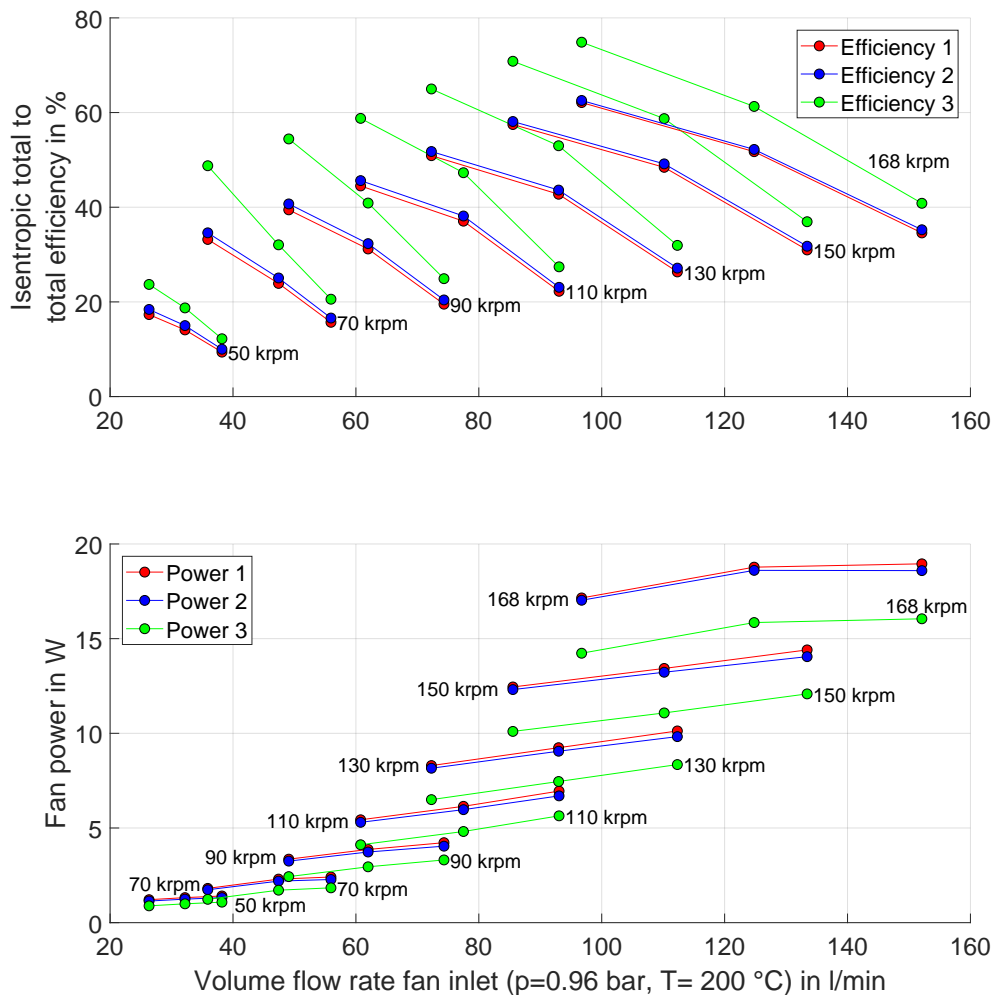


Figure 5.9 – Comparison of different efficiency and power definitions for the fan at hot conditions (200 °C).

thus increase the measured efficiency, and vice versa for a heat flux from the environment to the turbine fluid domain.

### 5.5 Fan and turbine operated with hot air at 200 °C

Figure 5.10 shows the setup of the test rig using hot air at 200 °C. The prototype with all measurement sensors is inside a ceramic oven (volume of 60 l) that maintained a constant temperature of 200 °C, simulating the actual environment of the FTU in the SOFC hot box. The fan test temperature of 200 °C is a trade-off between the maximum temperatures for the shaft DLC coating (~250 °C), the maximum temperature of high-temperature plastics (~260 °C) such as PTFE, as well as the entire SOFC system design (Chapter 3). Since the volume of the oven is small and the fan ingests hot air directly from the oven volume, an air preheating system supplies the oven with excess hot air at 200 °C. The hot air distributor injects the preheated air into the oven parallel to the oven bottom (see lowest red arrow in Figure 5.10) to lower the vertical temperature gradient within the oven.

The fan test setup inside the oven used the standard test method “outlet side test ducts - category B test installation with inlet duct (category D)” in the ISO 5801 norm [69]. With respect to this norm, the test rig (Figures 5.10 and 5.11) features several differences:

- Fan inlet volume flow rate measurement with a bellmouth
- Fan inlet temperature measurement (3x)
- Fan outlet temperature measurement (2x)
- No shaft torque measurement

As mentioned in Section 5.3, the fan and turbine powers were measured thermodynamically using the inlet and outlet temperatures and pressures, as well with the measured inlet mass flow rate.

**Temperature and pressure measurement:** Table 5.1 provides an overview of the type and placement of the temperature and pressure sensors. Class 1 k-type TCs with a 1.5 mm diameter measure the temperatures, whereas a Scanivalve (DSA 3218) measures the static pressures. At the fan outlet, an additional differential capacitance manometer from MKS (MKS 226A) measures the static pressure, since it is more precise than the Scanivalve. This MKS measures the differential pressure between the fan outlet and the oven environment and has a slightly increased pressure with respect to the environment (less than 1 mbar).

Generally, at the machine inlet and outlet, the four pressure taps with a diameter of 0.7 mm are placed 12 mm upstream of the two immersed TCs. The static pressure taps and the TC probes are rotated by 45° to minimize flow distortion. The distance between the first measurement probe (static pressure tap) and the next upstream flow distortion (e.g., a straight

## 5.5. Fan and turbine operated with hot air at 200 °C

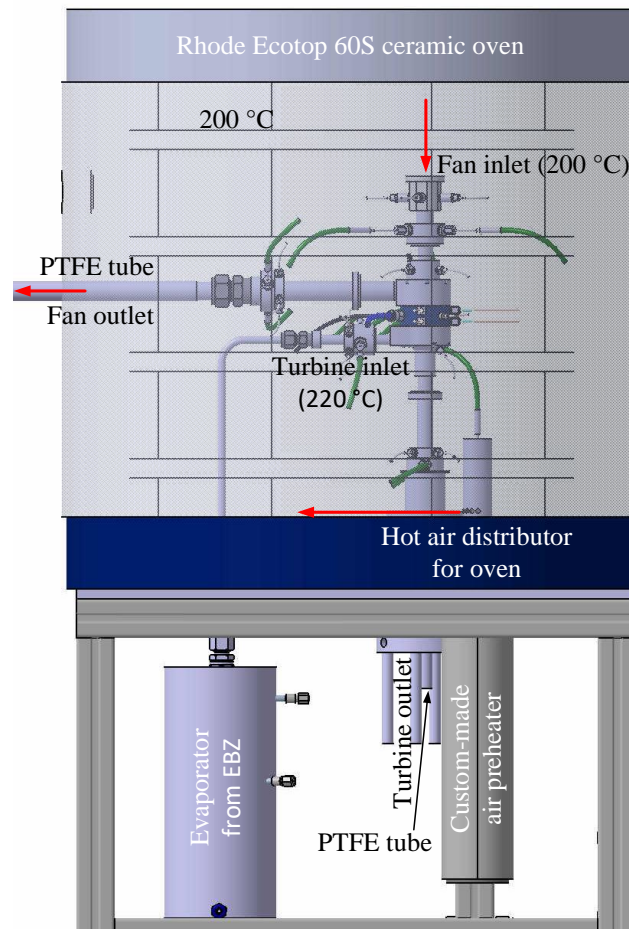


Figure 5.10 – Overview of the fan test rig for hot air at 200 °C (without glass fiber insulation).

pipe connector or a nozzle) is five-times the diameter. However, at the fan inlet this length is only  $0.7 \cdot d_1$ , since the fluid from the oven environment is considered as nearly-undistorted (low turbulence). The TCs are immersed by  $\frac{2}{3}$  of the pipe radius. A general rule of thumb is an immersion depth of five to 10-times that of the TC diameter [107]. At the fan inlet, the immersion depth is not critical, since the fluid total temperature is equal to the oven environment (about 200 °C). The maximum fan total temperature increase is on the order of 13 °C (Table 4.4); hence, an immersion depth of 4-times the TC diameter is sufficient at the fan outlet. However, the immersion depth at the turbine inlet (2) and outlet (2.7) is relatively small compared to the temperature gradient, which is 20 °C at the turbine inlet down to -30 °C at the outlet (Table 4.8). The temperature measurement could therefore be influenced by heat conduction.

Additionally, heat conduction between the measurement tubes and the environment or the oven environment occurs. This heat conduction of the metallic test section tubes to the environment is limited by decoupling it with a PTFE tube. These PTFE tubes, shown in Figures 5.10 and 5.11, reduce the heat conduction within the tubes by 60-times that of standard steel tubes.

## Chapter 5. Fan-Turbine Unit Experiments

Table 5.1 – Fan and turbine inlet and outlet temperature and pressure measurements.

Sensor	Position	Number <sup>a</sup>	Distance <sup>b</sup>	Immersion <sup>c</sup>	Pipe diameter in mm
Total temperature <sup>d</sup>	Fan inlet	3	$0.7 \cdot d_1$	$2.7 \cdot d_{TC}$	12
	Fan outlet	2	$6 \cdot d_8$	$4 \cdot d_{TC}$	16
	Turbine inlet	2	$7 \cdot d_1$	$2 \cdot d_{TC}$	6
	Turbine outlet	2	$6 \cdot d_{12}$	$2.7 \cdot d_{TC}$	12
Static pressure <sup>e</sup>	Fan outlet	4 <sup>g</sup>	$5.2 \cdot d_8$	0	16
	Turbine inlet	4 <sup>g</sup>	$5 \cdot d_1$	0	6
	Turbine outlet	4 <sup>g</sup>	$5 \cdot d_{12}$	0	12
Static pressure <sup>f</sup>	Fan outlet	4 <sup>g</sup>	$5.2 \cdot d_8$	0	16

<sup>a</sup> number of probes that are evenly-distributed within the pipe ( $\frac{360^\circ}{\text{number}}$ )

<sup>b</sup> distance to the next upstream flow distortion (such as a nozzle or a straight pipe connector) with respect to the pipe inner or hydraulic diameter

<sup>c</sup> immersion of the (thermocouple) probe into the pipe with respect to its diameter

<sup>d</sup> measured with k-type thermocouple that have a diameter ( $d_{TC}$ ) of 1.5 mm

<sup>e</sup> measured with a 0.7 mm pressure tap that is connected to a Scanivalve (DSA 3218)

<sup>f</sup> measured with a 0.7 mm pressure tap that is connected to an MKS (MKS 226A)

<sup>g</sup> pneumatically-averaged to one pressure line

In addition, the temperature gradient between the oven (200 °C) and the ambient is limited on the fan outlet side. Outside of the oven, electric heating tape (Figure 5.14) is wrapped around the PTFE tube to maintain a temperature of 170 °C.

Since thermodynamic measurements determine the fan power, an adiabatic system is essential. Thus, high-temperature glass fiber insulation is wrapped around the entire FTU body and all pipes inside and outside the oven to limit heat loss. Figure 5.11 shows the glass fiber tape for the fan outlet side test section and the turbine inlet side test section. During testing, tape covers the entire FTU and all tubes. If the FTU is stationary and the electric heater at the oven outlet is not in operation, the temperature difference between the three TCs at the fan inlet and the two TCs at the fan outlet side test section were within a  $\pm 1$  °C range. The four TCs at the turbine inlet and outlet section were within a  $\pm 2$  °C range. Because of the vertical temperature gradient within the oven, which is higher at the bottom of the oven, as well as the short and unheated turbine outlet PTFE tube (Figure 5.10), the difference between the inlet and outlet TCs is higher for the turbine side when the FTU is not operational. However, these TCs show the same temperature within the measurement uncertainty of  $\pm 0.5$  °C, while hot air flows through the non-rotating turbine. Since the turbine outlet side features no heating wires, the possible heat loss within the PTFE tube from the oven to the environment is 0.1 W,

$$\dot{Q} = \frac{0.25}{0.09} \pi (0.01^2 - 0.005^2) (200 - 20) \text{ W} = 0.1 \text{ W} \quad 5.8$$

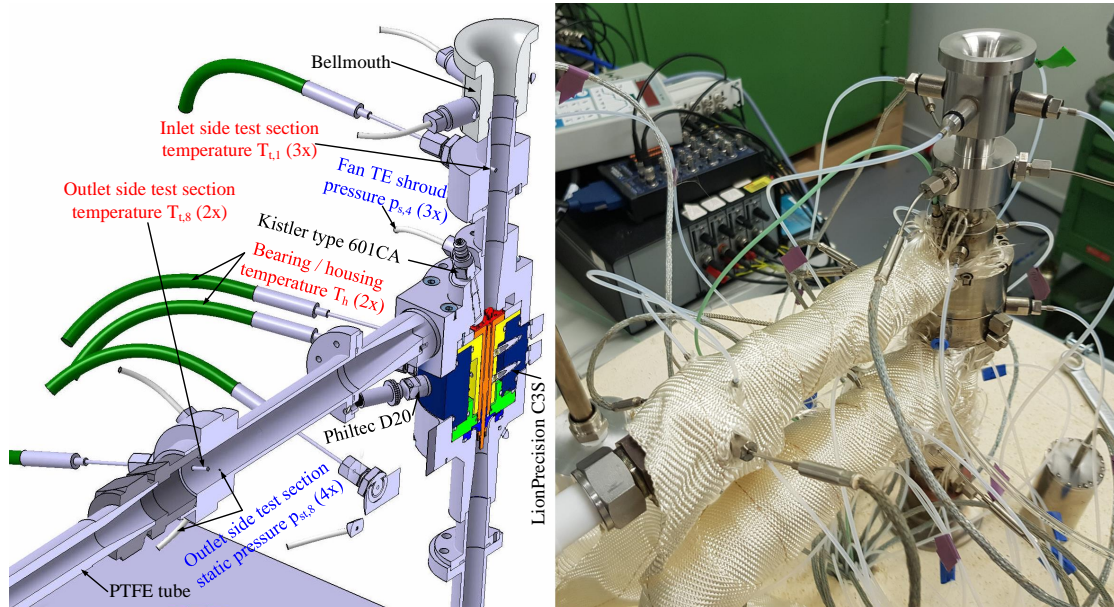


Figure 5.11 – Digital image of the fan test rig with the measurement positions (left) and real implementation (right), partly covered with glass fiber insulation.

considering a temperature gradient of 180 °C within the oven wall (90 mm on all sides). The oven walls feature several holes for the tubes, as well as the sensor cables. All these holes are insulated with mineral wool to limit the heat conduction from the oven to the environment. The test rig features four additional TCs: one at the top of the oven, one inside the volume flow rate measurement device in the outlet side test section (fluid outlet density calculation), and two inside the fan housing, close to the journal bearings (Figure 5.11 and red dots in Figure 4.1). The Scanivalve measures the gauge static pressures inside the oven, before the volume flow rate measurement device at the outlet (fluid outlet density calculation), inside the FTU housing, inside the turbine seal (Figure 4.1 on the left side in the middle), at the fan TE (Figure 4.1 on the left side at the top), and at the turbine rotor-stator interface (Figure 4.1 on the left side at the bottom). The fan volute features three evenly-distributed static pressure measurements with a diameter of 0.4 mm located at a diameter of 18.55 mm (the fan TE is 19.2 mm). The first is located at 0°, coinciding with the end of the volute logarithmic spiral, and thus the volute outlet section (Figure 4.18). The turbine stator features a half circle pressure tap with a radius of 0.15 mm that measures the static rotor-stator pressure at the turbine shroud. The half circle center is positioned at a diameter of 15.3 mm. A Lufft Opus 20 room climate tracker measures the ambient pressure.

**Mass flow rate measurement:** A low-ratio long-radius bellmouth according to the ISO 5167-3 norm [95] limits the pressure loss at the fan inlet. An MKS 223B (0.01 bar) measures the differential pressure between the bellmouth (four pneumatically-averaged static pressure

measurements) and the oven environment, thus allowing for the fan inlet volume flow rate ( $\dot{V}_1$ ) to be calculated. Since the inlet Reynolds number based on the outer bellmouth diameter ( $Re_D$ ) is lower than the limit value in the ISO 5167 norm, the implemented bellmouth is calibrated with the volume flow rate measurement device at the fan outlet.

An orifice plate with wall taps in accordance to the ISO 5167-2 norm [95] measures the fan outlet volume flow rate. An MKS 226A (0.133 bar) measures the quarter circle nozzle differential pressure. In order to deswirl the fan exhaust flow a cross-shaped flow straightener with a length-to-diameter ratio ( $l/D_8 = 24/12$ ) of two is placed at  $45D_8$  after the fan volute outlet diffuser, a Zanker flow conditioner plate is placed at  $63D_8$ , and the quarter circle nozzle is placed at  $93D_8$  (devices not visible in Figure 5.10).

A Coriolis mass flow meter from Emerson (D S006S) is placed at the turbine inlet.

**Rotational speed measurement:** As mentioned in Appendix C, two devices measure the shaft rotational speed at high temperatures (Figure 5.11):

- A high-temperature Philtec D20 optical probe (green dot in Figure 4.1).
- A high-temperature Kistler Type 601CA piezoelectric pressure sensor measuring the blade passing frequency at a diameter of 18.55 mm (Figure 4.1 on the left side at the top).

**Fan characteristic:** Figure 5.12 shows the fan characteristic with the total-to-total isentropic efficiency ( $\eta_{i,s,1}$ ), the total-to-total fan pressure rise, the static gauge pressure at the fan impeller shroud at a diameter of 18.55 mm (Figure 4.18), the housing gauge pressure, as well as the measured fan power without corrections ( $P_1 = P_{fan}$ ). As stated previously, correlations from the ISO 5801 norm [69] adjust all experimental values to a constant rotational speed, a constant ambient pressure (0.96 bar), and a constant total fan inlet temperature (200 °C).

The nominal speed line (168 krpm) has the same Mach number, based on the total inlet conditions, as the design case (SOFC anode off-gas consisting of water vapor, hydrogen, carbon monoxide, and carbon dioxide), and is therefore representative of operation when coupled with the SOFC. A black dot marks the nominal design point. At nominal operation, the total-to-total pressure rise was 55 mbar and therefore 15 mbar lower than the specified fan total-to-total pressure rise. This is due to following three reasons: (1) Since the test campaign features a 100  $\mu\text{m}$  shim, the clearance is elevated. Hence, the isentropic efficiency, and thus the fan pressure rise, are lower than the nominal values (design clearance is 50  $\mu\text{m}$ ). According to Table 4.4, the fan with a design clearance of 50  $\mu\text{m}$  has its pressure rise increased by 25 mbar to 80 mbar. (2) For a fan inlet total pressure of 1.05 bar, instead of 0.96 bar, the pressure rise according to the ISO 5801 norm [69] is 87.5 mbar ( $\frac{1.05}{0.96} 80$  mbar). (3) The anode off-gas has a lower heat capacity ratio (1.3) than air (1.4); hence, the pressure rise is lower, even though the Mach number is constant. The pressure rise is therefore approximately equal to the initially specified 70 mbar with the design clearance of 50  $\mu\text{m}$  (Table 4.5).



### 5.5. Fan and turbine operated with hot air at 200 °C

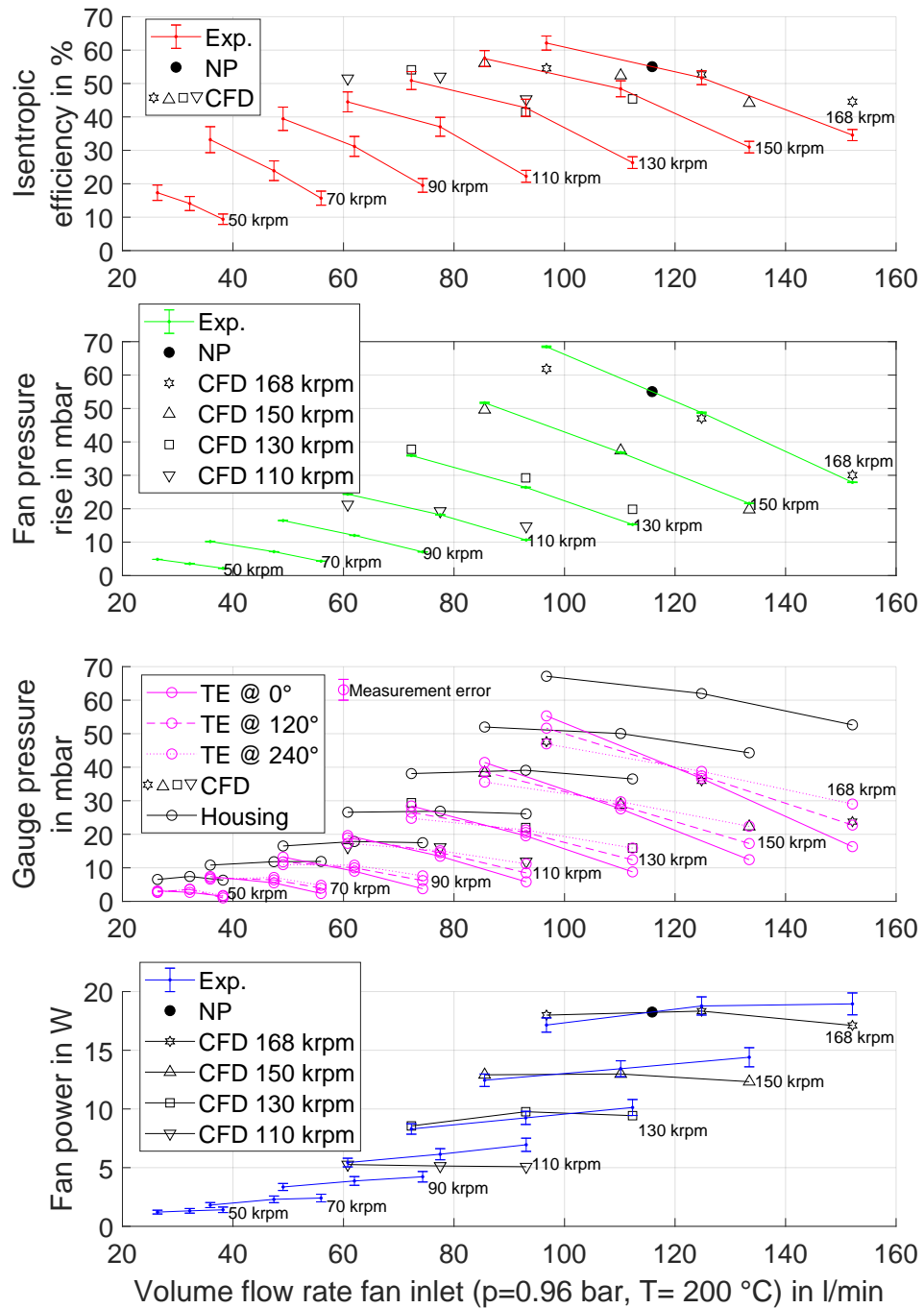


Figure 5.12 – The fan characteristic obtained from experiments (Exp.) with the respective measurement uncertainties and from numerical simulations (CFD). The black dot refers to the nominal point (NP) that has the same Mach number and flow coefficient as the design point with the anode off-gas.

At the design point, the volute specifies with respect to conservation of momentum ( $rc_u = \text{const.}$ ) and constant volute pressure. This is in agreement with the experimental data, since the difference between the measured fan TE shroud pressure at  $0^\circ$ ,  $120^\circ$ , and  $240^\circ$  was near zero (see magenta lines in Figure 5.12 at a constant speed line of 168 krpm). At higher mass flow rates, the fluid is accelerated within the volute, leading to a static pressure drop at  $0^\circ$  and a rise at  $240^\circ$ , and vice versa for lower mass flow rates.

With respect to the experiments and the CFD simulations, the fan TE shroud pressure, as well as the total-to-total fan pressure rise correlate well with the nominal point (center point at 168 krpm), as well as the non-throttled point (right point at 168 krpm). Near the nominal operation point, the efficiency and power of the CFD simulation and the experiment suggest excellent agreement. The difference between the measured and simulated power is  $-0.3 \text{ W}$  ( $-1.6\%$ ) and  $0.9$  percentage points for the isentropic efficiency. Both values are therefore within the measurement uncertainty.

For the non-throttled case, the difference in power is  $-1.8 \text{ W}$ , which is equal to  $-10\%$  with respect to the measured values. The measured efficiency 1 ( $34.6\%$ ) is therefore 10 percentage points lower than the simulated values. The simulated value ( $44.6\%$ ) is close to efficiency 3, according to eq. 5.7, which is  $43\%$ . Since the measured and simulated fan pressure rise and fan blade TE shroud pressure correlate well, the authors assume the numerical simulation as valid at this non-throttled point. A heat input into the fan fluid control volume is thus not negligible. This heat input is favored due to high fan mass flow rates, which increase the heat transfer coefficient between the fan impeller and the fluid.

At the throttled point (left point on the nominal 168 krpm speed line), the steady CFD simulation does not fully capture the increasingly unsteady fan flow. The difference between the measured and simulated total-to-total pressure rise is  $5 \text{ mbar}$ . The simulated fan power is within the measurement uncertainty. However, the simulated isentropic efficiency ( $54.4\%$ ) is significantly lower than the measured one ( $62.1\%$ ), due to the different total-to-total pressure rise.

The turbine used air at  $220^\circ\text{C}$  to drive the shaft, and thus the fan impeller. The higher the shaft power, the higher the turbine inlet pressure, the higher the expansion within the turbine, and the lower the turbine outlet temperature. Below rotational speeds of  $120 \text{ krpm}$ , the turbine outlet temperature was higher than  $200^\circ\text{C}$  and thus above the oven environment temperature and the fan inlet temperature of  $200^\circ\text{C}$ . The heat conduction from the turbine to the fan and the dissipated heat due to bearing losses crossing the fan fluid domain were therefore higher than those at rotational speeds above  $120 \text{ krpm}$ . The measured power and efficiency for rotational speeds at  $50 \text{ krpm}$ ,  $70 \text{ krpm}$ ,  $90 \text{ krpm}$ , and  $110 \text{ krpm}$  were therefore influenced by increased heat fluxes crossing the fan fluid domain. The difference between simulated and measured isentropic efficiency is between 7 percentage points for the throttled case up to 23.1 percentage points for the non-throttled case at the  $110 \text{ krpm}$  speed line. The center point and left point (throttled case) of the  $130 \text{ krpm}$  and  $150 \text{ krpm}$  cases showed better correlation ( $\pm 4\%$  points), since the heat fluxes crossing the fan impeller domain were lower.

### 5.5. Fan and turbine operated with hot air at 200 °C

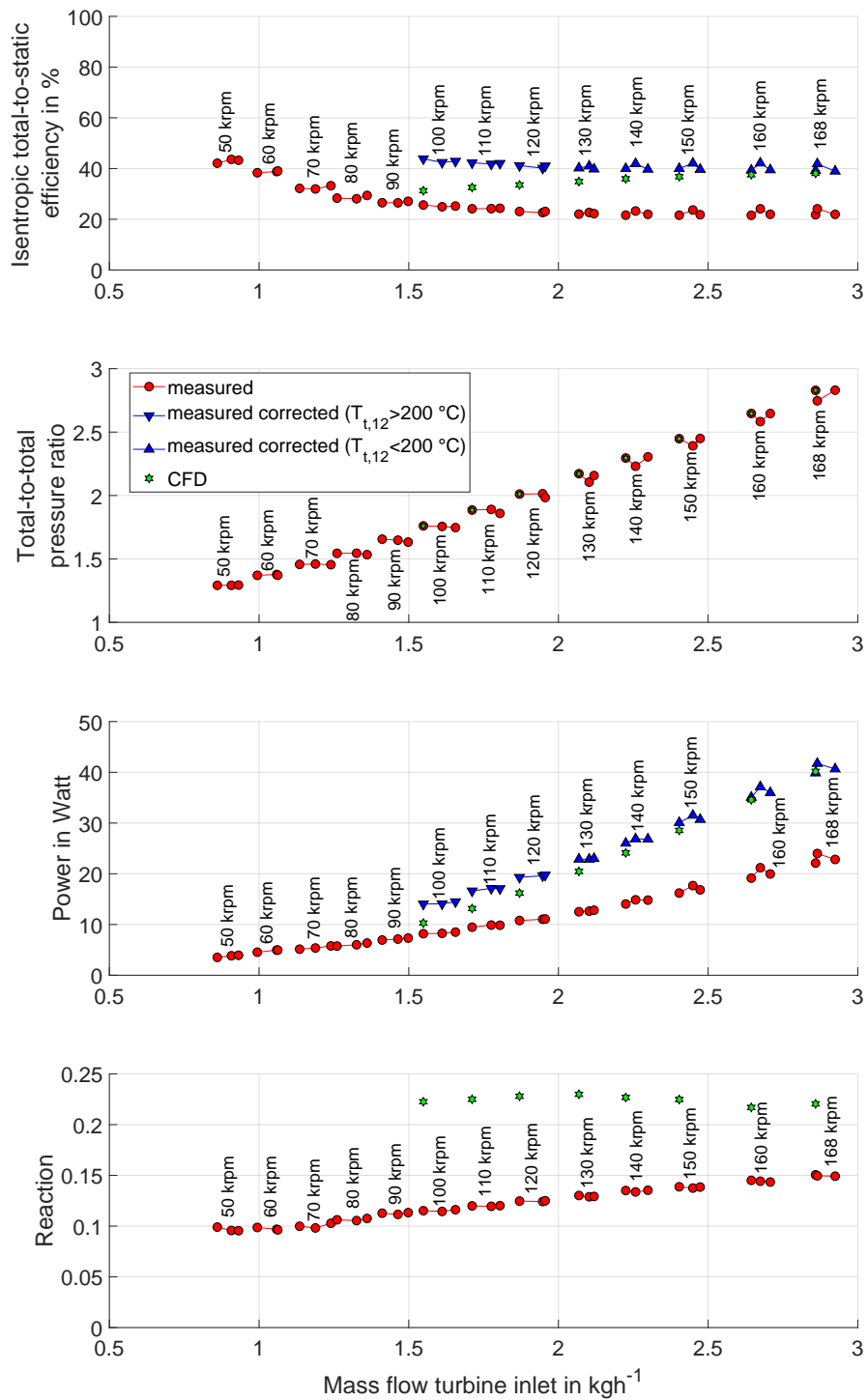


Figure 5.13 – The measured and simulated turbine characteristic with hot air at a total inlet temperature of  $220 \pm 2^\circ\text{C}$  and an ambient pressure of  $0.96 \text{ bar} \pm 0.004 \text{ bar}$ .

**Turbine characteristic:** Figure 5.13 shows the measured (red circles) and simulated (green hexagrams) turbine characteristic at 100 krpm, 110 krpm, ..., 150 krpm, 168 krpm. Section 4.5.4 describes this turbine single passage CFD simulation. The graph shows the turbine total-to-static isentropic efficiency, the total-to-total pressure ratio, the power, and the reaction based on the pressures according to eq. 4.17. The turbine inlet total temperature was  $200^{\circ}\text{C} \pm 2^{\circ}\text{C}$  and the turbine outlet static pressure was equal to the ambient pressure ( $0.96\text{ bar} \pm 0.004\text{ bar}$ ). The turbine inlet total temperature was constant, whereas the turbine outlet total temperature decreased with increasing turbine total-to-total pressure ratio. Based on an isentropic expansion, a temperature below  $200^{\circ}\text{C}$ , and thus below the oven temperature, was theoretically reached for pressure ratios higher than 1.3, which corresponds to rotational speeds higher than 50 krpm. However, due to the non-isentropic expansion process, the actual rotational speed required was higher.

With respect to the measured case from 50 krpm to 90 krpm, the turbine outlet total temperature ( $T_{t,12}$ ) was above  $200^{\circ}\text{C}$ ; hence, the turbine fluid cooled to  $204^{\circ}\text{C}$  (50-80 krpm case) and  $201^{\circ}\text{C}$  (120 krpm case). The measured power and efficiency at these points were therefore false, because the turbine fluid was cooled. However, the measured total-to-total pressure ratio, as well as the turbine reaction were not influenced by this cooling effect and were therefore correct.

The measured points at 130-168 krpm expanded the fluid sufficiently and reached temperatures of  $200^{\circ}\text{C}$  down to  $193^{\circ}\text{C}$  (168 krpm). These efficiency and power values that were corrected with the dissipated heat by the mechanical shaft losses tend towards the numerical simulation (blue up-pointing triangles). The blue down-pointing triangles correspond to the corrected efficiency and power values for those the measured turbine outlet total temperature ( $T_{t,12}$ ) is higher than  $200^{\circ}\text{C}$ . Section 4.5.4 describes the hot air single passage simulation.

For the hot air case, the measured reaction continuously increases from initial 10 % (50 krpm) towards 15 % at 168 krpm. With increasing mass flow rate and pressure ratio, the velocity increases and thus the rotor profile losses; hence, the reaction increases. The difference of the simulated values (22 %) is therefore significant. The author hypothesizes following two reasons: (1) the steady turbine CFD simulation cannot fully capture the unsteady turbine stator interactions. (2) A comparison of the experimental static pressure tap (a half circle with a radius of 0.15 mm) measurement and the numerical evaluation with a line surface at 15.18 mm (corresponding to the diameter that divides the half circle pressure tap in two equal surface areas) is not accurate enough.

### 5.6 Fan operated with hot air at $200^{\circ}\text{C}$ and turbine operated with water vapor at $220^{\circ}\text{C}$

Figure 5.14 shows the test rig that measures the turbine characteristic for water vapor at  $220^{\circ}\text{C}$ . A KNF SIMDOSE 10 membrane pump draws water from a deionized water tank. Within the actual SOFC system, the condensed water vapor coming from the SOFC stack and the burner

## 5.6. Fan operated with hot air at 200 °C and turbine operated with water vapor at 220 °C

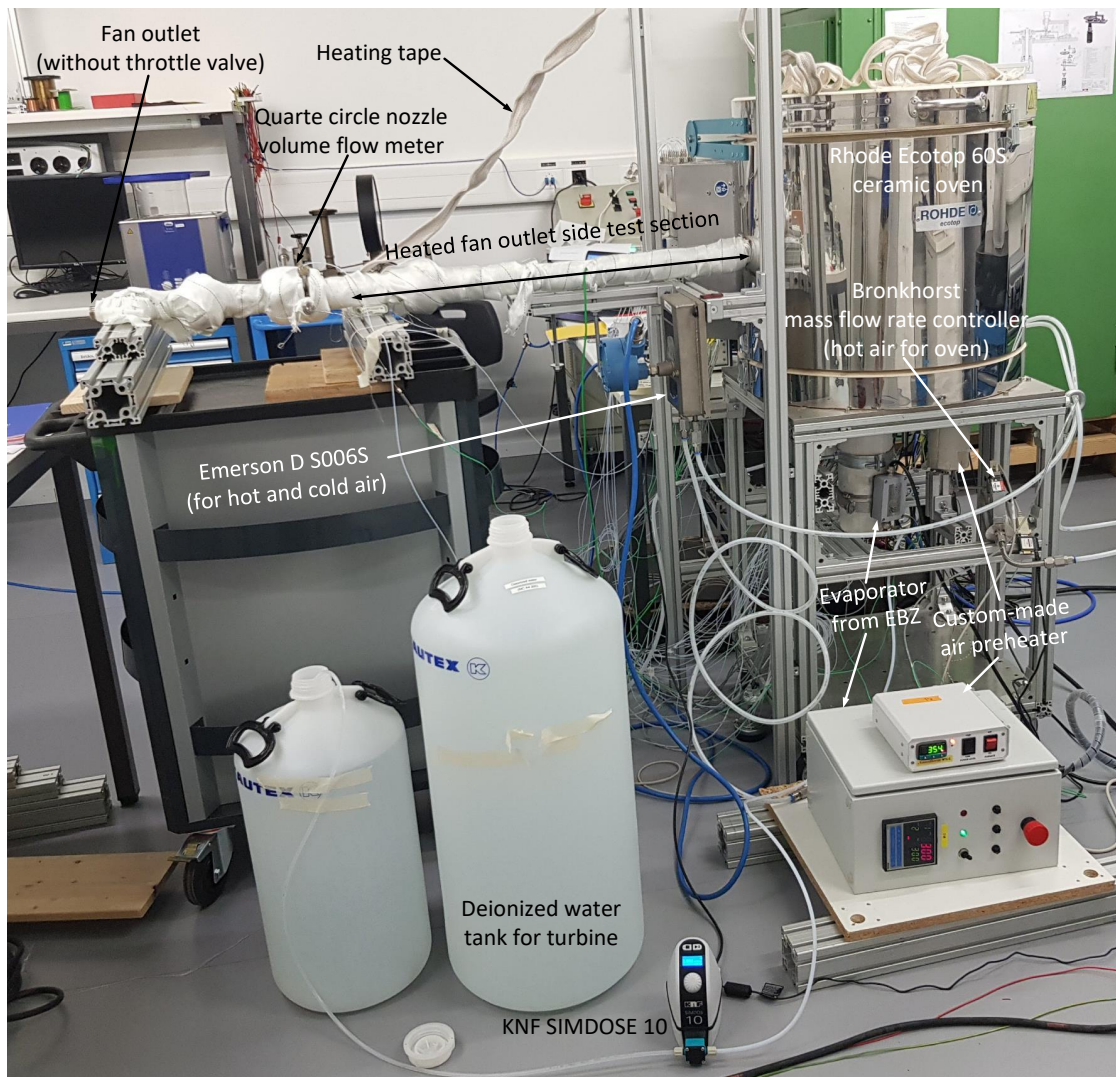


Figure 5.14 – The test rig for FTU measurements with hot air at 200 °C for the fan and water vapor at 220 °C for the turbine.

is acidic, due to the formation of carbon acids. Within these initial tests, the deionized water is pH neutral. A 35  $\mu\text{m}$  mesh filters the water from the tank. The KNF pump feeds the EBZ evaporator that heats, evaporates, and superheats the water vapor. The evaporator works at temperatures between 300-350 °C. The super-heated water vapor propels the turbine. The turbine inlet temperature is maintained at 220 °C. After the expansion within the turbine unit, the water vapor is released to the environment. The turbine outlet does not feature a condenser for this experimental setup.

Otherwise, the test setup is similar to the setup for the hot air characterization that Section 5.5 describes in detail. The four differences for the turbine system are as follows: (1) The fluid is water vapor instead of hot air. (2) A membrane pump from the company KNF delivers

the necessary turbine inlet pressure instead of pressurized air. (3) The mass flow rate measurement is performed with the KNF SIMDOSE 10 pump instead of the Emerson D S006S Coriolis mass flow meter. (4) Condensation of water vapor inside the pressure lines occurs. (5) Due to the membrane pump, the turbine inlet mass flow rate is pulsating whereas it is nearly-continuous for the hot air case, due to the large volume of the pressurized air tank. Because of the pulsating flow, the turbine is not able to operate at a constant shaft rotational speed, but fluctuates  $\pm 1$  krpm over time.

**Turbine characteristic:** Figure 5.15 shows the measured turbine characteristic, as well as the simulated design point (green square) and the simulated off-design points at 103 krpm, 118 krpm, 128 krpm, 138 krpm, and 147 krpm (green hexagrams). Section 4.5.4 describes this turbine single passage CFD simulation. The graph shows the turbine total-to-static isentropic efficiency, the total-to-total pressure ratio, the power, and the reaction based on the pressures according to eq. 4.17. The turbine inlet total temperature was  $220\text{ }^\circ\text{C} \pm 2\text{ }^\circ\text{C}$  and the turbine outlet static pressure was equal to the ambient pressure ( $0.96\text{ bar} \pm 0.003\text{ bar}$ ). Since turbine control with the membrane pump was very slow, due to the thermal inertia of the evaporator, the measured shaft rotational speeds correspond within  $\pm 3$  krpm to the previous hot air case. The rotational speed of 54 krpm corresponds to the initial speed of the turbine after startup. The turbine started at a total-to-total pressure ratio of 1.24, which was equal to a mass flow rate of  $0.7\text{ kg h}^{-1}$ . The pump mass flow rate was then steadily increased; hence, the total-to-total pressure ratio and the shaft rotational speed increased.

The mean turbine reaction was  $0.115 \pm 0.01$  for all measured points between 54 krpm and 147 krpm. During the acceleration from the 147 krpm operational point to the 159 krpm operational point, the turbine reaction dropped from 0.126 to 0.051. The reason for this drop were particles released from the evaporator. These particles blocked part of the turbine stator vanes, exactly upstream of the turbine rotor-stator shroud pressure tap ( $p_{st,7}$  in Figure 4.21 and a white half circle in Figure 4.25). The turbine total-to-total pressure ratio was thus higher and the isentropic efficiency decreased, as compared to the case without stator blockage. The measured parameters at 159 krpm correspond therefore not to the actual turbine characteristic without blockage.

The turbine inlet total temperature was constant, whereas the turbine outlet total temperature decreased with increasing turbine total-to-total pressure ratio. Based on an isentropic expansion, a temperature below  $200\text{ }^\circ\text{C}$ , and thus below the oven temperature, was theoretically reached for pressure ratios higher than 1.5, which corresponds to rotational speeds higher than 100 krpm. With respect to the measured cases at 54, 59, 69, 77, 87, and 103 krpm, the turbine outlet total temperature ( $T_{t,12}$ ) was therefore above  $200\text{ }^\circ\text{C}$ . The turbine fluid cooled to  $207\text{ }^\circ\text{C}$  (54-77 krpm case),  $205\text{ }^\circ\text{C}$  (87 krpm case) and  $204\text{ }^\circ\text{C}$  (103 krpm case). The measured power and efficiency values at these points were therefore incorrect, because the turbine fluid was cooled. However, the measured total-to-total pressure ratios, as well as the turbine reactions were not influenced by the cooling effect and were therefore correct. The measured points at 118 and 128 krpm expanded the fluid sufficiently and reached temperatures below

## 5.6. Fan operated with hot air at 200 °C and turbine operated with water vapor at 220 °C

the oven temperature of 200 °C. However, the dissipated heat from the mechanical losses heated the fluid to slightly above 200 °C.

**Comparison to CFD:** For the 138 krpm and the 147 krpm cases, the turbine outlet total temperature was below 200 °C: 199 °C and 196 °C, respectively, suggesting that the majority of the dissipated heat crossed the turbine fluid domain. A single passage simulation (Section 4.5.4) is therefore compared to the experiments. The inlet boundary condition is the total temperature and pressure and the outlet boundary condition is determined based on the measured ambient pressure and the calculated pressure losses of the turbine outlet side test section. The total-to-total pressure ratio for both the experiment and numerical simulation are therefore similar. The mass flow rate of the single passage simulation at 147 krpm is multiplied by 11.56 to obtain a similar mass flow rate as measured in the experiment (13 stator rows). The resulting corrected power (eq. 4.28) is shown as green hexagrams in Figure 5.15. This simulated power tends towards the blue up and down-pointing triangles (corrected measured power). The simulated total-to-static isentropic efficiency tends towards the measured total-to-static efficiency (red squares). In the CFD simulation, the isentropic efficiency is evaluated between turbine section 4 and 9, whereas the experiment evaluates the efficiency between section 1 and 12. Since at section 9 the velocity is relatively high ( $280 \text{ m s}^{-1}$ ) compared to the section 12 ( $5 \text{ m s}^{-1}$ ), the total-to-static isentropic efficiency is generally higher at section 12 compared to section 9 due to the pressure recovery within the turbine diffuser (section 10 to 11).

**Comparison to the design point:** Figure 5.15 also features the simulated design point at 175 krpm (green-filled squares), based on a total inlet pressure of 2.2 bar at section 4 and a static outlet pressure of 1 bar at section 9. Thus, the total-to-total pressure ratio is 1.89, the inlet mass flow rate is  $2.12 \text{ kg h}^{-1}$ , the isentropic total-to-static efficiency of 38 %, the reaction 0.13, yielding a power of 36 W. This simulations correlates well to the experiment c10 (Table 6.1). Considering the experiment c10, the mass flow rate was  $1.98 \text{ kg h}^{-1} \pm 0.12 \text{ kg h}^{-1}$ , the pressure ratio was 1.86, and the reaction was 0.148 at a rotational speed of 173.2 krpm. However, the turbine power and efficiency were not measured in experiment c10, due to the missing insulation.

**Comparison to hot air:** At a rotational speed of 147 krpm (84 % of the design speed) with water vapor at 220 °C, the measured turbine total-to-total pressure ratio was 1.90, resulting in a power of 24.8 W and a total-to-total efficiency of 40.6 %. The turbine also operated with hot air at 221 °C (Section 5.5). At a measured total-to-total pressure ratio of 2.45, the turbine rotated at 150 krpm, yielding a power of 30.1 W and an isentropic total-to-total efficiency of 40.0 %.

The two main reasons for the different turbine power and turbine pressure ratio between the water vapor and air cases are as follows: (1) The velocity of sound for the water vapor ( $545 \text{ m s}^{-1}$  at 220 °C), as compared to air ( $443 \text{ m s}^{-1}$  at 220 °C) is high. Thus, the pressure ratio of water vapor (1.9) is lower, as compared to air (2.45). (2) The dynamic viscosity of water

## Chapter 5. Fan-Turbine Unit Experiments

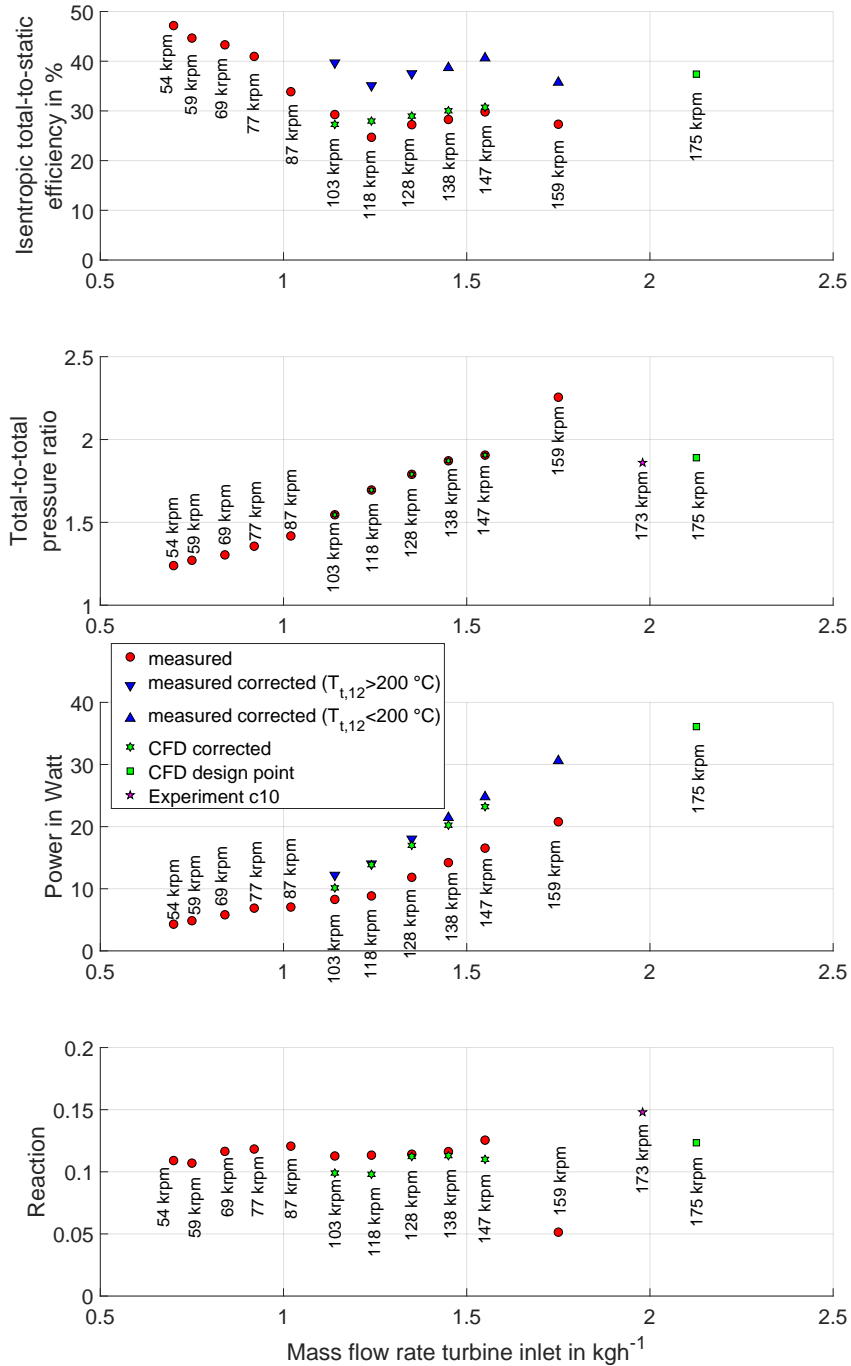


Figure 5.15 – The measured and simulated turbine characteristic with water vapor at a total inlet temperature of  $220 \pm 2^\circ\text{C}$  and ambient pressure of  $0.96 \text{ bar} \pm 0.003 \text{ bar}$  for the operation with a non-throttled fan. The green square indicates the design point with a total inlet temperature of  $220^\circ\text{C}$ , a total inlet pressure of 2.2 bar and a static pressure at section 9 of 1.0 bar.



vapor at 220 °C is  $1.70 \cdot 10^{-5}$  Pas, whereas it is  $2.69 \cdot 10^{-5}$  Pas for hot air. The losses of the water-vapor-lubricated journal and thrust gas film bearings are thus  $1 - \frac{\mu_{\text{vapor}}}{\mu_{\text{air}}}$  lower than for the air-lubricated bearings. For a rotational speed of 150 krpm, the air-lubricated bearing losses are 13.9 W, whereas it is 8.3 W for the water-vapor-lubricated bearings. The turbine power is therefore 5.6 W lower for the water-vapor-lubricated bearings at a rotational speed of 150 krpm.

## 5.7 Chapter conclusion

This chapter introduces the experiments on the FTU. The journal and thrust gas film bearings operate stable over the entire operational range. The measured radial vibrations at ambient conditions were lower than 0.002 mm and the axial vibrations were lower than 0.001 mm for the balanced shaft. Since the displacement signals yield no sub-synchronous components, the bearings operate in a very stable manner.

The thrust gas film bearing can operate in two modes: as a dynamic gas film bearing with an thrust bearing axial clearance on the order of 0.01 mm or as a static gas film bearing (supplied with pressurized air) with an axial clearance higher than 0.02 mm. A comparison of both thrust bearing operational modes (static and dynamic) suggested a more stable operation for the static bearing, since no sub-synchronous axial vibrations occurred. The static bearing operating mode is therefore preferred for the FTU.

To the best of the author's knowledge, a direct measurement of the thrust force of such a small-scale unit with gas film bearings is not possible due to the size constraints for small-scale machines and the low load capacity, and thus small tolerance for misalignment of the fluid film bearings. Nevertheless, the thrust force is an important parameter in the pre-design of the FTU. A reliable thrust force model is therefore essential.

Experimental measurements of the thrust bearing axial clearance can be related to the thrust force using a model by Schiffmann based on the narrow-groove theory [12]. According to performed measurements, the maximum static pressure at the end of the bearing spiral groove is overestimated by 42 % with the model by Schiffmann, leading to an experience correction coefficient of 0.7. This correction coefficient was confirmed by Nibourel [92] using CFD simulations of this specific spiral-grooved thrust bearing geometry. The investigated bearing is located between a radius of 8 mm and 9.4 mm and features 20 grooves; hence, yielding a low length-to-width ratio that is inconsistent with the assumption of an infinite number of grooves by the narrow-groove theory.

With this correction factor of 0.7 for the maximum static pressure within the groove, the indirectly measured thrust force with the thrust bearing axial clearance, and the calculated thrust force with the measured static pressures showed good agreement ( $\pm 7\%$ ).

However, the author wishes to emphasize that the effect of finite grooves on the axial force was

not investigated systematically. A validation of the thrust force models was also not possible, due to the lack of a direct thrust force measurement.

Another major limitation with respect to the performed turbomachinery measurements was the determination of the shaft torque: (1) the shaft diameter at 8 mm is very small, (2) the load capacity of the gas film bearings is low, (3) the torque was between 0 to 0.001 N m and therefore very low, (4) the temperatures were elevated (up to 220 °C), and (5) the available space for any measurement device is restricted to a few millimeters. To the best of the author's knowledge, such a device is not available off-the-shelf. A determination of the fan and turbine power and isentropic efficiency was therefore only possible with a thermodynamic approach involving the temperatures and pressures at the machine inlet and outlet, as well as the measured machine inlet mass flow rate. However, the high area-to-volume ratio involving high heat transfer and the bearing mechanical losses that are in the same order of magnitude as the fan and turbine power, made this thermodynamic approach very challenging.

Reasonable results were obtained by insulating the entire unit with glass fiber tape and decoupling the unit from the ambient with PTFE tubes. Despite these challenges, the single passage and full passage CFD simulations show good agreement within the measurement uncertainty ( $\pm 0.8$  W) for the experimentally determined fan power (18.8 W) at the nominal point (rotational speed of 168 krpm for air at 220 °C). A reliable measurement at off-design conditions involving more turbulent flow in the fan impeller and fan volute was, however, not possible. Measured and simulated power deviate by up to 30 % for the investigated conditions with hot air.

The measured turbine power was significantly lower than the value obtained from the CFD simulation. This deviation is within the windage and bearing mechanical loss measurements. Thus, the author assumes that the entire dissipated heat by the mechanical losses crossed the turbine control volume, leading to a decreased measured turbine power, and thus to a decreased measured isentropic efficiency. Another limitation was the significant deviation of the measured turbine discharge coefficient (0.76, rotational speed of 168 krpm for air at 220 °C) from the simulated coefficient (0.92). This difference was the result of partial stator blocking and stator blade plastic deformation due to the manufacturing process (milling). A comparison of the simulated turbine power to the corrected (with the heat dissipation) measured turbine power shows good correlation, within the measurement uncertainty ( $\pm 0.5$  W) at the design point. The measured turbine rotor-stator static pressure (1.23 bar) was 9 % lower than the simulated one (1.36 bar).

The measured turbine power for hot air at 168 krpm was 40 W, whereas the simulated turbine power was 36 W for water vapor at 175 krpm. Due to the lower viscosity, the water-vapor-lubricated bearing yields lower losses than the hot-air-lubricated bearing. However, the author could not validate these numbers, and the measurement setup for the turbine characteristic requires modification for an exact determination of the turbine power and efficiency.

The determination of the windage and bearing mechanical losses is essential to the design of the FTU and the determination of the (corrected) turbomachinery characteristic. The comparison of an analytical loss model to experimental run-out tests showed reasonable correlation (within  $\pm 20\%$ ). However, due to risk mitigation, the run-out was only performed up to a rotational speed of 60 krpm. The measured mechanical loss was then extrapolated to the design rotational speed (175 krpm).



# 6 Integration of the Fan-Turbine Unit with the SOFC System

This chapter provides an overview of the coupling of the SOFC with the FTU.

## 6.1 Measurement setup

For the first proof-of-concept, the SOFC stack and the FTU were in separate electrical ovens and not thermally coupled. The actual SOFC system with the HEX, as described in Chapter 3, was therefore not realized at this initial stage.

Figure 6.1 shows a) a schematic of the entire test rig, b) a digital image of the oven that contains the FTU, c) a digital image of the two Venturi nozzles that measure the RR, and d) a photo of the implemented FTU test rig next to the oven for the SOFC stack.

**Anode off-gas cooling:** On the anode side, the off-gas exits the SOFC at a temperature of up to 800 °C. Since the FTU is designed for an operational temperature of 200 °C, an HEX cools the off-gas actively with ambient air to 200 °C. Within the FTU oven, the off-gas temperature is adjusted to 200 °C in long pipes (1 and 3 in Figure 6.1) for passive heating and cooling. Thus, a constant temperature at the fan inlet is guaranteed, favoring stable operation of the FTU.

**Measurement of the recirculation ratio:** Downstream of this anode outlet HEX, the off-gas enters a custom-made double Venturi nozzle in accordance with ISO 5167-4 norm [95], as shown in Figure 6.1 c). The entrance is at 1 (anode off-gas), the exit to the burner is at 2, and the exit to the AOR fan is at 3. Thus, the burner mass flow rate is measured in the Venturi I and the AOR mass flow rate in Venturi II. This design is advantageous, since the temperature, pressure, and gas composition, and thus the density in both Venturi nozzles are approximately equal. Therefore, the RR is a function of the Venturi nozzle differential pressures ( $\Delta p$ ) between the positive and negative pressure tap (+/- in c of Figure 6.1) and the discharge coefficient

## Chapter 6. Integration of the Fan-Turbine Unit with the SOFC System

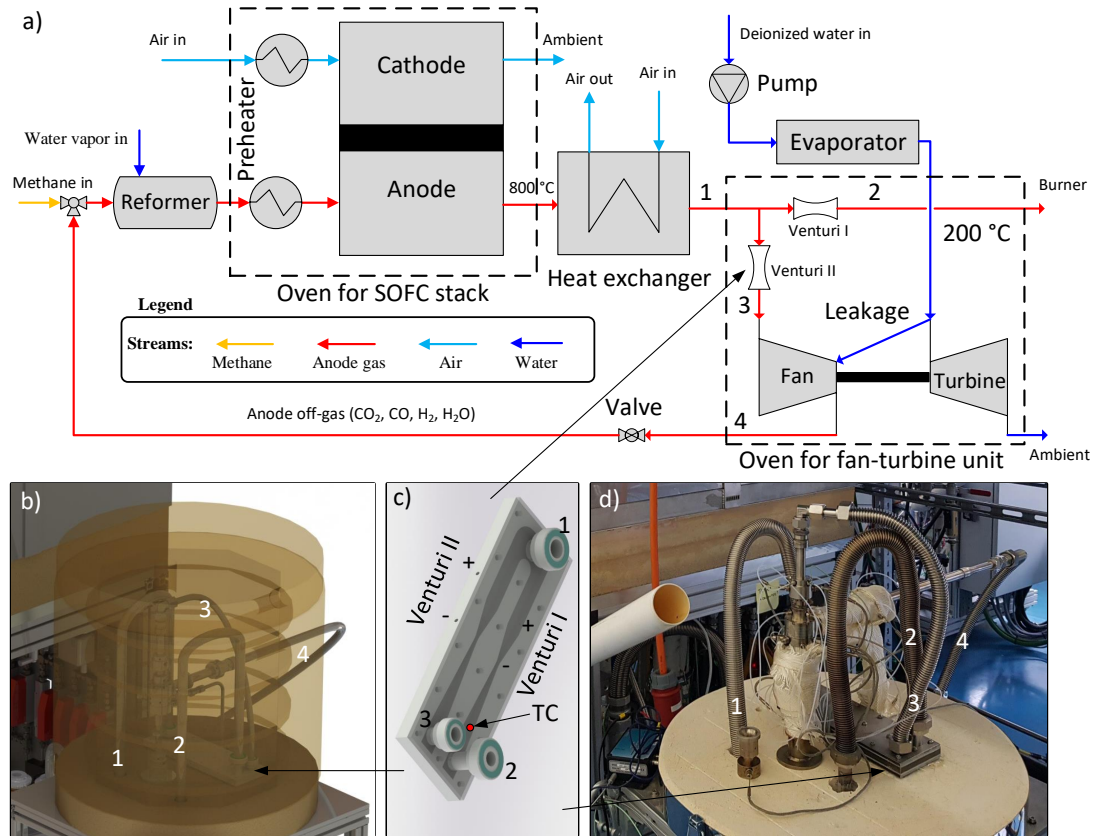


Figure 6.1 – a) Schematic of the FTU test rig coupled with the SOFC, as well as b) a digital image with mounted oven, c) the two Venturi nozzles for the recirculation rate measurement, and d) a photo with unmounted oven for the FTU test rig section.

( $CD$ ) that is a function of the Reynolds number based on the throat hydraulic diameter ( $Re_{d_h}$ ),

$$RR = \frac{1}{\frac{CD_I(Re_{d_h,I})}{CD_{II}(Re_{d_h,II})} \sqrt{\frac{\Delta p_I}{\Delta p_{II}}} + 1} \quad 6.1$$

assuming a similar fluid density and geometry for both Venturi nozzles. A 1.5 mm diameter k-type TC (see red point in c of Figure 6.1) measures the fluid temperature downstream of Venturi nozzle I. The negative pressure tap (see - in c of Figure 6.1) measures the differential pressure to ambient. With these two variables and the ambient pressure, it is possible to calculate the fluid density, viscosity, and velocity, to then compute the Reynolds number and the discharge coefficient. However, the exact fluid composition remains unclear and can either be estimated with the reformer, respectively SOFC stack model and their respective measured variables or analyzed with an anode off-gas extraction. According to the ISO 5167-4 norm [95], the Venturi nozzle discharge coefficient is constant for high Reynolds numbers (above  $2 \cdot 10^5$ ). However, for lower Reynolds numbers, this discharge coefficient drops with de-

ing Reynolds number. “It is believed that there is sufficient evidence available to justify the statement that the discharge coefficient of this type of Venturi tube [author’s note: machined convergent section] is a function of  $Re_d$ ” [95] and thus not of  $Re_D$ . The Reynolds number is therefore calculated with the throat hydraulic diameter of 7 mm (rectangular throat with 5x10 mm). For a Reynolds number of  $1.5 \cdot 10^4$ , the discharge coefficient is 0.967, and therefore, close to the value suggested by the ISO 5167-4 norm for machined Venturi nozzles (0.97 at  $Re_d = 4 \cdot 10^4$ ). For lower Reynolds numbers, however, the measured discharge coefficient drops to 0.85 at a Reynolds number of  $0.14 \cdot 10^4$ . At such an operational point, it is therefore important to calculate the discharge coefficient for an exact RR determination (eq. 6.1). During nominal SOFC operation the  $Re_{d_h}$  value is below 15000. Because of this and the Venturi nozzle geometry deviating from the norm (minimum diameter of 50 mm), the Venturi nozzles were calibrated in-house.

**Valve at fan outlet:** In order to prevent the fluid from bypassing the SOFC stack if the FTU is not operational, the fan outlet features a ball valve that is closed during SOFC startup (see valve in a of Figure 6.1). Once the SOFC stack reached nominal operation, the FTU starts (with a closed valve at the fan outlet) and rises the pressure at the fan outlet to greater than the reformer inlet pressure. Then the valve can be opened and the FTU begins to recirculate the anode off-gas. The initial water vapor supply to the reformer is decreased and the AOR increased gradually until the reformer water vapor supply can be turned off and the stack operates with the AOR exclusively.

**Evaporator:** Water vapor at 215 °C propels the FTU. A pump draws deionized water from a tank into an electrical evaporator (see a of Figure 6.1). At this initial stage, the deionized water supply of both systems are decoupled. This evaporator provides the steam to the turbine. The setup is similar to the one shown in Figure 5.14.

**Measurement of efficiency and power:** Due to risk mitigation (leakage of CO), it is not possible to use PTFE tubing at the fan and the turbine outlet. Hence, a reliable measurement of the turbine and fan power, as well as the efficiency was not possible, due to increased heat conduction from the oven to the environment.

## 6.2 Test at ambient conditions

In a first step, the FTU was tested at ambient conditions with nitrogen in order to evaluate the startup, shutdown, and RR measurement with the two Venturi nozzles.

Figure 6.2 shows the startup, steady operation, and shutdown of the FTU. The start of the AOR occurs after the valve (see valve in a of Figure 6.1) at the fan outlet is opened. This occurs between 106 s and 113 s (between the two dashed black lines). From 113 s to 276 s, the FTU accelerated and steady operation was observed from 276 s to 491 s (between the two solid black lines). The shutdown process then starts and the valve is closed between 595 s and 600 s (between the two dashed-dotted black lines). Finally, the FTU decelerated to zero speed (650 s).

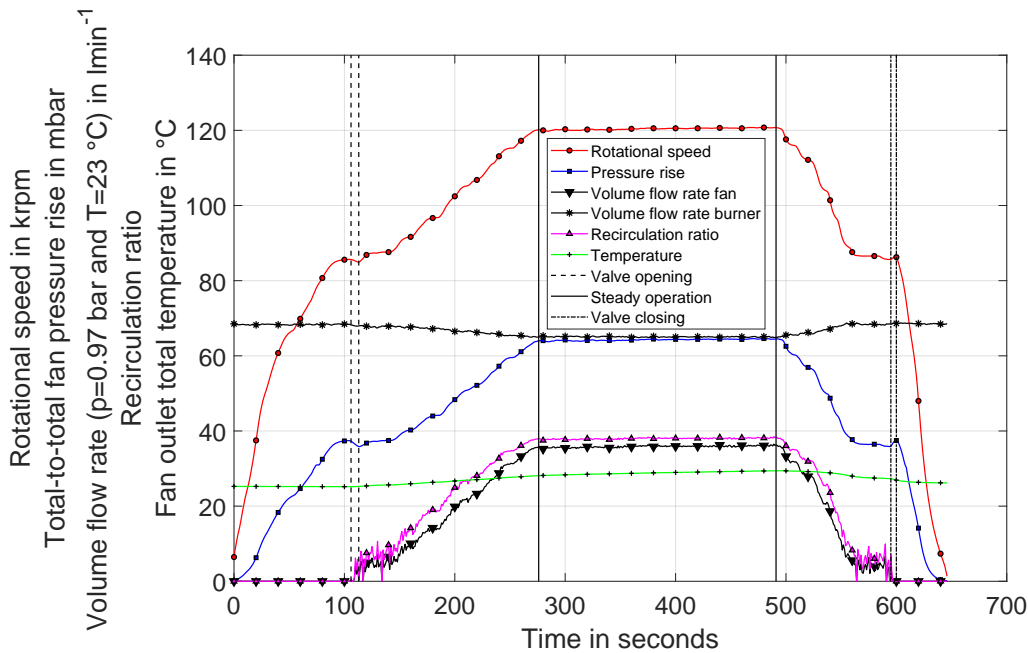


Figure 6.2 – Measured rotational speed, fan pressure rise, volume flow rates of both Venturi nozzles, recirculation rate, and temperatures for the test with  $80 \text{ l s min}^{-1}$  nitrogen at ambient conditions (stack not operational).

At zero speed, the fan inlet and outlet pressure is 14 mbar. The FTU accelerates and reaches 86 krpm (red line with circles in Figure 6.2) and the pressure at the outlet is 51 mbar; hence, the pressure rise is 37 mbar (blue line with squares). This corresponds to a pressure loss at the reformer, the SOFC stack, and the HEX at this operational point for a volume flow rate of  $87 \text{ l min}^{-1}$  at the conditions of the two Venturi nozzles (pressure of 0.97 bar and temperature of  $23 \text{ }^\circ\text{C}$ ), which corresponds to  $80 \text{ l s min}^{-1}$  at standard conditions (pressure of 1.013 bar and temperature of  $20 \text{ }^\circ\text{C}$ ). The tested setup therefore had a leakage rate of  $19 \text{ l min}^{-1}$ , since the measured volume flow rate that entered the burner (Venturi I in a of Figure 6.1) was  $68 \text{ l min}^{-1}$  (black lines with stars). During the valve opening process, the rotational speed and the pressure rise decrease, whereas the volume flow rate increases slightly. Since the valve is opened at a pressure slightly above the reformer inlet pressure, the fan volume flow rate is nearly-zero and increases with increasing speed. The fan outlet total temperature (green line with crosses) increased from the initial  $25 \text{ }^\circ\text{C}$  up to  $29.4 \text{ }^\circ\text{C}$ . As mentioned before, during this test, the set up featured a leakage; hence, the volume flow rate to the burner decreases from the initial  $68 \text{ l min}^{-1}$  to  $65 \text{ l min}^{-1}$ . Because the mass flow rate increased ( $87 \text{ l min}^{-1}$  plus the recirculated volume flow rate), the pressure loss in the reformer, stack, and HEX increased. This leads to a higher differential pressure between the piping and the ambient conditions, which leads to an increased leakage rate, and thus a reduction of the burner volume flow rate. At a rotational speed of 120 krpm, the pressure rise was 64 mbar and the recirculated volume flow rate was  $36 \text{ l min}^{-1}$ , which corresponds to an RR of 38%. For the shutdown process, the FTU was



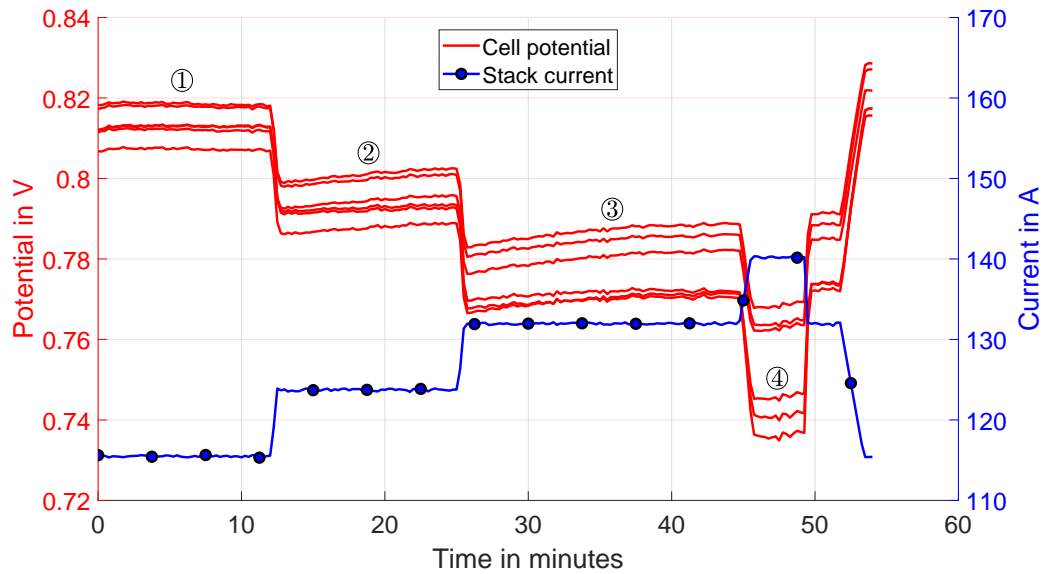


Figure 6.3 – Measured cell potentials and total stack current for four experiments (1-4, as listed in Table 6.2).

decelerated until a rotational speed of 86 krpm was obtained, corresponding to 37 mbar and the valve was closed (pressure and rotational speed of the FTU increased slightly). In the final step, the FTU was decelerated to zero.

### 6.3 Test with operational SOFC

The steam-driven FTU was successfully coupled with a 6 kW<sub>el</sub> SOFC system in the facilities of SOLIDpower in Yverdons-les-Bains, Switzerland, from December 13 to 14, 2018. To the best of the author's knowledge, this is the first proof-of-concept of such a steam-driven AOR fan. Electrical gross DC efficiencies, based on the LHV, of 66 % in part load (4.5 kW<sub>el</sub>) and 62 % in full load (6.4 kW<sub>el</sub>) for a global fuel utilization of 85 % were obtained.

During the initial measurement campaign, the turbine stator was blocked by deposits, released from the evaporator (Appendix E). As a result, the turbine admission was 5 % at the end of the experimental campaign, and thus much lower than the design value of 21 %. The decrease in admission led to a turbine pressure ratio of 4.2, a steam mass flow rate of 1.7 kg h<sup>-1</sup>, and a shaft rotational speed of 220 krpm. Despite the elevated pressure ratio and rotational speed, as well as the penetrated particles, the FTU was operating very stable.

Since the turbine was operated far in the off-design during the initial measurement campaign, a second one was performed in the facilities of SOLIDpower. All parts (e.g., evaporator, piping, turbine volute, turbine stator, etc.) were thoroughly cleaned. Additionally, deionized water

( $0.5 \mu\text{Scm}^{-1}$ ) was used to propel the steam turbine.

Figure 6.3 shows the cell potentials and the current of the  $6 \text{ kW}_{\text{el}}$  SOFC stack at the design-point with four different global FUs. The four numbers (①), (②), (③), and (④) in Figure 6.3 correspond to the four experiments listed in Table 6.2: experiment 1, 2, 3, and 4. The global FU was 0.7, 0.75, 0.8, and 0.85, respectively. The six cell potential curves were obtained from six different measurement locations in the stack. During experiment 1 (global FU of 0.7), the difference between the maximum measured cell potential (0.819 V) and the minimum measured cell potential (0.807 V) was 0.012 V, suggesting a homogeneous distribution of the fuel and similar cell efficiencies. The cell voltage efficiency ( $\eta_V$ ), as defined in eq. 2.16, was 79 % and 78 %, respectively, at this operational point. The cell potential dropped to 0.769 V and 0.737 V, respectively, for experiment 4 (global FU of 0.85). This is equal to a cell voltage efficiency of 74 % and 71 %, respectively. Since the difference between the maximum and minimum cell potential (0.032 V) was relatively high at this operational point, the SOFC stack was only operated for several minutes at a FU of 0.85. Due to risk mitigation, a FU higher than 0.85 was not investigated.

**Coupling procedure:** Table 6.1 shows the results of the coupling procedure (FTU with the SOFC stack). During the first experiment (c0), the steam for the reforming process was supplied from an external evaporator. The blue arrow marked with “water vapor in” in Figure 6.1 marks the steam injection position. During the coupling process, the methane mass flow rate was maintained at  $0.74 \text{ kg h}^{-1}$ . The steam-to-methane ratio

$$S/CH_4 = \frac{\gamma_{H_2O}}{\gamma_{CH_4}} \quad 6.2$$

was 2.1 at this operational point (experiment c0). During the coupling procedure, the steam-to-methane ratio was targeted to be 2.1. The external steam injection in the reformer was reduced from  $1.74 \text{ kg h}^{-1}$  to 0, resulting in 12 steps (as indicated by experiment c1 to c12 in Table 6.1). The RR was accordingly increased from 0 (c1) to 47 % (c12) to maintain the targeted steam-to-methane ratio of 2.1. This recirculation ratio was realized with turbine steam mass flow rates of  $1.5 \text{ kg h}^{-1}$  and  $2 \text{ kg h}^{-1}$ , respectively, which corresponded to turbine total-to-total pressure ratios of 1.50 and 1.84, respectively, and a shaft rotational speeds of 149 krpm and 170 krpm, respectively. The measured turbine characteristic of experiment c10 correlates well to the CFD simulation of the design point with a rotational speed of 175 krpm: the mass flow rate is  $2.12 \text{ kg h}^{-1}$ , the pressure ratio is 1.89, and the reaction is 0.13 (Figure 5.15 and Table 4.6). Considering the experiment c10, the mass flow rate is  $1.98 \text{ kg h}^{-1} \pm 0.12 \text{ kg h}^{-1}$ , the pressure ratio is 1.86, and the reaction is 0.148 at a rotational speed of 173.2 krpm.

Before the coupling of the AOR fan with the stack (experiment c0), the fan outlet total pressure was adjusted slightly above the reformer inlet total pressure. After the valve was opened (valve in Figure 6.1), the AOR started, which resulted in a slight drop of the total-to-total fan pressure rise from 51 mbar (experiment c0) to 47 mbar (c1). Since the anode mass flow rate increased with increasing RR, the fan total-to-total pressure rise increased from 47 mbar (experiment

Table 6.1 – Coupling process of the FTU (steam-driven) with a 6 kW<sub>el</sub> SOFC stack (240x80 cm<sup>2</sup> cells). The cathode air mass flow rate was maintained at 5.1 kg h<sup>-1</sup>. The global fuel utilization was constant (0.7). The turbine and fan inlet total temperatures were maintained at 215 °C ± 5 °C and at 195 °C ± 5 °C, respectively. The injected steam to the reformer was gradually replaced by anode off-gas recirculation.

Exp.	$\dot{m}$ CH <sub>4</sub> in kg/h	$\dot{m}^g$ H <sub>2</sub> O in kg/h	FU <sup>a</sup> local	RR	U stack in V	I stack in A	P <sub>el</sub> stack in kW <sub>e</sub>	$\eta_{el,gross}^b$ (DC LHV) in %	T <sup>c</sup> anode in °C	n <sub>rot</sub> shaft in krpm	$\dot{m}$ turbine in kg/h	$\Pi_{tt}^d$ turbine -	$\dot{m}^e$ fan in kg/h	$\Delta p_{tt}^f$ fan in mbar
c0	0.74	1.74	0.70	0.00	47.8	115.4	5.51	53.50	740.0	149.0	1.50	1.55	0.00	51
c1	0.74	1.74	0.69	0.04	47.6	115.4	5.50	53.34	740.0	149.0	1.50	1.54	0.16	47
c2	0.74	1.66	0.68	0.08	47.7	115.4	5.50	53.40	750.5	150.0	1.50	1.53	0.35	49
c3	0.74	1.50	0.67	0.13	47.7	115.4	5.51	53.47	752.5	152.0	1.56	1.54	0.58	50
c4	0.74	1.33	0.66	0.16	47.8	115.4	5.52	53.57	753.0	154.0	1.62	1.61	0.75	51
c5	0.74	1.16	0.65	0.21	47.9	115.4	5.53	53.69	753.5	156.5	1.68	1.66	1.00	53
c6	0.74	1.00	0.63	0.26	48.1	115.4	5.55	53.83	753.5	161.7	1.74	1.70	1.23	56
c7	0.74	0.83	0.62	0.30	48.2	115.4	5.56	53.93	753.5	163.0	1.80	1.73	1.40	57
c8	0.74	0.67	0.62	0.31	48.3	115.4	5.57	54.04	753.0	166.2	1.86	1.77	1.44	58
c9	0.74	0.50	0.59	0.39	48.3	115.4	5.57	53.93	752.0	170.7	1.92	1.81	1.86	60
c10	0.74	0.33	0.57	0.42	48.3	115.4	5.58	54.14	752.0	173.3	1.98	1.86	2.05	62
c11	0.74	0.17	0.57	0.44	48.6	115.4	5.61	54.41	751.0	170.7	1.98	1.85	2.10	60
c12 <sup>h</sup>	0.74	0.00	0.55	0.47	48.8	115.4	5.63	54.65	750.0	169.8	1.98	1.84	2.21	59

<sup>a</sup> Calculated with eq. 2.29

<sup>b</sup> Calculated with eq. 2.20 based on the LHV, without considering the DC/AC conversion efficiency ( $\eta_{DC/AC}$ )

<sup>c</sup> Mean anode temperature. The anode and cathode inlet temperatures were maintained at 710 °C ± 1 °C

<sup>d</sup> Measured between turbine section 1 and 12 (ambient), as defined in Figure 2.7

<sup>e</sup> Mass flow rate calculation based on the estimated anode off-gas composition. The exact gas composition was not measured

<sup>f</sup> Measured between fan section 1 and 8, as defined in Figure 2.3

<sup>g</sup> Injected in the reformer for the steam reforming process

<sup>h</sup> Experiment c12 is equal to experiment 1 in Table 6.2

c1) up to 62 mbar (c10). For the last three coupling steps (experiments c10, c11, and c12), the turbine inlet steam mass flow rate was constant ( $1.98 \text{ kg h}^{-1}$ ). The anode off-gas mass flow rate decreased from  $4.85 \text{ kg h}^{-1}$  (experiment c10) to  $4.68 \text{ kg h}^{-1}$  (c12); hence, the fan total-to-total pressure rises decreased from 62 mbar (c10) to 59 mbar (c12).

The cathode air mass flow rate was  $5.1 \text{ kg h}^{-1}$  for all experiments (Tables 6.1 and 6.2). This corresponded to an EAR, as defined in eq. 2.9, of 4.4 for the coupling procedure (methane mass flow rate of  $0.74 \text{ kg h}^{-1}$ ). The auxiliary power ( $P_{aux}$ ) (e.g., the cathode fan electrical power) was not measured. Thus, a calculation of the electrical net efficiencies was not possible (eq. 2.21) and Tables 6.1 and 6.2 only present the electrical gross DC efficiency (eq. 2.20, without considering the converter efficiency  $\eta_{DC/AC}$ ).

During the coupling procedure, the global FU was maintained at 0.7. Since the RR gradually increased, the local FU decreased from 0.7 (experiment c0) to 0.55 (c12), and thus the mean cell voltages increased from 0.797 V (c0) to 0.813 V (c12). As a result, the electrical power output and the electrical gross DC efficiency increased by  $0.12 \text{ kW}_{el}$  and 1.15 percentage points, respectively.

**Characterization:** Table 6.2 shows the characterization of the  $6 \text{ kW}_{el}$  SOFC stack and the steam-driven FTU. The system was characterized at different loads (corresponding to different methane mass flow rates).

- 100 % load ( $0.74 \text{ kg h}^{-1}$ ): experiment 1-4
- 92 % load ( $0.68 \text{ kg h}^{-1}$ ): experiment 5-10
- 66.7 % load ( $0.50 \text{ kg h}^{-1}$ ): experiment 11-14
- 50 % load ( $0.37 \text{ kg h}^{-1}$ ): experiment 15-18

The power densities at 92 % and 66.7 % load correspond to the power density of the BlueGEN from SOLIDpower and the system simulation of Chapter 3, respectively. For each load case, four different global FUs (i.e., 0.7, 0.75, 0.8, and 0.85) were investigated. The turbine steam mass flow rate was fixed at  $1.98 \text{ kg h}^{-1}$ ,  $1.74 \text{ kg h}^{-1}$ ,  $1.50 \text{ kg h}^{-1}$ , and  $1.38 \text{ kg h}^{-1}$  for the 100 %, 92 %, 66.7 %, and 50 % load cases, respectively. For the 92 % load case, turbine steam mass flow rates of  $1.98 \text{ kg h}^{-1}$  (FU of 0.7, 0.75, 0.8, and 0.85) and  $1.74 \text{ kg h}^{-1}$  (FU of 0.8 and 0.85) were investigated. The turbine inlet temperature was maintained constant ( $215^\circ\text{C} \pm 5^\circ\text{C}$ ), as well as the fan inlet temperature ( $195^\circ\text{C} \pm 5^\circ\text{C}$ ).

The higher the FU, the higher the water vapor molar ratio in the anode off-gas, and the denser the anode off-gas. According to eq. 2.70, the fan pressure rise increases for higher fluid densities, or the fan rotational speed decreases if the pressure rise is constant, but the fluid density increases. Thus, the shaft rotational speed decreased with increasing FU, although the anode pressure loss, and thus the fan pressure rise, increased with increasing FU. A high FU therefore decreased the fan power. However, the exact fan and turbine power measurement was infeasible, since an insulation of the measurements section with PTFE tubes was not possible, due to risk mitigation (leakage of CO).

Table 6.2 – 6 kW<sub>el</sub> SOFC stack (240x80 cm<sup>2</sup> cells) with anode off-gas recirculation (FTU, steam-driven). The cathode air mass flow rate was maintained at 5.1 kg h<sup>-1</sup>. The turbine and fan inlet total temperatures were maintained at 215 °C ± 5 °C and at 195 °C ± 5 °C, respectively.

Exp.	$\dot{m}$ CH <sub>4</sub> in kg/h	FU global	FU <sup>a</sup> local	RR	$U$ stack in V	$I$ stack in A	$P_{el}$ stack in kWe	$\eta_{el, gross}$ <sup>b</sup> (DC LHV) in %	$T^c$ anode in °C	$n_{rot}$ shaft in krpm	$\dot{m}$ turbine in kg/h	$\Pi_{tt}$ <sup>d</sup> turbine -	$\dot{m}^e$ fan in kg/h	$\Delta p_{tt}^f$ fan in mbar
	1	0.74	0.7	0.55	0.47	48.8	115.4	5.6	54.7	750	169.8	1.98	1.84	2.21
2	0.74	0.75	0.61	0.48	47.7	123.8	5.9	57.3	750	169.4	1.98	1.84	2.35	62
3	0.74	0.8	0.67	0.48	46.7	131.9	6.2	59.8	755	168.0	1.98	1.84	2.46	64
4	0.74	0.85	0.75	0.48	45.1	140.1	6.3	61.4	756.5	165.5	1.98	1.83	2.54	65
5	0.68	0.7	0.54	0.50	49.5	105.7	5.2	55.5	751.5	170.9	1.98	1.83	2.32	60
6	0.68	0.75	0.60	0.50	48.3	113.3	5.5	58.0	749.5	169.2	1.98	1.83	2.41	61
7	0.68	0.8	0.66	0.51	47.3	120.7	5.7	60.5	748.5	166.5	1.98	1.83	2.50	62
8	0.68	0.85	0.74	0.51	45.9	128.4	5.9	62.4	748.5	164.6	1.98	1.83	2.55	63
9	0.68	0.8	0.69	0.44	47.8	120.7	5.8	61.2	752.5	149.7	1.74	1.73	2.02	51
10	0.68	0.85	0.76	0.45	46.3	128.4	5.9	63.0	753	148.2	1.74	1.73	2.06	53
11	0.50	0.7	0.57	0.42	51.8	77.3	4.0	58.1	733	130.8	1.50	1.57	1.38	37
12	0.50	0.75	0.62	0.45	50.8	82.7	4.2	61.0	732	129.2	1.50	1.57	1.61	37
13	0.50	0.8	0.69	0.46	49.7	88.3	4.4	63.7	732.5	128.7	1.50	1.57	1.69	39
14	0.50	0.85	0.75	0.46	48.4	93.7	4.5	65.8	733	128.1	1.50	1.57	1.74	39
15	0.37	0.7	0.55	0.47	52.8	57.9	3.1	59.2	734.5	116.4	1.38	1.51	1.40	31
16	0.37	0.75	0.61	0.48	51.9	62.1	3.2	62.3	735.5	115.7	1.38	1.51	1.47	31
17	0.37	0.8	0.67	0.48	50.7	66.1	3.4	64.9	736	115.5	1.38	1.51	1.50	32
18	0.37	0.85	0.75	0.48	49.2	70.3	3.5	66.9	737.5	115.2	1.38	1.51	1.57	32

<sup>a</sup> Calculated with eq. 2.29

<sup>b</sup> Calculated with eq. 2.20 based on the LHV, without considering the DC/AC conversion efficiency ( $\eta_{DC/AC}$ )

<sup>c</sup> Mean anode temperature. The anode and cathode inlet temperatures were maintained at 710 °C ± 1 °C

<sup>d</sup> Measured between turbine section 1 and 12 (ambient), as defined in Figure 2.7

<sup>e</sup> Mass flow rate calculation based on the estimated anode off-gas composition. The exact gas composition was not measured

<sup>f</sup> Measured between fan section 1 and 8, as defined in Figure 2.3

For a global FU of 0.85, electrical gross DC efficiencies of 61.4 %, 63.0 %, 65.8 %, and 66.9 % were reached for the 100 %, 92 %, 66.7 %, and 50 % load cases, respectively. This corresponds to a current density of  $0.58 \text{ A cm}^{-2}$ ,  $0.54 \text{ A cm}^{-2}$ ,  $0.39 \text{ A cm}^{-2}$ , and  $0.29 \text{ A cm}^{-2}$ , respectively. Considering a quadratic extrapolation for a global FU of 92.5 %, an electrical gross DC efficiency of 68.8 % could be obtained for the  $0.39 \text{ A cm}^{-2}$  case, which correlates to the system optimization in Table 3.6 (68.7 % for a current density of  $0.40 \text{ A cm}^{-2}$ , a global FU of 92.5 %, and a RR of 54 %).

### 6.4 Chapter conclusion

This chapter presents the coupling of a  $6 \text{ kW}_{\text{el}}$  SOFC stack with the designed FTU. For the first proof-of-concept, the SOFC stack and the FTU were in separate electrical ovens and not thermally coupled.

The FTU startup strategy was validated at ambient conditions. The FTU starts up fully throttled; hence, the recirculation mass flow rate is zero and the fuel at the anode inlet cannot bypass the stack. Once the fan outlet pressure is higher than the measured pressure at the reformer inlet, the AOR starts by opening the fan outlet throttle valve.

The anode off-gas recirculation rate is measured with two in-house manufactured and calibrated Venturi nozzles that are implemented in one rectangular steel block. Hence, the fluid temperatures and densities in the flow to the burner and the flow to the anode off-gas loop are comparable.

The steam-driven FTU was coupled with a  $6 \text{ kW}_{\text{el}}$  SOFC system in the facilities of SOLIDpower in Yverdons-les-Bains, Switzerland, from December 13 to 14, 2018. To the best of the author's knowledge, this is the first proof-of-concept of such a steam-driven AOR fan. Electrical gross DC efficiencies, based on the LHV, of 66 % in part load ( $4.5 \text{ kW}_{\text{el}}$ ) and 62 % in full load ( $6.4 \text{ kW}_{\text{el}}$ ) for a global fuel utilization of 85 % were obtained. The results correlate well to the system optimization presented in Chapter 3.

# 7 Summary and Conclusions

## 7.1 Summary

The thesis presents the design and experimental investigation of a patented 10 kW<sub>el</sub> solid oxide fuel cell (SOFC) system with a thermally-driven anode off-gas recirculation (AOR) fan. This system offers several advantages over state-of-the-art SOFC systems:

- The SOFC system can operate at higher global fuel utilization; hence, the system efficiency is increased.
- High electrical net DC efficiency based on the lower heating value (LHV) on the order of 65 % and high net utilization ratio on the order of 90 %.
- The SOFC system can operate at a lower local fuel utilization, and thus, increases the stack lifetime.
- The AOR fan has a high lifetime and is temperature-proof, due to the gas film bearings. The steam-turbine-driven fan is explosion-proof, oil-free, flexible, and low-cost.
- The SOFC system with thermally-driven anode off-gas recirculation requires no external water source, since the AOR provides de-ionized and pH neutral steam for the reforming process.
- Simplified water treatment is utilized (i.e., filter for small particles).
- The evaporator is approximately 30 % smaller than to the state-of-the-art direct steam supply systems, which reduces capital cost.
- Anode off-gas and steam supply are separated, thus avoiding dilution of the AOR loop and therefore reducing the Nernst potential in the SOFC cells.
- Separation of the anode and cathode off-gas allows for higher condensing temperatures and thus higher cogeneration, as well as a smaller condenser, and thus lower pressure losses compared to the mixing of the anode and cathode off-gas.
- The fan that supplies the burner with fresh air allows for more flexible operation of the SOFC system.

The feasibility of the system is demonstrated with a system simulation and an integrated opti-

mization based on experimentally verified models. A Pareto front corresponding to optimal systems with respect to the electrical net DC efficiency and net utilization ratio is identified. The heat exchanger network design for the system with the highest electrical net efficiency is presented.

Based on the system simulation, a thermally-driven AOR fan, the fan-turbine unit (FTU) was designed, manufactured, and experimentally tested. The focus of the component design was to achieve low manufacturing and material cost. The radial inducer-less fan with a tip diameter of 19.2 mm features backward-curved prismatic blades with constant height. Prior to coupling it with the SOFC, the fan was experimentally characterized with air at 200 °C. At the nominal design point of 168000 rpm, the measured inlet mass flow rate was  $4.9 \text{ kg h}^{-1}$  with a total-to-total pressure rise of 55 mbar, an isentropic total-to-total efficiency of 55 %, and a power of 18 W. Although the consumed power is very low, this FTU can increase the net efficiency of a  $10 \text{ kW}_{\text{el}}$  SOFC system by 5 percentage points. The tested AOR fan is the smallest that the author is aware of.

The fan and shaft are propelled by a radial-inflow, partial-admission (21 %), and low-reaction (13 %) steam turbine with prismatic blades. It has a diameter of 15 mm and consists of 59 rotor blades with a radial chord of 1 mm and a blade height of 0.6 mm. At the design point, it has a total-to-total pressure ratio of 1.9 and a mass flow rate of  $2.1 \text{ kg h}^{-1}$ , yielding a power of 36 W. To the best of the author's knowledge, it is one of the smallest steam turbines in the world. The shaft features two herringbone-grooved journal bearings and a single-sided spiral-grooved thrust gas film bearing. During nominal operation, the bearings operated with water vapor at temperatures up to 220 °C. The bearings were tested with ambient air, hot air, and water vapor to rotational speeds up to 220000 rpm suggesting very stable operation. The unit achieved more than 300 h of operation.

In the final step, the FTU was coupled in-situ to a  $6 \text{ kW}_{\text{el}}$  SOFC system, reaching electrical gross DC efficiencies, based on the LHV, of 66 % in part load ( $4.5 \text{ kW}_{\text{el}}$ ) and 62 % in full load ( $6.4 \text{ kW}_{\text{el}}$ ) for a global fuel utilization of 85 %. To the best of the author's knowledge, this was the first time that a steam-driven AOR fan was demonstrated in-situ with an SOFC system.

## 7.2 Future work

For the baseline fan design, a specific speed of 0.8 and a fan inlet temperature of 200 °C were chosen. A system simulation and optimization suggests that an increase of the fan specific speed to 1.1-1.2 would be beneficial for the overall FTU efficiency, since the turbine can operate at higher rotational speeds. Consequently, it would be interesting to test this new integrally-optimized solution.

The fan inlet temperature of 200 °C leads to the maximum system electrical net efficiency,



but increases the system cost by adding two additional heat exchangers to cool the anode off-gas. Higher AOR temperatures therefore lead to smaller or no heat exchangers within the AOR loop, lowering the system cost. The addition of a third optimization objective, the system cost, could thus help to find a market-oriented trade-off between cost and system efficiency. Although a high-level economic analysis suggests reduced cost at higher AOR temperatures, this trade-off was not fully identified. Further, an increase in temperature is challenging with respect to the FTU materials and the stable operation of the unit.

The baseline FTU has a limited temperature gradient between the turbine and the fan: 200 °C for the fan inlet and 220 °C for the turbine inlet. A higher turbine inlet temperature, and thus a higher temperature gradient, could therefore reduce the water vapor mass flow rate necessary to propel the turbine. The evaporator size could then be further decreased. However, this would certainly require a detailed thermal management investigation on the FTU to ensure the stable operation of the bearings that operate with clearances on the order of several micrometers.

The investigation of the fan characteristic with a smaller blade tip clearance (i.e., 0.1 mm and 0.05 mm) could validate the computational fluid dynamics (CFD) simulations performed in this thesis. The author's hypothesis of residual swirl in the fan outlet side test section could be tested. For example, a honeycomb flow straightener could allow for a more precise fan outlet mass flow rate measurement. This could also allow for a more precise determination of the turbine-to-fan leakage mass flow rate, which is particularly interesting, since the analytical, numerical, and experimental results obtained in this thesis deviate significantly (0 to 0.7 kg h<sup>-1</sup>).

The measurement of the turbine characteristic was very challenging, due to dissipated heat that crossed the turbine control volume. In order to reduce the control volume and to minimize the effect of non-adiabatic flows, extremely thin thermocouples (TCs) could be placed just upstream of the turbine stator leading edge (LE) and downstream of the turbine rotor trailing edge (TE). The TCs should be placed as close as possible to the LE to minimize the heat input to the turbine fluid domain and as far as possible to reduce the influence of the TCs on the flow (wake). In order to obtain more reliable experimental data on the turbine, the materials of the impeller and housing could be changed to minimize heat conduction. Additionally, a pressure tap at the turbine section 9 would allow for a more accurate definition of the outlet boundary condition of the CFD simulation (static pressure).

The current research prototype could be adopted as a commercial product by removing all the measurement sensors, simplifying the geometry, and adapting it for a series production. Another remaining task for a commercial product is the automation that requires an imple-

## **Chapter 7. Summary and Conclusions**

---

mented FTU control strategy. The integration of the FTU concept in a commercial SOFC system is yet an extensive work package.

# A Commercial, Precommercial, and Postcommercial SOFC Systems

Commercial SOFCs are currently available as small-scale systems at power ratings as low as 0.1 kW<sub>el</sub>, as well as large-scale systems up to 250 kW<sub>el</sub>. Table A.1 provides an overview of commercial products from companies in East Asia, North America, and Europe. It also shows their power and efficiencies, as defined in eqs. 2.21 and 2.23. The electrical net efficiencies range from 25 % up to 65 %. In general, industrial systems have higher efficiencies than small systems. The BoP components, such as fans, are more efficient for large-scale systems, and thus the relative auxiliary power ( $P_{aux}/\dot{m}_{fuel}HV_{fuel}$ ) is lower, which leads to higher system efficiencies. Large-scale systems also allow for more complex BoP equipment. As stated in Section 2.1.3, SR is more efficient than CPOX reforming. However, SR technology also requires additional BoP equipment, including water treatment equipment, a pump, and an evaporator for the systems with direct steam supply. The smallest system with SR is the Japanese Ene Farm type with 0.7 kW<sub>el</sub> and 52 % electrical net AC efficiency, whereas the largest system with CPOX is the ARP1500 from Atrex with 1.5 kW<sub>el</sub> and 35 % efficiency. Together with the 1 kW<sub>el</sub> Galileo 1000 N, these systems have the highest electrical net efficiency of all systems with CPOX. As CPOX reforming is an exothermic reaction and SR endothermic reaction, the highest utilization ratios are obtainable with CPOX. At 95 %, the Galileo 1000 N from Hexis has the highest utilization ratios of all commercial systems. Additionally, this system is easier to operate, and maintenance is less complex due to the lack of the water treatment equipment, as compared to SR systems with direct steam supply.

The most efficient commercial SOFC is the Energy Server 5 from Bloom Energy with a minimum 60 % electrical net AC efficiency, which can increase up to 65 %. The system has no heat cogeneration, and it uses SR. As the Energy Server 5 does not require an external water supply, it most likely uses either hot AOR (option a, b, or c of Figure 2.1) or it condenses the anode off-gas, pumps the condensed water to an evaporator, and uses the steam for the SR (direct steam supply, option e of Figure 2.1). The author did not find any scientific publications from Bloom Energy with a detailed description of the Energy Server 5, except for 300 patents on SOFC technology. The company was founded in 2002 with knowledge from the NASA Mars

## Appendix A. Commercial, Precommercial, and Postcommercial SOFC Systems

---

exploration program.

The most efficient commercial SOFC system with cogeneration of heat is the BlueGEN, provided by the company SOLIDpower. In 2015, SOLIDpower acquired CFCL GmbH, which was affiliated to the Australian company CFCL Ltd. CFCL GmbH manufactures and sells the BlueGEN, a 1.5 kW<sub>el</sub> SOFC with 60 % electrical net AC efficiency. The BlueGEN lifetime is expected to be more than 60,000 hours [108]. A similar technology to that in the BlueGEN just achieved more than 10 years of continuous operation [109]. Although the SR uses part of the condensed water in the exhaust (direct steam supply, option e in Figure 2.1), the BlueGEN requires an external water supply.

Another hub of SOFC research is in Northern Europe, where the VTT is located in Helsinki. The Finnish company Convion sells an industrial 58 kW<sub>el</sub> SOFC with a minimum electrical net AC efficiency of 53 %. This is, therefore, the third most-efficient system available. This system can use cells from the Austrian company Plansee or the Estonian company Elcogen. As with the Energy Server 5, the C50 does not require an external water supply. The C50 uses AOR, but Convion has not disclosed the exact nature of this AOR. Thus, the options a, b, or c of Figure 2.1 are spossible.

By far, the largest SOFC market is in Japan due to the “Ene farm” subsidies program. It was launched in 2009 with PEM fuel cells exclusively, and SOFCs have been added in 2011. Up until May 2017, the “Ene farm” program sold more than 200 000 units (both PEM and SOFC) [110]. A Japanese consortium builds and sells the fourth most-efficient SOFC (“Ene farm” type) at only 0.7 kW<sub>el</sub> and an electrical net AC efficiency of 52 %. More recently, Kyocera announced a 3 kW<sub>el</sub> SOFC with the same efficiency. These systems do not require any external water supply, since the condensed water within the system is used (option e of Figure 2.1). The Ene farm products are sold exclusively to the Japanese market.

Table A.1 – Commercial, precommercial, and postcommercial SOFC systems, power, and efficiency as defined in eqs. 2.21 and 2.23.

Company	Country	Product	Power in kW <sub>el</sub>	$\eta_{el,net}$ in %	$\zeta_{net}$ in %	Reference
Bloom Energy	USA	Energy Server 5 <sup>s,p</sup>	50 <sup>a</sup>	60-65 <sup>b</sup>	-	[111]
SOLIDpower	Italy	BlueGEN <sup>s,p,w,d</sup>	1.5	60	85	[112]
Convion	Finland	C50 <sup>s,p,e</sup>	58	>53	>80	[113, 114]
Various <sup>f</sup>	Japan	Ene Farm type s <sup>s,t,i</sup>	0.7 and 3	52	87	[115, 116]
Sunfire	Germany	Powerplus <sup>s,p,j</sup>	20	50	90	[117]
SOLIDpower	Italy	EnGen <sup>TM</sup> -2500 <sup>s,p,w,g</sup>	2.5	50	90	[108]
Huatsing Power	China	HS-201 type <sup>s,p,w</sup>	1	50	85	[118]
Buderus / Junkers	Germany	FC 10 type <sup>s,t,w,h</sup>	0.7	45	85	[119]
Atrex Energy	USA	ARP1500 <sup>c,t</sup>	1.5	35	-	[120]
Hexis	Germany	Galileo 1000 N <sup>c,p</sup>	1	35	95	[121]
Sunfire	Germany	Home <sup>c,p,j</sup>	0.7	33	90	[122]
Sunfire	Germany	Remote <sup>c,p,j</sup>	30	30	85	[123]
New Enerday	Germany	EN 400 <sup>c,p</sup>	0.5	30-35	-	[124]
New Enerday	Germany	EN 200 <sup>c,p</sup>	0.25	30-35	-	[125]
Atrex Energy	USA	ARP1000 <sup>c,t</sup>	1	30	-	[120]
Atrex Energy	USA	ARP500 <sup>c,t</sup>	0.5	25	-	[120]
Atrex Energy	USA	RP250 <sup>c,t</sup>	0.25	25	-	[120]

#### Technology

<sup>s</sup> Steam reforming

<sup>c</sup> CPOX reforming

<sup>p</sup> Planar cell

<sup>t</sup> Tubular cell

<sup>w</sup> External water supply necessary

#### General information

<sup>a</sup> Power of one energy server. Several servers can be combined to 200 kW<sub>el</sub>, 250 kW<sub>el</sub>, 300 kW<sub>el</sub>, etc.

<sup>b</sup> Efficiency of at least 60 % and up to 65 %

<sup>d</sup> In 2015, SOLIDpower bought the BlueGEN technology from CFCL

<sup>e</sup> The system can use cells from the German company Plansee or the Estonian company Elcogen

<sup>f</sup> Kyocera Corporation, Osaka Gas, Aisin Seiki Co Ltd, Toyota Motor Corporation, Norritz, and Chofu Seisakusho Co Ltd.

<sup>g</sup> Discontinued due to superior performance of the BlueGEN (postcommercial)

<sup>h</sup> Buderus names it Logapower FC 10, whereas Junkers names it Cerapower FC 10

<sup>i</sup> Only available on the Japanese market

<sup>j</sup> In development or evaluation (precommercial)



## B Mesh Sensitivity Analysis for the Fan Impeller

The mesh sensitivity analysis uses air at ambient temperature (20 °C), a total inlet pressure of 1.05 bar, a rotational speed of 132.5 krpm, and a mass flow rate of 6.86 kg h<sup>-1</sup>. The fan geometry is as follows: the blade channel width is 1.9 mm (original design), the blade height is 1.83 mm, and the blade tip clearance is 0.07 mm, consisting of 17 span-wise elements. The mesh sensitivity analysis uses air at ambient temperature as the fluid. Table B.1 summarizes the outcome of the mesh sensitivity analysis. The baseline mesh with 1.17 million elements is refined by a factor 1.5 to 1.78 to achieve 2.66 million and 5.7 million mesh elements, respectively. Table B.1 also shows the fan power  $P_{fan}$ , the total-to-static pressure rise ( $\Delta p_{tst,4,1.1}$ ), the total-to-total pressure rise ( $\Delta p_{tt,4,1.1}$ ), and the total-to-total isentropic efficiency ( $\eta_{is,4,1.1}$ ) between the nozzle inlet (section 1.1 as defined in Figure 2.3) and the fan blade TE (section 4). For the mesh with 1 million elements, the pressure field is well converged; hence, the change in power ( $P = M\omega$ ) and total-to-static pressure difference is lower than 1 %. However, the velocity and temperature field still changes by up to 2 % in comparison to the finest mesh for the isentropic efficiency and the total-to-total pressure rise. For this analysis, the author considers a mesh with one million elements for a single passage CFD simulation and four million elements for a full passage simulation, as the accuracy was deemed acceptable.

Table B.1 – Mesh sensitivity analysis with relative change (RC) between two consecutive values.

Elements in $\cdot 10^6$	$\Delta p_{tst,4,1.1}$ in mbar	RC in %	$\Delta p_{tt,4,1.1}$ in mbar	RC in %	$\eta_{is,4,1.1}$ in %	RC in %	$P_{fan}$ in W	RC in %
1.17	63.20	<b>-0.11<sup>a</sup></b>	95.38	<b>2.00<sup>a</sup></b>	56.31	<b>-1.62<sup>a</sup></b>	18.47	<b>0.43<sup>a</sup></b>
1.78	63.49	0.46	96.16	0.82	56.17	-0.25	18.55	0.43
2.66	63.07	-0.66	96.28	0.13	55.57	-1.07	18.50	-0.27
5.70	63.13	0.10	97.29	1.05	55.40	-0.31	18.55	0.27

<sup>a</sup> Relative change between the coarsest and the finest mesh with respect to the coarsest mesh





## C Measurement Uncertainty and Calibration of Equipment

This appendix provides an overview of the measurement uncertainty of the equipment used for the experiments within this work. The measured parameters were total temperature ( $T_t$ ), ambient conditions of the laboratory (pressure, temperature, and relative humidity), static pressure with wall taps ( $p_{st}$ ), volume flow rate ( $\dot{V}$ ), mass flow rate ( $\dot{m}$ ), shaft rotational speed ( $\omega$ ), and displacement ( $s$ ). Table C.1 summarizes all the measurement equipment and the respective measurement uncertainties.

**Total temperature:** The test rig uses class 1 k-type TCs featuring 1.5 mm diameter and high-temperature-resistant glass fiber insulated cables. All of these TCs are from the same manufacturing batch and therefore exhibit very similar characteristics. The reference temperature is obtained from the built-in cold-junction correction of the National Instruments DAQ system. The author calibrated the TCs from 15 °C to 175 °C. For the calibration procedure, each TCs was inserted into a slot within a stainless steel block that was decoupled from the calibration thermostat (Lauda RE 312 with Kyro 20 fluid) with high-temperature plastic spacers. Two Omega DP9602 Pt 100 ( $\pm 0.01$  °C) platinum reference probes were inserted into two slots in the middle of the stainless steel block. The averaged Pt 100 reference temperature at a steady point (waiting time of one 1 h) was compared to the temperature measurement of the TCs. Figure C.1 on the left shows the calibration curve from 15 °C to 175 °C. The maximum absolute error within this temperature interval is within  $\pm 0.5$  °C, whereas the relative temperature difference between the different TCs is within  $\pm 0.1$  °C over the entire range. The FTU was operated between 0 and 225 °C, and therefore out of the calibration range (Lauda RE 312 limited to 180 °C). Although no calibration over the entire operational range is carried out, this thesis assumes an uncertainty of  $\pm 0.5$  °C for all TCs.

**Ambient conditions:** A Lufft Opus 20 tracked the ambient conditions (pressure, temperature, and relative humidity). The ambient pressure served as reference to convert the measured differential pressures to absolute values. Since the laboratory is at an elevation above mean sea level of 440 m, 0.96 bar is a common ambient pressure. For the tests with cold air (Sec-

## Appendix C. Measurement Uncertainty and Calibration of Equipment

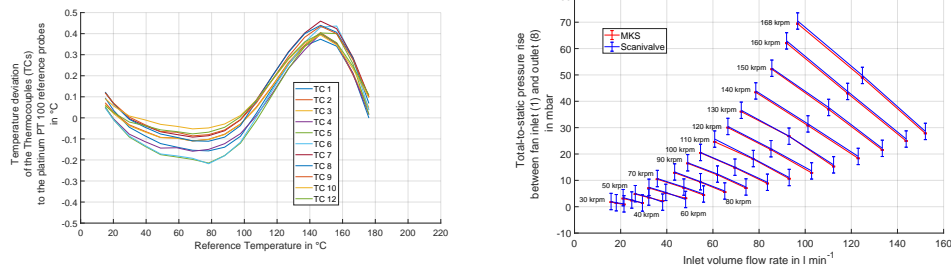


Figure C.1 – Left: calibration of Thermocouples (TCs) with two platinum PT 100 reference probes from 15 °C to 175 °C (FTU operating temperature from 0-220 °C). Right: comparison of the measurement uncertainty of the Scanivalve DSA 3218 (0.05 % of 250 PSI is 3.1 mbar) and the MKS 226A (0.3 % on the read).

tion 5.3), the fan ingested the ambient air that features a certain degree of humidity. The local pressurized air network supplied the air for the turbine (Sections 5.2, 5.3, and 5.5) that was dehumidified, thus the relative humidity was nearly-zero.

**Static pressure:** Pressure measurement devices from Scanivalve (DSA 3218) and MKS (226A and 223B) measured the differential pressure. The differential capacitance manometers from MKS offer a high accuracy ( $\pm 0.3\%$  on the read) and measured the differential pressure of the long-radius bellmouth at the fan inlet and at the quarter circle nozzle at the fan outlet, as well as the fan total-to-static pressure rise. The author assumed this accuracy valid for three orders of magnitude with respect to the full range. The Scanivalve measured various static pressures: at the fan TE, the turbine rotor-stator interface, inside the FTU housing, etc. Since its range is very large (250 Psi), the error at 3.1 mbar is also very large with respect to the design fan pressure rise (70 mbar). Both the MKS 226A and the Scanivalve logged the fan pressure rise and Figure C.1 on the right features a comparison of these two pressure rises and the respective measurement uncertainties. The two measured values for different FTU operational points with respect to the volume flow rate and the rotational speeds (30 krpm, 40 krpm, 50 krpm, ..., 160 krpm, 168 krpm) were within  $\pm 0.8$  mbar and therefore much lower than 3.1 mbar. An automatic zero offset calibration of the Scanivalve device could limit the measurement uncertainty and was therefore carried out before each measurement series.

**Mass flow rate:** On the fan side, the test rig used a low-ratio long-radius bellmouth at the inlet and a quarter circle nozzle at the outlet. On the turbine side, an Emerson D S006S measured the inlet mass flow rate for the air experiments, whereas a KNF SIMDOSE 10 was used for the water vapor experiments.

**Quarter circle nozzle:** An orifice plate with wall taps in accordance to the ISO 5167-2 norm [95] measured the fan outlet volume flow rate. For low Reynolds number applications, quarter circle nozzles are preferred to orifices with sharp edges such as those stated within the ISO 5167-2 norm. The discharge coefficient of quarter circle nozzles is nearly constant down to

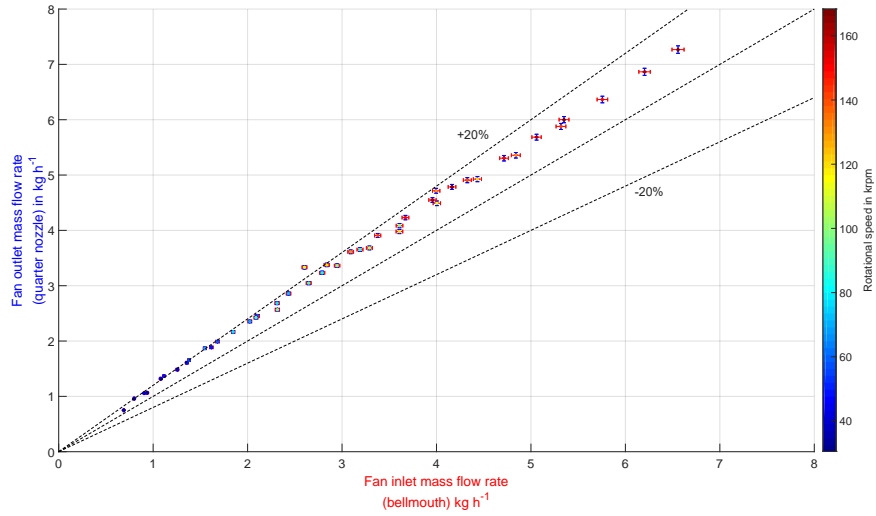


Figure C.2 – Measurement uncertainty of the mass flow rate at the fan outlet measured with the quarter circle nozzle (blue error bar) and comparison to the measurement uncertainty of the fan inlet mass flow rate measured with the bellmouth (red error bar) at different speeds between 30 krpm (dark blue dot) up to 168 krpm (dark red dot). The fan outlet mass flow rate measurement is up to 21 % higher than the fan inlet mass flow rate for the measurements with air at 200 °C.

Reynolds numbers based on the outer diameter ( $Re_D$ ) of 500. The VDI/VDE 2041 [126] is an addition to the ISO 5167 norm and states norms for such quarter circle nozzles. The quarter circle nozzle at the fan outlet with an outer diameter ( $D_8$ ) of 12 mm is well below the minimum value in VDI/VDE 2041 (50 mm). Thus, the German company Tetrattec manufactured and calibrated this quarter circle nozzle with a calibrated measurement uncertainty of  $\pm 0.91\%$  on the read within a 95 % confidence interval. A German calibration laboratory accredited Tetrattec's calibration procedure according to the ISO 17025 norm. An MKS 226A (100 TORR) measured the quarter circle nozzle differential pressure (measurement uncertainty of  $\pm 0.3\%$  on the read). Thus, the measurement uncertainty calculation accounted for  $\pm 0.91\%$  on the read uncertainty of the calibrated discharge coefficient and the measurement uncertainty of the differential pressure measurement, according to the ISO 5167 norm [95]. The error for the nozzle outer diameter ( $D_q$ ), the inner diameter ( $d_q$ ), and for expansion factor (minimal 0.995) was already included within the error of the calibrated discharge coefficient ( $\pm 0.91\%$ ). The error in the density for the ambient air case was  $\sqrt{\left(\frac{0.5}{300}\right)^2 + \left(\frac{0.0005}{0.96}\right)^2 + \left(\frac{0.0031}{0.96}\right)^2} = 0.36\%$  and 0.34 % in the case at 200 °C, which was very low. The total measurement uncertainty for the mass flow rate calculated with the quarter circle nozzle was thus,

$$\delta_q = \sqrt{0.0091^2 + \frac{1}{4}0.003^2 + \frac{1}{4}\left(\frac{0.5\text{K}}{T_q}\right)^2 + \frac{1}{4}\left(\frac{0.5\text{mbar}}{p_{amb} + p_q}\right)^2 + \frac{1}{4}\left(\frac{3.1\text{mbar}}{p_{amb} + p_q}\right)^2} \quad \text{C.1}$$

composed of the uncertainty for the discharge coefficient calibration ( $\pm 0.91\%$ ), the quar-

## Appendix C. Measurement Uncertainty and Calibration of Equipment

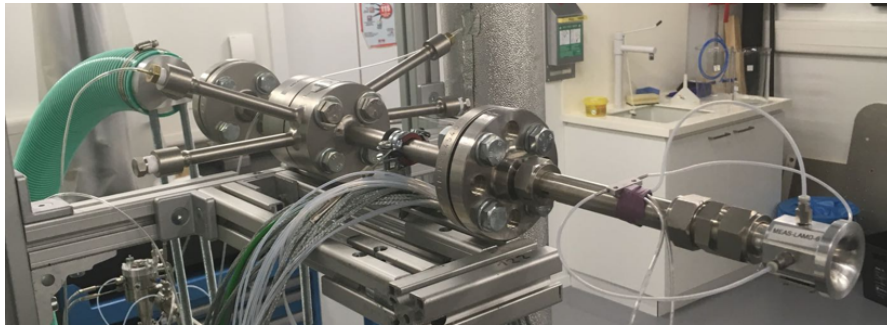


Figure C.3 – Calibration of the bellmouth (right) that measures the fan inlet side test section volume flow rate and mass flow rate with the quarter circle nozzle measurement device (left) that measures the fan outlet side test section volume flow rate and mass flow rate.

ter circle nozzle differential pressure measurement uncertainty ( $\pm 0.3\%$ ), the temperature measurement uncertainty (0.5 K), the ambient pressure measurement with the Lufft Opus 20 (0.5 mbar), and the Scanivalve differential pressure measurement uncertainty (3.1 mbar). The quarter circle nozzle temperature ( $T_q$ ) and the pressure ( $p_{amb} + p_q$ ) calculated the density, whereas the quarter circle nozzle pressure difference ( $\Delta p_q$ ) and the calibrated discharge coefficient calculated the volume flow rate. The fan outlet mass flow rate measurement uncertainty was therefore 0.93 % (see the blue error bars in Figure C.2).

**Swirl** within the fan outlet side test section could further influence the accuracy of the fan outlet mass flow rate measurement. Brennan et al. [127] suggest that the orifice discharge coefficient was up to 6 % higher when swirl at an angle of  $17^\circ$  was present within the measurement tube that had an outer diameter ( $D$ ) of 100 mm and a ( $d/D$ ) ratio of 0.67. Zimmerman [128] suggests that the “required straight lengths for nozzles” from the ISO 5167 norm [95] is not sufficient and recommends a doubling of the given length-to-diameter ratios  $l_8/D_8$ . For the worst-case-scenario of “two or more  $90^\circ$  bends in different planes”, the ISO 5167 norm [95] suggest an  $l_8/D_8$  of 52 for a quarter circle nozzle inner-to-outer diameter ratio  $d_q/D_q = 7.66/12 = 0.64$  to obtain “zero additional uncertainty”. However, the ISO norm does not give any suggestions for rotating machines. Thus, the fan test rig used a cross-shaped flow straightener with a length-to-diameter ratio ( $l/D_8 = 24/12$ ) of two, placed  $45D_8$  after the fan volute outlet diffuser, a Zanker flow conditioner plate at  $63D_8$ , and the quarter circle nozzle at  $93D_8$ . However, despite these installations, the fan outlet side test section mass flow rate measurement showed irregularities at transient operational regions of the fan; hence, this measurement was not accurate enough.

**Bellmouth:** At the nearly-undisturbed fan inlet section, a low-ratio long-radius bellmouth according to the ISO 5167-3 norm [95] measured the volume flow rate and mass flow rate. For this measurement, an MKS 223B (1000 Pa, measurement uncertainty of  $\pm 0.3\%$  on the read) measured the differential pressure between the ambient and the bellmouth inlet. The bellmouth outer diameter is 32.4 mm; hence, the geometry is smaller than allowed by the ISO 5167-3 norm (50 mm). The Reynolds number based on the outer diameter ( $Re_D$ ) was

within the maximum of 3000 (for the tests with hot air), but was out of the normed range for the discharge coefficient (minimum 10000). Therefore, an in-house calibration between the bellmouth and the volume flow rate measurement device (quarter circle nozzle) at the fan outlet was conducted (Figure C.3). The measurement uncertainty of the bellmouth calibration,

$$\delta_{b,cal} = \sqrt{0.0091^2 + \frac{1}{4}0.003^2 + \frac{1}{4}0.003^2 + \frac{1}{4}\left(\frac{0.3\text{ K}}{T_{amb}}\right)^2 + \frac{1}{4}\left(\frac{0.5\text{ mbar}}{p_{amb}}\right)^2} = 0.0096 \quad \text{C.2}$$

was a function of quarter circle nozzle measurement uncertainty (0.0091), the MKS differential pressure measurement uncertainties ( $2 \times 0.003$ ), as well as the ambient pressure and temperature measurement uncertainties for the Lufft Opus 20 (0.5 mbar and 0.3 K) for free inflow from the ambient (Figure C.3). The final bellmouth measurement uncertainty was thus,

$$\delta_b = \sqrt{\delta_{b,cal}^2 + \frac{1}{4}0.003^2 + \frac{1}{4}\left(\frac{0.5\text{ K}}{T_b}\right)^2 + \frac{1}{4}\left(\frac{0.5\text{ mbar}}{p_{amb}}\right)^2} \quad \text{C.3}$$

a function of the bellmouth inlet temperature ( $T_b$ ) and the ambient pressure ( $p_{amb}$ ). Figure C.2 shows the bellmouth measurement uncertainty, which was 1 % in the case with hot air at 200 °C for various rotational speeds. The fan outlet side test section mass flow rate was up to 21 % higher than at the fan inlet side test section mass flow rate, measured with the bellmouth. The author considered the mass flow rate measurement with the bellmouth more accurate than the quarter circle nozzle measurement and this thesis therefore uses the mass flow rate measurements at the nearly-undisturbed fan inlet side test section.

**Rotational speed:** The FTU used three different shaft rotational speed measurement devices (Figure 5.11):

1. A lion Precision C3S capacitive probe (not usable at 200 °C)
2. A high-temperature Philtec D20 optical probe
3. A high-temperature Kistler Type 601CA piezoelectric pressure sensor measuring the blade passing frequency at the blade TE (diameter of 18.55 mm)

Options 1 to 3 showed coherent measurements at ambient temperatures (Section 5.3). Figure C.4 shows an example for 168.5 krpm. Option 2 and 3 measured the rotational speed at high temperatures of 200 °C.

## Appendix C. Measurement Uncertainty and Calibration of Equipment

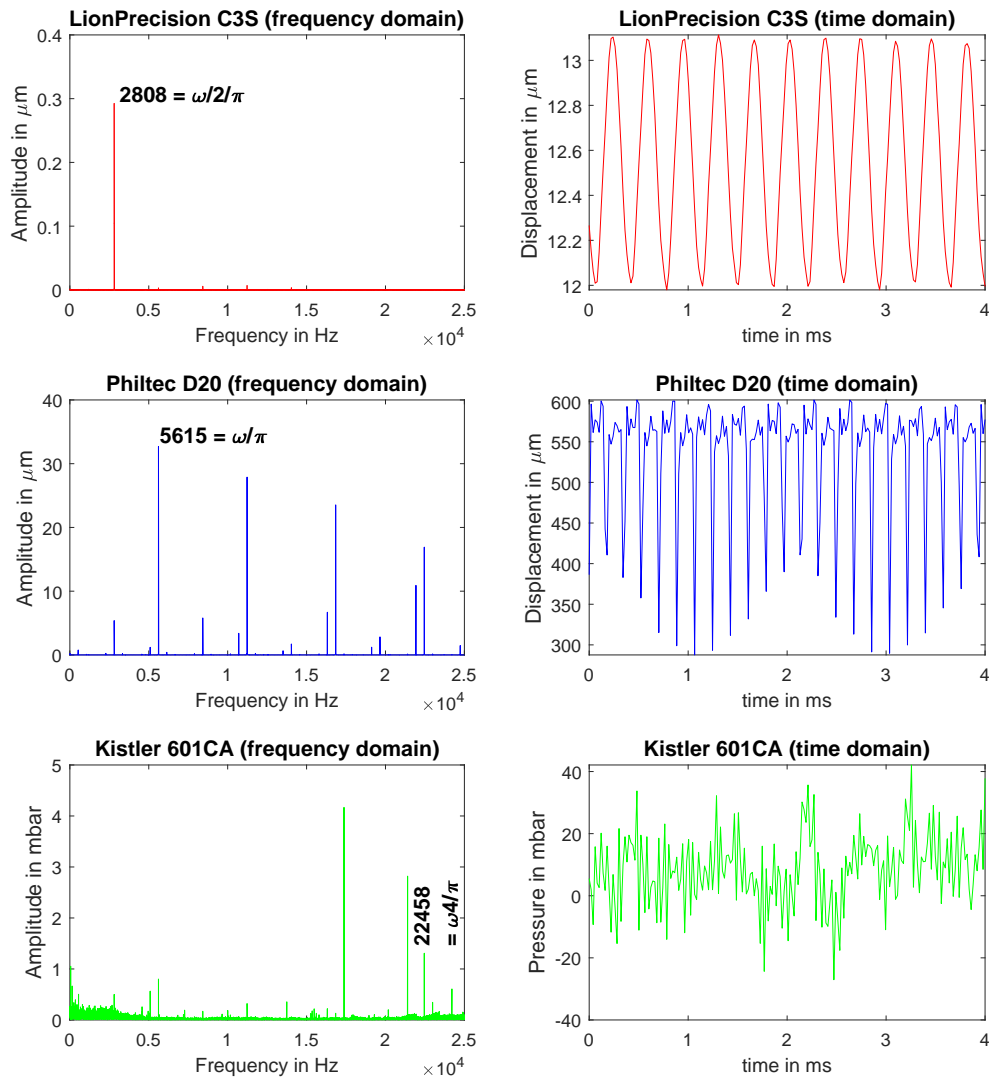


Figure C.4 – Rotational speed at 168.5 krpm measured with the LionPrecision C3S probe (red), the Philtec D20 probe (blue), and the Kistler 601 CA (green). The left side shows the signal in the frequency domain (FFT with 50000 samples) and the right side shows 200 samples in the time domain (50 kHz sampling rate). The C3S measures the rotor orbit in one direction ( $2608 \cdot 0.06 = 168.48 \text{krpm}$ ), the Philtec D20 measures two grooves on the shaft ( $\frac{5615}{2} \cdot 0.06 = 168.45 \text{krpm}$ ), and the pressure sensor measures the blade passing frequency of the eight blades ( $\frac{22458}{8} \cdot 0.06 = 168.435 \text{krpm}$ ).

Table C.1 – Measurement uncertainties of utilized equipment.

<b>Total temperature</b>	
Class 1 k-type thermocouple	$\pm 0.5\text{ }^{\circ}\text{C}^{\text{a}}$ calibration from 15-175 $^{\circ}\text{C}$
<b>Ambient pressure, temperature, and relative humidity</b>	
Lufft Opus 20	$\pm 0.5\text{ mbar}$ , $\pm 0.3\text{ }^{\circ}\text{C}$ , and $\pm 2$ percentage points
<b>Total-to-static differential pressure</b>	
Scanivalve DSA 3218 (250 Psi)	$\pm 0.018\text{ \%}^{\text{b}}$ of full scale (FS) = $\pm 3.1\text{ mbar}$
MKS 226A (100 Torr)	$\pm 0.3\text{ \% OR}^{\text{c}}$ (used for quarter circle nozzle)
MKS 226A (100 Torr)	$\pm 0.3\text{ \% OR}^{\text{c}}$ (used for fan pressure rise)
MKS 223B (1000 Pa)	$\pm 0.3\text{ \% OR}^{\text{c}}$ (used for bellmouth)
<b>Volume flow rate</b>	
Bellmouth (fan inlet)	$\pm 0.96\text{ \% OR}^{\text{d}}$ / $\pm 0.3\text{ \% OR}$ (calibration / MKS 223B)
Quarter circle nozzle (fan outlet)	$\pm 0.91\text{ \% OR}^{\text{c}}$ / $\pm 0.3\text{ \% OR}$ (calibration / MKS 226A)
KNF SIMDOSE 10 (turbine inlet)	$\pm 2\text{ \% FS} = \pm 0.02\text{ ml min}^{-1}$ ( $\pm 0.12\text{ kg h}^{-1}$ at ambient)
<b>Mass flow rate</b>	
Emerson D S006S (turbine inlet)	$\pm (0.002 + \frac{0.006}{\dot{m}})100\text{ \% OR}$ , $\dot{m}$ in $\text{kg h}^{-1}$
<b>Rotational speed</b> $\pm 0.5\text{ krpm}$ (@ 50 kHz sampling)	
Philtec D20	FFT of signal and displacement
Kistler type 601CA (250 bar)	FFT of signal (blade passing frequency)
LionPrecision C3S	FFT of signal and rotor orbit (max. temp. 50 $^{\circ}\text{C}$ )
<b>Displacement</b>	
LionPrecision C3S	$\pm 0.25\text{ \% FS} = \pm 0.125\text{ }\mu\text{m}^{\text{d}}$ (max. temp. 50 $^{\circ}\text{C}$ )
Philtec D20	$\pm 1\text{ \% linearity}$ on the “far side” (0.14-0.36 mm) <sup>d</sup>

<sup>a</sup> Assumption for the entire operational range from 0 to 225  $^{\circ}\text{C}$  (in-house calibration)

<sup>b</sup> Maximum error of all 16 channels on the entire 250 Psi range (verified by Scanivalve)

<sup>c</sup> External calibration

<sup>d</sup> In-house calibration





## D Balancing of the Fan-Turbine Unit

Without balancing, the FTU can typically safely operate up to a rotational speed of 30-40 krpm. Due to manufacturing and assembly tolerances, the inertia axis of the rotor does not correlate with the rotational axis of the machine; hence, the rotor orbit increases steadily with increasing speeds and eventually touches the journal bearings, or the unbalance forces surpasses the (low) load capacity of the bearings (chapter 6.2 in [12]).

The machine therefore requires a balancing procedure to reach the design speed of 175 krpm. It is a two-plane in-situ balancing procedure using the influence coefficient method. “The method is based on the assumption that the measured vibration on the two planes at a fixed speed is a linear function of the unbalance levels (amplitude & phase) at each plane and of the influence coefficients” [12]. In order to find the unbalance level in terms of amplitude and phase, the rotor operates with a trial mass at the front and back at a certain angular position between 0 and 360°. Eight holes with a diameter of 0.9 mm and a length of 2 mm can accommodate a trial mass in the form of a small cable at intervals of 45°. Figure 4.4 on the left shows these holes for the fan and Figure D.1 shows the holes in the middle for the turbine



Figure D.1 – The radial inflow turbine with a diameter of 15 mm (left), the screw that fixes the turbine on the shaft with holes for balancing (middle) after several balancing procedures (second from the left) and before balancing (second from the right). A “dummy turbine” for removing the entire shaft during the balancing procedure is shown on the right.

## Appendix D. Balancing of the Fan-Turbine Unit

---

(after and before several balancing procedures). These holes are essential, since a material, such as a glue or sticky plasticine, cannot withstand the centrifugal forces at high rotational speeds. A test with no unbalance, unbalance at the front at a certain angular position, and unbalance at the back at the same angular position can indicate therefore the amplitude and position of the shaft unbalance.

Figure D.2 shows a typical balancing procedure. Without balancing, at iteration 0, the rotor orbit on the turbine side is  $2.1\ \mu\text{m}$ , which is relatively large with respect to the bearing clearance (red dots in the second graph), whereas it is  $1.5\ \mu\text{m}$  on the fan side for a rotational speed of 27 krpm (red dots in the upper graph). The graph also features the phase on the fan and turbine side, where a positive phase points in the direction of the rotational speed. The FTU balancing required seven iterations that corresponded to the removal of material at the following positions (with respect to the direction of the rotational speed).

- Iteration 1: Turbine side at a position of  $330^\circ$  (four steps)
- Iteration 2: Fan side at a position of  $300^\circ$  (four steps)
- Iteration 3: Fan side at a position of  $315^\circ$  (two steps)
- Iteration 4: Turbine side at a position of  $280^\circ$  (one step)
- Iteration 5: Fan side at a position of  $335^\circ$  (one step)
- Iteration 6: Fan side at a position of  $340^\circ$  (one step)
- Iteration 7: Turbine side at a position of  $260^\circ$  (one step)

A hand drill is sufficient for removing material (Figure D.1). Within the first iteration, a typical balancing procedure removes material on the order of several gmm; hence, a standard high-precision scale is not a viable option. The drilling at each iteration is therefore conducted in several steps to avoid excessive material removal (four steps for the first iteration and one step for the last iterations). The yellow diamonds in Figure D.2 show such a case: the phase at the front changes by  $180^\circ$  between iteration 4 and iteration 7, indicating that excessive material was removed. For the last iterations, the removed material was on the order of several 0.1 gmm. After the balancing procedure (iteration 7), the rotor orbit was lower than  $0.3\ \mu\text{m} \pm 0.125\ \mu\text{m}$  at a speed of 88 krpm, which is sufficient for the entire operational range up to 175 krpm.

The previous example had 14 individual steps, or drilling operations, and seven iterations (each with three FTU startups: no trial mass, mass on the fan and the turbine side). This resulted in a minimum of 35 FTU startups. Since the assembly and disassembly of the turbine volute is time-intensive, air nozzles propel the FTU on the fan side (Section 5.1), since the turbine side with its small blades (0.59 mm) does not allow for this operation. The volute-less operation allows for easy manipulation of the turbine (drilling and putting a trial mass).

When the FTU with the turbine impeller is assembled, it is fixed inside the housing and removal of the shaft is impossible without complete shaft disassembly. In the author's experience, a disassembly of the shaft requires complete rebalancing of the rotor, since an equivalent manual reassembly of the rotor with its five components (fan, shaft, turbine, screw within the shaft,

and turbine nut in Figure 4.1) is nearly-impossible. A “dummy turbine” (Figure D.1 on the right) allows for the removal of the shaft during the balancing procedure.

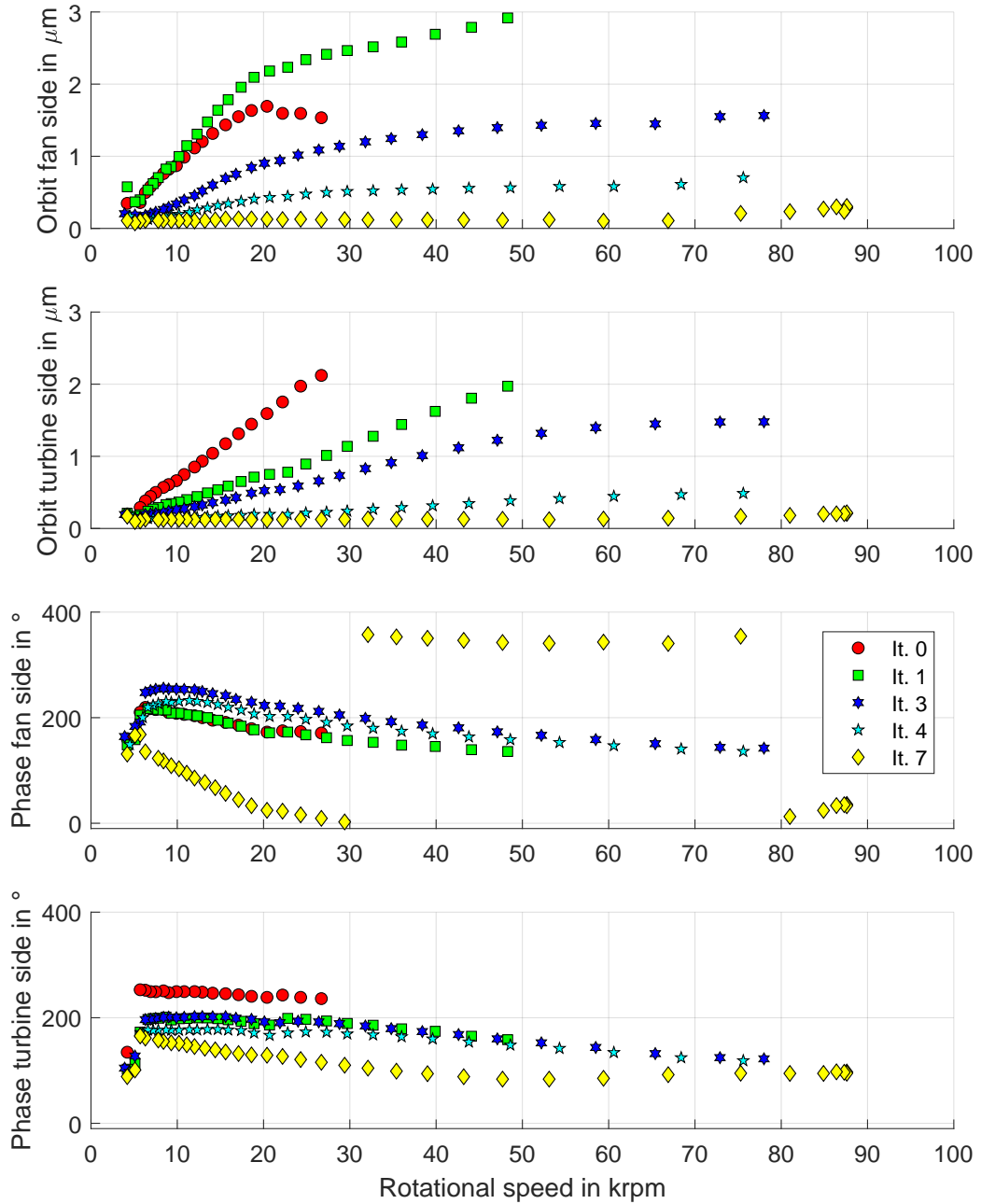


Figure D.2 – The measured rotor orbits on the fan and turbine side with the respective phases (positive in the direction of rotation) for different iterations (it.) of the balancing procedure and the initial state (It.0).



## E Turbine Stator Blockage

Figure E.1 and Figure E.2 show the turbine stator blockage, which occurred during the coupling of the FTU with a 6 kW<sub>el</sub> SOFC system. The deposits were composed of ceramics, glass fibers, and salt (identified with a scanning electron microscope). During the FTU test rig assembly, ceramics from the oven, as well as fibers from the insulation tape penetrated the evaporator. Additionally, the utilized water was not sufficiently deionized (50 μS cm<sup>-1</sup>). During operation, these particles were continuously released from the evaporator and blocked the turbine stator. Due to the centrifugal forces acting on these particles in the turbine inducer, the heavier particles were separated (left side in Figure E.2). In the end of the experimental campaign, only three turbine stator rows were partially open (Figure E.2). Thus, the admission was 5 % instead of 21 % at the design point, which corresponds to a decrease of admission by 76 %. The turbine operated in off-design, leading to a pressure ratio of 4.2 and a steam mass flow rate of 1.7 kg h<sup>-1</sup>. The shaft rotational speed was 220 krpm. Despite the elevated pressure ratio and rotational speed, due to the partial turbine stator blockage, the FTU was operating very stable. An operation without turbine blockage was achieved by cleaning of all parts, a careful assembly process, and sufficiently deionized water (0.5 μS cm<sup>-1</sup>).

## Appendix E. Turbine Stator Blockage



Figure E.1 – Turbine volute and stator (left), as well as turbine seal and rotor (right) with deposits: ceramics, salt, and glass fibers.

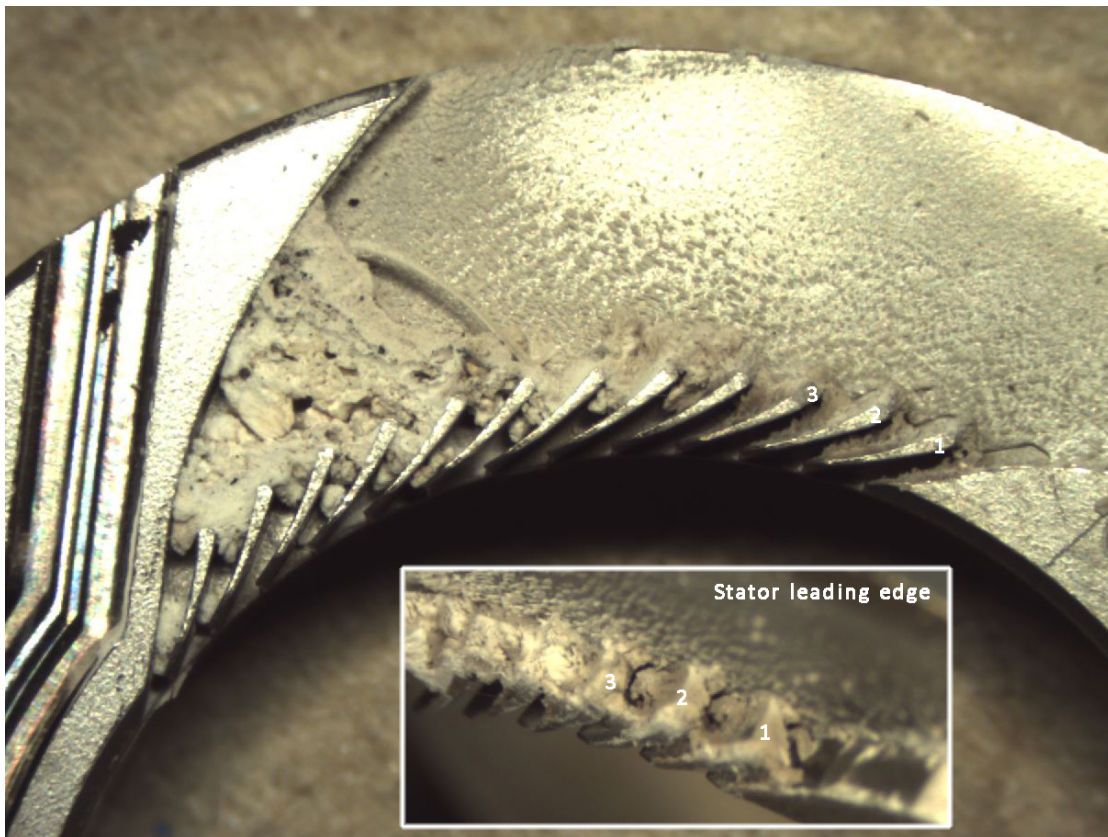


Figure E.2 – Deposits in the turbine rotor and zoom of the turbine stator leading edge. Only three stator rows (marked with 1, 2, and 3) out of 13 were partially open.

## Bibliography

- [1] Sasaki, K., and Teraoka, Y., 2003. "Equilibria in Fuel Cell Gases II. The C-H-O Ternary Diagrams". *Journal of The Electrochemical Society*, **150**(7), July, pp. A885–A888.
- [2] Balje, O. E., 1981. *Turbomachines : a guide to design, selection and theory*. Wiley, New York etc.
- [3] Nations, U., 2018. The Paris Agreement. <https://unfccc.int/process-and-meetings/the-paris-agreement/the-paris-agreement>. Accessed: 2018-05-20.
- [4] Pacala, S., and Socolow, R., 2004. "Stabilization Wedges: Solving the Climate Problem for the Next 50 Years with Current Technologies". *Science*, **305**(5686), Aug., pp. 968–972.
- [5] Alanne, K., and Saari, A., 2006. "Distributed energy generation and sustainable development". *Renewable and Sustainable Energy Reviews*, **10**(6), Dec., pp. 539–558.
- [6] Töpler, J., and Lehmann, J., eds., 2016. *Hydrogen and fuel cell: technologies and market perspective*. Springer, Heidelberg New York Dordrecht London.
- [7] Molyneaux, A., 2002. "A practical evolutionary method for the multi-objective optimisation of complex integrated energy systems including vehicle drivetrains". PhD thesis, EPFL, Lausanne. Thesis number 2636.
- [8] Leyland, G., 2002. "Multi-objective optimisation applied to industrial energy problems". PhD thesis, EPFL, Lausanne. Thesis number 2572.
- [9] Palazzi, E, Favrat, D., Maréchal, F., and Van herle, J., 2004. Energy Integration and System Modelling of Fuel Cell Systems. Tech. rep.
- [10] Bolliger, R., 2010. "Méthodologie de la synthèse des systèmes énergétiques industriels". PhD thesis, EPFL, Lausanne. Thesis number 4867.
- [11] Facchinetti, E., 2012. "Integrated Solid Oxide Fuel Cell - Gas Turbine Hybrid Systems with or without CO2 Separation". PhD thesis, EPFL, Lausanne. Thesis number 5323.
- [12] Schiffmann, J., 2008. "Integrated design, optimization and experimental investigation of a direct driven turbocompressor for domestic heat pumps". PhD thesis, EPFL, Lausanne. Thesis number 4126.

## Bibliography

---

- [13] Carré, J.-B., 2015. “Experimental investigation of electrical domestic heat pumps equipped with a twin-stage oil-free radial compressor”. PhD thesis, EPFL. Thesis number 6764.
- [14] Demierre, J., 2012. “Theoretical and Experimental Study of a Thermally Driven Heat Pump Based on a Double Organic Rankine Cycle”. PhD thesis, EPFL, Lausanne. Thesis number 5201.
- [15] Mounier, V., 2018. “Potential and Challenges of ORC driven Heat Pumps Based on Gas Bearing Supported Turbomachinery”. PhD thesis, EPFL, Lausanne. Thesis number 8567.
- [16] Van herle, J., 1993. “Oxygen reduction reaction mechanisms at solid oxide fuel cell cathodes”. PhD thesis, EPFL, Lausanne. Thesis number 1187.
- [17] Larrain, D., 2005. “Solid oxide fuel cell stack simulation and optimization, including experimental validation and transient behavior”. PhD thesis, EPFL, Lausanne. Thesis number 3275.
- [18] Autissier, N., 2008. “Small scale SOFC systems: design, optimization and experimental results”. PhD thesis, EPFL, Lausanne. Thesis number 4015.
- [19] Wullemin, Z., 2009. “Experimental and modeling investigations on local performance and local degradation in solid oxide fuel cells”. PhD thesis, EPFL, Lausanne. Thesis number 4525.
- [20] GE Power, 2018. Breaking the Power Plant Efficiency Record...Again! <https://www.ge.com/power/about/insights/articles/2018/03/nishi-nagoya-efficiency-record>. Accessed: 20198-01-30.
- [21] Elgowainy, A., and Wang, M., 2008. Fuel Cycle Comparison of Distributed Power Generation Technologies. Tech. rep., Center for Transportation Research, Argonne National Laboratory.
- [22] Atrex Energy, 2018. About Atrex Tubular SOFC. <http://www.atrexenergy.com/technology/about-atrex-tubular-sofc>. Accessed: 2018-07-08.
- [23] Bocarsly, A., 2011. *Fuel cells and hydrogen storage*, Vol. 141 of *Structure and bonding*. Springer, Berlin.
- [24] Shao, Z., 2016. *Intermediate-temperature solid oxide fuel cells : materials and applications*. Springer, Berlin.
- [25] Kupecki, J., ed., 2018. *Modeling, Design, Construction, and Operation of Power Generators with Solid Oxide Fuel Cells: From Single Cell to Complete Power System*. Springer International Publishing.



- [26] Angeli, S. D., Monteleone, G., Giaconia, A., and Lemonidou, A. A., 2014. "State-of-the-art catalysts for CH<sub>4</sub> steam reforming at low temperature". *International Journal of Hydrogen Energy*, **39**(5), Feb., pp. 1979–1997.
- [27] Faes, A., 2011. "RedOx Stability of Anode Supported Solid Oxide Fuel Cells". PhD thesis, EPFL, Lausanne. Thesis number 4893.
- [28] Nakajo, A., 2011. "Thermomechanical and Electrochemical Degradation in Anode-Supported Solid Oxide Fuel Cell Stacks". PhD thesis, EPFL, Lausanne. Thesis number 4930.
- [29] Diethelm, S., Van herle, J., Modena, S., Bertoldi, M., and Alyousef, Y. M., 2011. "Performance of SOFC stacks under partial internal reforming of methane". In Proceedings of 15th European Fuel Cell Forum 2011.
- [30] NIST, 2018. Standard reference data. <https://www.nist.gov/srd>. Accessed: 2018-07-06.
- [31] Greco, F., 2018. "Improved thermo-mechanical reliability of anode-supported solid oxide fuel cells". PhD thesis, EPFL, Lausanne. Thesis number 8470.
- [32] HTceramix S.A., 2016. WO 2016/087389 A1: SOFC system and method of operating a sofc system.
- [33] Schuler, J. A., 2012. "Chromium Poisoning: The Needle in the SOFC Stack". PhD thesis, EPFL, Lausanne. Thesis number 5428.
- [34] Madi, H., 2016. "Investigations into the Effects of Biofuel Contaminants on Solid Oxide Fuel Cells". PhD thesis, EPFL, Lausanne. Thesis number 7161.
- [35] EPFL, SOLIDpower, 2018. EP 18 188 237.4: SOFC System With Anode Off-Gas Recirculation (under review).
- [36] Bossel, U., 2015. Personal communication via e-mail, Aug.
- [37] European Committee for Standardization, 2013. EN 62282: Fuel cell technologies - Part 3-201 : stationary fuel cell power systems - Performance test methods for small fuel cell power systems.
- [38] ASME, 2002. ASME PTC 50: 2002 - Fuel Cell Power Systems Performance . <https://www.asme.org/products/codes-standards/ptc-50-2002-fuel-cell-power-systems-performance>. Accessed: 2018-07-10.
- [39] Boaro, M., and Aricò, A. S., eds., 2017. *Advances in Medium and High Temperature Solid Oxide Fuel Cell Technology*. CISM International Centre for Mechanical Sciences. Springer International Publishing.
- [40] Alzate-Restrepo, V., and Hill, J. M., 2010. "Carbon deposition on Ni/YSZ anodes exposed to CO/H<sub>2</sub> feeds". *Journal of Power Sources*, **195**(5), Mar., pp. 1344–1351.

## Bibliography

---

- [41] Powell, M., Meinhardt, K., Sprenkle, V., Chick, L., and McVay, G., 2012. "Demonstration of a highly efficient solid oxide fuel cell power system using adiabatic steam reforming and anode gas recirculation". *Journal of Power Sources*, **205**, May, pp. 377–384.
- [42] Immisch, C., Dietrich, R.-U., and Lindermeir, A., 2012. "Technical progress of partial anode offgas recycling in propane driven Solid Oxide Fuel Cell system". In Proceedings of 10th European SOFC Forum 2012.
- [43] Dietrich, R.-U., Lindermeir, A., Immisch, C., Spieker, C., Spitta, C., Stenger, S., Leithner, R., Küster, T., and Oberland, A., 2013. "SOFC System Using a Hot Gas Ejector for Offgas Recycling for High Efficient Power Generation from Propane". *ECS Transactions*, **57**(1), Oct., pp. 171–184.
- [44] Halinen, M., Pohjoranta, A., Kujanpää, L., Väisänen, V., and Salminen, P., 2014. Summary of the RealDemo – project 2012-2014. Tech. rep., VTT Technical Research Centre of Finland.
- [45] Halinen, M., Rautanen, M., Saarinen, J., Pennanen, J., Pohjoranta, A., Kiviaho, J., Pastula, M., Nuttall, B., Rankin, C., and Borglum, B., 2011. "Performance of a 10 kW SOFC Demonstration Unit". *ECS Transactions*, **35**(1), Apr., pp. 113–120.
- [46] Peters, R., Engelbracht, M., Tiedemann, W., Hoven, I., Deja, R., Nguyen, V. N., Blum, L., and Stolten, D., 2017. "Development and Test of a Solid Oxide Fuel Cell Subsystem with a Low Temperature Anode Off-Gas Recirculation". *ECS Transactions*, **78**(1), May, pp. 2489–2495.
- [47] Rechberger, J., Reissig, M., and Hauth, M., 2013. "AVL SOFC Systems on the Way of Industrialization". *ECS Transactions*, **57**(1), Oct., pp. 141–148.
- [48] Rechberger, J., Reissig, M., Mathe, J., and Reiter, B., 2016. "Solid Oxide Fuel Cell APUs for Transport Applications". In Proceedings of 12th European SOFC & SOE Forum 2016.
- [49] Hauth, M., Seidl, M., Postl, A., Sallai, C., Soukup, N., Albert, J., Weinländer, C., Rieberer, R., and Hochenauer, C., 2017. "Development of a Highly Flexible SOFC CCHP System Towards Demand-Oriented Power Generation from Renewable Fuels". *Meeting Abstracts*, **MA2017-03**(1), July, pp. 14–14.
- [50] Agnew, G. D., Collins, R. D., Jörgen, M. B., Pyke, S. H., and Travis, R., 2007. "The Components of a Rolls-Royce 1 MW SOFC System". *ECS Transactions*, **7**(1), May, pp. 105–111.
- [51] Goettler, R., 2014. SECA Coal-Based Systems - LGFCS. Tech. rep., LG Fuel Cell Systems Incorporated, Jan.
- [52] Goettler, R., 2016. SECA Coal-Based Systems – LGFCS. Tech. rep., LG Fuel Cell Systems Incorporated, Mar.

- [53] LG Fuel Cell Systems Incorporated, 2018. Solid Oxide Fuel Cell (SOFC) Prototype System Testing. <https://www.netl.doe.gov/research/coal/project-information/proj?k=FE0031180>. Accessed: 2018-06-28.
- [54] Borglum, B. P., and Ghezel-Ayagh, H., 2015. "Development of Solid Oxide Fuel Cells at Versa Power Systems and FuelCell Energy". *ECS Transactions*, **68**(1), June, pp. 89–94.
- [55] Ghezel-Ayagh, H., 2016. SOFC Systems with Improved Reliability and Endurance. Tech. rep., Fuelcell Energy, Incorporated, Dec.
- [56] Weeber, K., Horstmann, P., and Miersch, J., 2018. "Changes in Power Generation and Distribution and the role of SOFC". In Proceedings of 13th European SOFC & SOE Forum 2018.
- [57] Baba, S., Kobayashi, N., Takahashi, S., and Hirano, S., 2014. "Development of Anode Gas Recycle System Using Ejector for 1 KW Solid Oxide Fuel Cell". *Journal of Engineering for Gas Turbines and Power*, **137**(2), Sept., p. 021504.
- [58] CAP Co., Ltd. Anode Gas Recycle Blower for SOFC. <http://www.cap-co.jp/SOFCE.html>. Accessed: 2015-03-03.
- [59] Tanaka, Y., Sato, K., Yamamoto, A., and Kato, T., 2013. "Development of Anode Off-Gas Recycle Blowers for High Efficiency SOFC Systems". *ECS Transactions*, **57**(1), Oct., pp. 443–450.
- [60] Johnson, M. C., 2010. R-MCJ10042201-1A\_PADT\_PhaseII-report-final. Tech. rep., Apr.
- [61] Agrawal, G., 2010. Advances in fuel cell blowers. [www.netl.doe.gov/file%20library/events/2009/seca/presentations/Agrawal\\_Presentation.pdf](http://www.netl.doe.gov/file%20library/events/2009/seca/presentations/Agrawal_Presentation.pdf). Accessed: 2015-04-14.
- [62] Agrawal, G. L., Buckley, C. W., and Shakil, A., 2012. Foil gas bearing supported high temperature centrifugal blower and method for cooling thereof, July. U.S. Classification 417/373, 417/423.8, 415/178; International Classification F04B39/02, F04B39/06; Cooperative Classification F04D29/057, F04D29/584; European Classification F04D29/58C3, F04D29/057.
- [63] Hooshang Heshmat, 2016. High Temperature Anode Recycle Blower for Solid Oxide Fuel Cell. Tech. rep., Mohawk Innovative Technology, <https://www.netl.doe.gov/research/coal/project-information/proj?k=FE0027895>. Accessed: 2018-08-16.
- [64] Dicks, A. L., and Martin, P. A., 1998. "A fuel cell balance of plant test facility". *Journal of Power Sources*, **71**(1), Mar., pp. 321–327.
- [65] Liu, M., Lanzini, A., Halliop, W., Cobas, V. R. M., Verkooijen, A. H. M., and Aravind, P. V., 2013. "Anode recirculation behavior of a solid oxide fuel cell system: A safety analysis and a performance optimization". *International Journal of Hydrogen Energy*, **38**(6), Feb., pp. 2868–2883.

## Bibliography

---

- [66] Peters, R., Deja, R., Blum, L., Pennanen, J., Kiviaho, J., and Hakala, T., 2013. "Analysis of solid oxide fuel cell system concepts with anode recycling". *International Journal of Hydrogen Energy*, **38**(16), May, pp. 6809–6820.
- [67] Engelbracht, M., Peters, R., Blum, L., and Stolten, D., 2015. "Comparison of a fuel-driven and steam-driven ejector in solid oxide fuel cell systems with anode off-gas recirculation: Part-load behavior". *Journal of Power Sources*, **277**, Mar., pp. 251–260.
- [68] Wu, C.-H., 1952. A General Theory of Three-Dimensional Flow in Subsonic and Supersonic Turbomachines of Axial-, Radial, and Mixed-Flow Types. Tech. rep., Jan.
- [69] International Organization for Standardization, 2007. ISO 5801: Industrial fans - Performance testing using standardize airways.
- [70] Eckardt, D., 1976. "Detailed Flow Investigations Within a High-Speed Centrifugal Compressor Impeller". *Journal of Fluids Engineering*, **98**(3), Sept., pp. 390–399.
- [71] Dalbert, P., Ribí, B., Kmeci, T., and Casey, M. V., 1999. "Radial compressor design for industrial compressors". *Proceedings of the Institution of Mechanical Engineers, Part C: Journal of Mechanical Engineering Science*, **213**(1), Jan., pp. 71–83.
- [72] Dietmann, F., 2015. "Zum Einfluss der Reynolds-Zahl und der Oberflächenrauigkeit bei thermischen Turbokompressoren". PhD thesis, Universität Stuttgart.
- [73] Javed, A., Arpagaus, C., Bertsch, S., and Schiffmann, J., 2016. "Small-scale turbocompressors for wide-range operation with large tip-clearances for a two-stage heat pump concept". *International Journal of Refrigeration*, **69**, Sept., pp. 285–302.
- [74] Bruno Eck, 2003. *Ventilatoren : Entwurf und Betrieb der Radial-, Axial- und Querstromventilatoren*, 6. aufl. ed. Springer, Berlin etc.
- [75] Leonhard Bommers, 2003. *Ventilatoren*, 2. aufl. ed. Vulkan-Verlag, Essen.
- [76] Thomas Carolus, 2013. *Ventilatoren : aerodynamischer Entwurf, Schallvorhersage, Konstruktion*, 3., überarb. u. erw. aufl. ed. Vieweg+Teubner, Wiesbaden.
- [77] Japiske, D., 1996. *Centrifugal compressor design and performance*. Concepts ETI, Wilder, VT.
- [78] Whitfield, A., and Baines, N. C., 2002. *Design of radial turbomachines*, pearson education print on demand edition ed. Longman [u.a.], Harlow, Essex.
- [79] Nicholas C. Baines, M., 2005. *Fundamentals of turbocharging*. Concepts NREC, White River Junction, Vermont.
- [80] Moustapha, H., and Zelesky, M. F, eds., 2003. *Axial and radial turbines*. Concepts NREC, White River Junction, Vt.

- [81] Wilcox, D. C., 2008. "Formulation of the  $k-\omega$  Turbulence Model Revisited". *AIAA Journal*, **46**(11), Nov., pp. 2823–2838.
- [82] Johnson, M. C., 2010. R-MCJ10042201-1a\_padt\_phaseii-report-final. Technical Report R-MCJ10042201-1A, Phoenix Analysis & Design Technologies, United States, Apr.
- [83] Ronald H. Aungier, 2000. *Centrifugal compressors: a strategy for aerodynamic design and analysis*. ASME Press, New York.
- [84] Leidel, W., 1967. "Einfluß von Zungenradius und Zungenabstand auf Kennlinie und Geräusch eines Radialventilators". PhD thesis, TU Berlin.
- [85] Johann Friedrich Gülich, 2010. *Centrifugal pumps*, 2nd ed. ed. Springer, Heidelberg.
- [86] Singh, V., Wagner, P. H., Wuillemin, Z., Diethelm, S., Schiffmann, J., and Herle, J. V., 2015. "Towards the Next-Generation of Solid Oxide Fuel Cell Systems". *ECS Transactions*, **68**(1), June, pp. 2373–2386.
- [87] Shukla, I., 2014. "Dimensioning of a SOFC system integrating recirculation of the exhaust". Master's thesis, EPFL, Lausanne.
- [88] Wagner, P. H., Wuillemin, Z., Diethelm, S., Van herle, J., and Schiffmann, J., 2017. "Modeling and Designing of a Radial Anode Off-Gas Recirculation Fan for Solid Oxide Fuel Cell Systems". *Journal of Electrochemical Energy Conversion and Storage*, **14**(1), May, pp. 011005–011005–12.
- [89] Facchinetti, E., Favrat, D., and Marechal, F., 2014. "Design and Optimization of an Innovative Solid Oxide Fuel Cell–Gas Turbine Hybrid Cycle for Small Scale Distributed Generation". *Fuel Cells*, **14**(4), Aug., pp. 595–606.
- [90] Van herle, J., Maréchal, F., Leuenberger, S., and Favrat, D., 2003. "Energy balance model of a SOFC cogenerator operated with biogas". *Journal of Power Sources*, **118**(1–2), May, pp. 375–383.
- [91] Wiesner, F. J., 1979. "A new appraisal of Reynolds number effects on centrifugal compressor performance". *ASME Transactions Journal of Engineering Power*, **101**, pp. 384–392.
- [92] Nibourel, P., 2018. CFD simulation for a grooved thrust gas bearing. Tech. rep., Lausanne.
- [93] Malanoski, S. B., and Pan, C. H. T., 1965. "The Static and Dynamic Characteristics of the Spiral-Grooved Thrust Bearing". *Journal of Basic Engineering*, **87**(3), pp. 547–555.
- [94] Pfleiderer, C., 1961. *Die Kreiselpumpen für Flüssigkeiten und Gase: Wasserpumpen, Ventilatoren, Turbogebläse, Turbokompressoren*, fünfte, neubearb. Aufl. ed. Springer, Berlin etc.
- [95] International Organization for Standardization, 2003. ISO 5167: Measurement of fluid flow by means of pressure differential devices inserted in circular cross-section conduits running full.

## Bibliography

---

- [96] Sato, S., Jovanovic, S., Lang, J., and Spakovszky, Z., 2011. “Demonstration of a Palm-Sized 30 W Air-to-Power Turbine Generator”. *Journal of Engineering for Gas Turbines and Power*, **133**(10), May, pp. 102301–102311.
- [97] Jovanovic, S., 2008. “Design of a 50-watt air supplied turbogenerator”. Master’s thesis, MIT.
- [98] Soderberg, C., 1949. Unpublished notes, Gas Turbine Laboratory, MIT.
- [99] R. I. Lewis, 1996. *Turbomachinery performance analysis*. Arnold, London.
- [100] Glassman, A. J., 1994. Turbine design and application volumes 1, 2, and 3. Tech. rep., June.
- [101] Font, A. M., 2019. “Analytical and numerical investigation of a small-scale radial-inflow turbine”. Master’s thesis, EPFL, Lausanne.
- [102] Dunavant, J. C., and Erwin, J. R., 1956. Investigation of a related series of turbine-blade profiles in cascade. Tech. rep., Oct.
- [103] Zweifel, O., 1945. The spacing of turbomachine blading, especially with large angular deflection. *Brown Boveri Review*, 32, 12.
- [104] Stenning, A. H., 1953. Design of turbines for high-energy-fuel low-power-output applications. Tech. rep. Report number 79, Department of Mechanical Engineering, MIT, Sept.
- [105] Daily, J. W., and Nece, R. E., 1960. “Chamber Dimension Effects on Induced Flow and Frictional Resistance of Enclosed Rotating Disks”. *Journal of Basic Engineering*, **82**(1), Mar., pp. 217–230.
- [106] Demierre, J., Rubino, A., and Schiffmann, J., 2014. “Modeling and Experimental Investigation of an Oil-Free Microcompressor-Turbine Unit for an Organic Rankine Cycle Driven Heat Pump”. *Journal of Engineering for Gas Turbines and Power*, **137**(3), Oct., pp. 032602–1–032602–10.
- [107] Körtvelyessy, L., 1998. *Thermoelement-Praxis. Neue theoretische Grundlagen und deren Umsetzung*. 3. Auflage. Vulkan-Verlag, Essen.
- [108] Bertoldi, M., Bucheli, O., and Ravagni V., A., 2016. “High-efficiency cogenerators from SOLIDpower SpA”. In Proceedings of 12th European SOFC & SOE Forum 2016.
- [109] Jülich Forschungszentrum, 2017. Anniversary for Jülich’s Slow Burner: Fuel Cell Running for 10 Years. <https://www.fz-juelich.de/SharedDocs/Pressemitteilungen/UK/EN/2017/2017-08-07-jubilaem-sofc.html>. Accessed: 2018-06-22.
- [110] Japan Gas Association, 2017. 家庭用燃料電池「エネファーム」累積20万台突破について. <http://www.gas.or.jp/newsrelease/2017ef20.pdf>. Accessed: 2018-05-19.

- [111] Bloom Energy, 2017. Energy server 5 datasheet. <https://www.bloomenergy.com/sites/default/files/es5-200kw-datasheet.pdf>. Accessed: 2018-06-16.
- [112] SOLIDpower, 2016. Bluegen datasheet. [http://www.solidpower.com/fileadmin/user\\_upload/pages/Logos\\_materialien/SOLIDpower\\_BlueGEN\\_Brochure\\_UK\\_web.pdf](http://www.solidpower.com/fileadmin/user_upload/pages/Logos_materialien/SOLIDpower_BlueGEN_Brochure_UK_web.pdf). Accessed: 2018-06-16.
- [113] Convion, 2018. Products. <http://convion.fi/products/>. Accessed: 2018-05-20.
- [114] Fontell, E., 2018. Personal communication via e-mail, July.
- [115] Yoda, M., Inoue, S., Takuwa, Y., Yasuhara, K., and Suzuki, M., 2017. "Development and Commercialization of New Residential SOFC CHP System". *ECS Transactions*, **78**(1), May, pp. 125–132.
- [116] Elsevier Ltd., 2017. "Kyocera develops first 3 kW SOFC unit for small business cogen". *Fuel Cells Bulletin*, **2017**(7), July, p. 5.
- [117] Sunfire, 2018. Sunfire-PowerPlus. <https://www.sunfire.de/en/products-and-technology/sunfire-powerplus>. Accessed: 2018-06-17.
- [118] Huatsing Power, 2018. Kilowatt SOFC power generation system. [http://en.huatsing-power.com/products\\_detail/productId=61.html](http://en.huatsing-power.com/products_detail/productId=61.html). Accessed: 2018-06-21.
- [119] Buderus, 2018. Datenblatt Logapower FC10. [https://www.buderus.de/de/produkte/catalogue/alle-produkte/102411\\_logapower-fc10](https://www.buderus.de/de/produkte/catalogue/alle-produkte/102411_logapower-fc10). Accessed: 2018-06-22.
- [120] Atrex Energy, Inc. , 2018. Remote Power Generator Technical Data. [http://www.atrexenergy.com/assets/uploads/files/ARP-RP\\_Combined\\_Technical\\_Specs\\_12-05-16.pdf](http://www.atrexenergy.com/assets/uploads/files/ARP-RP_Combined_Technical_Specs_12-05-16.pdf). Accessed: 2018-06-21.
- [121] Hexis, 2018. Die Daten von Galileo 1000 N auf einen Blick. <http://www.hexis.com/de/systemdaten>. Accessed: 2018-06-17.
- [122] Sunfire, 2018. Sunfire-Home. <https://www.sunfire.de/en/products-and-technology/sunfire-home>. Accessed: 2018-06-17.
- [123] Sunfire, 2018. Sunfire-Remote. <https://www.sunfire.de/en/products-and-technology/sunfire-remote>. Accessed: 2018-06-17.
- [124] New enerday, 2018. Fuel cell system EN 200. [http://www.new-enerday.com/wp-content/uploads/2017/04/Product\\_sheet\\_EN200\\_en-1.pdf](http://www.new-enerday.com/wp-content/uploads/2017/04/Product_sheet_EN200_en-1.pdf). Accessed: 2018-06-21.
- [125] New enerday, 2018. Fuel cell system EN 400. [http://www.new-enerday.com/wp-content/uploads/2017/04/Product\\_sheet\\_EN400\\_en-1.pdf](http://www.new-enerday.com/wp-content/uploads/2017/04/Product_sheet_EN400_en-1.pdf). Accessed: 2018-06-21.
- [126] Verein Deutscher Ingenieure, 1991. VDI/VDE 2041: Measurement of Fluid Flow with Primary Devices - Orifice Plates and Nozzles for Special Applications.

## Bibliography

---

- [127] Brennan, J. A., McFaddin, S. E., Sindt, C. F., and Kothari, K. M., 1989. "The influence of swirling flow on orifice and turbine flowmeter performance". *Flow Measurement and Instrumentation*, **1**(1), Oct., pp. 5–8.
- [128] Zimmermann, H., 1999. "Examination of disturbed pipe flow and its effects on flow measurement using orifice plates". *Flow Measurement and Instrumentation*, **10**(4), Dec., pp. 223–240.



# List of Academic Activities

## Assistant for the following Bachelor's level courses

- Dynamique des systèmes mécaniques (dynamic effects in mechanical design), 2014
- Systèmes mécaniques (mechanical systems), 2015, 2016, and 2017

## Supervisor for the following projects

Below a list of supervised semester projects (SP) within Bachelor's or Master's level studies, Master's projects (MP), or internships. The projects marked in **bold** contributed to this thesis. The author would like to thank all the students for their fruitful collaboration.

### Mechanical design

- Rémi Beall, Julien Schneider (2015): Conception d'un Vélo Électrique Pliable II, SP
- Timothée Frei, Tom Voiblet, Julien Schneider (2015): Vélo Électrique Pliable III, SP
- Timothée Frei, Tom Voiblet (2016): Vélo Électrique Pliable IV, SP
- Emmanuelle Burdet (2016): Formulary for the mechanical systems cours, 1-month internship
- Etienne Droz (2018): System optimization of a submerged pressure differential Wave Energy Converter, MP at UC Berkeley, USA

### System simulation

- **Dirix Pietro (2018): Transient Simulation of an SOFC system, SP**

### Turbomachinery

- Cyril Picard (2015): Small-Scale Gas Turbine Engines, SP
- **Conti Romain (2015): Simulation of a Radial Fan using Ansys CFX, SP**
- **Konstantinos Drakopoulos (2015): Integration of Real Gas Properties and Grid Generation Functionalities to a Streamline Curvature Method Code, SP**
- Jordan Holweger (2015): High-Speed Turbopump Design for ORC Applications, SP
- **Luca Massera (2017): Blade Tip Loss in a Small-Scale Fan, SP**
- Arno Aeschbacher (2017): Numerical and Experimental Performance Investigations on a Reduced-Scale Centrifugal Compressor by using Variable Inlet Guide Vanes, MP

## List of Academic Activities

---

- **Bastien Rauzier (2018): Implementation and testing of a control for a radial turbine, sizing of a flow straightener, assembly of a differential pressure measurement device , 3-month internship**
- **Pierre Nibourel (2018): CFD simulation for a grooved thrust gas bearing, 3-month internship**
- **Marcos Armenteras Font (2019): Analytical and numerical investigation of a small-scale radial steam turbine, MP**

## List of courses

The author attended following courses:

### EPFL

- Modelling, optimization, design, and analysis of integrated energy systems (2 ECTS credits)
- Object oriented and component based programming techniques for complex energy systems development (4 ECTS credits)
- Summer school in rotordynamics (1 ECTS credit)

### Eurotech Universities

- Integrated approach to energy systems / Eurotech summer school (4 ECTS credits)

### Innosuisse - Swiss Innovation Agency

- Business concepts (4 ECTS credits)

### Technology Transfer Office (TTO) at EPFL

- MINTT: Management of innovation and technology transfer (2 ECTS credits)

# List of Publications

## Journal papers

- Wagner, P. H., Wullemin, Z., Diethelm, S., Van herle, J., and Schiffmann, J., 2017. “Modeling and Designing of a Radial Anode Off-Gas Recirculation Fan for Solid Oxide Fuel Cell Systems”. *Journal of Electrochemical Energy Conversion and Storage*, 14(1). DOI 10.1115/1.4036401.
- Wagner, P. H., Wullemin, Z., Diethelm, S., Van herle, J., and Schiffmann, J., 2019. “Integrated System Simulation and Optimization of a Novel Concept for a Thermally-Driven Anode Off-Gas Recirculation Fan for Solid Oxide Fuel Cell Systems”. (being prepared)
- Wagner, P. H., Wullemin, Z., Diethelm, S., Van herle, J., and Schiffmann, J., 2019. “Experimental Testing of a Solid Oxide Fuel Cell System with a Novel Thermally-Driven Anode Off-Gas Recirculation Fan”. (being prepared)

## Proceedings

- Wagner, P. H., Van herle, J., and S., Schiffmann, J., 2019. “Theoretical and experimental investigation of a small-scale, high-speed, and oil-free radial anode off-gas recirculation for solid oxide fuel cell systems”. Proceedings of the ASME 2019 Turbomachinery Technical Conference & Exposition Turbomachines for Clean Power and Propulsion Systems, Turbo Expo 2019, June 17 - 21, 2019, Phoenix, USA. (accepted for conference and suggested for journal publication)
- Singh, V., Wagner, P. H., Wullemin, Z., Diethelm, S., Schiffmann, J., and Van herle, J., 2015. “Towards the Next-Generation of Solid Oxide Fuel Cell Systems”. *ECS Transactions* 2015, 68(1). DOI 10.1149/06801.2373.

## Conferences

- Wagner, P. H., Wullemin, Z., Diethelm, S., Schiffmann, J., and Van herle, J., 2016. “Modelling and designing of a radial anode off-gas recirculation fan for a SOFC system”. MODVAL 13, Symposium for Fuel Cell and Battery Modeling and Experimental Validation, Lausanne, Switzerland, March 22-23, 2016. (lecture)

## List of Publications

---

- Wagner, P. H., Singh, V., Wullemin, Z., Diethelm, S., Van herle, J., and Schiffmann, J., 2015. “Radial Blower Design and Simulation for Small-Scale SOFC with Hot and Cold Anode Off-Gas Recirculation”. ECS Conference on Electrochemical Energy Conversion & Storage with SOFC-XIV, Glasgow, UK, July 25-31, 2015. (poster presentation)

## Patent

- Zacharie Wullemin, Daniel Favrat, Jan Van Herle, Jürg Schiffmann, and Patrick Wagner. “SOFC System With Anode Off-Gas Recirculation”. EP18188237.4 (patent filed)

# Curriculum Vitae

---

## Patrick Hubert Wagner

---

Nationality                      German

---

## Education

---

04/2014 - 04/2019            **Laboratory for Applied Mechanical Design (LAMD), École Polytechnique Fédérale de Lausanne (EPFL), Switzerland**  
Doctoral student

10/2007 - 02/2013            **Technical University of Munich (TUM), Germany**  
Diploma Aerospace, focus on "Flight Propulsion and Turbomachinery" and "Numerical Simulation"

01/2011 - 05/2011            **University of Glasgow, Scotland**  
Erasmus exchange in General Engineering

---

## Practical Experience

---

10/2012 - 08/2013            **Fraunhofer Institute for Solar Energy Systems (ISE), Freiburg, Germany**  
Research assistant in the area of *Energy Efficient Buildings* (part-time)

04/2012 - 09/2012            **German Aerospace Center (DLR), Stuttgart, Germany**  
Diploma thesis at the *Institute of Solar Research* (full-time)

09/2010 - 12/2010            **CFDnetwork Engineering, Munich, Germany**  
Practical work experience (full-time):

04/2010 - 08/2010            **The Bavarian Center for Applied Energy Research (ZAE Bayern), Garching, Germany**  
Term paper at the *Technology for Energy Systems and Renewable Energy* division (part-time)

03/2009 - 06/2009            **Technical University of Munich (TUM), Germany**  
Student research assistant at the *Institute of Machine Elements* (part-time)

---

## Alternative military service

---

08/2006 - 08/2007            Voluntary social year in Buenos Aires, Argentina

---

## Language Skills

---

German                              Native

English                              TOEFL iBT with total score of 107/120 (proficient user C1)

Spanish                              DELE Nivel Intermedio (high-intermediate level B2)

French                                B2 (self-evaluation)

---

## Activities

---

Mountain sports                Swiss Alpine Club, Neuchâtel section

Skiing                              Swiss Snowsports "Kids Instructor" and J+S monitor for ski sports  
Monitor at Swiss Ski School Neuchâtel-Les Bugnenets (ESSNB)

Swimming                        German Life Saving Association silver lifeguard

Cycling

